

Dissertation
submitted to the
Combined Faculties of the Natural Sciences and Mathematics
of the Ruperto-Carola-University of Heidelberg, Germany
for the degree of
Doctor of Natural Sciences

Put forward by
Alison Mairi Wallace Mitchell Bsc MPhys
born in Brighton, United Kingdom
Oral examination: 28-07-2016

**Optical Efficiency Calibration for Inhomogeneous IACT
Arrays and a Detailed Study of the Highly Extended
Pulsar Wind Nebula HESS J1825-137**

Referees: Prof. Dr. Werner Hofmann
Prof. Dr. Stefan Funk

To my father

Abstract

Very High Energy (VHE) γ -ray astronomy using Imaging Atmospheric Cherenkov Telescopes (IACTs) is entering an era of hybrid arrays (such as H.E.S.S. II and CTA), comprising telescopes of varied specifications to enhance the accessible energy range and angular resolution. New algorithms for telescope optical efficiency calibration are developed and adapted for multi-type arrays, for both absolute light yield calibration using muons, and for relative calibration through comparison of shower images. In comparison to previous methods, the stability and flexibility of these algorithms are considerably improved. These will play an important role for the future CTA observatory. The use of multi-type IACT arrays in providing an increased understanding of astrophysical objects and environments is demonstrated through an in-depth study of the Pulsar Wind Nebula HESS J1825-137, known to be highly extended with the presence of strong energy dependent morphology. In particular, measurements of HESS J1825-137 across the entire available energy range allow the particle transport inside the nebula to be constrained, favouring advection over diffusion as the dominant mechanism. Together with X-ray data, a map of the magnetic field of the nebula can be made through spectral modelling. It will also be shown that HESS J1825-137, at 100 pc across, is one of the biggest pulsar wind nebulae to have been discovered yet.

Kurzfassung

Die sehr hochenergetische γ -Astronomie mit Imaging Atmospheric Cherenkov Telescopes (IACTs) betritt gerade eine neue Ära, in der Teleskope verschiedener Bauart in hybride Arrays (wie H.E.S.S. II und CTA) zusammengefasst werden, um den erfassbaren Energiebereich zu vergrößern und Winkelauflösung zu verbessern. Sowohl für absolute Lichtausbeutekalibration mit Myonen, als auch für relative Kalibration durch den Vergleich von Luftschauerbildern, werden neue Kalibrations-Algorithmen für die Optische Effizienz des Teleskopes entwickelt, und für hybride Arrays angepasst. Im Vergleich zu vorherigen Methoden wird die Stabilität und Flexibilität der Kalibrations Algorithm deutlich verbessert. Dies wird für das zukünftige CTA Observatorium eine wichtige Rolle spielen. Anhand einer ausführlichen Studie des Pulsar Wind Nebels HESS J1825-137, bekannt als sehr ausgedehnt und mit starker energie-abhängiger Morphologie, wird gezeigt dass hybride IACT Arrays zum einen erhöhten Verständnis astrophysikalischer Objekte und ihre Umgebungen beitragen können. Insbesondere ermöglichen Messungen von HESS J1825-137 über den gesamten verfügbaren Energiebereich verschiedene Modelle von Teilchenstransport (innerhalb des Nebels) einzuschränken. Advektion wird gegenüber Diffusion als der dominierende Mechanismus bevorzugt. Zusammen mit Röntgendaten kann durch spektrale Modellierung eine Karte des Magnetfeldes des Nebels erstellt werden. Es wird auch gezeigt, dass HESS J1825-137 mit ~ 100 pc einer der größten Pulsar Wind Nebels ist die bisher entdeckt wurden.

Contents

1	Introduction	1
1.1	Introduction to Cosmic Rays	1
1.1.1	γ -ray Astronomy	2
1.2	Acceleration Mechanisms	2
1.2.1	Diffusive Shock Acceleration	3
1.2.2	Acceleration Sites	4
1.3	Emission Mechanisms	5
1.3.1	Bremsstrahlung	6
1.3.2	Synchrotron Radiation	6
1.3.3	Inverse Compton Scattering	7
1.3.4	Pion Decay	8
1.3.5	Summary	8
2	The Imaging Atmospheric Cherenkov Technique	10
2.1	Extensive Air Showers	10
2.1.1	Electromagnetic Showers	11
2.1.2	Hadronic Showers	12
2.1.3	Cherenkov Light Production	13
2.2	Imaging Atmospheric Cherenkov Telescopes	15
2.2.1	Imaging Atmospheric Cherenkov Technique	16
2.2.2	Current IACT Experiments	17
2.2.3	Cherenkov Telescope Array	18
2.3	The H.E.S.S. Experiment	19
2.3.1	H.E.S.S. II	20
2.3.2	Optics of the H.E.S.S. Telescopes	20
2.3.3	Cameras	21
2.3.4	Data Quality	21
2.4	Calibration Methods within H.E.S.S.	22
2.4.1	Camera Calibration	22
2.4.2	Pointing	23
2.4.3	Optical Efficiency Calibration	24
2.5	Event Reconstruction	24
2.5.1	Image Cleaning	25
2.5.2	Hillas Reconstruction	25
2.5.3	Data Analysis in H.E.S.S. Phase II	27

2.6	Background Estimation	27
2.6.1	Ring Background	28
2.6.2	Reflected Background	29
2.6.3	Signal Extraction and Significance	29
2.7	Monte Carlo Simulations	29
2.8	Performance of H.E.S.S. II	30
2.8.1	Angular Resolution	30
2.8.2	Effective Area	31
2.8.3	Energy Resolution	32
2.8.4	Sensitivity	32
2.9	Morphology and Sky Maps	34
2.10	Spectral Analysis	34
3	Optical Efficiency Calibration using Muons	36
3.1	Atmospheric Muon Production	37
3.1.1	Geometrical Description	37
3.1.2	Broadening of the Muon Ring	40
3.2	Optical Efficiency Calibration using Muons	42
3.2.1	Requirements for Muon Calibration for H.E.S.S. II	43
3.2.2	Usage of Muon Efficiency	44
3.3	Identification of Muon Images	45
3.3.1	Circle Fitting	45
3.3.2	Image Selection and Cleaning	46
3.4	Optical Efficiency Determination	46
3.4.1	Mirror Description	47
3.4.2	Interpolation of Flat Mirror Distance	47
3.4.3	2D Image Fit Model	51
3.5	Performance	52
3.5.1	Monte Carlo Studies	53
3.5.2	Performance on Data and Consistency Checks	54
3.6	Optical Efficiency Variation	57
3.6.1	Dependence on Hardware	59
3.6.2	Correlation with Other Muon Image Parameters	60
3.6.3	Positional Variation	61
3.6.4	Influence of Broken Pixels	63
3.6.5	Dependence on Environmental Parameters	65
3.6.6	Cosmic Ray Primaries	66
3.7	Application to Data Analysis	69
3.7.1	Definition of Muon Phases	70
3.7.2	Influence on the Effective Area	71
3.7.3	Statistical Variation	71
3.7.4	Conclusions on Muon Analysis	73
3.8	Muon Calibration in CTA	73
3.8.1	Performance for CTA	78

3.9	Conclusions on Muon Calibration	80
4	Cross Calibration using Event Images	82
4.1	Telescope Cross Calibration	82
4.2	Intercalibration using Cosmic Ray Event Images	82
4.2.1	Event Selection	83
4.2.2	Image Size Approach	84
4.2.3	Reconstructed Energy Approach	86
4.2.4	Monte Carlo Linearity	87
4.3	Application to Telescopes of Multiple Sizes	89
4.3.1	Adaptation of Image Size Approach	89
4.3.2	Adaptation of Reconstructed Energy Approach	91
4.4	Variation with Zenith Angle	93
4.5	Conclusions on Cross Calibration with H.E.S.S.	95
4.6	Cross Calibration for the Cherenkov Telescope Array	96
4.6.1	Intercalibration using Image Size	97
4.6.2	Intercalibration using Reconstructed Energy	98
4.6.3	Cross Calibration Principle	98
4.6.4	Monte Carlo Studies	99
4.6.5	Simulation Results	102
4.6.6	Other Studies	106
4.6.7	Conclusions on Cross Calibration for CTA	109
5	Complementarity of Optical Efficiency Calibration Methods	111
5.1	H.E.S.S. Optical Efficiency Calibration	112
5.1.1	Correlation of the Muon Efficiency with Image Size Cross Calibration	112
5.1.2	Combination of the Muon Efficiency with Reconstructed Energy Cross Calibration	113
5.1.3	Reversal of the Implementation	114
5.2	Scheme for CTA Optical Efficiency Calibration	117
5.2.1	Implementation of Calibration Methods	117
5.3	Further Applications	118
5.3.1	Calibration of Other Parameters using Muons	118
5.3.2	Cross Calibration of Other Variables	119
6	The Pulsar Wind Nebula HESS J1825-137	120
6.1	Introduction to Pulsar Wind Nebulae	120
6.1.1	Supernovae and Neutron Stars	120
6.1.2	Pulsars	121
6.1.3	Pulsar Wind Nebulae	124
6.2	Introducing HESS J1825-137 and its Field of View	127
6.3	Analysis of Currently Available H.E.S.S. Data	129
6.4	Cross Calibration	131
6.5	Morphology and Sky Maps	133
6.6	Spectral Analysis	137

6.6.1	Spectral Map	138
6.6.2	Spectral Softening	140
6.7	Morphological Analysis	147
6.7.1	Azimuthal Emission Profiles	147
6.7.2	Slice Emission Profiles	147
6.7.3	Energy Dependent Morphology	151
6.8	Conclusions on Analysis of HESS J1825-137	159
7	HESS J1825-137 in Context	160
7.1	Multiwavelength Data	160
7.1.1	Radio, Infrared and Optical Data	160
7.1.2	X-ray Data	161
7.1.3	γ -ray Data	163
7.2	Extent Measurements and Transport	166
7.2.1	Diffusive Particle Transport	167
7.2.2	Advective Particle Transport	169
7.2.3	Improving Transport Model Trends	170
7.3	Mapping the Magnetic Field	171
7.3.1	X-ray (Suzaku) Spectral Points	172
7.3.2	Fitting the Spectral Energy Distributions	173
7.3.3	Physical Properties of Nebula Regions	176
7.4	Previous Models of HESS J1825-137	180
7.5	One-Zone Pulsar Wind Nebula Model	181
7.5.1	Free Expansion Model: description	182
7.5.2	Parameter Constraints	184
7.5.3	Model 1	186
7.5.4	Model 2	186
7.5.5	Reverse Shock Evolution	188
7.6	Conclusions on Modelling of HESS J1825-137	193
8	Conclusion	195
A	Further Applications of Pair-wise Telescope Comparisons	197
A.1	Cosmic Ray Rate Comparison	197
A.2	Pointing Calibration	199
A.3	Light Yield	202
A.4	Timing Calibration	208
A.4.1	Comparisons Between Telescopes of the Same Type	208
A.4.2	Comparisons Between Telescopes of Different Types	208
A.4.3	Application	211
B	Derivation of the Mirror Distance for Muons	214
C	HESS J1825-137 Emission Profiles	217

1 Introduction

1.1 Introduction to Cosmic Rays

In 1912, Victor Hess made a balloon flight during which he measured the rate of ionisation radiation as a function of altitude. Although this rate initially decreased with increasing altitude as expected, beyond ~ 1 km, it started to noticeably increase. Hess concluded that this ionising radiation came from beyond the Earth's atmosphere, thereby discovering cosmic rays, for which he was awarded the 1936 Nobel prize [1].¹ Ever since then, efforts to understand where this cosmic radiation came from have been ongoing, with a large amount of data from numerous successive experiments currently available. Although occurring at a very low rate, some cosmic rays are surprisingly energetic, and hint at the presence of very powerful sources in the universe. The all particle spectrum of cosmic rays (figure 1.1), as measured over more than 10 orders of magnitude in energy and by many different experiments, exhibits two main features; a change in spectral index or 'spectral break' at $\sim 10^{15} - 10^{16}$ eV (commonly referred to as the "knee") and 10^{19} eV (the "ankle") (p.550 [2]), although recently evidence has been growing for an additional spectral feature (a "second knee" between the knee and the ankle [3]).

Nowadays, it is generally thought that solar flares from the sun account for the lowest energy cosmic rays, whilst galactic sources (such as supernovae) are directly responsible for cosmic ray acceleration up to the knee. The solar wind effectively shields the Earth from the majority of the low energy cosmic rays due to galactic sources. Beyond the spectral knee around $\sim 10^{15}$ eV, cosmic rays can no longer be confined by the magnetic fields and length scales of galactic objects such as supernova remnants, but are able to stream away from the source environment. Changes in the spectral index of cosmic rays are generally interpreted to indicate a change in acceleration mechanism. The knee and ankle features are thought to mark various stages in the transition from galactic to the extragalactic sources, the latter being potentially responsible for the highest energy cosmic rays [3]. However, the exact nature of the origin and location of these transitions, often associated with a change in the cosmic ray composition, is still under debate. An ultimate limit on the energies of cosmic rays is imposed by the Greisen-Zatsepin-Kuzmin (GZK) cut-off at around 5×10^{19} eV for protons (although heavier nuclei may reach higher energies), arising from interactions and energy loss of protons with Cosmic Microwave Background (CMB) photons [4, 5].

¹This prize was shared with Carl Anderson, who discovered the positron by studying Cosmic Rays.

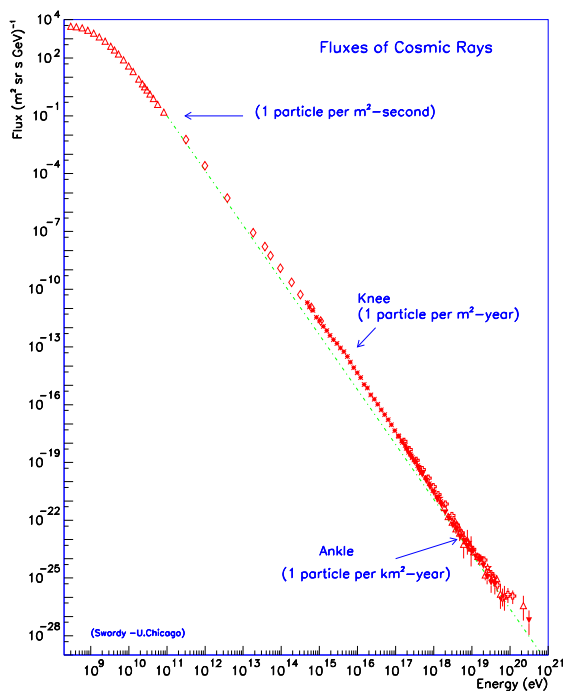


Figure 1.1: Spectrum of Cosmic Rays spanning 12 orders of magnitude in energy, taken from [6]. Data is compiled from several different experiments, major features such as the knee and ankle are indicated. The majority of the spectrum follows a power law with $\text{Flux} \propto E^{-2.7}$.

1.1.1 γ -ray Astronomy

Charged particles accelerated to high energies in the environments of extreme astrophysical objects form the cosmic ray flux detected at Earth, yet are deflected on their path through the universe by magnetic fields in the ambient medium, thereby losing all directional sense of their birth location and forming an isotropic flux at Earth. However, at the source location, highly energetic γ -rays are also produced through the interactions of charged particles with their environment. In contrast to cosmic rays, γ -ray photons are neutral and therefore not deflected by magnetic fields, retaining a sense of their original direction upon arrival at Earth. Hence, γ -ray observations form a useful probe to study the environments of the most powerful astrophysical accelerators.

1.2 Acceleration Mechanisms

Astrophysical acceleration mechanisms need to account for the observed characteristic power law energy spectrum of high energy cosmic rays and γ -rays:

$$\frac{dN}{dE} \propto E^{-\Gamma}, \quad (1.2.1)$$

with Γ generally around 2–3 (to match the observed cosmic ray spectrum). Additionally, they need to account for particle acceleration up to at least the highest energies of observed cosmic rays, around 10^{20} eV.

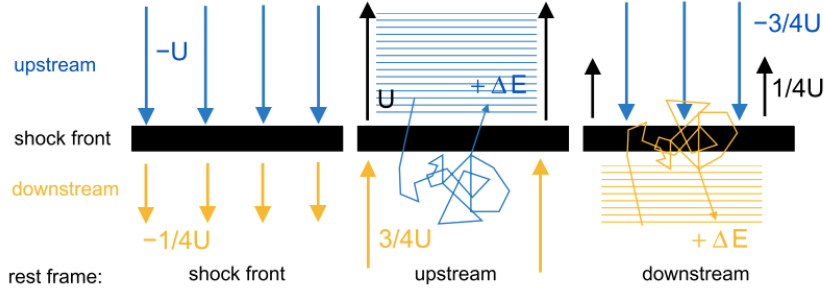


Figure 1.2: Schematic of Diffusive Shock Acceleration. Left: in the rest frame of the shock front, the upstream gas is moving with velocity U and the downstream gas with velocity $\frac{1}{4}U$. Middle: in the rest frame of the upstream medium, the shock front is advancing with velocity $\frac{3}{4}U$. Right: in the rest frame of the downstream medium, the shock front is advancing with velocity $\frac{3}{4}U$. Particles gain an energy ΔE on each shock front crossing. Figure taken from [7].

1.2.1 Diffusive Shock Acceleration

Diffusive Shock Acceleration (DSA) describes the acceleration of particles within the vicinity of strong shocks, where the energy gain is first order in the shock velocity [8]. Regardless of whether the particles are upstream or downstream of the shock front, in the particle rest frame, the gas is seen to be moving towards the particle with a velocity $\frac{3}{4}U$, where U is the velocity of the shock front through the medium. This is in the case of strong shocks in a fully ionised or monatomic gas, with the specific ratio of heat capacities $\gamma = \frac{5}{3}$. In strong shocks, a compression factor (ratio of the densities upstream ρ_1 and downstream ρ_2 of the shock) of $\rho_2/\rho_1 \approx \gamma + 1/\gamma - 1 = 4$ describes the shock front. By the equation of continuity, $\rho_1 v_1 = \rho_2 v_2$, the speed downstream of the shock, v_2 is less than the upstream speed v_1 by $v_2 = \frac{1}{4}v_1$. Considering a test particle in the medium, the particle gains energy as it crosses the shock, and is scattered or isotropised in the rest frame of the gas on one side of the shock, losing the sense of its original direction. This enables the particle to make multiple crossings of the shock front; it can be shown that the average gain in energy per shock front crossing is:

$$\left\langle \frac{\Delta E}{E} \right\rangle = \frac{2}{3} \left(\frac{V}{c} \right), \quad (1.2.2)$$

or double this in one round trip (two shock crossings), where $V = \frac{3}{4}U$ is the velocity of the gas approaching the particle. As shown in figure 1.2, the particle becomes scattered and isotropised in the flow on either side of the shock front after each crossing, gaining in energy by an amount ΔE each time. Defining $\beta = E/E_0$ as the energy gain after one collision and P as the probability that the particle remains in the shock region after one collision, then the resulting energy spectrum for particles accelerated by the diffusive shock acceleration mechanism is also of power law form:

$$N(E)dE \propto E^{-1 + \frac{\ln P}{\ln \beta}} dE = E^{-2} dE, \quad (1.2.3)$$

since $\ln P/\ln \beta = -1$. Therefore, achieving the $\sim O(-2)$ index of the cosmic ray spectrum requires only that particle acceleration takes place in the vicinity of strong shocks [8]. Acceleration via the diffusive shock mechanism can proceed within supernovae up to

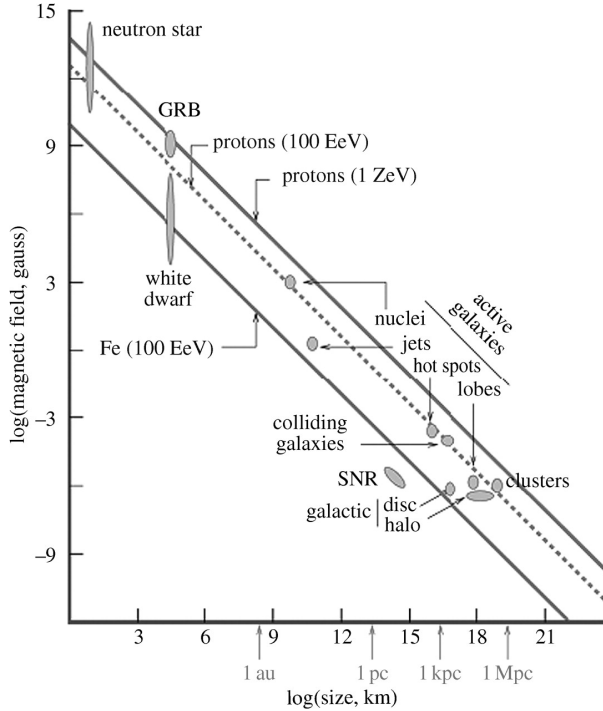


Figure 1.3: Various sites of astrophysical particle acceleration, plotted as a function of their magnetic field and physical size. Source classes must lie above the diagonal lines indicating the maximum energy from equation (1.2.4) to accelerate particles of a given charge to that energy [9] (figure taken from [10]).

energies $\sim O(10^{15})$ eV or potentially even higher, until the supernova shock wave dissipates. In order for particles to be accelerated beyond this limit up to 10^{18} eV energies of the most energetic observed cosmic rays, other influencing factors such as the magnetic fields in shock regions have to be considered, which increase the time for which particles are confined to the accelerator.

1.2.2 Acceleration Sites

Particle acceleration via mechanisms as outlined in section 1.2 can take place in a variety of different astrophysical environments. Potential sites of emission up to the highest observed cosmic ray energies of 10^{20} eV are shown in figure 1.3, plotted as a function of their magnetic field and physical size. For particles to be accelerated to high energies, the Larmor radius² of their gyration around the magnetic field lines must be less than the physical size of the object. This simple criteria on astrophysical accelerators leads to a maximum energy E_{\max} achievable for a given accelerator of size L and magnetic field B :

$$E_{\max} = Ze\beta cBL, \quad (1.2.4)$$

where Ze is the charge of the cosmic ray particle and βc its velocity [9]. From equation (1.2.4), stronger magnetic fields and heavier nuclei lead to larger maximum energies, E_{\max} . For the same accelerator size and properties, heavier nuclei (such as Iron) can be accelerated to higher energies than lighter nuclei (such as protons); this relation is confirmed

²The Larmor radius r_L , is given by $r_L = \gamma mc^2 / qcB$, where m, q and γ are the mass, charge and Lorentz factor of the particles respectively, B is the magnetic field strength and c is the speed of light [2].

observationally in the change in cosmic ray composition towards a larger contribution from heavier nuclei at higher energies. In figure 1.3, lines corresponding to the minimum B and L required for acceleration to energies of 100 EeV (10^{20} eV) and 1 ZeV (10^{21} eV) are indicated for protons and of 100 EeV for Iron. Source classes must lie above these lines in order to accelerate particles to such energies; supernovae lie below all three lines, with magnetic field strengths around 10^{-6} G and sizes of a few parsecs (pc), and are hence clearly not responsible for the highest energy cosmic rays, although a sizeable local contribution is nevertheless expected.

Example accelerators, and the source classes which make up the majority of detected sources in the VHE regime include binary stellar systems (comprising a compact object, such as a neutron star or white dwarf, and a normal or massive star in orbit around each other), supernova remnants, pulsars and pulsar wind nebulae at the galactic level. On extragalactic scales, VHE γ -ray emission has been detected from starburst galaxies and active galactic nuclei, whilst additional potential sources of VHE emission not yet verified include Gamma Ray Bursts (GRBs), galaxy clusters and some dark matter scenarios. As can be seen from figure 1.3, extragalactic sources tend towards larger length scales or higher magnetic fields than comparable Galactic sources, leading them to be considered plausible candidate accelerators for the highest energy cosmic rays above the ankle at around 10^{18} eV.

From these potential acceleration sites, the physics of pulsars and pulsar wind nebulae (PWNe) will be covered in more detail in chapter 6; the remaining source classes are well covered by recent comprehensive reviews of the field [11, 12, 13, 14].

1.3 Emission Mechanisms

As the accelerated particles travel through the region local to the source and beyond, they undergo energy losses through a variety of mechanisms, several of which lead to the production of VHE γ -rays. Strong, VHE γ -ray signals can therefore be expected from environments where there is a significant population of accelerated particles. The evolution of the cosmic ray population over time is well described by the diffusion loss equation:

$$\frac{\partial N(E)}{\partial t} = Q(E, t) + D\nabla^2 N(E) + \frac{\partial}{\partial E} [b(E)N(E)] , \quad (1.3.1)$$

where $Q(E, t)$ is a source term describing the rate and spectrum of particles being injected into the system, the second term in (1.3.1) describes diffusion of particles along spatial gradients with a diffusion coefficient D , and the last term describes energy losses, where $b(E) = -dE/dt$ is a sum of all the contributing emission processes. The dominant processes causing energy loss from a leptonic particle population leading to the production of VHE γ -rays include Bremsstrahlung, synchrotron radiation and Inverse Compton scattering, outlined in sections 1.3.1 to 1.3.3 below.

In hadronic particle populations, equation (1.3.1) can be used to describe the time evolution of each nuclear species separately, with the inclusion of additional terms describing the rate of gains and losses due to spallation (fragmentation of a nucleus due to an inelastic collision) and of losses due to radioactive decay. From a hadronic particle

population, VHE γ -rays may be produced from the decay of pions, created in such particle collisions; this is covered in section 1.3.4.

1.3.1 Bremsstrahlung

Electrons accelerated in the vicinity of the electrostatic fields due to other atomic nuclei and ions produce electromagnetic radiation. As electrons are more usually decelerated, losing energy to the photons created, the emission is termed ‘‘Bremsstrahlung’’ or braking radiation (p.88 [15]). Bremsstrahlung energy losses dominate over ionisation losses for electrons with energies above a critical energy threshold, of $\simeq 350$ MeV for electrons in hydrogen gas [16]. The lifetime of electrons with energy E_e to Bremsstrahlung losses, t_{br} , varies with the average energy loss rate $-dE_e/dt$ as:

$$t_{br} = \frac{E_e}{-dE_e/dt} \simeq 4 \times 10^7 n^{-1} (\text{cm}^{-3}) \text{yr} , \quad (1.3.2)$$

where n is the number density of the ambient gas. Since $-dE_e/dt \propto E_e$, the lifetime t_{br} is independent of the energy of the electrons, such that Bremsstrahlung losses alone do not modify the shape of the electron spectrum. Whilst this emission mechanism contributes to astrophysical high energy γ -ray production particularly in dense gaseous regions, at very high energies, the emission tends to be dominated by one of the following processes.

1.3.2 Synchrotron Radiation

For relativistically moving electrons in the vicinity of a magnetic field, due to the magnetic force, there is a component of the electrons velocity perpendicular to the magnetic field lines which induces circular motion of the electron around the field lines [8]. The electrons are thereby accelerated, emitting electromagnetic radiation that is linearly polarised in the plane of motion of the electrons. This emission is termed Synchrotron Radiation (p.592 [2]).³ On average, an electron loses energy by synchrotron radiation at a rate:

$$-\left(\frac{dE}{dt}\right) = \frac{4}{3} \sigma_T c U_{\text{mag}} \left(\frac{v}{c}\right)^2 \gamma^2 , \quad (1.3.3)$$

where γ is the Lorentz factor of an electron moving with velocity v , $\sigma_T = \frac{8\pi}{3} r_e^2 \approx 6.65 \times 10^{-25} \text{cm}^2$ is the Thomson scattering cross-section and $U_{\text{mag}} = B^2/2\mu_0$ is the energy density of the ambient magnetic field with field strength B .⁴ The lifetime of electrons losing energy by synchrotron radiation;

$$t_s = \frac{E_e}{-dE_e/dt} \propto B^{-2} E_e^{-1} , \quad (1.3.4)$$

decreases for high energy electrons in strong magnetic fields, to the extent that the lifetime is much shorter than the observed age for objects such as the Crab Nebula, implying continual acceleration of electrons within the source. For a monoenergetic population

³If motion along curved field lines dominates over the gyratory motion around the field line, then the ensuing emission is termed Curvature Radiation.

⁴Thomson scattering is the scattering of electromagnetic waves by free electrons moving non-relativistically.

of electrons with energy E_e , the characteristic energy E_s of the synchrotron photons produced is given by:

$$E_s \simeq 0.2B(10^{-5}\text{G})E_e^2(\text{TeV}) \text{ eV} , \quad (1.3.5)$$

such that for 100 TeV electrons in a 5 μG ambient magnetic field, synchrotron radiation of around 1 keV is produced [17].

1.3.3 Inverse Compton Scattering

Compton scattering occurs if a photon, with a wavelength much less than the size of an atom, is scattered by an (loosely bound) electron [2].⁵ This usually results in a loss of energy of the photon and gain in energy of the electron. Inverse Compton scattering refers to the opposite process; in systems with many electrons accelerated to high velocities, the electrons upscatter photons of the ambient radiation fields. Electrons lose energy via this process, imparting their energy to the photons, which are scattered up to VHE levels. The Inverse Compton scattering cross-section σ_{IC} can be expressed as a function of the initial energies of the photon $\omega_0 = h\nu$ and electron E_e only [17]. The total Inverse Compton scattering cross section is given by:

$$\sigma_{IC} = \frac{3\sigma_T}{8\varepsilon} \left[\left(1 - \frac{2(\varepsilon + 1)}{\varepsilon^2} \right) \ln(2\varepsilon + 1) + \frac{1}{2} + \frac{4}{\varepsilon} - \frac{1}{2(2\varepsilon + 1)^2} \right] , \quad (1.3.6)$$

where $\varepsilon = h\nu/m_e c^2$, and $E_e = m_e c^2$ in the rest frame of the electron [8]. At non-relativistic energies (the Thomson regime, $\varepsilon \ll 1$, in which the photon energy is much less than the electron rest mass energy in the centre of momentum frame), the cross-section approaches the Thomson cross-section σ_T ; $\sigma_{IC} \approx \sigma_T(1 - 2\varepsilon)$. However, at highly relativistic energies, the energy transfer between electrons and photons can no longer be treated as a continuous process, but must be considered in a discrete manner, as the electron loses a significant proportion of its energy on each interaction. This is termed the Klein-Nishina regime, with $\varepsilon \gg 1$, and the Inverse Compton cross-section can be approximated as $\sigma_{IC} \approx \frac{3}{8}\sigma_T \ln(4\varepsilon)/(\varepsilon)$. Although Inverse Compton scattering can occur between protons and photons as well as with electrons, the rate of proton interactions is suppressed with respect to electrons by a factor of $(m_e/m_p)^4$ [16].

In the Thomson regime, the rate at which an electron loses energy by Inverse Compton scattering is given by:

$$\frac{dE_e}{dt} = \frac{4}{3}\sigma_T c \omega_0 n_{ph} E_e^2 , \quad (1.3.7)$$

where n_{ph} is the number density of photons in the ambient radiation fields. In the relativistic Klein-Nishina regime, the energy loss rate takes the form:

$$\frac{dE_e}{dt} = \frac{3}{8} \frac{\sigma_T c n_{ph}}{\omega_0} (\ln(4\varepsilon) - 11/6) , \quad (1.3.8)$$

which is essentially independent of the electron energy, such that the fractional energy loss is greater in lower energy electrons, and the electron spectrum becomes harder (higher energy electrons forming a greater part of the spectrum) over time. In contrast, equation

⁵If the wavelength is much larger, then the scattering is termed Rayleigh scattering.

(1.3.7) shows that the energy losses in the Thomson regime depend on E_e^2 , such that higher energy electrons suffer a greater fractional energy loss, and the electron spectrum will become softer (more dominated by lower energy electrons) over time.

Typical examples of radiation fields which provide the ambient photons for Inverse Compton scattering include the dust of the interstellar medium, ambient starlight from other astrophysical objects, and the cosmic microwave background (CMB) radiation, with typical energy densities $\sim O(1\text{eV cm}^{-3})$.

For a monoenergetic population of electrons with energy E_e , the characteristic energy E_{IC} of the photons arising from Inverse Compton scattering is given by:

$$E_{IC} \simeq 5\omega_0(\text{meV})E_e^2(\text{TeV}) \text{ GeV} , \quad (1.3.9)$$

such that for 100 TeV electrons scattering off the CMB, (typical CMB photon energy $\sim 6 \times 10^{-4}\text{eV}$), Inverse Compton radiated photons of around 30 TeV are expected [17]. In the case that synchrotron and Inverse Compton photons arise from the same parent electron population, their characteristic energies (from equations (1.3.5) and (1.3.9)) are related through:

$$E_s(\text{keV}) \simeq 0.07E_{IC}(\text{TeV})B(10^{-5}\text{G}) . \quad (1.3.10)$$

The ratio of the expected fluxes of synchrotron $F_s(E_s)$ and Inverse Compton $F_{IC}(E_{IC})$ photons depends only on the magnetic field;

$$\frac{F_{IC}(E_{IC})}{F_s(E_s)} \simeq 0.1B^{-2}(10^{-5}\text{G}) , \quad (1.3.11)$$

which implies that the synchrotron component dominates over the Inverse Compton component only if the magnetic field exceeds at least $3.2\mu\text{G}$.

1.3.4 Pion Decay

Hadronic interactions, such as proton-proton or proton-nuclei collisions, often produce both charged and neutral pions as by-products of the interaction. The threshold energy for the production of neutral pions is $\sim 280 \text{ MeV}$. Charged pions decay mostly via the weak interaction into muons and neutrinos, whereas neutral pions undergo an electromagnetic decay $\pi_0 \rightarrow \gamma + \gamma$, with a much shorter lifetime (p.56 [15]). In regions of dense gas and ambient material with relativistically moving protons, the pions produced in these collisions are highly energetic, and their decay leads to the production of VHE γ -rays. In regions where hadronic interactions are dominant, this resulting VHE γ -ray spectrum exhibits a characteristic ‘pion bump’ at GeV - TeV energies.

1.3.5 Summary

The processes of Synchrotron Radiation and Inverse Compton scattering primarily originate from leptonic dominated particle populations, whereas pion decay accounts for VHE γ -rays from hadronic populations. Often, there are multiple possible emission mechanisms which could be responsible for emission from a given source; the term ‘hadronic

scenario” refers to the case where the emission is provided by pion decay, whereas the combination of Inverse Compton and Synchrotron radiation is termed the “leptonic scenario”. This degeneracy of emission mechanisms may be partially resolved by multiwavelength observations of a given source, forming a spectral energy distribution (SED); by fitting models of both scenarios to an SED, one scenario may be favoured over the other.

For leptonic particle populations in particular, the dominant loss processes affect the measured spectrum. The loss term $b(E) = A_1 + A_2E + A_3E^2$ in equation (1.3.1) is a sum of contributing processes; A_1 describes ionisation losses; A_2 encompasses both Bremsstrahlung and adiabatic losses (where the loss rate is proportional to the particle energy); and A_3 includes both synchrotron and Inverse Compton processes, where $-dE_e/dt \propto E_e$. Adiabatic losses typically arise due to the pressure exerted by a relativistic gas on its surroundings during (for example) the expansion of a supernova.

For a power law particle injection spectrum, $Q(E) \propto E^{-p}$ in equation (1.3.1), and in a steady state system with negligible diffusion, the dominant loss process modifies the observed particle spectrum. If ionisation loss dominates, the resulting particle spectrum follows $N(E) \propto E^{-(p-1)}$, whilst if synchrotron or Inverse Compton losses dominate, $N(E) \propto E^{-(p+1)}$. In the case of Bremsstrahlung losses dominating, the spectrum is unchanged.

These acceleration and emission processes are particularly relevant for studying VHE astrophysical sources, the primary goal of Imaging Atmosphere Cherenkov Telescope arrays, which will be introduced in the next chapter. Further consideration of the processes introduced in this chapter will form an important part of an in-depth study of the PWN HESS J1825-137 in chapters 6 and 7.

2 The Imaging Atmospheric Cherenkov Technique

To obtain a complete understanding of our universe, observations need to be undertaken across the entire electromagnetic spectrum. This ranges from the lowest energies and longest wavelengths in the radio regime, through infrared, microwave, visible, ultraviolet, X-ray and up to γ -rays at the highest energy end. The transparency of the atmosphere to electromagnetic radiation varies as a function of wavelength, thanks to the presence of various molecules in our atmosphere. Most noticeably, it is transparent in the optical and radio regimes, whilst being opaque to γ -rays. Consequently, in order to learn about the highest energies in our universe, observations have to take place either from above the atmosphere, or by using the atmosphere as part of the detector. Satellites have been launched to observe our universe in wavelength ranges which are opaque from the ground; including infrared, X-ray and γ -ray regimes. However, at the very highest energies, the affordable collection area of satellite based telescopes is no longer sufficient to detect the highest energy photons, and an alternative in the form of ground based γ -ray astronomy (and air shower physics) is used. This involves the detection of Extensive Air Showers; particle decay and interaction cascades generated in the atmosphere by highly energetic Cosmic Rays and γ -rays (see section 2.1).

2.1 Extensive Air Showers

Highly energetic ($\gtrsim O(\text{GeV})$) cosmic rays and individual γ -ray photons entering the Earth's atmosphere initiate an Extensive Air Shower (EAS), a cascade of particle collisions, scattering and decay, upon their first interaction. EAS fall into two main categories of hadronic and electromagnetic showers, depending on whether they originated from an initial charged hadron (proton dominated), or an energetic photon or lepton respectively. Hadronic EAS account for the majority of all air shower events, yet they arrive mostly isotropically from space. Whereas charged cosmic rays generally lose all sense of their arrival direction, γ -rays retain this information, and can be used to uncover details about their sources, the most powerful particle accelerators in the universe (see chapter 1).

2.1.1 Electromagnetic Showers

Electromagnetic showers are initiated by energetic γ -ray photons or electrons.¹ These two types of electromagnetic showers are essentially identical, differing only in the height of first interaction.²

Bremsstrahlung, pair-production and to a lesser extent ionisation, are the main physical processes governing the development of an electromagnetic air shower. Secondary particles are predominantly produced via pair-production in the vicinity of a nucleus as long as the initial photon energy is greater than twice the rest mass energy, $E_\gamma > 2mc^2$ for a particle of mass m . Secondary photons are produced by Bremsstrahlung emitted when a charged particle is deflected by travelling through the Coulomb field of a nucleus; this energy loss process is inversely proportional to the particle mass (see p.156 of [18]), and so dominates for lighter particles, such as electrons. In both cases, the average opening angle under which the secondaries travel is $O(1/\gamma) \sim O(mc^2/E)$. These processes are characterised by a length scale, X_0 , termed the *radiation length*, over which the energy of an electron is reduced to $1/e$ of its original value after travelling a distance X_0 . More generally, the particle energy $E(x)$ after travelling a distance x is given by:

$$E(x) = E_0 e^{-x/X_0} . \quad (2.1.1)$$

The radiation length for electrons emitting Bremsstrahlung in air is $X_0 \sim 37 - 38 \text{ gcm}^{-2}$; for photons undergoing pair production the interaction length is $X_{0,\gamma} = 9/7 X_0$ (p.153 [18]).

A simple model of shower development is the Heitler model, which uses three basic assumptions: (a) that the radiation length of Bremsstrahlung and pair-production are equal; (b) that these are the only dominant processes contributing and (c) that the energy is distributed evenly among the secondary particles at each step (where ‘particles’ is taken to include γ -ray photons, see figure 2.1) [19].

The typical height of first interaction of an air shower is typically at around 10 – 20 km altitude. As an EAS develops, secondary particles are produced and the shower increases along the forward, or longitudinal direction. Due to scattering and particle decays with a transverse momentum component, the lateral extent of the shower also increases. The size of an EAS depends on the energy of the initial (or primary) particle, the incident zenith angle and the height of first interaction. The depth of maximum development, $X_{\text{max}}(\text{gcm}^{-2})$, as measured from the top of the atmosphere, increases to greater depths with increasing energy. At higher energies, the interaction cross-section increases, yet the leading particle penetrates further into the atmosphere as the shower develops, retaining a significant proportion of the shower energy.

In this model, an interaction takes place once per radiation length, the shower vertex splitting each time as illustrated in figure 2.1, such that after a distance x , there are $N(x) = 2^{x/X_0}$ particles, each with energy $E(x) = E_0 2^{-x/X_0}$. The depth of shower

¹‘Electrons’ shall refer to both electrons and positrons hereafter.

²Electrons interact sooner than γ -ray photons of the same energy, due to their larger interaction cross-section.

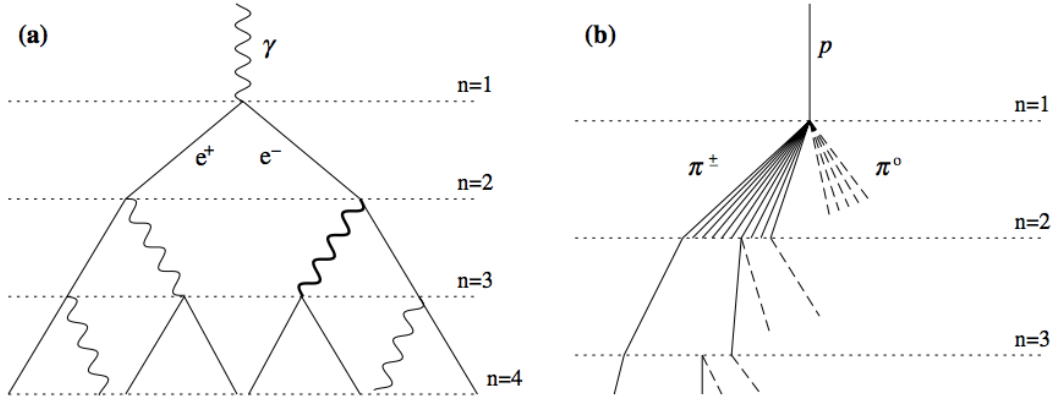


Figure 2.1: Schematic showing the development of an electromagnetic (a) and a hadronic (b) shower cascade under the Heitler model. Figure taken from [19].

maximum, X_{\max} is reached at:

$$X_{\max} = \frac{\ln E_0/E_c}{\ln 2} X_0, \quad (2.1.2)$$

where the critical energy E_c is the minimum energy at which Bremsstrahlung and ionisation losses are equal, and has a value of ~ 80 MeV.

At every interaction, the parent particle imparts a fraction of its energy to each of the secondary particles. The primary particle is typically travelling at relativistic speeds; for as long as the secondary particles in the shower also obtain sufficient energy to travel relativistically, Cherenkov radiation is produced as outlined in section 2.1.3. Extending the incident direction of the primary particle down to ground level defines the shower axis, along which the shower development is centred.

2.1.2 Hadronic Showers

The overwhelming majority of EAS are initiated by hadronic cosmic rays, rather than VHE γ -rays. Experiments seeking to utilise the directional properties of γ -ray initiated EAS, are designed to be sensitive to EAS signature signals. However, this typically results in a significant number of hadronic showers being detected; given the isotropy of cosmic ray arrival directions, these signals are often undesired and hadronic showers subsequently form a significant background noise contribution. Reduction of this hadronic background can be achieved by exploiting the intrinsic differences in the properties of electromagnetic and hadronic showers.

The early development of hadronic showers is dominated by strong interactions between the incident cosmic ray and atmospheric nuclei, with mesons (mostly pions and kaons) forming a significant proportion of the secondary products in shower development (see figure 2.1). Whilst charged pions decay into muons with a lifetime of 2.6×10^{-8} s, approximately one third of all pions created are neutral pions, which decay into γ photons with a much shorter lifetime of 0.8×10^{-16} s (p.57 [15]). The muons produced by the charged pions further decay into electrons and neutrinos; as their main energy loss is via

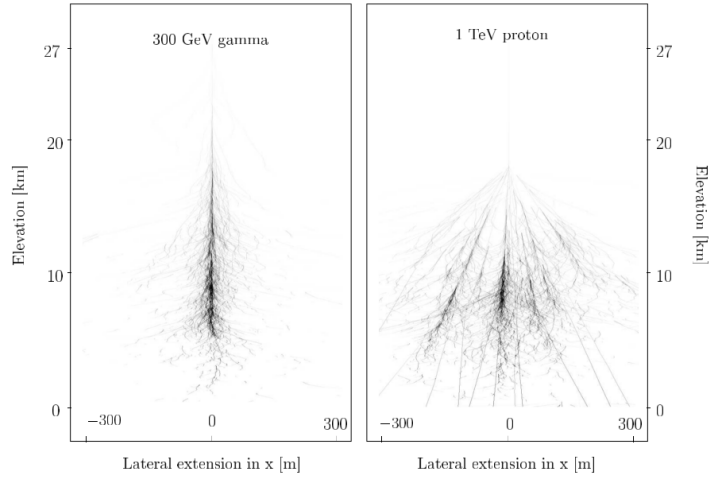


Figure 2.2: Examples of electromagnetic (left) and hadronic (right) air showers. The hadronic air shower comprises several subshowers and has a noticeably larger lateral spread. Figure taken from [20].

ionisation rather than decay, they form a penetrating part of the shower. As more pions and hadronic particles decay, electromagnetic processes begin to dominate further shower development. If γ photons are produced early in the shower and at reasonable angles to the primary shower axis, they can also produce electromagnetic subshowers, which are liable to be mistaken for a pure electromagnetic shower.

Hadronic showers initiated by protons or heavier cosmic ray nuclei have a far larger lateral spread than electromagnetic showers, mostly due to the transverse momentum imparted to the secondary particles in their production. By contrast, multiple Coulomb scattering is the primary contributor to the lateral spread of electromagnetic showers, which are consequently far more concentrated around the shower axis. This difference in lateral spread is the primary distinguishing characteristic between electromagnetic and hadronic showers, in combination with the higher level of fluctuations and subshowers occurring in the more complex hadronic interactions.

2.1.3 Cherenkov Light Production

Charged particles travelling in a dielectric medium (such as the atmosphere) cause a net polarisation of that medium, as surrounding atoms and molecules move to compensate the presence of the charge (p.837 [18]). This sets up a dipole field in the medium around the particle. As the medium relaxes after the charged particle has passed, dipole transitions occur, emitting electromagnetic radiation. Under non-relativistic conditions, the electromagnetic radiation produced from all parts of the particles track interferes destructively.

Highly energetic particles, however, travel faster than the phase velocity of light in that medium, ensuring that, as according to Huygen's construction, the radiation will add coherently along an angle Θ_C to the particle trajectory (see figure 2.3). This coherent radiation is called Cherenkov radiation, after Pavel Cherenkov, who first discovered the

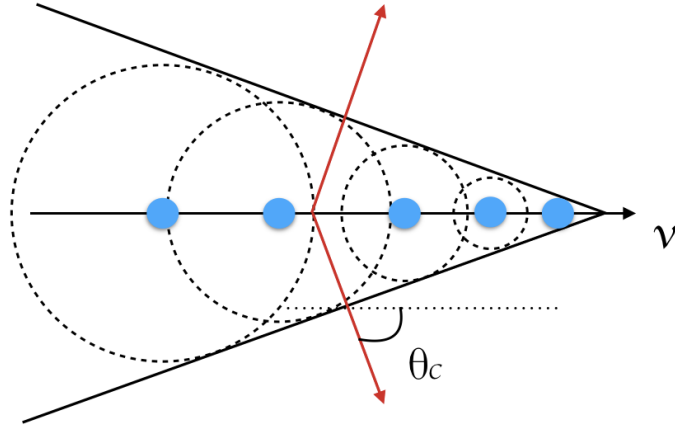


Figure 2.3: Schematic showing the production of Cherenkov radiation at an emission angle θ_C to the trajectory of a particle moving at v . The emission from all parts of the particles trajectory forms a coherent wavefront under Huygen's construction, which moves outwards at c .

effect.³ In EAS, the energy of the secondary particles is sufficient that they are also relativistic, moving with a velocity v faster than the speed of light in air $c_a = c/n$, where n is the refractive index of the atmosphere and c the speed of light in a vacuum. Each particle generates Cherenkov radiation around its own trajectory; collectively, this causes Cherenkov radiation to occur in a cone along the shower axis, in both cases with a narrow opening angle Θ_C given by:

$$\cos \Theta_C = \frac{c}{vn} . \quad (2.1.3)$$

This Cherenkov light from all parts of an air shower illuminates an area on the ground for the few nanoseconds duration of the air shower. The threshold minimum energy E_{\min} for a particle of mass m_0 to produce Cherenkov radiation is given by:

$$E_{\min} = \gamma_{\min} m_0 c^2 = \frac{m_0 c^2}{\sqrt{1 - n^{-2}}} . \quad (2.1.4)$$

Consequently, particles of lower mass with a lower threshold energy tend to dominate the Cherenkov radiation. The number of photons produced per unit wavelength λ and as a function of distance travelled l is given by the Frank-Tamm formula:

$$\frac{d^2 N}{dx d\lambda} = 2\pi\alpha Z^2 \lambda^{-2} \left(1 - \frac{1}{\beta^2 n^2(\lambda)} \right) . \quad (2.1.5)$$

From the wavelength dependence, this accounts for the peak of Cherenkov emission typically occurring towards the shorter wavelength blue to ultraviolet range, and for the bluish appearance of Cherenkov radiation in nuclear waste pools. However, below about ~ 300 nm, the atmosphere is not transparent, and Cherenkov light is no longer detected from EAS on the ground. Therefore, Cherenkov light in the atmosphere tends to peak

³for which he was awarded the 1958 Nobel prize, jointly with Il'ja Frank and Igor Tamm who first found an explanation for this phenomenon [21].

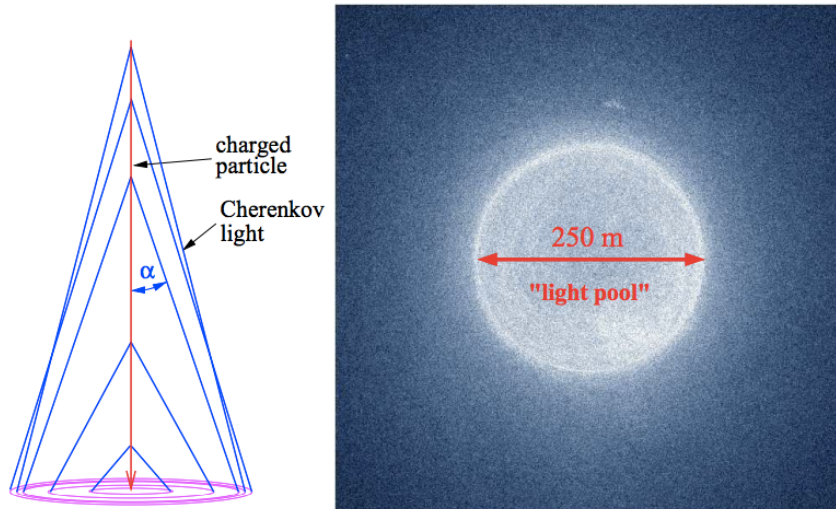


Figure 2.4: Changes in the refractive index with height lead to changes in the Cherenkov emission angle, labelled α here. This leads to a light pool of approximately 250 m diameter (seen at an observation level of 1800 m) with higher emission levels near the edge. Figure taken from [22].

close to optical wavelengths. The area on the ground illuminated by Cherenkov emission from an EAS is termed the Cherenkov light pool; the edge of which is defined by the overall cone formed around the shower axis from the sum of individual contributions. The presence of single particles within the shower also generating Cherenkov emission tends to fill in the centre of the ring on the ground (see figure 2.4).

The refractive index of the atmosphere changes with height h , as

$$n(h) = 1 + n_0 e^{-h/h_0} , \quad (2.1.6)$$

where $h_0 = 7250$ m and $n_0 = 0.00029$, such that the refractive index at sea level is 1.00029. As a result of the dependence of the opening angle of Cherenkov emission on refractive index (equation 2.1.3), the size of the Cherenkov light pool on the ground varies in radius depending on the height at which the emission was originally produced, and on the detection altitude.

Consequently, the light distribution tends to be reasonably flat within a shower, rising at the Cherenkov edge due to the emission angle varying with refractive index from multiple heights, and dropping again afterwards.

2.2 Imaging Atmospheric Cherenkov Telescopes

Direct observation of EAS can be done by measuring the number, energy and type of particles within each shower, a method employed by air shower array experiments such as KASCADE. Alternatively, indirect observation of extensive air showers can be made through the Cherenkov light produced as the highly energetic particles travel through the atmosphere, a technique demonstrated to perform well for γ -ray astronomy, by experiments such as Whipple and HEGRA. The history of ground-based γ -ray astronomy is comprehensively addressed in a recent review [23]. The Cherenkov effect takes place in any

medium transparent to UV-optical light which is denser than a vacuum. It has also been successfully utilised in water (by experiments such as ANTARES [24], Pierre Auger [25] and HAWC [26]), for observations of neutrinos, Cosmic Rays and γ -rays respectively, and similarly also for neutrino experiments in ice (such as IceCube [27]).

2.2.1 Imaging Atmospheric Cherenkov Technique

One approach to observing EAS is achieved via the imaging atmospheric Cherenkov technique: as an EAS illuminates an area on the ground, light from different heights within the air shower is emitted under slightly different angles. Telescopes with large mirror dishes reflect this light onto a fast imaging camera in the focal plane. The reflection angle is dependent on the incident angle, such that light from different parts of an EAS is reflected under different angles. Consequently, a typical γ -ray photon initiated EAS will generate a characteristically elliptical image in the camera. Hadronic EAS, by contrast, generate irregular images due to the presence of subshowers and massive secondaries, with no characteristic shape (see figure 2.2). The length of an elliptical image generated in a camera depends on both the inclination of the EAS with respect to the telescope pointing direction, and the distance of the shower core to the telescope. On average, the duration of an EAS is $\sim O(10 \text{ ns})$, whereas the much brighter Night Sky Background (NSB) light from background stars is near constant. The cameras are therefore fast recording, to help discriminate the weaker yet transient shower signal from the constant NSB light.

Due to the highly relativistic nature of the particles, the deviation of the secondary particles trajectories from that of the original primary particle is small in electromagnetic showers. This enables the direction of the original shower axis to be reconstructed from the Cherenkov light produced by the secondary particles.

This technique is used by Imaging Atmospheric Cherenkov Telescopes (IACT), which are optimised to a peak efficiency in the blue wavelength range, and record air showers on nanosecond timescales with fast cameras. The first IACTs opened up a window on the high energy universe, with a typical energy threshold for the technique of around $\sim 50 \text{ GeV}$.

The imaging geometry is shown schematically in figure 2.5. IACTs image in angular space; that is, emission reflected under different angles appears at different positions in the camera, such that the camera system coordinates are measured in degrees. Cherenkov light reflected under different angles corresponds to emission from different heights, as shown in figure 2.5. The difference between the angles of reflection for emission from the top and bottom of the shower (points A and B), $\Delta\phi = \phi_1 - \phi_2$, corresponds to the length of the shower image in the camera.

By adding more telescopes, an EAS may be simultaneously viewed from different angles, an approach known as stereoscopy. Images recorded simultaneously in multiple telescopes are identified with the same particle shower. These images can be combined in analysis, enabling the core location of the shower to be better constrained and leading to an improved reconstruction of the original direction of the primary particle. The additional information also enables more accurate shower energy estimation and better γ /hadron separation power.

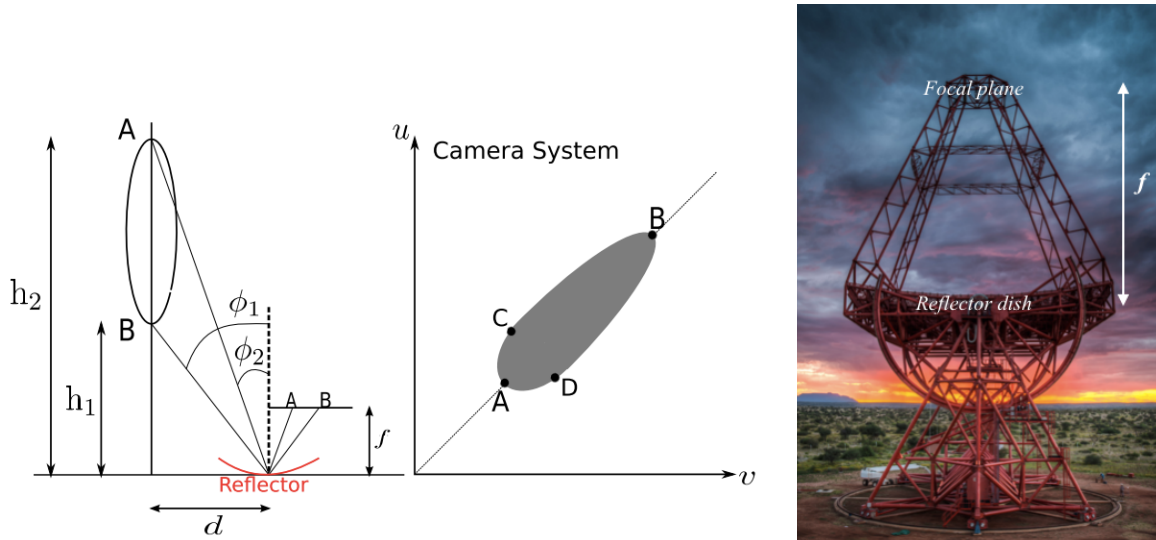


Figure 2.5: Left: schematic demonstrating the imaging geometry of IACTs, reflecting the Cherenkov light from an extensive air shower onto the camera. Right: Photo of the fifth H.E.S.S. telescope, showing the large reflector dish and the camera, onto which the light is focused. Figures taken from [28] and [29].

The effective area of a telescope array (area over which information from incident Cherenkov showers is collected), may be increased by optimising the inter-telescope spacing. This is a trade off between collection area and observing air showers with multiple telescopes to improve the reconstruction accuracy, but is ultimately also related to the area illuminated by the Cherenkov light pool from a typical air shower.

2.2.2 Current IACT Experiments

The current, third generation of IACT based experiments comprising H.E.S.S. [30], MAGIC [31] and VERITAS [32], all use multiple IACTs in conjunction, and have proven the technique to be very sensitive, enabling a transition from a period of discoveries to one of more detailed analyses and surveys. These include detailed morphological, spectral and time-based studies as well as coordinated multi-wavelength efforts, and have ensured that the IACT approach and VHE γ -ray astronomy are now well-established fields of research. Since 2012, the H.E.S.S. experiment has also used multiple sizes of IACTs in conjunction.

Observations with IACTs have a comparatively poor duty cycle. As Cherenkov light is much weaker than ordinary starlight, data taking has to be restricted not only to hours of astronomical twilight (sun at least 18° below the horizon) but also to times when the level of moonlight is low. Consequently, only a comparatively small percentage of a year remains as possible observation time, in contrast to ground-level air shower detectors (such as HAWC [26]) and radio astronomy, which in principle (barring instrumental downtime) are able to observe 100% of the time.

The major currently operational IACT experiments, H.E.S.S., MAGIC and VERITAS, are located at latitudes of 23.2713° S, 28.7619° N and 31.675° N respectively, primarily due to source observability and favourable weather conditions which provide a reasonable darktime percentage each year. Other aspects contributing to site location include the strength of the Earth's magnetic field, which can deflect particles within air showers

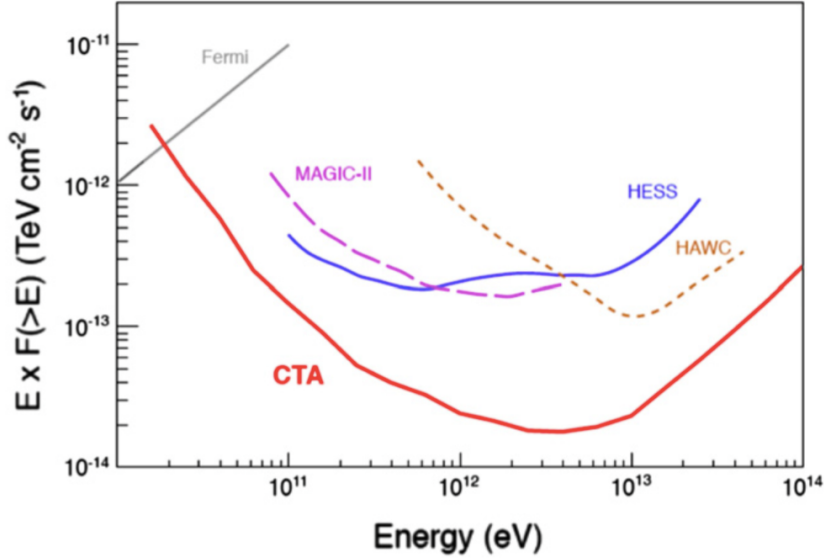


Figure 2.6: Integral sensitivity of CTA (obtained from MC studies) in comparison to 50 hours of IACT observations with MAGIC and H.E.S.S., and 1 year of Fermi and HAWC observations. Figure taken from [33]

thereby distorting the images created; the height above sea level and the average humidity.

Figure 2.6 shows the sensitivity of several currently operational instruments; the Fermi-LAT is sensitive to sources up to ~ 100 GeV after 1 year of observations, although energies up to a few TeV are achievable with current analyses. The H.E.S.S. curve, comparable to that of VERITAS, corresponds to H.E.S.S. phase I. Over the wide energy range, high energy coverage is enhanced by the overall ground area covered, whereas low energy coverage is augmented by increased mirror area, as demonstrated by the lower energies reached by MAGIC-II (with larger reflector areas) with respect to H.E.S.S. phase I. HAWC, a water Cherenkov based detector, performs well at high energies, and is most sensitive around 10 TeV. It is worth noting that whilst the Fermi-LAT and HAWC curves in figure 2.6 correspond to 1 year of observations, these include coverage of the whole sky, whereas the IACT curves correspond to 50 hours of dedicated observations, with a field of view only a few degrees across. The future IACT based Cherenkov Telescope Array should outperform the current generation instruments.

2.2.3 Cherenkov Telescope Array

Currently, a global effort of the community is gearing towards the Cherenkov Telescope Array (CTA) a major future facility in the field of VHE γ -ray astronomy, currently in the prototyping phase. An enhanced sensitivity and angular resolution of an order of magnitude over current experiments (see figure 2.6) is foreseen to be achieved through a combination of detector types; principally three different telescope sizes [33]. These will be spread over two sites, in the Northern and Southern hemisphere respectively, enabling a full view of the astronomical sky. Site negotiations are currently ongoing with Chile and La Palma, Spain, with construction due to commence in 2016. Due to the abundance of sources in the Milky Way, visible primarily from the Southern hemisphere, the Southern site will be the



Figure 2.7: The H.E.S.S. experiment in its second phase, showing all five telescopes, taken from the official H.E.S.S. website [29]. The fifth telescope situated in the centre of the array has $\sim 6\times$ the mirror area of one of the smaller telescopes.

major site with a greater number of telescopes than the Northern site.⁴ A concentration of Large Sized Telescopes (LSTs) near the centre of the array will provide the low energy sensitivity, with good coverage over a wide energy range provided by the Medium Sized Telescopes (MSTs). The high energy sensitivity of CTA will be provided by a sparse array of many SSTs, covering a large ground area. CTA is designed to considerably enhance the sensitivity and angular resolution available in ground based VHE γ -ray astronomy above that currently achieved. As such, progress towards answering some of the known open questions in the field, such as identifying sources of the most energetic cosmic rays, as well as some unforeseen discoveries are anticipated.

2.3 The H.E.S.S. Experiment

The High Energy Stereoscopic System (H.E.S.S.), an array of IACTs named in honour of Victor Hess (for his discovery of cosmic rays [1]), first started observations in 2003 (figure 2.7). H.E.S.S. is situated in the Khomas Highlands of Namibia, at 1800 m above sea level. The location was chosen for its dry climate with regularly clear skies, the low geomagnetic field strength and a latitude $23^{\circ}16'18''$ S. This offers a good view of the Milky Way in the Southern Hemisphere whilst optimising the possible observing time. As a consequence, the contribution of the H.E.S.S. experiment alone to establishing the field is considerable, with more than half of the currently known (as of 2016) TeV γ -ray sources being discovered by H.E.S.S. [34]. H.E.S.S. utilises the principle of stereoscopy - with multiple telescopes, an EAS can be simultaneously viewed from several different angles, enabling enhanced background rejection and image parameterisation.

The site altitude of 1800 m is an important consideration for the telescope separation, due to the dependence of the size of the Cherenkov light pool on the height in the atmosphere. As the characteristic depth of first interaction of highly penetrating γ -rays is approximately consistent, with a characteristic value of Cherenkov opening angle for light

⁴All further references to CTA will refer to the Southern site rather than the Northern, unless explicitly stated otherwise.

emission of $\theta_c = 1.2^\circ$ at the altitude of the H.E.S.S. site, this generates a characteristic size of the Cherenkov light pool due to such Extensive Air Showers (EAS) of approximately 300 m^2 on the ground. For γ -rays originating from zenith, the light pool has a typical radius of about $120 - 130 \text{ m}$. In order to optimise the number of showers which are caught stereoscopically, the four original telescopes of H.E.S.S. are arranged on the corners of a square with 120 m sides, such that it is possible for the entire H.E.S.S. array to be illuminated by a single Cherenkov light pool.

2.3.1 H.E.S.S. II

The second phase of H.E.S.S. began in 2012, with the inauguration of a fifth telescope⁵ situated in the centre of the original four telescope array.⁶ With a reflector dish six times the area of those of the smaller H.E.S.S. telescopes (CT1-4), this enabled the sensitivity of H.E.S.S. to be extended towards lower energies. One of the major scientific motivations of lowering the energy threshold is the enhanced sensitivity in a new, previously unattainable energy range, with the aim of bridging the gap between ground-based and satellite data, enabling the upper limits of many γ -ray emitting sources known only by satellites to be probed, as well as constraining key spectral features of a wide variety of objects. Additionally, the much faster repointing time possible with CT5 lends itself to studies of transient sources.

2.3.2 Optics of the H.E.S.S. Telescopes

All H.E.S.S. telescopes consist of a large single reflector dish comprised of many individual mirror facets, focusing the light onto a fast-imaging camera. The 13 m diameter reflector dishes of the four original telescopes (CT1-4) employ Davies-Cotton optics, comprising 382 circular mirror facets with 60 cm diameter, for a total reflector dish area of 107 m^2 .

The optical reflector dish of CT5 is $23 \text{ m} \times 33 \text{ m}$ and comprises 875 individual hexagonal mirror facets with a 90 cm edge to edge distance, for a total reflector dish area of 614 m^2 . Hexagons were chosen for CT5, as hexagons provide the maximum area per single facet for a shape which tessalates exactly. Each individual mirror facet is separately adjustable by a set of actuators; although for the most part this is utilised only in the initial positioning of each facet and calibration/focusing of the whole reflector.

Whereas the reflector dishes of CT1-4 use Davies-Cotton optics, the CT5 dish is designed with a parabolic shape. The mirrors are coated and consist of aluminised glass with a quartz coating [35]. They must have high optical reflectivity in the ultraviolet and at blue visible wavelengths, as well as being reasonably hard-wearing and resistant to environmental variation.

The focal lengths of the reflector dishes are 15 m and 36 m in the case of CT1-4 and CT5 respectively, with a design specification point spread function of 0.03° on axis, up to 0.06° at 2° off axis [29]. Light reflected off the dishes is then focused onto a fast-imaging camera, at a distance corresponding to the focal length.

⁵Referred to as CT5 (Cherenkov Telescope 5) hereafter.

⁶Referred to as CT1-4 (Cherenkov Telescope 1-4) hereafter.

2.3.3 Cameras

The cameras of the H.E.S.S. telescopes comprise photosensors and front-end electronics divided into drawers of 16 pixels each, subdivided into two cards of 8 pixels each, and a back-end electronics crate [36]. Each camera pixel consists of a Winston Cone, which collect the light photons, and a photomultiplier tube (PMT) which amplifies and converts the signal into photoelectrons. There are two acquisition (read-out) channels covering different signal charge ranges (low gain and high gain for large and small signal charges respectively) as well as a trigger channel. The signal from these channels is sent through an analogue to digital converter (ADC) with the final output then recorded in terms of ADC counts.

In total, the CT1-4 cameras have 960 pixels of 0.16° each for a total field of view (FoV) of 5 degrees. The considerably larger CT5 camera has 2048 pixels of 0.067° each for a total 3.2 degree FoV [29].

An air shower triggers the camera when a number of pixels within a sector (group of ~ 64 neighbouring pixels) of the camera have all seen a signal above a threshold charge within a short time window of a few nanoseconds (ns). This pixel coincidence test is done continuously for several arbitrary camera sectors which overlap. If the camera is triggered, then the signal from the previous 16 ns is read out.

Events occurring in a single telescope are termed mono (monoscopic) events, whereas events triggering more than one telescope simultaneously are termed stereo (stereoscopic) events. In H.E.S.S. II, mono events are only stored for CT5; for the remaining telescopes, a stereoscopic trigger is required before an event is read out. The stereoscopic trigger requirement helps to minimise the amount of spurious events due to Night Sky Background (NSB) noise, as well as the number due to single muons, which as the most penetrating component of a hadronic shower, form a significant contribution to the background level. Consequently, the overall trigger rate is also reduced, making the rate of data flow more manageable.

Nevertheless, mono events in CT5 are still recorded, as these permit access to a far lower energy threshold than is possible with CT1-4 alone. Stereo triggers of CT5 in conjunction with one of CT1-4 have also increased the overall array trigger rate with respect to H.E.S.S. phase 1. For many events which would previously have been rejected as monoscopic in one of CT1-4, the much increased mirror area of CT5 enables it to also detect the shower, turning what would previously have been a rejected mono event into a recorded stereoscopic one.

2.3.4 Data Quality

The trigger rate for a given set of observations is, aside from hardware issues, primarily affected by the zenith angle of the observations and the atmospheric conditions. This zenith angle dependence, characterised by an increasing trigger rate with decreasing zenith angle as a source rises, is a feature arising from the characteristic depth of first interaction of Cosmic Rays and γ -rays incident to the Earth's atmosphere. As this first interaction typically takes place at a height of $\sim 16 - 20$ km above sea level, the subsequent EAS also

reach a maximum at a consistent altitude, typically ~ 10 km [37]. For EAS observed at larger zenith angles, the inclination of the shower leads to a larger area being illuminated on the ground, such that for the same shower energy, the photon and particle densities at ground decrease with increasing zenith angle (p.371 [18]). This in turn makes the received signal weaker, such that in general only the higher energy events penetrate, with the effect of both raising the energy threshold of the observations and lowering the trigger rate.

The quality of the data taken is affected by atmospheric conditions, particularly clouds, which temporarily obscure part of the sky thereby lowering the trigger rate, and by aerosol content, with higher aerosol levels leading to increased scattering of light. To quantify this effect, the Cherenkov Transparency Coefficient (CTC) was introduced as a measure of the haziness of the atmosphere to Cherenkov observations [38].

2.4 Calibration Methods within H.E.S.S.

Any experiment aiming to produce reliable and accurate measurements must be robustly calibrated. To this end, a suite of calibration procedures are used within H.E.S.S., ensuring that the system is well understood and enabling confident analysis and interpretation of the data. Several aspects must be taken into account, originating in both the telescope structures and the cameras, which directly affect important parameters of the analysis. These include the direction of origin, the shower energy and the time of the shower event in each telescope (for trigger coincidence purposes), for which the telescope pointing, camera behaviour and mirror reflectivity must be well understood. The standard methods by which this is achieved are outlined in sections 2.4.1 to 2.4.3 below.

2.4.1 Camera Calibration

Camera calibration for H.E.S.S. is covered in-depth in [36], whilst a summary of the key aspects is provided here. The final pixel signal amplitude A^{HG} (A^{LG}) for the High (Low) gain channels used for data analysis is obtained post-calibration via the following equations:

$$A^{HG} = \frac{ADC^{HG} - P^{HG}}{\gamma_e^{ADC}} \times FF \quad (2.4.1)$$

$$A^{LG} = \frac{ADC^{LG} - P^{LG}}{\gamma_e^{ADC}} \times (HG/LG) \times FF \quad (2.4.2)$$

where ADC^{HG} is the measured number of ADC (Analogue to Digital Converter) counts and P^{HG} the pedestal position (baseline ADC value, see below) in the High Gain channel, and similarly for the Low Gain channel. The quantity γ_e^{ADC} for the gain of the high gain channel in ADC counts per photoelectron must be adjusted for the low gain channel by the amplification ratio HG/LG . The flat-field coefficient FF is common to both channels, and provides a measure of the pixel efficiency relative to the mean over the camera. The values of the parameters γ_e^{ADC} and FF are determined in specific camera calibration runs, whereas P^{HG} and the amplification ratio between the two channels are obtained from Cherenkov events.

Gain and counts

Single photoelectron (p.e.) calibration uses an LED flasher to fire a signal generating 1p.e. on average onto each pixel - the response (resulting ADC counts in the high gain channel) of each camera pixel to this signal is then recorded. The gain value is obtained via a fit to the pixel-wise distribution of ADC counts following a single p.e. run. This fit function is a convolution of the poissonian signal from the LED flasher with the instrument response, which is assumed to comprise a Gaussian electronic pedestal and a Gaussian single photoelectron response [36].

Flat-field Coefficients

Variation in the efficiencies of the photocathodes and Winston cone light collection produce some camera inhomogeneity, manifest in response variation to uniform illumination. These differences are corrected for by flat-field coefficients, measured in dedicated flat-fielding runs. An LED flasher at wavelengths of 390 to 420 nm (or a laser for CT5) is shone uniformly over an area larger than the camera FoV, and the signal generated in each pixel is recorded. By taking the ratio of the response of each individual pixel to the average across the camera, a correction coefficient (FF_i , equation (2.4.2)) can be found for each pixel i . Any pixel-wise variation can be corrected for by applying these coefficients to “flatten” the response of the camera.

Pedestal Estimation

The camera pedestal refers to the mean ADC value or response of the camera in the absence of Cherenkov light, and is a measure of the baseline response of the cameras. Electronic pedestal runs measure the baseline intensity of the photomultiplier tubes in the dark (HVI_0); typically the mean of a narrow Gaussian distribution generated by electronic noise, and are taken by software triggering with the camera lids closed, such that the response to a zero pe signal is measured. The pedestal position is sensitive to the camera temperature, such that a stable temperature is sought for this measurement. The pedestal itself is estimated from data by averaging the ADC counts of pixels which did not contribute to the shower image. A new estimate is made every few thousand events. The pedestal width can be used as a measure of the NSB level in the camera, as can the high voltage current HVI , with the NSB rate typically proportional to the high voltage current measured above the baseline level:

$$NSB = \alpha HVI + HVI_0 . \quad (2.4.3)$$

2.4.2 Pointing

Calibration of the telescope pointing precision is achieved by comparison to known positions of stars. Primarily, this is done by dedicated pointing runs in which the telescopes are pointed at a succession of stars in random order, from a list of stellar targets satisfying careful selection criteria (including apparent magnitude). A set of LEDs mounted on the telescope camera lid are turned on and used as reference positions. For each star, a set

of images of the night sky are taken with the so-called SkyCCD (mounted parallel to the optical axis) and correspondingly of the night sky and telescope with LEDs turned on by the LidCCD (mounted in the middle of the telescope reflector dish and viewing the camera lid). These are used in conjunction to measure discrepancies between the expected and measured positions of the LEDs relative to the known positions of the background stars, as well as distortions of the star images on the camera lid.

Alternative, yet less robust, methods of pointing calibration may be achieved from the data itself. Stars already within the telescopes FoV form part of the NSB and lead to bright signals in isolated pixels. Whilst these pixels are removed in standard data analysis, this enables the actual position of the stars to be tracked precisely, and may be exploited to cross-check calibration of the telescope pointing accuracy. Comparisons of the average orientation differences of shower images between telescopes may also be used to this effect, in a method outlined in [39] (see appendix A.2).

2.4.3 Optical Efficiency Calibration

Aside from the use of LEDs and lasers for initial adjustment of the point spread function and mirror alignment monitoring, the optical reflectivity of the mirrors is only monitored in conjunction with the optical efficiency of the entire telescope camera system, as outlined in chapter 3. However, in this case if other components of the system are well calibrated independently, then the degradation of the mirror reflectivity is the dominant contributor to changes in the optical efficiency.

The intensity of the shower image recorded has a direct influence on the energy reconstruction; consequently, a reliable calibration of telescope optical throughput efficiency is required for source flux and energy interpretation. Telescope optical throughput efficiency is a measure of the overall reduction in the received image intensity, and is a cumulative effect of several contributing factors, including the mirror reflectivity, shadowing of the mirror due to the telescope structure and the quantum efficiency of the photodetectors. It is also used to monitor the degradation of telescope components over time.

Methods for determining the optical efficiency of the telescopes are dealt with in more detail in chapters 3 to 5.

2.5 Event Reconstruction

After the calibration has been applied, the remaining information includes the image pixel amplitudes for each camera which triggered on a given event. Next, the data must be analysed, in order to interpret the properties of each event and subsequently the signal (or lack thereof) from a given astronomical source. Data analysis includes both image cleaning and reconstruction of the properties of each event. The standard procedure has been described in detail for H.E.S.S. in its first phase in [40], in the context of an analysis of the Crab Nebula. In the case of monoscopic events seen by CT5 only, the reconstruction procedure is described in [41].

2.5.1 Image Cleaning

The first stage in the analysis is to clean the images, typically done using split-level cuts. This procedure is a threshold based cut, where all pixels above a high threshold with a neighbouring pixel above a lower threshold (or vice versa) are kept. Typical standard values are combinations of 10 p.e. and 5 p.e., or 7 p.e. and 4 p.e. for the high and low thresholds respectively. In this manner, random weak signals due to NSB fluctuations (for which all pixels fall below the high threshold), or isolated bright pixels due to stars in the NSB or hardware issues such as an afterpulse of the PMT (with no neighbouring pixels passing the cut), tend to be eliminated.

This may not be an ideal solution, however, as with degrading efficiency of detector components, the hard cut leads to a bias against low energy events triggering near to the camera threshold. Whilst the tailcuts approach is rather crude, various improvements have been suggested, including use of timing information to reject noise/NSB. This timing information may be usable for enhanced image cleaning, based on the arrival time relative to the peak signal of the photons in each pixel. This is due to the typical spatial and temporal pulse shape of a γ -ray being more peaked than the inherently random NSB and hadronic signals. Use of timing in Cherenkov image cleaning has been demonstrated on the MAGIC experiment [42]. Among the H.E.S.S. telescopes, only CT5 stores timing information; recording the time of maximum charge arriving rather than the complete time profile. Timing information is hence not currently used as standard for image cleaning within H.E.S.S..

2.5.2 Hillas Reconstruction

Parameterisation and γ -hadron separation

Classical image processing proceeds with determination of the so-called Hillas parameters (see figure 2.8), usually parameterising the image ellipse with a width and length parameter, which are then scaled per telescope and, in stereoscopic systems, the mean over all triggered telescopes is found [43]. Hillas parameters, including the centroid position of the ellipse and its distance from the camera centre, as well as the ellipse width and length, are calculated for each camera image. These parameters along with the image amplitude (total charge of all pixels passing the image cleaning cuts) are used to characterise the image, whilst images with a centroid too far from the camera centre are removed, as they could be truncated, biasing the elliptical fit. Images of leptonic γ -ray showers tend to produce elliptical images in the camera, whereas hadronic showers generally produce more messy showers, often with subshowers leading to ‘islands’ in the camera images, due to the fluctuations in their shower development (see figure 2.2). In the simplest approach, approximating the image by an ellipse and determining its width and length enables the likelihood of an image to be signal (γ -ray shower) or background (hadronic shower) to be determined. If the shower image is non-ellipsoidal, it is rejected as background.

From lookup tables generated via Monte Carlo, the expected image width $\langle w_i \rangle$ and length are found and compared to the measured widths w_i for each telescope i . These values are then combined for all triggered telescopes N_{tel} to obtain the mean reduced

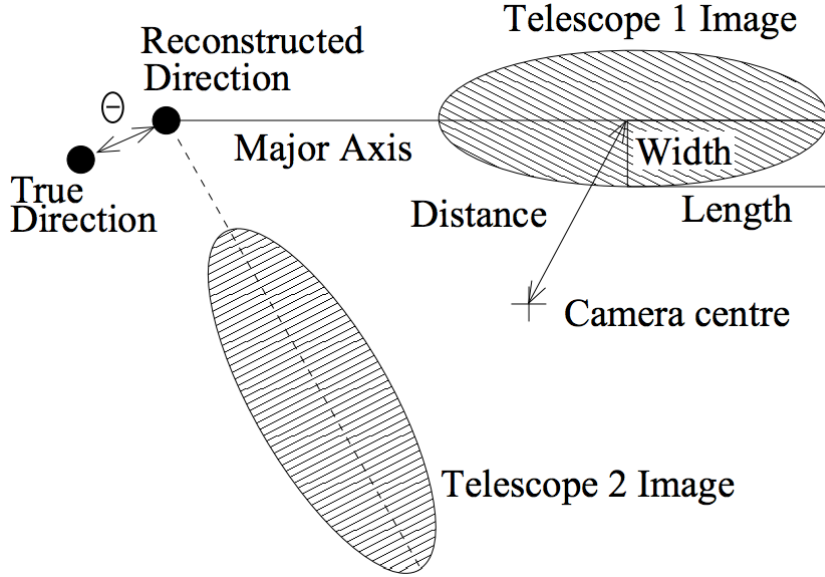


Figure 2.8: Definition of the Hillas parameters used to describe Cherenkov images. The intersection of the major axes of ellipses from multiple telescopes better constrains the reconstructed direction. Figure taken from [40].

scaled width ($MRSW$) and length ($MSSL$) for a given event:

$$MRSW = \frac{1}{N_{\text{tel}}} \sum_i^{N_{\text{tel}}} \frac{w_i - \langle w \rangle_i}{\sigma_i}, \quad (2.5.1)$$

where σ_i is the mean rms (root mean square) spread from the lookup tables. The expression for $MSSL$ is analogous to equation (2.5.1). A cut on the MSCW is one of the most discriminating variables which can be used for γ -hadron separation, especially as it combines information from each telescope that views the same shower from a different angle.

Direction Reconstruction

Using multiple images of the same shower as viewed from different angles, the images can be combined to provide a high accuracy stereoscopic imaging method. The major axes of the ellipses from each of the shower images can be extrapolated, and the point of intersection found, which indicates the shower direction. Such events, involving images from multiple cameras, are termed stereo events. In the case of CT5, which has a lower energy threshold than CT1-4 and thereby triggers on many events singly (monoscopic, or mono events), there is only one image, leading to an ambiguity in the original direction. To break this ambiguity, the intensity distribution across the Cherenkov image is used [41]. Nevertheless, the overall angular precision of mono events is generally less than that achievable by stereoscopy. The offset of the reconstructed direction to the expected source position is quantified by the angle θ , as defined in figure 2.8.

Energy Reconstruction

Based on the zenith angle of observations, the image amplitude and image distance to the camera centre (related to the distance of the shower core from the telescope, or impact parameter), an energy estimate is obtained for each telescope from the lookup tables generated from simulations. As the image amplitude is proportional to the shower energy, and affected by the optical efficiency, these energy estimates E_{MC} must be corrected by the ratio of the simulated optical efficiency ε_{MC} to the current measured optical efficiency ε_t , for each telescope t , such that the estimated energy is $E_t = \frac{\varepsilon_t}{\varepsilon_{MC}} E_{MC}$. Combining the energy estimates from different telescopes, an overall energy estimate $E_{\text{est.}}$ is obtained: $E_{\text{est.}} = (\sum_t E_t)/N_t$ for N_t telescopes.

Other Reconstruction Approaches

In practice, many more advanced methods exist for background rejection and γ -hadron separation, including using TMVA and Boosted Decision Trees, which use a more complex combination of discriminatory parameters [44, 45]. Template-based analyses are powerful analysis approaches, which make use of the full image information (including pixel amplitudes), rather than just the overall shape. Two such reconstruction methods used within H.E.S.S. are the likelihood reconstruction Model analysis [46] and an Image Pixel-wise fit for Atmospheric Cherenkov Telescopes (ImPACT) [47]. After initial image cleaning, typically two rows of pixels around the edge of the cleaned image are re-included to avoid hard cut biases, and the image is fit with a model prediction obtained from Monte Carlo, reconstructing the direction and energy of the image simultaneously. Typically, an improvement of a factor 2 in sensitivity is seen over a Hillas parameter based reconstruction when employing these methods. A summary of possible approaches to analysing Cherenkov images in IACTs is given in [48].

2.5.3 Data Analysis in H.E.S.S. Phase II

In the first phase of the H.E.S.S. experiment, all events were of a stereoscopic nature, since a trigger of more than one telescope was required for an event to be recorded. In the second phase of H.E.S.S., however, whilst this requirement remains for CT1-4, it does not apply to CT5. Shower events triggering the largest telescope only are also recorded. Data analysis performed using CT5 only is termed a mono, or monoscopic analysis, as the shower was seen by only one telescope. An analysis of shower events triggering at least two telescopes⁷ is termed a stereo, or stereoscopic analysis.

2.6 Background Estimation

An overview of different methods of background modelling for γ -ray astronomy with IACTs and their applicability is given in [49]. Of these, two primary methods are of particular relevance; the so called ring and reflected background methods. Both the ring

⁷typically CT5 and one or more of CT1-4; due to its lower sensitivity threshold and much larger reflector dish, the vast majority of showers are seen by CT5

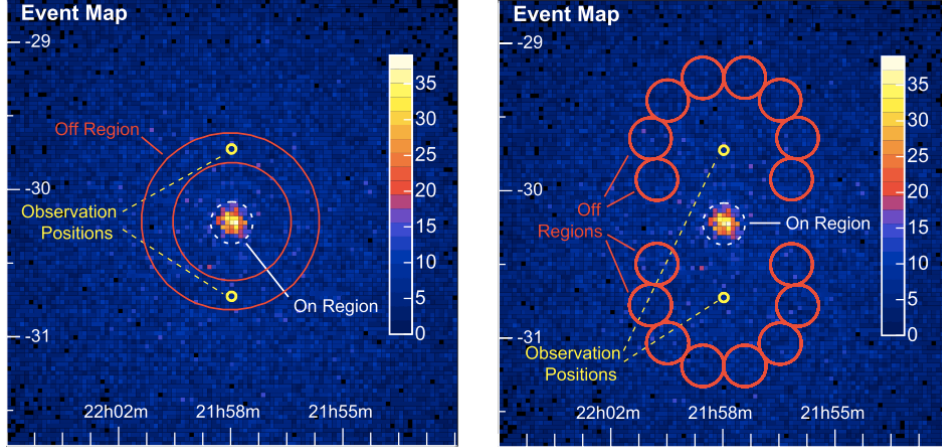


Figure 2.9: Illustration of the Ring background and Reflected background methods, taken from [49].

and reflected methods employ the classical approach of comparing the number of counts from an OFF region, where no emission from the source is expected but within the same field of view, to that in the test ON region, modified by a factor accounting for the different areas and camera acceptance. The acceptance is the relative rate of events appearing like γ -rays passing selection cuts, and is a function of the events position in the camera's field of view (FoV) as well as its energy [49]. Regions of known emission or in which emission is expected are excluded from the background estimate by the use of exclusion region masks applied during the analysis. To assist the background estimation process, observations with IACTs are usually taken offset with respect to the source position (see figure 2.9). A set of observations dedicated to a particular source usually comprise at least four positions around it, of equal offset in four directions. These are commonly termed wobble positions, or wobble mode observations. This helps to average out any systematics arising from camera hardware issues, or asymmetric camera acceptance.

2.6.1 Ring Background

In this approach, the background estimate is taken from a ring around the test on source position, of a specified inner radius and thickness. For isolated extragalactic point-like sources, this approach is comparatively straightforward. In the case of complex regions with multiple sources or of extended sources, the size of the ring may be adapted across the field of view, either by varying the inner radius and keeping the ring thickness fixed, or vice versa, thereby ensuring that background estimates are taken beyond exclusion regions (so-called masks which exclude regions of expected significant emission). As the γ -ray acceptance corresponding to each region is different, this must be taken into account when computing the background estimate.

2.6.2 Reflected Background

In this case, the OFF region has the same size and shape as the ON region, both regions being equally offset from the observation position. Thanks to this equal offset, a radial acceptance correction is not required for this background method, although radial symmetry of the camera acceptance is assumed [49]. In complex regions with multiple sources or extended sources filling the field of view, a variant known as the reflected pixel background method may be used. To all extents and purposes this is the same as the reflected background approach, except that where only part of the reflected region falls outside of an excluded area of known emission, this part may be used. The background regions are rotated around the observation position at the same angular distance as that of the signal position [50].

2.6.3 Signal Extraction and Significance

Significance calculations in γ -ray astronomy are typically done using an approach from Li and Ma [51]. Observations generally comprise a certain number of on source counts, N_{on} , from within the area attributed to the source, and a number of off source counts, N_{off} , taken from a suitable area for background estimation where no known sources are situated. To account for differences in the exposure time between the two areas, the parameter α is defined as the ratio of the exposure times $\alpha = t_{on}/t_{off}$, where t_{on} and t_{off} are the times spent observing the ON and OFF regions respectively. Then, the significance S may be calculated from equation 17 of [51]:

$$S = \sqrt{2} \left\{ N_{on} \ln \left[\frac{1 + \alpha}{\alpha} \left(\frac{N_{on}}{N_{on} + N_{off}} \right) \right] + N_{off} \ln \left[(1 + \alpha) \left(\frac{N_{off}}{N_{on}} + N_{off} \right) \right] \right\}^{1/2}. \quad (2.6.1)$$

The ring or reflected background methods outlined in sections 2.6.1 and 2.6.2 are good examples of how the region from which the N_{off} counts are taken is defined, although other approaches are possible [49].

2.7 Monte Carlo Simulations

Simulations of the air showers from the moment the incident particle hits the atmosphere through to the signal recorded in the telescope cameras are crucial to ensure a thorough understanding of the detector behaviour, enabling the process to be reversed through data analysis to determine the properties of incident particles in the data. Simulation of air shower development is done for the Monte Carlo used in this work with the CORSIKA (COsmic Ray SIMulations for KAScade) package, developed in Karlsruhe [52]. CORSIKA calculates the particle interactions, shower development and expected amount of Cherenkov light produced by an EAS. Simulation of the detector response is done using *sim_hessarray* [53], which accounts for all necessary aspects of the H.E.S.S. telescopes; the reflector optics, shadowing by telescope masts, optical reflectivity of the mirrors, camera geometry and camera response.⁸ The final output is then the camera images generated;

⁸The extended version of this package, *sim_telarray*, is used for CTA simulations.

the expected response of the camera to a given shower event. Testing and development of the H.E.S.S. software and of new algorithms is usually done with Monte Carlo prior to its application on data, which helps to ensure the expected behaviour occurs. This Monte Carlo is also used to generate reference lookup tables, storing (for example) the expected energy for a given event based on the image size and the zenith angle of the observations. As the overall optical efficiency of the system changes over time, with natural degradation as well as hardware adjustments, upgrades and mirror cleaning; the Monte Carlo are periodically reproduced with updated parameters describing the telescope system more accurately.

2.8 Performance of H.E.S.S. II

The addition of CT5 to the H.E.S.S. array enables a lower energy threshold and improved angular resolution and sensitivity of the H.E.S.S. system. Together with improvements in analysis techniques, such as those outlined in section 2.5.2, this leads to enhanced performance of the H.E.S.S. system.

2.8.1 Angular Resolution

The angular resolution of the system is a measure of the precision to which the origin of γ -ray emission can be determined. This is of particular relevance when considering possible associated objects from other wavelength bands to unidentified or ‘dark’ γ -ray sources; of separating multiple sources which appear close together on the sky; and of identifying morphological features within large, extended γ -ray sources. From simulations of a γ -ray point source, the distribution of the squared angular distances θ^2 between the simulated and reconstructed arrival directions of the γ -rays can be formed (see figure 2.8). The 68% containment radius of this distribution provides the point spread function (PSF) of the instrument; its value is the angular resolution.

Figure 2.10 shows the angular resolution of H.E.S.S. as a function of energy, both with and without CT5. Template-based analyses clearly outperform a classical Hillas-based analysis of CT1-4, with the angular resolution lower at all energies. With the addition of CT5, the stereoscopic angular resolution is similar to that of CT1-4. However, in a mono analysis using CT5 alone, the angular resolution is noticeably worse, due to the direction reconstruction with a single telescope being inherently worse than using multiple telescopes in a stereoscopic approach. Better performance is seen for the conservative ‘safe’ cuts, where improved performance is a tradeoff for a higher energy threshold. Nevertheless, the angular resolution of the IACT technique is fundamentally limited by the development of a typical air shower, particularly, the level of Coulomb scattering and shower fluctuations, to $\sim O(0.4')$ at 1 TeV, although as shown by figure 2.10, improvements are possible before this limit is reached [55].

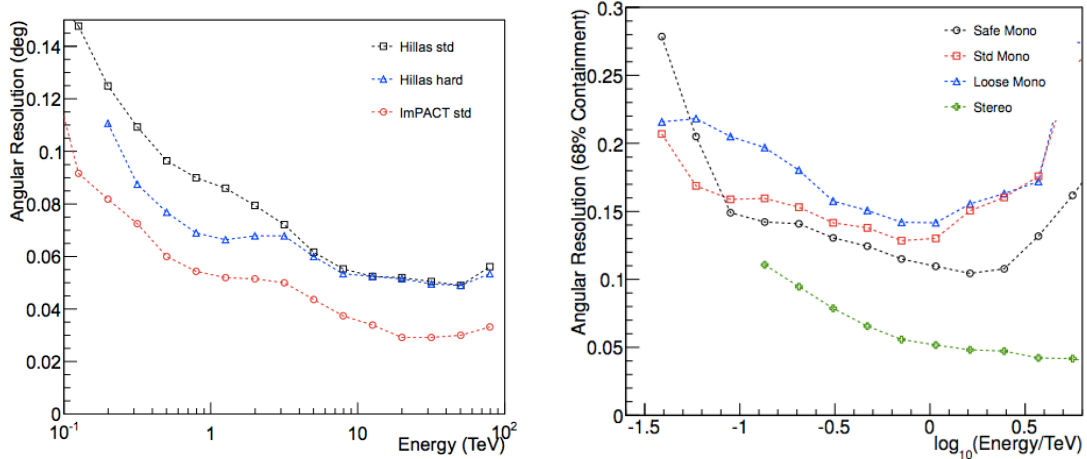


Figure 2.10: Angular resolution of H.E.S.S. as a function of energy. Left: likelihood based analyses show improved performance over Hillas based analyses; Right: the performance of CT5 in a mono analysis with three different cut levels and a stereoscopic analysis, using a likelihood based analysis. Figures taken from [47] and [54].

2.8.2 Effective Area

The effective area, A_{eff} , is a function of the shower energy E , the offset of the event from the centre of the field of view, the zenith angle and azimuth angle of the observations, the combination of telescopes which detected the shower and their optical efficiencies. It is typically determined from Monte Carlo, covering a range of the parameter space, and stored in a set of lookup tables from which values corresponding to a specific set of parameters during data analysis are interpolated as required. For a simulated number of γ -ray events N_{γ}^{MC} thrown over an area A_{MC} , the effective area is obtained from:

$$A_{eff} = \frac{N_{\gamma}}{N_{\gamma}^{MC}} A_{MC} , \quad (2.8.1)$$

where N_{γ} is the number of events which both triggered the array and passed all selection cuts. There are two types of effective areas which may be constructed, corresponding to a point source and an extended source (full enclosure) respectively, and hence depending on the size of the on-source region. The point source effective area accounts for the fact that some of the source flux appears over a region larger than the actual source size due to the point spread function (PSF) of the instrument, whereas the full enclosure effective area is appropriate for on-source regions larger than the instruments PSF, and hence for analyses of extended sources.

Figure 2.11 shows the effective area as a function of energy for H.E.S.S. in both phases of its operation. The curve rises steeply at low energies, where the detection is limited by the Cherenkov light and by the image amplitude cuts (hence looser cuts have a lower energy threshold). Towards higher energies, there is a slight decrease in effective area due to decreasing cut efficiencies, as cuts are typically optimised for a particular (narrow) energy range. The effective areas for the mono analysis of CT5 are lower in the mid energy range than those of the stereo analysis and of H.E.S.S. I, due to the decreased number of telescopes participating and collection area.

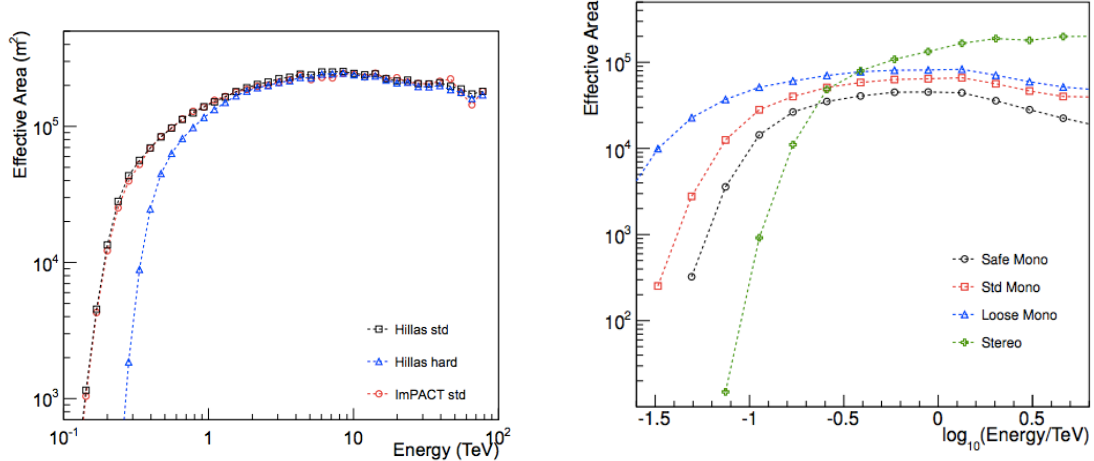


Figure 2.11: Effective area of H.E.S.S. as a function of energy. Left: In H.E.S.S. phase I, harder cuts increase the energy threshold of the experiment. Right: CT5 clearly improves the effective area of the experiment at low energies in comparison to the left hand plot for H.E.S.S. phase I. Figures taken from [47] and [54].

2.8.3 Energy Resolution

The error in the reconstructed energy is defined as $\Delta E = (E_r - E_t)/E_t$, where E_r and E_t are the reconstructed and true energies respectively. This quantity is also known as the energy bias and is plotted in figure 2.12. Close to the threshold, there is a bias in the energy estimates, arising due to the telescopes preferentially triggering on upward shower fluctuations, which generate brighter images; such as those towards the higher end of that particular energy bin. In this case, the reconstructed energies are then biased towards overestimation, leading to a positive energy bias. At high energies, the opposite effect occurs, leading to a slight negative bias, although here the effect is less dramatic as the limiting factor is the collection area, rather than the trigger threshold. Depending again on the zenith angle, a safe energy threshold is additionally imposed, beyond which the energy bias, obtained from a bias histogram lookup, is less than 10%. This effectively defines the energy threshold of the instrument; the trigger threshold, above which events are recorded, is generally lower but suffers from a high energy bias.

The energy resolution corresponding to a particular energy bin is defined as the width of the ΔE distribution, which can be well described by a Gaussian [40]. The energy threshold of the experiment clearly increases as a function of increasing zenith angle (figure 2.13).

2.8.4 Sensitivity

The sensitivity of an instrument is a measure of the minimum intrinsic source flux required for that source to be detected. Figure 2.14 shows the differential flux sensitivity of H.E.S.S. II with a combined analysis (both mono and stereo events), as well as that of CT1-4 only. The curves show the intrinsic source flux required for a 5σ detection within 50 hours of observation; for reference, dashed lines indicate fluxes corresponding to 10% and 1% of the Crab Nebula flux respectively. The energy threshold of the H.E.S.S. II array is

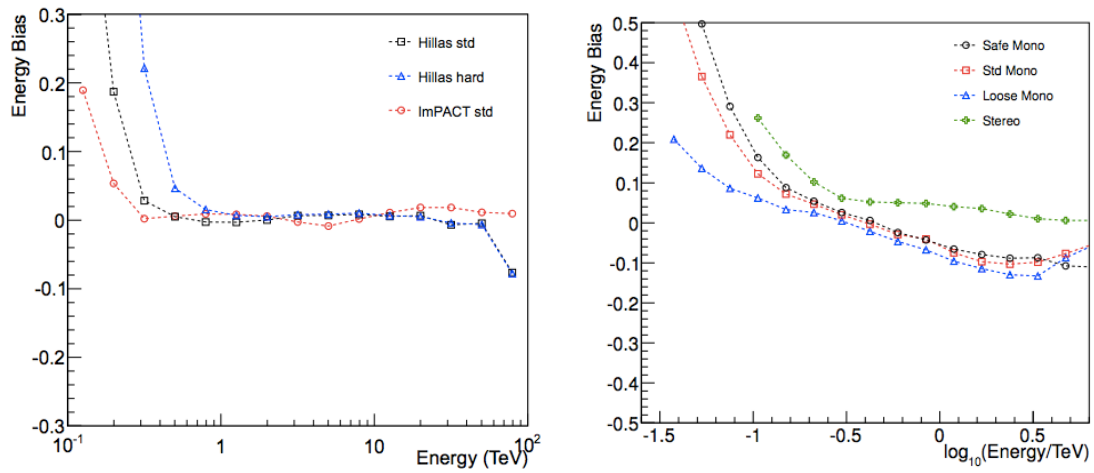


Figure 2.12: Energy bias of H.E.S.S. as a function of energy. Left: likelihood based analyses show improved performance over Hillas based analyses. Right: The energy threshold is considerably lowered by CT5. Figures taken from [47] and [54].

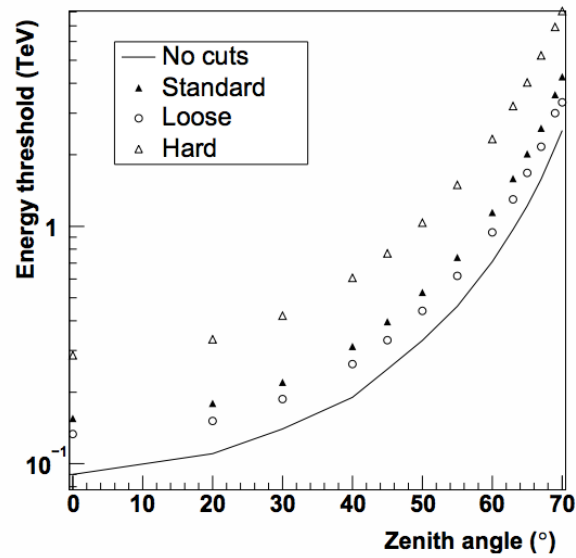


Figure 2.13: The energy threshold of the analysis clearly increases with increasing zenith angle. More conservative cuts lead to a more reliable analysis, at the cost of a higher energy threshold. Figure taken from [40].

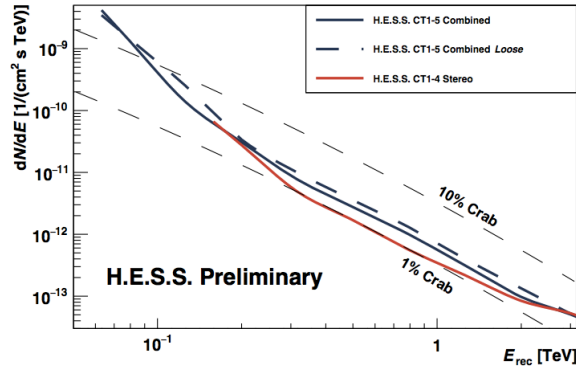


Figure 2.14: Differential sensitivity of H.E.S.S. II using a combined analysis (mono and stereo events), for observations at $\sim 12^\circ - 22^\circ$ zenith angle. The performance is significantly better than that of CT1-4 only at low energies. Figure taken from [56].

considerably lowered with respect to CT1-4 only; although the performance across the mid energy range is not quite as good at the time of [56] due to continuing cut optimisation.

The sensitivity of the instrument typically degrades with increasing source size, which is of particular relevance in studies of extended Galactic objects. This is due to the reduced amount of off regions that can be used for background estimation within the field of view, as well as a typically looser cut on the event offset (via θ^2) being applied.

2.9 Morphology and Sky Maps

From the reconstructed directions, events can be binned in sky coordinates to obtain an image of a particular region of the sky. An excess map shows the amount of counts after background subtraction, with the γ -ray excess counts calculated as $N_{excess} = N_{on} - \alpha N_{off}$, where $\alpha = t_{on}/t_{off}$ is the ratio of the exposure time in the ON and OFF regions. The raw counts are usually smoothed with a smoothing radius of $\sim O(0.1^\circ)$ for point-like sources and of $\sim O(0.3^\circ)$ for extended sources (depending on the analysis approach used). This more intuitively displays the inherent uncertainties in the reconstructed directions of each event. A cut on the events which are attributed to the source is usually made in terms of θ^2 , where θ is the offset between the reconstructed and true directions in degrees (see figure 2.8). Events with reconstructed directions within a certain distance of the source position (often within the PSF) are attributed to the source. This cut is adjusted according to whether or not the source under analysis appears extended.

2.10 Spectral Analysis

In a spectral analysis, the energy estimates are far more important than for detection only. Higher quality data (better atmospheric conditions) are often required for detailed spectral analyses as opposed to basic analysis aimed at detection or sky maps only. The reflected background approach lends itself to spectral analyses, as it does not require an energy dependent acceptance correction to be applied. The differential source energy

spectrum, $F(E)$, is a measure of the number of γ -rays, N_γ per unit area A and time t :

$$F(E) = \frac{1}{\varepsilon A} \frac{dN_\gamma}{dE dt}, \quad (2.10.1)$$

where ε is a measure of the efficiency and selection cuts, and the product $\varepsilon A = A_{eff}$, the effective area (see section 2.8.2). The differential flux is typically measured in units of ($\text{cm}^{-2}\text{s}^{-1}\text{TeV}^{-1}$).

The effective area is used along with the number of excess events after background subtraction to estimate the γ -ray flux. It is a function of the zenith angle of observations, the selection cuts (whether the analysis has been optimised for low energies, high energies, or the majority of the energy range) and the event energy. As such, it is also calculated from Monte Carlo, and accessed via a set of lookup tables.

Depending on the strength of the signal, the flux can be measured across an energy range divided into a series of (typically equal significance) energy bins. The flux in each bin i can then be obtained via

$$\frac{dF(E_i)}{dE} = \frac{1}{T\Delta E_i} \left(\sum_{j=0}^{N_{ON}} A_j^{-1} - \alpha \sum_{k=0}^{N_{OFF}} A_k^{-1} \right), \quad (2.10.2)$$

where the sums of on-source and off-source counts are weighted by the effective area A , and the overall difference is weighted by the livetime T and bin width ΔE_i corresponding to the energy bin [40]. In practice, the energy reconstruction is more complex due to the finite energy resolution of the instrument (see section 2.8.3), which leads to a certain probability P that an event with a true energy of E_t is reconstructed with an energy E_r . This modifies the measured γ -ray rate as:

$$\frac{dN_\gamma}{dE_r dt} = \int P(E_t, E_r, \dots) A_{eff}(E_t, \dots) F(E_t) dE_t, \quad (2.10.3)$$

where P and A_{eff} are also functions of other system parameters, as listed in section 2.8.2. To recover the flux $F(E_t)$ in this case, methods such as forward-folding, fitting the equation to the data for a given expected spectral shape, must be used [57].

Over time, the optical efficiency of the telescopes may degrade, such that for a γ -ray event of a given energy, the received light yield will be less than expected. To ensure that the event energy is correctly reconstructed regardless of this degradation, the telescope optical efficiency must be robustly calibrated. Two independent methods of achieving this, absolute efficiency calibration using muons and relative efficiency calibration using γ -ray showers, are outlined in chapters 3 and 4 respectively.

3 Optical Efficiency Calibration using Muons

In order for IACTs (Imaging Atmospheric Cherenkov Telescopes) to accurately reconstruct the energy of an initial γ -ray based on the detected air shower, the relation between the detected Cherenkov light yield and the γ -ray energy must be known to a precision of a few percent. Hence, knowledge of the overall telescope optical throughput, the fraction of light emitted by the air shower which is actually recorded, is an important factor in data analysis. Over time, the optical efficiency of the detector system will change; typically degradation of the mirror reflectivity and collection efficiency of the photomultiplier tubes is expected with exposure to weather and extended use. Optical efficiency performance may be recovered to some degree with replacement or maintenance of camera components, or by recoating the mirror surfaces. This alteration in optical throughput of the telescope system can have a profound effect on the energy reconstruction; often different energy lookup tables are required corresponding to different optical efficiencies. Therefore, the optical throughput must be monitored over time and data calibrated accordingly.

This monitoring has been proven [58] to be achievable through the use of atmospheric muons. Relativistic muons producing Cherenkov light constitute a sizeable proportion of the background events caught by IACTs, particularly when single telescope triggers are employed. Whilst the use of a telescope coincidence trigger will reduce the number of muons recorded, they still comprise a significant number of events, typically triggering the 100 m² mirror area H.E.S.S. telescopes (CT1-4) at a rate of ~ 1.5 Hz [58]. Muons generate characteristic ring-like images in the camera, with a radius dependent on the muon energy. Over the short distance during which the Cherenkov light produced due to the muon is visible to the telescopes, the path taken by the muon is mostly straight. As the refractive index of the atmosphere also does not change significantly through this atmospheric depth, the opening angle of the Cherenkov cone is also approximately constant. This property enables light from all regions of the Cherenkov light cone to be recorded by a single telescope, should the muon pass directly through the reflector dish. Through analysis of recorded muon images, the relation between the Cherenkov light produced due to a relativistic muon and the light collected by the telescope may be found. This relation is quantified by a muon efficiency parameter, which may subsequently be used in calibration of telescope optical throughput. As a natural source, this is a powerful approach towards calibrating the response of the system to Cherenkov light, independent from external instruments.

3.1 Atmospheric Muon Production

Muons triggering IACTs are produced primarily in hadronic air showers from incident cosmic rays, at a typical altitude of 10-20 km. As incident primary cosmic rays interact with the atmosphere, they fragment into smaller nuclei with the production of charged mesons (pions and kaons). These mesons decay to produce atmospheric muons predominantly through the decay chains:

$$\pi^\pm \rightarrow \mu^\pm + \nu_\mu(\bar{\nu}_\mu) \quad (\sim 100\%) \quad (3.1.1)$$

$$K^\pm \rightarrow \mu^\pm + \nu_\mu(\bar{\nu}_\mu) \quad (\sim 63.5\%) \quad (3.1.2)$$

where the branching ratios for the decay chains is given in brackets. Whereas heavier charged leptons and mesons decay far more rapidly, and lighter leptons tend to be poorly isolated from other shower components (especially low momentum particles which are more easily scattered), muons form a penetrating component of extensive air showers, travelling for longer times and distances in-between scattering interactions. Muon decay proceeds with a lifetime of $\tau \simeq 2.2 \times 10^{-6}$ s, insufficient for non-relativistic muons to reach the ground, yet ample time for a relativistic muon (p.32 [15]). Highly energetic muons maintain the structure of the Cherenkov light cone around their direction of motion; as muons often have a large transverse momentum component, muon events can be more easily isolated from the parent air shower.

3.1.1 Geometrical Description

For a charged particle travelling through a medium with refractive index $n(\lambda)$ with speed $\beta > \beta_0 = \frac{1}{n(\lambda)}$, the expected light intensity distribution (in terms of the number of photons N) around the ring image as a function of azimuth angle ϕ and path length l within a wavelength range λ_1 to λ_2 , is given by:

$$\frac{d^2N}{dl d\phi} = \alpha \int_{\lambda_1}^{\lambda_2} \frac{\phi(\lambda)}{\lambda^2} \left(1 - \frac{1}{\beta^2 n(\lambda)^2}\right) d\lambda, \quad (3.1.3)$$

where α is the fine structure constant and $\phi(\lambda)$ is the wavelength dependent photon collection efficiency of the detector [58]. The Cherenkov angle θ_c is defined as the angle of emission relative to the direction of motion of the particle, and is given by:

$$\cos(\theta_c) = \frac{1}{\beta n(\lambda)}. \quad (3.1.4)$$

Over the optical wavelength range of Cherenkov emission (to which the instruments are sensitive) ~ 300 nm – 600 nm, the refractive index is assumed to be independent of wavelength ($n(\lambda) \rightarrow n$). The total intensity of Cherenkov radiation is given by $I = \int_{\lambda_1}^{\lambda_2} \frac{\phi(\lambda)}{\lambda^2} d\lambda$, such that equation (3.1.3) may be expressed as:

$$\frac{dN}{d\phi} = \frac{\alpha I}{2} \sin(2\theta_c) D(\rho, \phi), \quad (3.1.5)$$

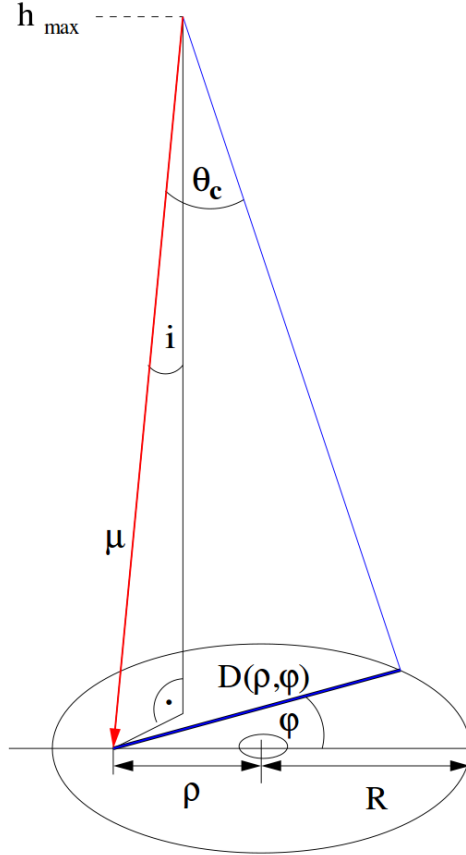


Figure 3.1: Geometrical representation of a muon incident upon a Cherenkov telescope, shown for the case of circular geometry. The muon is assumed to originate from the height of maximum shower development. The relativistic muon follows a trajectory inclined at an angle i to the telescopes optical axis, with an opening angle θ_c of Cherenkov emission. The “impact parameter”, ρ , is the distance from the point of impact of the muon on the mirror dish to the centre of the mirror dish. Figure taken from [59].

where $D(\phi) = \int dl$ is the length of the chord defined by the distance from the impact position of the muon on the mirror with the mirror edge as a function of azimuth angle (see figure 3.1). Essentially, equation (3.1.5) demonstrates that the number of Cherenkov photons produced is a function of the opening angle of the Cherenkov cone θ_c and geometrical parameters only.

Integrating over the azimuth angle in equation (3.1.5), which may be expressed by replacing $d\phi = \frac{\omega}{\theta_c}$ for an opening angle θ_c and an angular pixel size of ω , the intensity profile can be found and, if desired, the pixelwise expected intensity may be calculated. In terms of known parameters, the expected intensity per pixel is given by:

$$I_{pe} = \varepsilon dN = \frac{1}{2} \alpha I \frac{\omega}{\theta_c} \sin(2\theta_c) D(\rho, \phi) \quad (3.1.6)$$

where ε is the optical efficiency;¹ a global scaling parameter which relates the expected light intensity in photons for a given pixel (dN) to the total intensity in photoelectrons I_{pe} actually contained within the pixel. For telescopes with approximately circular mirrors (radius R), the expression for $D(\rho, \phi)$ has an analytical solution, depending on whether

¹This parameter ε may also be termed the muon efficiency, ε_μ to distinguish it from the optical efficiency determined by other means.

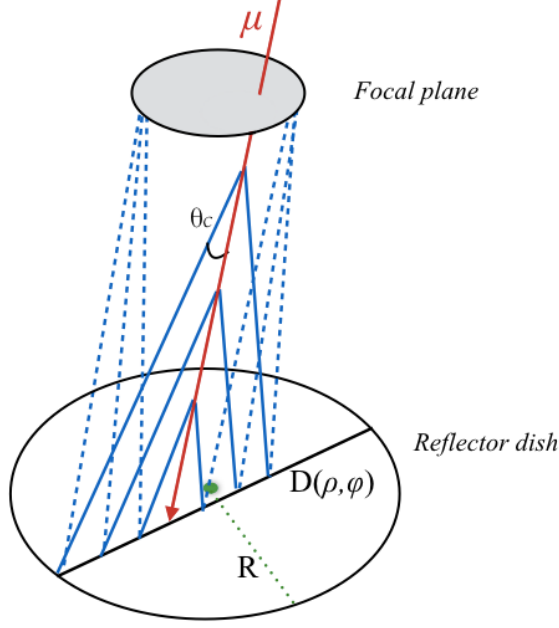


Figure 3.2: Cherenkov light emitted along a given azimuthal angle is reflected under the same angle back towards the focal plane. All light reflected along the chord $D(\rho, \phi)$ between the muon impact position and the reflector dish edge reaches the same point in the camera; light from either side of the muon impact position along the same chord reflects to opposite sides of the camera. The chord D does not necessarily pass through the centre of the reflector dish (green point), of radius R . The resulting camera images take on a ring-like form.

the impact position (at a distance ρ from the mirror centre) is within or outside of the telescope mirror radius R :

$$D(\rho, \phi) = \begin{cases} 2R\sqrt{1 - \left(\frac{\rho}{R}\right)^2 \sin^2 \phi} & (\rho > R) \\ R \left[\sqrt{1 - \left(\frac{\rho}{R}\right)^2 \sin^2 \phi} + \frac{\rho}{R} \cos \phi \right] & (\rho \leq R) \end{cases} \quad (3.1.7)$$

The light reaching a telescope reflector from such a muon cone hits the reflector at a slightly different angle from each azimuthal point around the cone. As the muon travels, light from this cone reaches many different parts of the reflector dish, yet the angle of incidence is the same for each azimuthal point around the cone. Light hitting the mirror at the same angle is reflected to the same pixel within the camera, which images in angular space (see figure 3.2). Hence, the images generated by muons retaining the whole cone are ring-shaped within the camera.

This is only in the case that the trajectory of the muon passes directly through the reflector dish, such that light from all azimuthal points is collected. If the muon arrival direction is aligned with the telescope optical axis, the ring is centred on the centre of the camera; otherwise, the ring image is seen with an offset from the camera centre, the size of which corresponds to the inclination angle. Should the muon fall nearby, yet not through the dish, only part of the Cherenkov light cone will hit the mirror and an arc-shaped image is produced (see figure 3.3). As the impact distance increases, the length of this arc reduces, until the muons run the risk of being mistaken for γ -rays [60, 61].

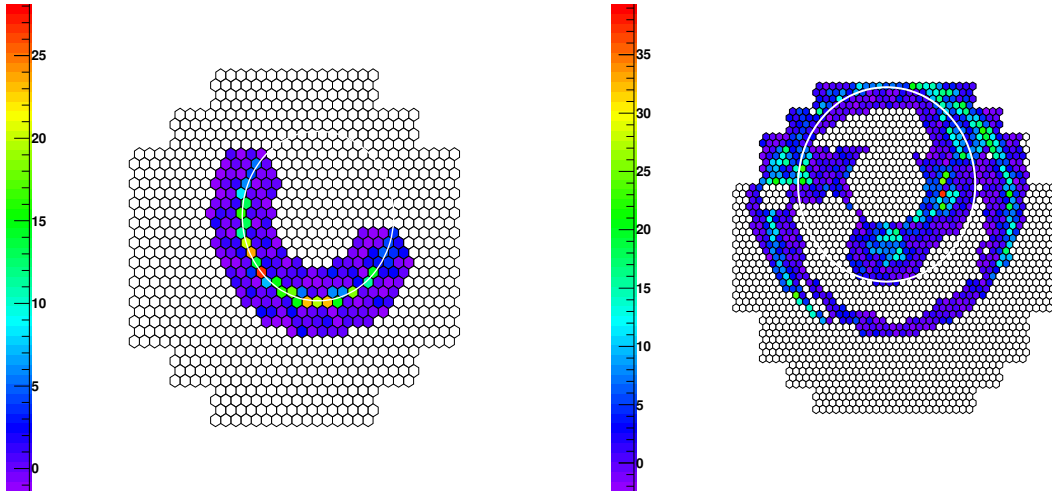


Figure 3.3: Muon Events as seen in the cameras of CT3 (left) and CT5 (right), shown with the first pass circle fit (prior to selection cuts). Left: an event originating from a muon which has fallen outside of the telescope dish, forming an arc-shaped image in the camera. Right: an event showing both a muon ring and Cherenkov light from the parent hadronic shower, partially filling in the middle of the ring. Subsequently, the first pass circle fit (see section 3.3.1) falls between the muon ring and the hadronic shower. The colour scale corresponds to the pixel charges.

As muons are mostly produced in hadronic showers, many images of muons also contain Cherenkov light from the parent hadronic shower, either filling in the centre of the ring or in the surrounding field of view (figure 3.3). However, muons may also be produced through the decays (3.1.2) at quite large angles from the original shower axis. As they are more penetrating than other leptonic counterparts, with many other hadronic shower components decaying or interacting more rapidly (especially in low energy showers), these muons are often detected as so-called “single muons”; without evidence of the parent hadronic shower, generating comparatively clean images. Such clean images are easily identifiable and may be used for optical efficiency calibration [58].

3.1.2 Broadening of the Muon Ring

The radius of the muon ring, defined by the Cherenkov angle θ_c varies as a function of energy; this can easily be seen through the dependence of the Cherenkov cone opening angle θ_c on the parameter $\beta = v/c_a$ in equation (2.1.3). Figure 3.4 illustrates this dependence for muons; it can be seen that above energies of $\sim 15 - 20$ GeV, the ring radius is asymptotic towards a constant value of $\sim 1.21^\circ$, such that it can be treated as approximately constant with energy.

In the absence of any additional effects, the muon ring generated in the camera would be infinitely thin, producing a ring-shaped image with a width of one pixel. However, in practice a combination of effects contribute towards a net broadening of the muon ring. A list of effects is outlined in [58], and the relative contributions to the CT1-4 cameras have been previously investigated by [59, 62]. These effects, quantified by the fractional broadening $\Delta\theta/\theta$, fall into two categories; those of instrumental and of a physical origin.

- **Mirror aberration:**

Due to the limited resolution of the telescope mirror, the ring is broadened by a

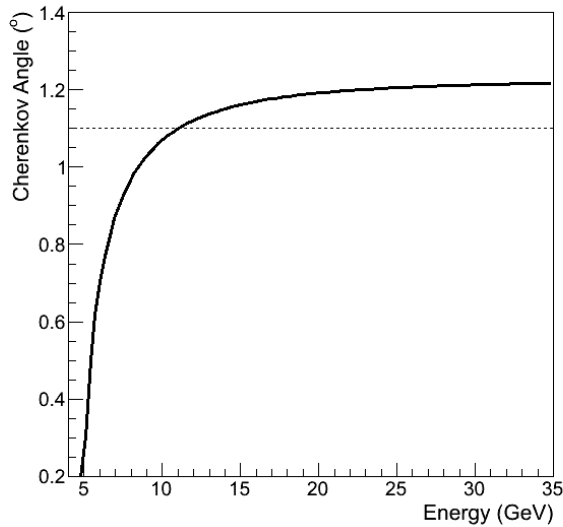


Figure 3.4: Muon ring radius (opening angle of the Cherenkov cone) as a function of energy. Above $\sim 15 - 20$ GeV, the Cherenkov angle θ_c approaches a constant value of $\sim 1.21^\circ$. The lower bound on the ring radius used in selection of muon events for calibration in CT5 is marked by a dashed line.

fraction $\Delta\theta/\theta$ depending on the angular resolution σ_{ab} as:

$$\frac{\Delta\theta}{\theta} = \frac{\sigma_{ab}}{\theta} . \quad (3.1.8)$$

- **Finite pixel size:**

Due to the discrete and finite nature of the pixelisation, the ring is broadened by an amount:

$$\frac{\Delta\theta}{\theta} = \frac{\sigma_{pix}}{\theta} , \quad (3.1.9)$$

where $\sigma_{pix} = \frac{1}{2}\omega^{3/2}/\sqrt{2\pi\theta}$ is the uncertainty in the radius due to the discrete pixelisation, expressed as a function of the angular pixel size ω for the case that the muon passes through the reflector dish.

The ring broadening has been so far expressed as a function of the ring radius θ_c , although these effects may also be expressed as a function of the muon energy, through the interrelation demonstrated in figure 3.4 (for muons with energies $\lesssim 20$ GeV). Although the mirror aberration and finite pixel size depend on parameters of the instrument explicitly, the following physical effects also contain an implicit dependence on the instrument, through either the dish size (radius R) or the response of the camera with wavelength. Contributing physical effects include:

- **Changes in the refractive index with altitude:**

The refractive index changes with altitude, decreasing exponentially with increasing altitude as the density of the atmosphere becomes thinner. The fractional ring broadening varies with the dish size and the ring radius as:

$$\frac{\Delta\theta}{\theta} \propto R\theta^{-3} . \quad (3.1.10)$$

- **Changes in the refractive index with wavelength:**

Although the refractive index is often assumed to be independent of wavelength over the range of interest, the true variation contributes to the ring broadening at the order of a few percent. For a given wavelength, this dependence varies with ring radius as:

$$\frac{\Delta\theta}{\theta} \propto \theta^{-2} . \quad (3.1.11)$$

- **Multiple Scattering:**

Coulomb scattering of the particle along its trajectory is the dominant effect contributing to the broadening of rings from the majority of muon events. Along the muons trajectory, Cherenkov photons are scattered according to an approximately Gaussian distribution, with standard deviation σ_{ms} , such that

$$\frac{\Delta\theta}{\theta} = \frac{\sigma_{ms}}{\theta} , \quad (3.1.12)$$

where σ_{ms} is a function of R , θ and β .

- **Ionisation losses:**

From figure 3.4, it is clear that as the muon loses energy, the opening angle of the Cherenkov emission must decrease. To the extent that this occurs along the part of the trajectory seen by the telescope, this also contributes to ring broadening, albeit to a lesser extent. In this case,

$$\frac{\Delta\theta}{\theta} \propto R\theta^{-3} . \quad (3.1.13)$$

Details of the full expressions governing these physical effects are given in [58].

3.2 Optical Efficiency Calibration using Muons

As explained in section 3.1, in the case of single muons travelling directly through the reflector dish light is collected from all parts of the Cherenkov cone, resulting in a ring-shaped image being formed in the camera. From the correspondence of the ring radius to the muon energy, the expected Cherenkov yield and light intensity distribution around the ring image can be found, through equations (3.1.5) and (3.1.6) [58]. The variation in amount of light reaching different parts of the camera and with partial muon images is also analytically predictable, through the dependence on the impact parameter ρ via (3.1.7). By comparing this analytically predicted amount of light to the total charge recorded in the camera image, the analysis of muon events yields a parameter capable of monitoring the optical efficiency of the telescope camera system. This method of optical efficiency calibration based on muon images, first suggested in [60], has since been employed by the majority of IACT based experiments [58, 59, 62, 63, 64, 65]. A major advantage of using muons in this manner, is that as a natural calibration source, with a spectrum closely matching that of air shower Cherenkov light, they do not generate

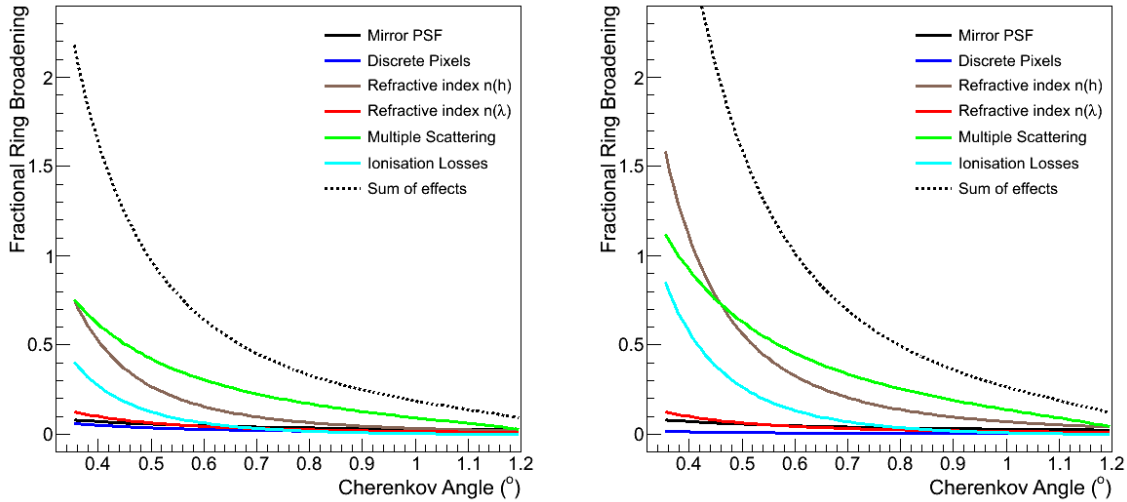


Figure 3.5: Effects contributing to broadening of the muon ring, shown for CT1-4 (left) and CT5 (right). Low energy muons, with smaller ring radii (equivalently Cherenkov angles, see figure 3.4) are substantially more susceptible to broadening effects. In the selection of muon events, a cut on the ring radius is made at 1° (1.1° for CT5), keeping the fractional broadening to $\lesssim O(0.3)$

the additional sources of uncertainty that an external calibration source would introduce for the same measurement. Nevertheless, the Cherenkov spectrum from muon events peaks at a slightly lower wavelength than that of γ -ray initiated air showers, due to their higher production altitude in the atmosphere. As muons travel along straight paths for longer distances through the atmosphere, when a muon passes directly through the telescope, the light collected by the camera has originated from greater altitudes than for a typical γ -ray or hadronic shower, in which the Cherenkov light received is a sum of contributions from many shower components over a range of altitudes. The height of shower maximum from γ -ray showers occurs lower down in the atmosphere and the Cherenkov spectrum subsequently peaks at a slightly longer wavelength. The magnitude of this effect is typically considered to be negligible under the assumption of wavelength independent changes in the optical efficiency (see figure 3.6).

For muon calibration, ring images as complete as possible are desired; these are identified and selected as outlined in section 3.3. Changes to the method of optical efficiency determination for H.E.S.S. II are described in section 3.4, and the performance of this approach is studied in section 3.5. Section 3.6 explores variation in the optical efficiency over time and with various environmental and hardware parameters. The application of this calibration to H.E.S.S. II data analysis is described in section 3.7. Finally, the comparatively generic algorithm is extended to the Cherenkov Telescope Array in section 3.8.

3.2.1 Requirements for Muon Calibration for H.E.S.S. II

Calibration using muon rings has been implemented within the H.E.S.S. software as standard since the early days of the experiment. Within the French calibration chain, this

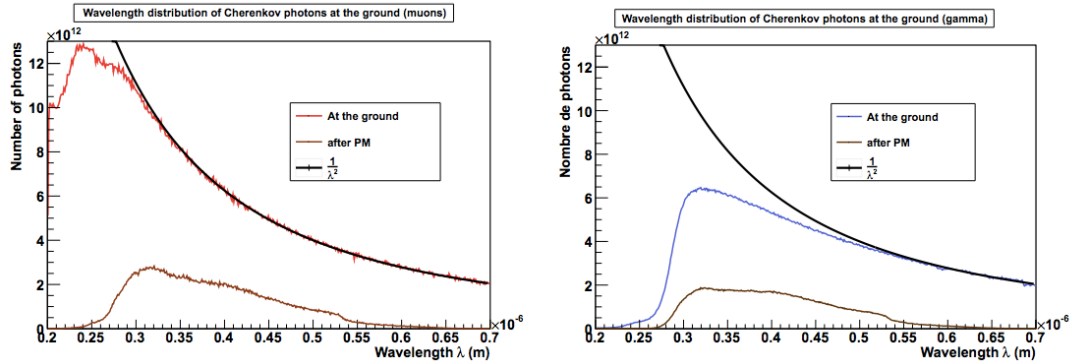


Figure 3.6: Left: the spectrum of Cherenkov light due to muons, and right: the spectrum of Cherenkov light due to incident γ -rays. Lines indicate the spectrum at emission, at ground level and after passing through the photomultipliers of the detector respectively. The muon spectrum clearly peaks at shorter wavelengths than for γ ; however, after transmission by the detectors and photomultipliers is taken into account, the difference in the spectrum of Cherenkov light arriving is negligible to a first approximation. Figure taken from [66].

was originally implemented by Nicolas Leroy [62] and within the Heidelberg calibration chain by Oliver Bolz [59]. Both pieces of software performed robustly over the intervening years; however, with the advent of H.E.S.S. II adjustments were necessary to the muon calibration in both chains. Following the construction of CT5, the main compatibility issues within the Heidelberg chain for the muon calibration were as follows:

- That the expected muon ring light profile distribution was calculated analytically based on approximating the telescope mirror as a circle; which no longer holds true for the CT5 mirror.
- That many telescope and camera parameters specific to CT1-4 were hard-coded, and needed to take on different values for CT5.
- That many, if not all, of the cuts used in image selection and performing muon ring reconstruction were also hard-coded for CT1-4 and needed to be adjusted for CT5 and reoptimised.
- That the structure of the code, though robust, was ill-suited for future adjustments and maintenance.

With this justification, the algorithm within the Heidelberg H.E.S.S. analysis package and calibration framework was revisited, and rewritten (together with the development of new algorithms) in a more flexible manner, in order to also account for CT5.

3.2.2 Usage of Muon Efficiency

The muon efficiency parameter values obtained from Monte Carlo are used as reference values for the efficiency calibration. Over time, different Monte Carlo phases are defined to best represent the current status of the telescopes for producing lookup tables for shower reconstruction. For a given run and/or over a given time frame, the energy estimates (rather than image amplitudes) are corrected for the discrepancy between the actual

telescope response efficiency and that used in the simulations by a muon correction factor, defined by the ratio of the Monte Carlo obtained muon efficiency to the muon efficiency parameter obtained from the data,

$$C_\mu = \varepsilon_\mu^{\text{MC}} / \varepsilon_\mu^{\text{data}} . \quad (3.2.1)$$

This correction is applied to the energy estimates, rather than the image amplitudes (in total pixel charge), as the latter is sensitive to the image cleaning algorithm used, broken pixels, instrument noise and background light, whereas the energy estimates are based on a fit to the image which helps to reduce the effect of these contributions on the image amplitude. Hence, ensuring that muons originating from different processes give unbiased results is important, an effect studied in sections 3.5.1 and 3.6.6.

A set of reference Monte Carlo muon efficiency parameters are defined for each Monte Carlo phase, which typically have different combinations of telescopewise efficiencies for each phase. Compatibility between the previous and new codes over the Monte Carlo phases is an important check. Due to the different approaches adopted in the methodology, the absolute muon efficiency value is not necessarily expected to agree between the two algorithms - nonetheless, any intrinsic difference should be manifest as a systematic offset. As the correction factor is defined by the ratio of the muon efficiency parameter obtained on Monte Carlo to that obtained on data (by the same reconstruction code), such intrinsic differences should cancel out in the application to data, and the ratio of the two codes should be stable (see section 3.5.2).

3.3 Identification of Muon Images

Identification of muon rings is performed using a loose set of image cleaning cuts and circle fitting procedure as follows. Images are first cleaned with split-level cuts at thresholds of 5 and 7 p.e. (see section 2.5.1) and a minimum of 20 pixels remaining in the image. Examples of candidate muon images at this stage are shown in figure 3.3.

3.3.1 Circle Fitting

The circle fitting was done using the Chaudhuri-Kundu formula [67], previously implemented in [59]. Rather than a minimisation procedure, this approach searches for solutions to an analytical expression for a circle, dependent only on the charges m_i and positions x_{i1}, x_{i2} for each pixel i in the camera image. Although the approach can be generalised to multiple dimensions, in 2D the radius r_0 of a circle is given by:

$$r_0 = \frac{\sum_{i=1}^N m_i [(x_{i1} - c_1)^2 + (x_{i2} - c_2)^2]}{\sum_{i=1}^N m_i} , \quad (3.3.1)$$

where c_1 and c_2 are the coordinates of the centre of the circle in an image with N pixels. The parameters c_1 and c_2 are also obtained through analytical expressions, each of which is again a function of the pixel charges and locations (see [67] for details). If a solution is found, then the presence of a ring is inferred; if no solution is found, then the image is

discarded and the procedure is performed a second time. A first circle fit to the cleaned image initialises the parameters defining the ring (position of the ring centre and ring radius). Following this, a second circle fit is performed, which includes only those pixels falling within 2.5 pixel widths of the ring radius (obtained from the first pass). This second pass improves on the parameter values found. If the circle fit again succeeded, then the ring image is extended; all pixels falling within 0.5° of the ring radius and that have passed a looser set of 3,7 tail cuts, are reinstated in the image. Whilst a clean image reduces possible biases in the circle fit, it is important to include low charge pixels in the intensity fit, to avoid underestimating the optical efficiency through an underestimate in the total charge. Figure 3.11 in section 3.4.3 shows the circle fit to a muon event following this stage of the cleaning; only those pixels retained at this point are shown, along with the fitted circle.

3.3.2 Image Selection and Cleaning

Following the circle fitting procedure, only those images passing cuts as stated in table 3.1 are retained for the next stage of the calibration. A lower threshold placed on the image size (in photoelectrons) and on the number of pixels contained in the image ensures that a sufficient proportion of the muon image is viewed within the camera for a reliable fit. This also ensures that the fit is not biased by anomalously hot pixels (due to hardware issues or bright stars in the field of view). As the muon energy increases, the ring radius saturates, such that by cutting on the fitted radius of the muon ring, only relativistic muons for which the ring radius approaches its asymptotic value are selected, via a cut on the ring radius (see figure 3.4). This ring radius cut effectively removes low energy muons which tend to be more affected by processes such as multiple Coulomb scattering which broaden the ring and could lead to some scattered light not reaching the telescope (see section 3.1.2). There is also a cut made on the ring width, to select more well defined muon rings; inherently these are either more energetic muons or muons which originate closer to the telescope, as they have typically undergone less scatter.

Additionally, for an unbiased fit the ring image generated by the muon should be well contained within the camera; as such the ring should be as near complete as possible, usually achieved when the muon passes directly through the telescope mirror. Hence a cut on the outer radius is also applied at this stage; this is the sum of the ring radius and the offset of the fitted ring centre from the centre of the camera. For well contained images, a cut on the number of edge pixels (those contained within the image but falling on the edge of the camera) is also applied. As hardware issues such as broken pixels along the muon ring may also bias the resulting fit (see section 3.6.4), a threshold on the maximum amount of broken pixels allowed in a fit is also applied.

3.4 Optical Efficiency Determination

Parameters describing the ring as found in the circle fitting procedure are used to calculate an analytical prediction for the intensity. This is done for each pixel present in the image.

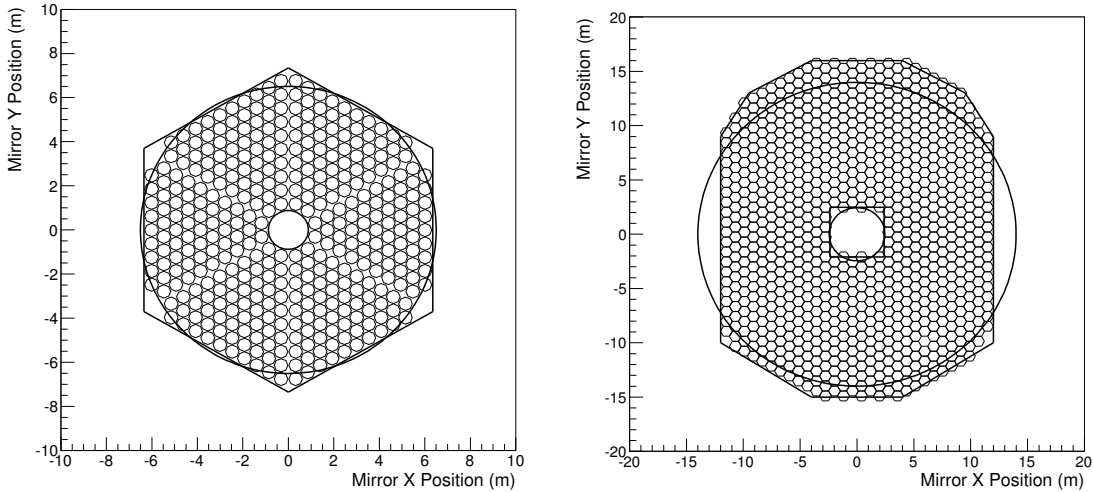


Figure 3.7: Mirror descriptions used in the muon calibration code in order to calculate the distance to the mirror edge for integration. Whilst the approximation of using an analytical formula describing a circle is sufficient for a typical CT1-4 mirror (left), this is clearly inadequate for CT5 (right). The improved mirror description now used for the line integration is also shown.

The intensity image is then fitted using a 2D log-likelihood procedure [46], described in section 3.4.3 in more detail.

3.4.1 Mirror Description

In order to calculate the theoretical expectation for the light distribution around a muon ring (equation (3.1.6)), it is necessary to know the distance from the impact point of the muon to the edge of the mirror, over which the light is integrated (see figure 3.1). In the case of an approximately circular mirror (such as the HESS I telescopes, figure 3.7), the analytical expression (3.1.7) may be used. As the expression for light distribution around a muon ring (3.1.6) is independent of azimuth angle except for the variation in chord length, a plot of the chord length variation with azimuth angle reflects the variation in light intensity around the ring, as depicted in figure 3.8. A dip in the intensity profile corresponding to the location of the hole in the centre of the telescope mirror can clearly be seen in the profile variation curve in figures 3.8 and 3.9.

Whilst expression (3.1.7) may be used in the case of the H.E.S.S. I telescopes without considerable loss of accuracy, in the case of CT5, the mirror shape is distinctly non-circular, rendering the analytical expression (3.1.7) impractical (see figure 3.7). Instead, a method of line integration is used to find $D(\rho, \phi)$.

3.4.2 Interpolation of Flat Mirror Distance

The analytical expression 3.1.7 previously used for the H.E.S.S. I telescopes may result in an under or overestimation in the predicted amount of light recorded by CT5, as this does not account for any deviations from radial symmetry. The collected light is bound to be underestimated in one direction whilst being overestimated in another, leading to systematic biases, such as misreconstructing the predicted location of the hole in the

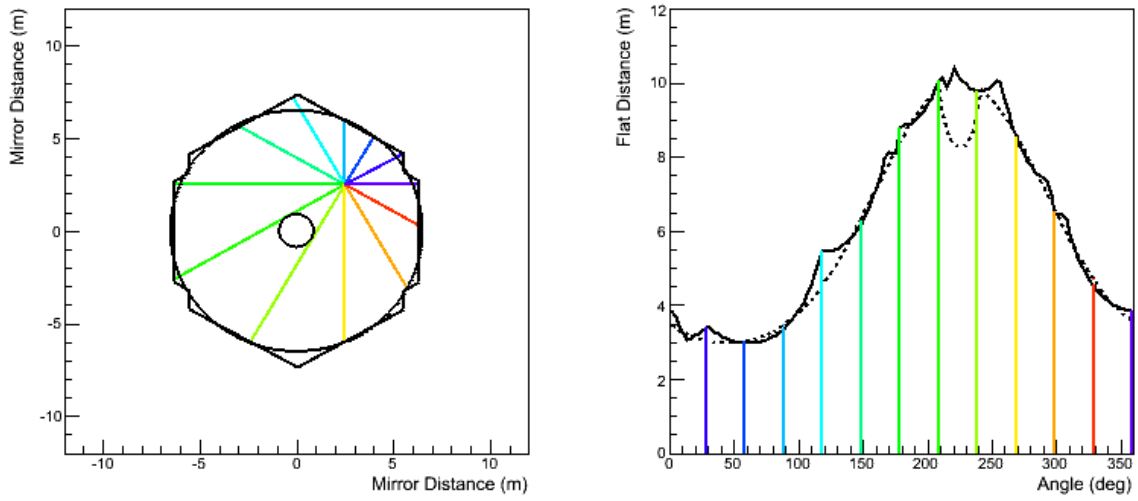


Figure 3.8: Variation of the distance to the mirror edge with azimuth angle for a given impact position, shown for the H.E.S.S. I telescopes under a circular approximation and using interpolation between a set of points. A circle is a good approximation to the mirror shape, and deviations are only minor. An example muon with an impact position offset from the mirror centre is chosen to illustrate the asymmetrical effect on the 1D profile.

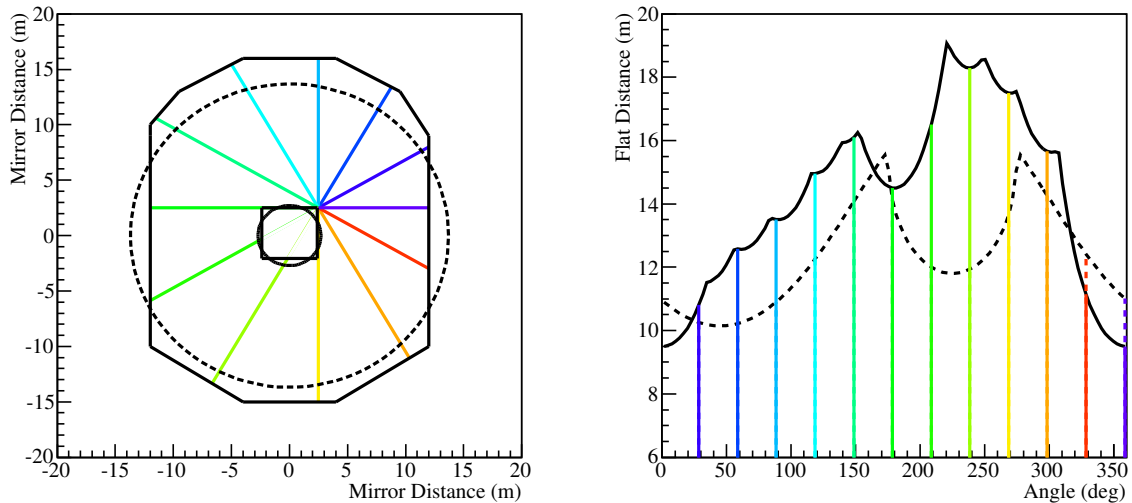


Figure 3.9: As figure 3.8 for CT5, shown for the true mirror profile and under a circular approximation. The circular approximation may under or overestimate the integration distance, leading to an apparent shift in the location of the central hole with azimuthal angle.

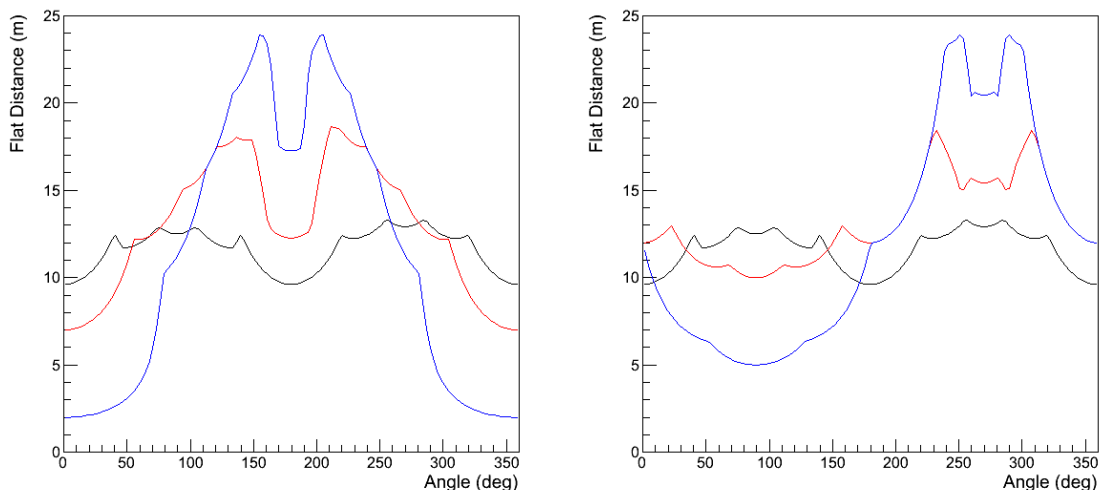


Figure 3.10: Variation in the distance $D(\rho, \phi)$ across the CT5 reflector dish with azimuth angle, shown (left) for fixed vertical position at 0 m and horizontal displacements of 0 (black), 5 (red) and 10 m (blue), and (right) for fixed horizontal position at 0 m and vertical displacements of 0 (black), 5 (red) and 10 m (blue). The effect of the corners and mirror edges is clearly noticeable in the profile shape as a function of azimuth angle.

centre of the mirror dish along the 1D azimuthal light intensity profile (see figures 3.7, 3.9, 3.10).

Instead of a circle approximation for the mirror shape, an interpolation between a set of points describing the mirror edges was used. The total distance $D(\rho, \phi)$ across the mirror is given by the distance from the impact position to the outer edge of the mirror, $D_o(\rho, \phi)$, less the distance along that same azimuthal angle ϕ traversing the central hole, $D_i(\rho, \phi)$, such that $D(\rho, \phi) = D_o(\rho, \phi) - D_i(\rho, \phi)$. These distances are obtained by finding the coordinates of the points at which a line from the impact position along angle ϕ intersects the interpolated mirror edge.

The effect of the non-circular mirror shape of CT5 can be seen in the variation of chord distance with azimuth angle for different impact parameters in figure 3.10. Due to accounting for the corners of the mirror, the slope is less smooth than in the case of a circle approximation (figure 3.9). It is clear from figure 3.10 that such a line interpolation accounts for smaller scale variations with azimuthal angle (such as near corners of a mirror dish) than is possible with the circle approximation.

This approach enables greater flexibility when describing mirror shapes; complex shapes can be described more precisely, whilst circular and smooth, curved mirror edges may still be described to reasonable accuracy by using a large number of points lying on a circle to define the outer edge. Nevertheless, the mirror is still described as a 2D flat projection; the radius of curvature of the mirror is not accounted for here. For CT1-4 with 12 m diameter dish, muon light could be received from as far back as $12 \text{ m} / \tan(\theta_c) \sim 600 \text{ m}$, where $\theta_c = 1.2^\circ$, the asymptotic value. As the radius of curvature of $\sim 15 \text{ m}$ is just a small fraction of this distance, treating the mirror as a 2D flat projection would lead to a systematic error $\sim O(1 - 2\%)$, a negligible effect. Parameters relevant for CT5 lead to a similar order of magnitude.

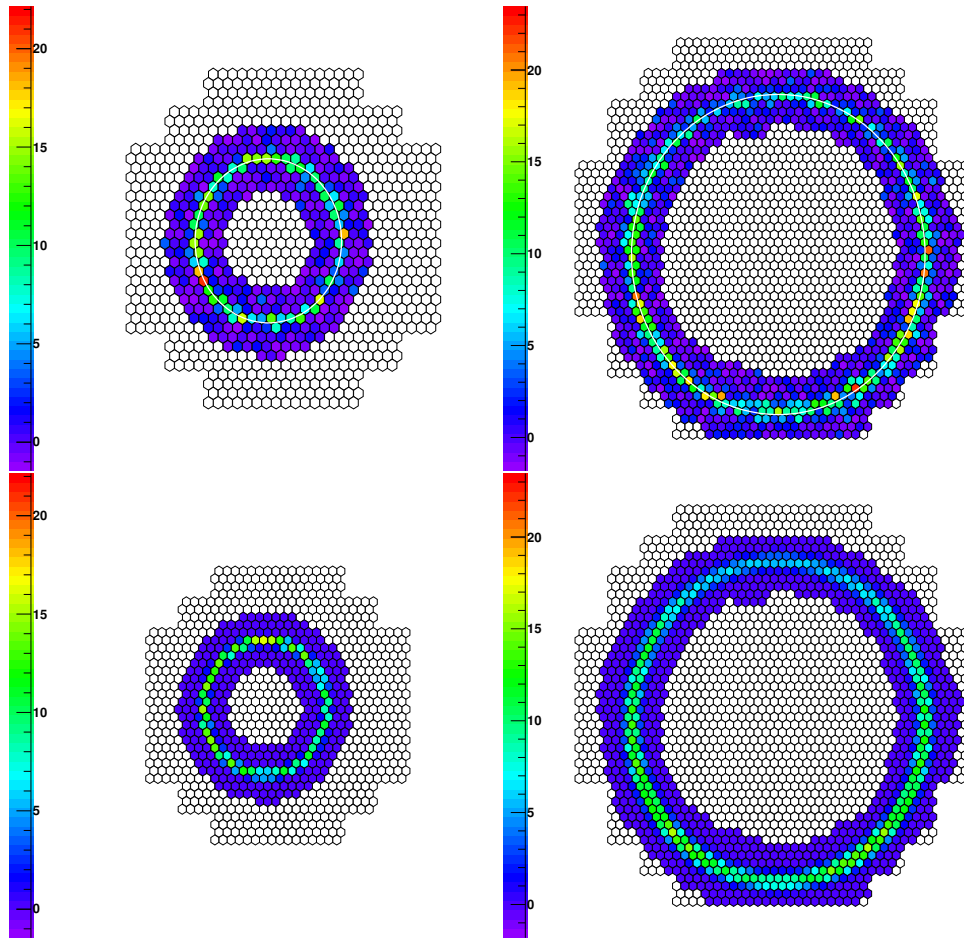


Figure 3.11: Muon Events as seen in the cameras of CT1 (left) and CT5 (right). Above: After the second pass image cleaning, showing the circle fit. Below: Analytically calculated model expectations corresponding to these muon events, using equation (3.1.6). The colour scale corresponds to the pixel charges.

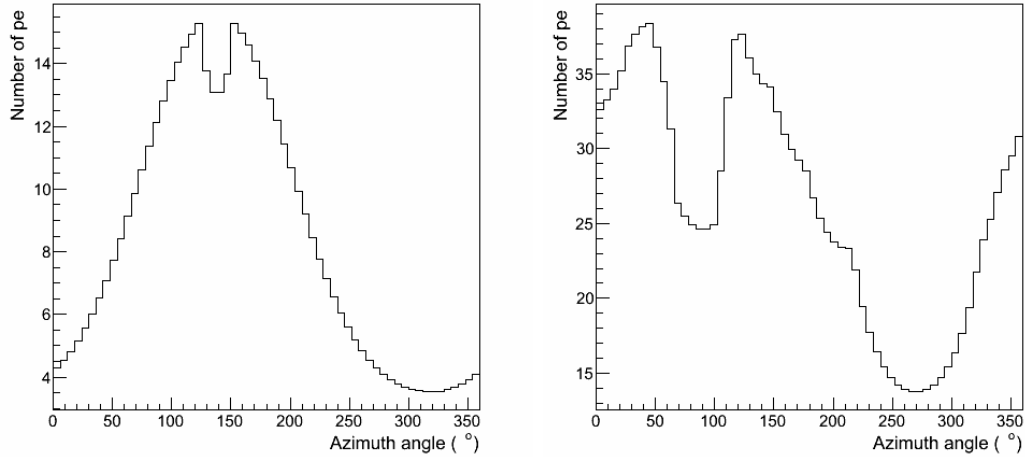


Figure 3.12: Distribution of light intensity around the muon ring, plotted as a function of azimuth angle for muon events in the CT1 (left) and CT5 (right) cameras. The distribution is reminiscent of the chord distance as shown in section 3.4.2, as the two are directly proportional as given by equation (3.1.6)

3.4.3 2D Image Fit Model

The raw muon image is translated into a profile as follows. The amplitudes of all pixels contained in the image after cleaning are summed and stored in a one dimensional histogram of amplitude with azimuth angle. A corresponding one dimensional theoretical light profile is then calculated corresponding to the raw light profile angular distribution (figure 3.12), the shape of which is reminiscent of the chord distance in figure 3.10. In calculating the expected intensity, both the corresponding azimuth angle and the muon ring parameters (centre position, radius and width) must be known. To ensure that the histogram bins in the theoretical profile histogram of charge with azimuth angle correspond correctly to the number of pixels summed which contribute to the same azimuth angle in the raw light profile, it is necessary to multiply by a scaling factor $2\pi R/\omega N_{rbx}$, where N_{rbx} is the number of bins along the x axis of the raw light profile, and ω is the angular pixel size.

The theoretical expected intensity per histogram bin is then given by equation (3.1.6) multiplied by the scaling factor and the efficiency. This theoretical intensity profile is then smoothed by a Gaussian function in the radial direction, with width given by the fitted ring width, spreading out the expected charge over the width of the muon ring. Again, here it is important to ensure that the total charge in each radial direction remains the same before and after smoothing. This is achieved by normalising each bin in the smoothed histogram by the ratio (found per azimuth angle) of the theoretical charge per bin before smoothing to the integrated charge contained along the radial direction after smoothing.

Using a log-likelihood minimisation procedure, the intensity profile is then fitted in order to obtain the image parameters; impact position (x,y in metres), ring width (in degrees) and muon efficiency; within a given range. Figure 3.11 shows two example muon events and their model prediction, whilst figure 3.12 illustrates the one-dimensional light intensity

distribution around the ring.

In calculating the expectation for the likelihood minimisation, the number of pixels in the camera corresponding to the number of bins in the smooth profile for the same azimuth angle must be accounted for, by a factor which may be termed a “pixel area factor”, A_p :

$$A_p = \frac{\omega^2 N_{xb}}{w_{by} 2\pi R} \quad (3.4.1)$$

where w_{by} is the width of a bin in the radial direction of the two dimensional smoothed histogram, and N_{xb} is the number of bins at ring radius R which correspond to the full 360° in azimuth angle.

The following equation from [46] is then used to calculate the pixel log-likelihood L from a Gaussian approximation:

$$\ln L = -2 \times \ln P(s|\mu, \sigma_p, \sigma_\gamma) \quad (3.4.2)$$

where P is the probability of observing a signal s in a pixel with expectation value μ , given a pedestal width of σ_p and a single photoelectron peak width of σ_γ . (The parameter μ corresponds to the predicted intensity in each pixel in this application.) In the case of high model prediction μ compared to the observed signal s (valid for muon calibration):

$$P(s|\mu \gg 0, \sigma_p, \sigma_\gamma) \approx \frac{1}{\sqrt{2\pi(\sigma_p^2 + \mu(1 + \sigma_\gamma^2))}} \exp\left(-\frac{(s - \mu)^2}{2(\sigma_p^2 + \mu(1 + \sigma_\gamma^2))}\right), \quad (3.4.3)$$

where the log-likelihood (3.4.2) behaves like a χ^2 in this limit [46]. A minimisation is then done using the Minuit [68] algorithm to find the best fit parameters describing the muon event. Parameters from the circle fit (ring centre coordinates in the camera frame and the ring radius, $x_c(^{\circ}), y_c(^{\circ}), r(^{\circ})$) are kept fixed, whilst the impact position of the muon on the mirror, $x(\text{m}), y(\text{m})$, the ring width $\Delta r(^{\circ})$ and the optical efficiency ε are left as free parameters of the fit. The impact parameter, distance of the impact position of the muon from the centre of the mirror, is calculated as $\rho = \sqrt{x^2 + y^2}$. Following the minimisation procedure, only those events passing the ring width and impact parameter cuts as defined in table 3.1 are retained. From the impact parameter cut, muons are constrained to have passed through the reflector dish. The average number of neighbouring pixels is found to be an effective cut in distinguishing ring-like images from more clumpy or broader hadronic images, with a value close to 3 well describing a circle.

3.5 Performance

As far as possible, it is desirable that the new muon calibration code produces results compatible with the previous version on the H.E.S.S. I telescopes and on pre 2012 data, and also that the code performs robustly under various degradation levels. Tests characterising the performance of this updated muon calibration algorithm, on both simulations and data, are outlined in this section.

Selection	Cut Parameter	CT1-4	CT1-4	CT5	CT5
		Lower	Upper	Lower	Upper
Preselect	N_{pix}	30	960	100	2048
	N_{brkpix}	0	70	0	50
	N_{edgepix}	0	10	0	30
	$\langle \text{NN} \rangle$	0	3.5	0	3.5
	$r(^{\circ})$	1.0	1.5	1.1	1.4
	$r_o(^{\circ})$	0.	2.	0.	1.7
Postselect	$\Delta r(^{\circ})$	0.04	0.08	0.04	0.08
	$\rho(\text{m})$	0.9	6.4	2.0	14.0

Table 3.1: Muon image selection cuts used to select the most appropriate muon rings for calibration, which need to be adjusted between different telescope types. N_{pix} is the number of pixels in the image, where the upper limit is the total number of pixels in the camera; N_{brkpix} and N_{edgepix} are the number of broken pixels and the number of pixels falling on the edge of the camera respectively; $\langle \text{NN} \rangle$ is the average number of neighbouring image pixels; $r(^{\circ})$, $r_o(^{\circ})$ and $\Delta r(^{\circ})$ are the ring radius, outer radius and ring width; and ρ is the impact parameter. Preselection cuts are applied after the circle fitting stage and muon identification stage, whilst the postselection cuts on Δr and ρ are applied after intensity fitting.

3.5.1 Monte Carlo Studies

The performance of the muon calibration code for H.E.S.S. II was tested on Monte Carlo (MC) with CT1-4 at 70% and CT5 at 80% of nominal optical efficiency, on both dedicated muon only simulations, and on proton simulations. In the latter case, only secondary muons from decays in the hadronic showers occur. Cross-checking these simulations is important to ensure that the muon calibration is not biased towards single muons without hadronic background; and indeed good agreement was shown between the reconstructed muon efficiency parameter on muon only simulations and on proton simulations, as shown in figure 3.13. The mean of this distribution of muon events from simulations is used to define the correction in equation (3.2.1).

As can be seen in figure 3.14, the ratio of the codes is approximately stable to within 5% over different MC phases, such that the obtained efficiencies track the same variation with changes in the simulated optical efficiency of the telescopes.

An important check for the robustness and performance of the code under varying conditions is that the muon calibration does not become biased as the telescope degrades further. This is an important issue, as a miscalibration at large degradations could severely affect the image reconstruction. In practice, through monitoring of the telescopes over time, one would expect that the level of telescope degradation as a fraction of its nominal efficiency is known to within 10%, with corresponding lookups available such that correction factors of more than 20-30% are not required. Nevertheless, this behaviour may be checked on Monte Carlo by plotting the linearity of the correction factors obtained by the muon calibration code to those expected based on the true input telescope optical efficiency. This is shown in figure 3.15, where the current, more generic muon calibration algorithm is seen to out-perform the previous in terms of linearity under degradation (or equivalently, robustness).

With the encouraging Monte Carlo results, further checks of the performance and

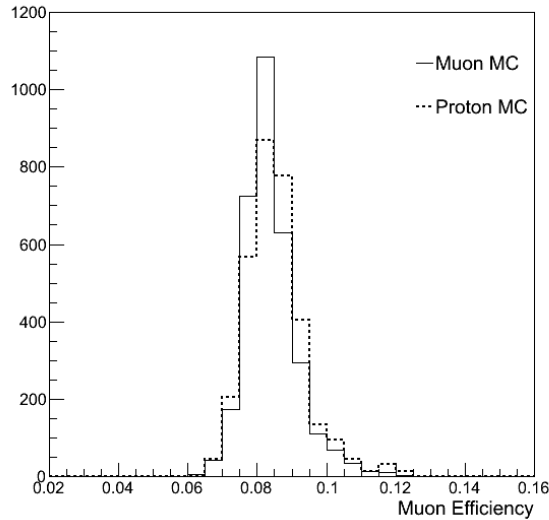


Figure 3.13: Muon efficiency distributions for CT5 at a degradation level 80% of nominal optical efficiency as obtained from Monte Carlo. The distributions obtained from dedicated single muon simulations, and from using secondary muons from hadronic showers in proton simulations are overlaid. No significant bias is seen between the two results.

comparisons to the previous muon calibration algorithm were performed on data.

3.5.2 Performance on Data and Consistency Checks

As a first check of the performance on data of the current algorithm in comparison to the previous, the efficiency distribution obtained after a single run of H.E.S.S. II data by both versions for CT5 is shown in figure 3.16. Due to the different reconstruction approaches used, the location of the mean of the distributions shown differ between the two codes; however, both approaches yield consistent correction factors. The CT5 correction factor back to the Monte Carlo reference of 80% of the nominal optical efficiency showed only a 2.3% difference between the two algorithms. The assessment that CT5 is in fact more efficient than assumed by Monte Carlo is consistent with both approaches. The distribution for the previous calibration code clearly suffers from a slight bias towards underestimating the telescope efficiency, leading to a mildly asymmetric distribution (figure 3.16). This accounts for the difference in the correction factors, with a slightly higher correction factor obtained by the previous algorithm (figure 3.15), an expected consequence of underestimating the mirror area via the circle approximation. With the current generic algorithm, the overall distribution is clearly improved; not only has the asymmetric part been removed, but also the peak is increased and the spread of the distribution reduced for a similar number of muons, reflecting the more appropriate reconstruction and set of cuts that have been used.

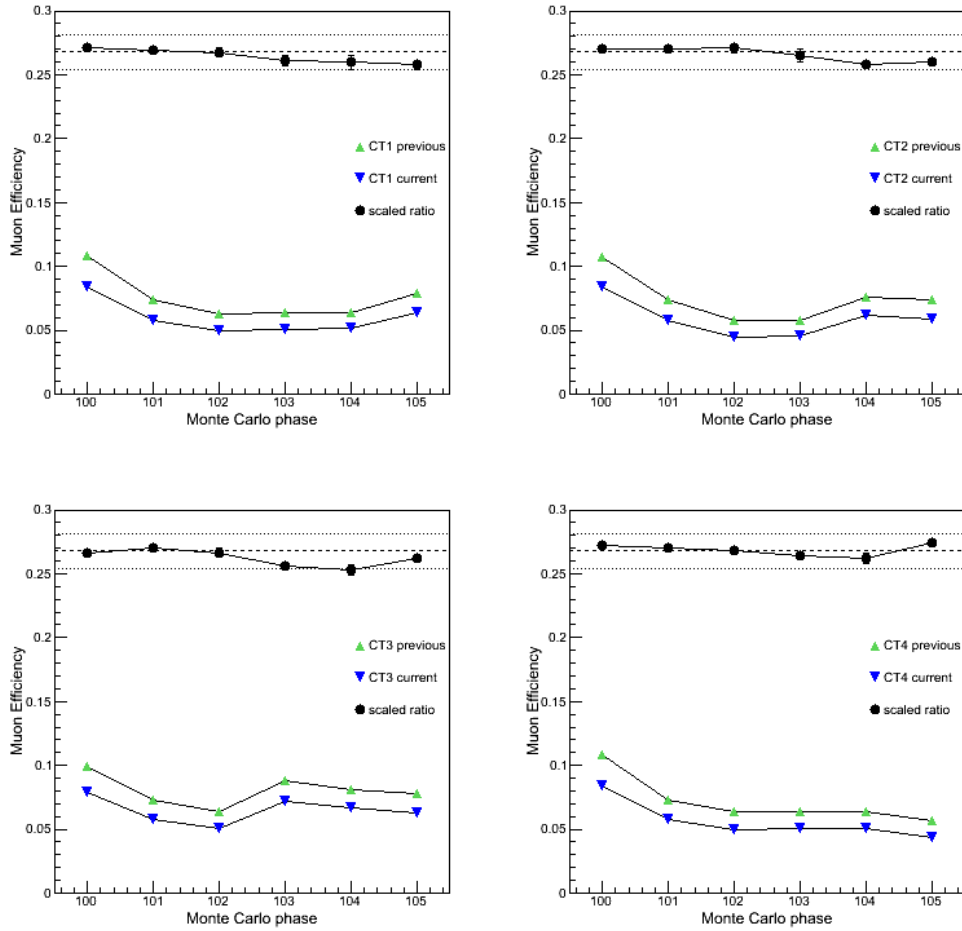


Figure 3.14: Muon efficiencies found by the previous and current versions of the muon calibration, shown with arbitrary Monte Carlo phase (see table 3.2) for each of the four H.E.S.S. I telescopes. Each MC phase (100-106) corresponds to a different combination of optical efficiencies. The ratio between the two algorithms (scaled to arbitrary values) is found to be reasonably stable with MC phase; dotted lines mark deviations of 5% from the mean value (dashed line).

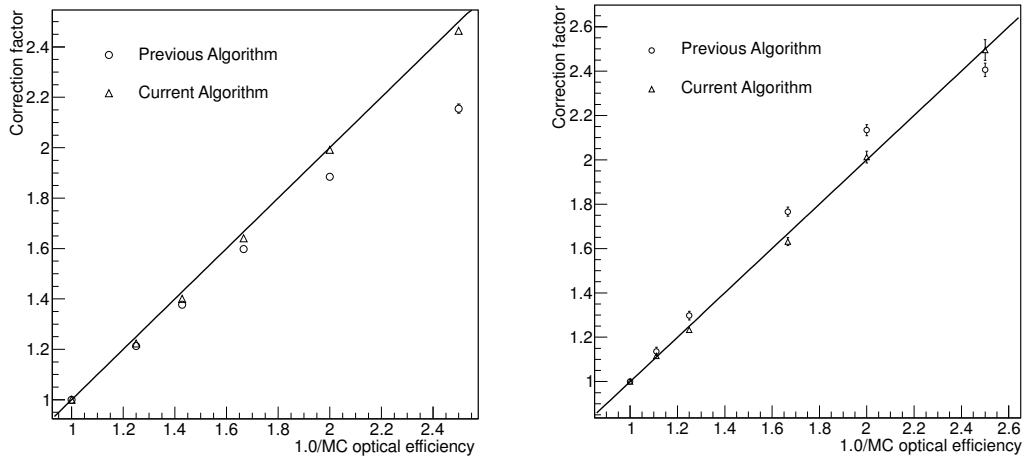


Figure 3.15: Linearity of the correction factor obtained using the muon calibration, plotted against the expected correction factor from the degradation level simulated. In all cases, the correction back to 100% nominal optical efficiency, at (1,1), is shown. In the case of H.E.S.S. I degradation (left), the previous algorithm starts to deviate from linear behaviour at 40-50% discrepancy, whereas the current version remains linear up to very high correction factors (corresponding to 40% efficiency). Similarly, the linearity of the current calibration with degradation of CT5 (right) remains up to high correction factors. Under typical operating conditions, correction factors rarely exceed 1.5.

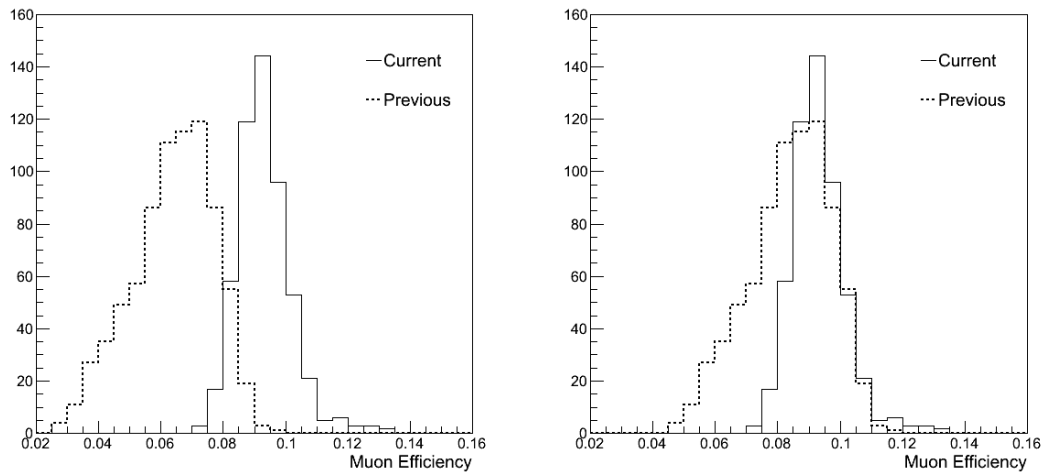


Figure 3.16: Distribution of CT5 muon efficiencies obtained from a single run of data taking, using both the previous algorithm and the current algorithm for muon calibration. Left: the absolute muon efficiencies from both codes. Right: the distribution from the previous algorithm has been shifted by the expected systematic ratio between the two codes (see figure 3.14).

3.6 Optical Efficiency Variation

An important aspect of the muon calibration is the opportunity it provides for monitoring the telescope degradation over time. To this end, the evolution of the muon efficiency parameter over the course of approximately ten years of H.E.S.S. data taking period is shown in figure 3.17, for the four H.E.S.S. I telescopes with comparable optical efficiencies, and for CT5 which, being more recently constructed, has a much higher optical efficiency and hence appears offset. By showing the muon efficiency as a fraction of its nominal value, the transition between the two muon calibration algorithms can be smoothly bridged.

During the H.E.S.S. I four telescope era, particularly notable features include the recoating of the mirrors of each of CT1-4, occurring in turn from MJD 55300 to 55900. As the muon calibration is performed in a run-wise manner, some scatter around the average values is seen. These values at large offsets are typically due to truncated runs or runs with known hardware issues; although error bars are not shown in figure 3.17 for clarity, these scattered values often have large errors, still lying within $1-2 \sigma$ of the average.

The start of the H.E.S.S. II era is marked by the first few magenta CT5 points in figure 3.17. Whilst the optical efficiencies of CT1-4 are mostly stable over the H.E.S.S. II period, the evolution of CT5 optical efficiency shows a steep decline, with the gradient gradually reducing over time. This may be partly due to a known degradation in the gain of the camera (see chapter 2) over this period, which has not been accounted for elsewhere. Rather than monthly averaged values, only two values of the camera gain (see equation (2.4.2)) are used in calibration over this period, and the effect of switching the gain value used in the calibration can be seen clearly around MJD 56450. Additionally, degradation of the various telescope components is known to be more rapid soon after commissioning, with the rate of degradation expected to slow down and stabilise over time.

Near to the start of H.E.S.S. II, there is a period of time for which there are two muon efficiency values in each of CT1-4; this is due to these runs being processed by both the previous and the current calibration algorithms. From the start of H.E.S.S. II, the reference value used for figure 3.17 was the correct value for the new algorithm, leading to an arbitrary shift in the values obtained for CT1-4 using the previous algorithm. Whilst figure 3.17 shows all values stored in the database at the time of access, in data analysis, only the most recent entry is used for calibration. The true date for transition to the reference values with the current calibration algorithm is slightly later than indicated in figure 3.17 at around MJD 56350, corresponding to the date at which CT5 began regular data acquisition and at which multiple muon efficiencies for CT1-4 are shown. Therefore, in practice, there is no such arbitrary shift in muon efficiencies propagating through to the data analysis level, and the apparent discrepancy around MJD 56300- 56400 is not a cause for concern.

As a further consistency check, regardless of the efficiencies obtained by both versions of the muon calibration code, the correction factor (ratio of the muon efficiency from the reference Monte Carlo set to muon efficiency from data) should remain the same. This is shown in figure 3.18, with the evolution of correction factor as obtained by the previous

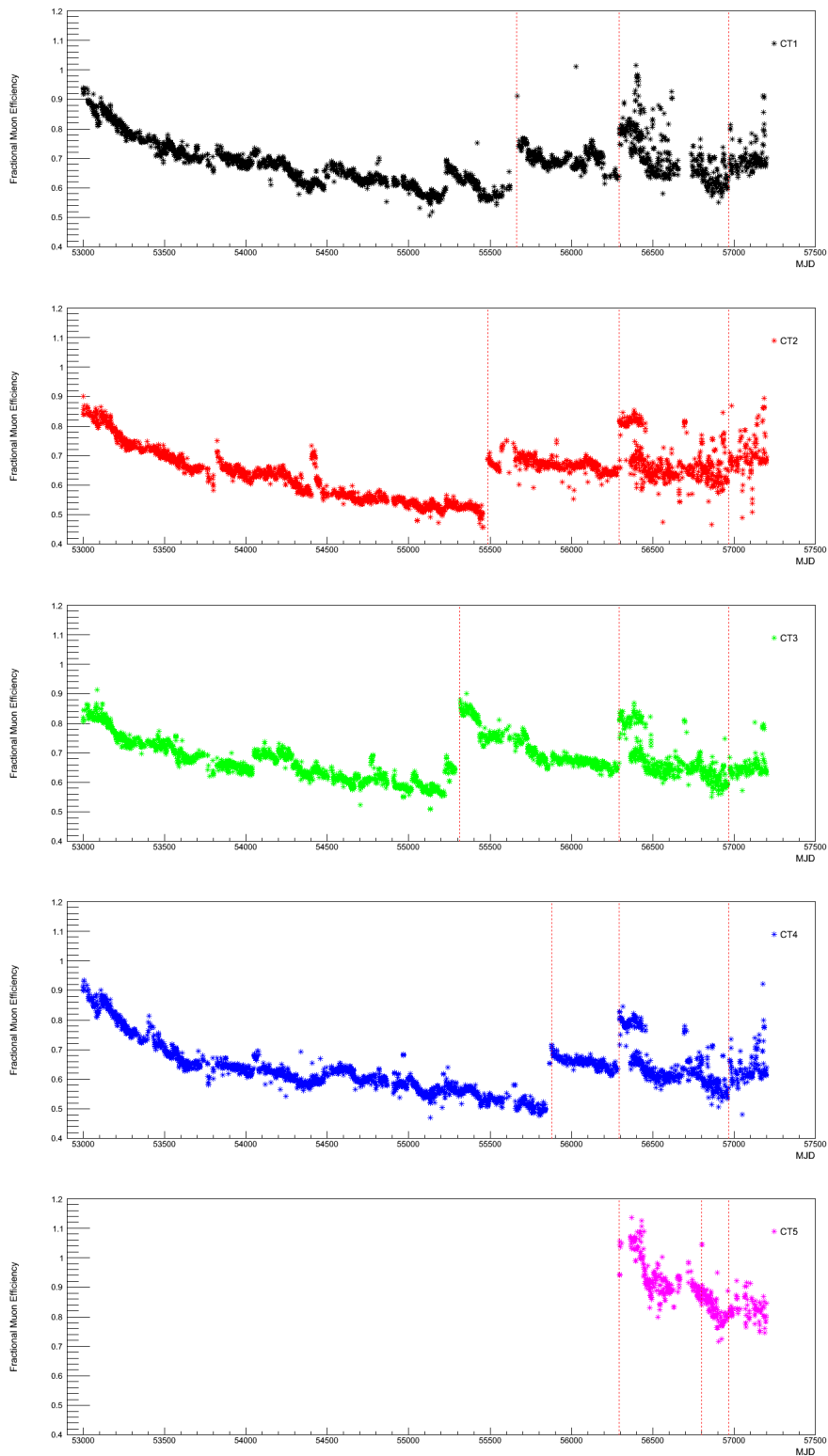


Figure 3.17: Evolution of the fractional muon efficiency with MJD, shown for all five H.E.S.S. telescopes over approximately 10 years of operation. The optical efficiency of the newer CT5 is clearly above that of the older H.E.S.S. I telescopes at the start of CT5 data taking. Dashed lines mark the mirror recoating for each of CT1-4 respectively, the start of H.E.S.S. phase II and the cleaning of the Winston cones.

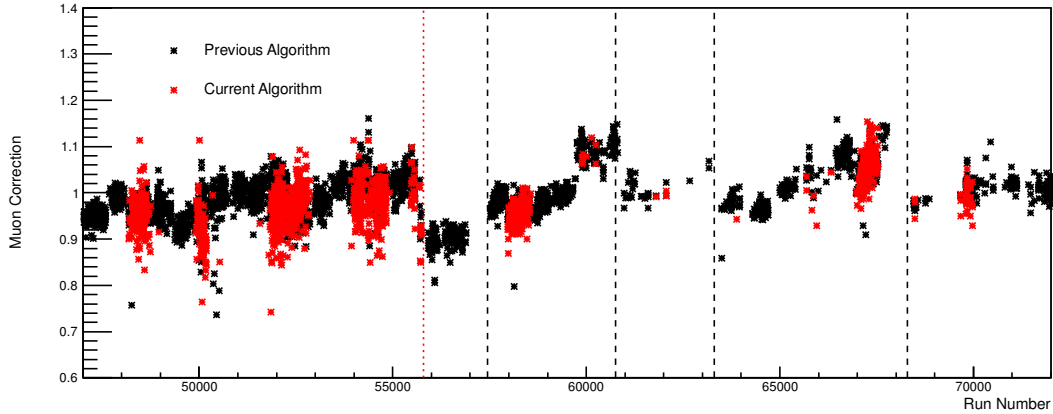


Figure 3.18: The correction factors (shown for CT3) obtained by both the previous (black) and current (red) muon calibration algorithms seem to agree reasonably over a wide range of H.E.S.S. data. Transitions between Monte Carlo simulation phases (see table 3.2) are indicated by black dashed lines, whilst the red line indicates a period of camera maintenance.

(in black) and current (in red) muon calibration codes shown as a function of run number for CT1-4. Jumps in the correction factor may be seen typically corresponding to changes in the Monte Carlo phase; the set of lookups used and the reference telescope efficiencies; or hardware changes.

3.6.1 Dependence on Hardware

As the muon efficiency is a global calibration parameter, acting as a scaling coefficient in equations (2.4.2), it is a measure of the global optical efficiency of the entire telescope system (camera and mirror combined), determined after calibration of all the individual components. Thus it is susceptible to changes in any of these components. In 2010-2011, the mirrors of the CT1-4 telescopes were recoated, leading to an improved optical efficiency, seen as a jump in the evolution over time (with a preceding gap, when the telescope was out of service due to the mirror recoating).

In figure 3.17, several examples of such known hardware changes are indicated by red lines. The first, dashed line corresponds to recoating of the CT1-4 mirrors, which took place at different times for each telescope. The start of HESS phase II is marked by a dashed line around MJD 56300. Adjustments in the gain of the camera, done for all telescopes, occurred around MJD 56800 (only marked for CT5). For CT5, the gain was stabilised across the camera where previously a slight gradient was seen; the efficiency can be seen to increase for one night and then return to a similar level to that previously, corresponding to different camera settings trialed during this maintenance period. The net effect of the gain adjustment at MJD 56800 on CT1-4 was a slight reduction in the overall efficiency. The final red dashed line corresponds to another camera maintenance campaign, during which the Winston cones on CT1-4 (but not CT5) were cleaned, leading to an efficiency increase in CT1-4. Due to the lower energy threshold of CT5 and its higher sensitivity, the trigger rate of the overall array increases dramatically when CT5 is included in data taking. As the CT1-4 telescopes rely on a stereo trigger, there are many events which previously would not have been recorded, as they triggered only one

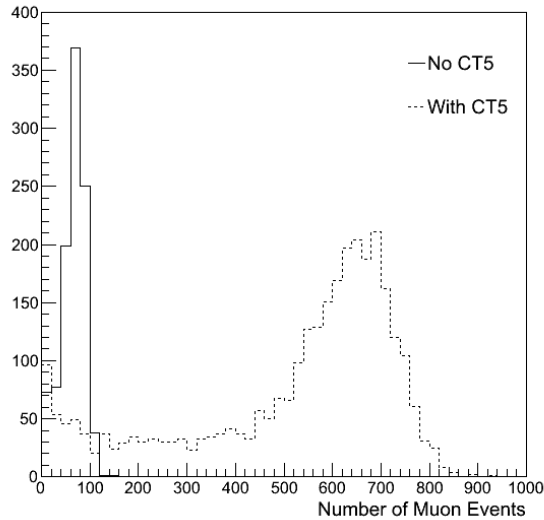


Figure 3.19: The average number of muons per observation run seen by a single telescope recording only stereo triggered events increases dramatically with the inclusion of CT5, as shown here for CT3.

telescope. However, with CT5, a significant proportion of events trigger CT5 and one of CT1-4; that is, with inclusion of CT5, the trigger rate of each individual telescope also increases. Consequently, there are more muons per run for CT1-4 in the H.E.S.S. II data that were previously seen on average (figure 3.19), as in the case of a muon triggering one of CT1-4, there is an increased likelihood of the parent hadronic shower simultaneously triggering CT5.

3.6.2 Correlation with Other Muon Image Parameters

As is to be expected, some of the parameters describing a muon ring are intrinsically linked to the muon efficiency, whilst others should be independent. One of the main motivations for applying cuts on the muon images is to avoid biasing the obtained optical efficiency parameter due to these correlations. Due to changes in the refractive index over the path travelled by the muon, telescope effects (such as the point spread function) and contributions from scattering, the width of the ring image becomes broader (see section 3.1.2). In this case the same amount of Cherenkov radiation produced by the muon over the typical path length is consequently spread over more pixels; hence each individual pixel receives less light. This effect may cause a bias in the reconstruction, towards underestimating the telescope optical efficiency. The stringent cut on the ring width aims to minimise this.

It is important to ensure that the muon efficiency is not systematically biased by parameters of the image, such as by the level of scattering of the Cherenkov light or the offset of the muon trajectory from the mirror (quantified by the ring width and impact parameter respectively). A check for such correlations is shown in figure 3.20, where it can be seen that after applying cuts as in table 3.1, no significant correlation remains. Assuming a random scatter of events, the number of muons increases roughly linearly

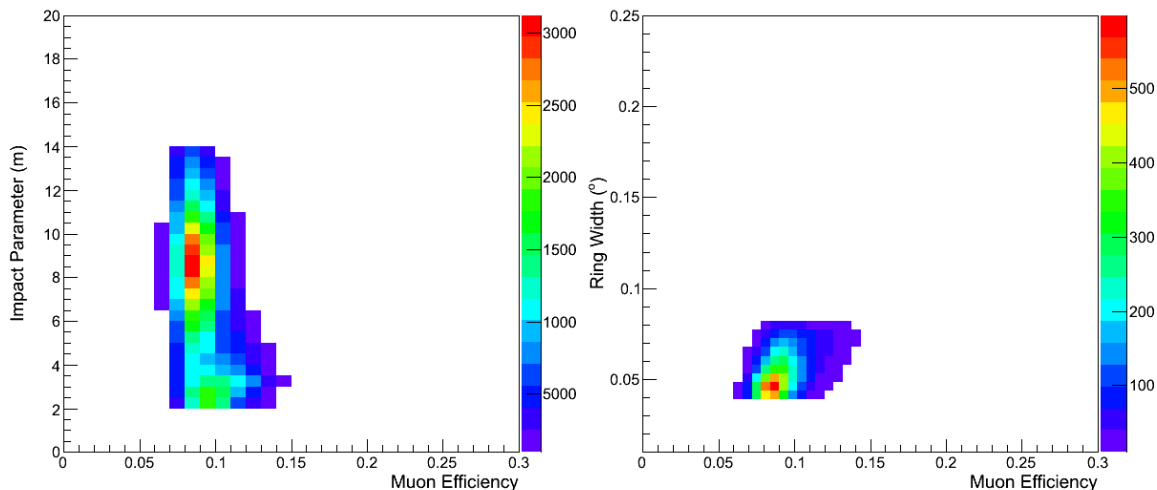


Figure 3.20: Reconstructed parameters of the muon event against muon efficiency for CT5. Left: impact parameter against muon efficiency. Right: ring width against muon efficiency. In both cases there is no significant correlation.

with radius, until beyond an impact parameter of ~ 10 m, the number of muon rings which are well contained within the camera and which subsequently pass the selection cuts decreases with increasing radius.

Similarly, it is important to check for a possible dependence of the efficiency on the number of pixels contained within the image. If there are many broken pixels within the ring image, or the ring is only partial, then the location of the peak in the 1-dimensional intensity distribution may be liable to mis-reconstruction, such as a shifted location. The previous 1-dimensional χ^2 fit algorithm is more susceptible to this than the current 2-dimensional log-likelihood fit algorithm; whereas the 1-dimensional χ^2 approach smooths the intensity distribution over four pixel widths along the ring, thereby smoothing out breaks in the raw intensity profile due to pixels, the 2-dimensional model approach deals with this in a more robust way as broken pixels enter into the model prior to the fit minimisation. No significant bias of the muon efficiency with the number of pixels in the image was seen.

3.6.3 Positional Variation

Positional variation in the muon efficiency value may be seen independently in the camera, on the mirror dish and with the sky pointing position. The reasons behind each variation are outlined below.

Variation across the Camera

Positional variation in the camera stems from both the intrinsic variation in efficiency of the camera components and due to the camera acceptance. As well-contained muon images are selected for the calibration, this ensures that the majority of muon images used arrived parallel to the telescope optical axis, with the ring image centred near to the centre of the camera. Indeed, the strongest variation observed with a decrease towards the

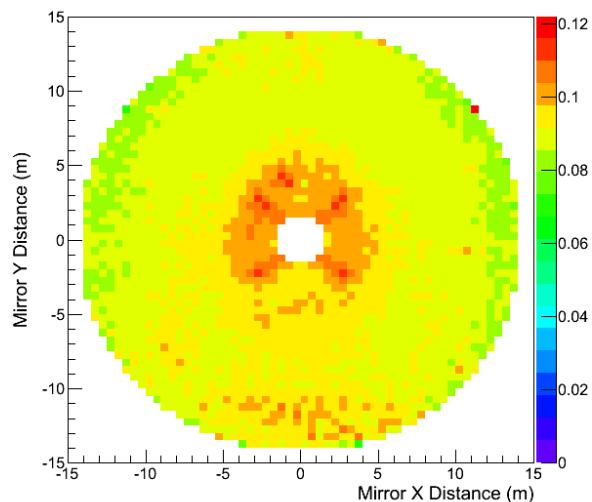


Figure 3.21: Muon Efficiency as a function of impact position on the telescope mirror. A gradient is seen across the mirror, with lower efficiency seen on the side closer the ground due to abrasion by sand particles. The effect of the telescope masts can be seen near to the mirror centre.

camera edges occurs as a result of the muon image selection cuts imposed, particularly on the outer radius and edge pixel cuts (see table 3.1). Other camera variation effects which may occur include a gradient across the camera, possibly related to the camera gain.

Variation across the Reflector Dish

Variation with impact position on the mirror dish (see figure 3.21) may show a similar general trend of increasing efficiency towards the mirror centre due to selection bias. However, in this case a shadowing effect due to the telescope masts can also be observed. This leads to a bias towards higher muon efficiency values since only the brightest muon events are seen at the positions affected by shadowing. In each reflector dish, there is one absent mirror facet corresponding to the location of the sky CCD used for the telescope pointing calibration (see section 2.4.2); this may also be identified in the muon results by the comparative lack of muon events occurring at that point in the mirror.

Variation with Observation Position

Variation with observing position may be attributed to many factors, including night sky brightness, atmospheric conditions and seasonal variation, particularly apparent for those regions of the sky which are only observable for part of the year. Although there is no significant variation with observation angle (see figure 3.22), there are two azimuth angle regions at which the muon efficiency seems to drop. Whilst on the whole a semi-uniform coverage of all azimuth angles is given by the data, for these two angles, the date of the data taken is significantly later on average than for other azimuth angles. This can happen if the corresponding region of the sky is comparatively empty (away from the Galactic plane) and there are no proposals for a given year to observe extragalactic objects in that region. The net effect is that the efficiency probed by these runs reflects the degraded

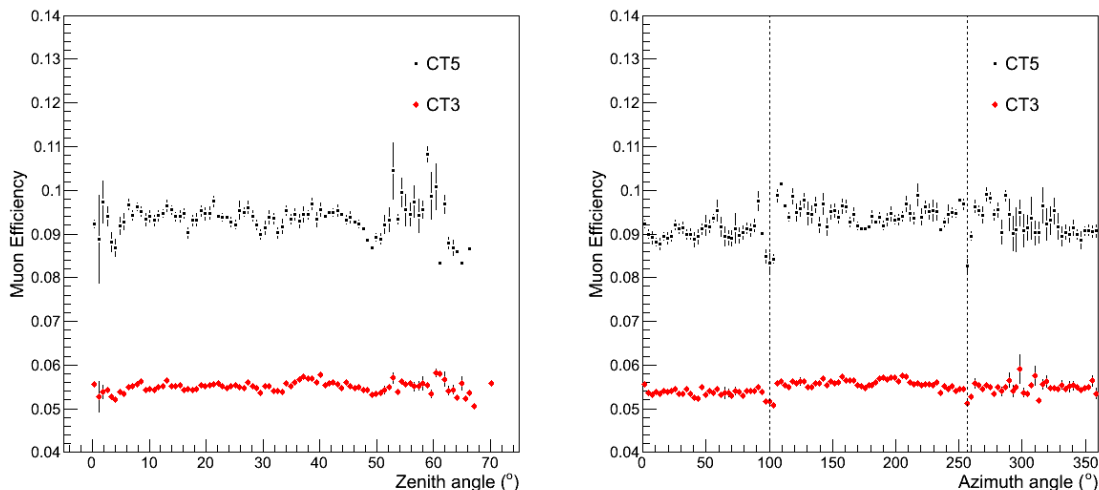


Figure 3.22: CT5 Muon Efficiency with observation position. There is no significant variation in muon efficiency with zenith angle, although there is some larger variation at high zenith angles above about 55° , due to the lower frequency with which data is taken. The muon efficiency can be seen to drop at two azimuthal angles, indicated by dashed lines; these correspond to comparatively empty regions of the sky (away from the Galactic plane), for which the majority of the data was taken at later times, such that the average efficiency is lower.

state of the system at a later date with respect to other azimuthal angles.

3.6.4 Influence of Broken Pixels

The number of broken pixels occurring in any given set of data is a comparatively unpredictable quantity, which may influence the reconstructed muon efficiency. Pixels may be classified as broken for a variety of reasons, both intrinsic to the pixel itself and extrinsic. For example, if a bright astronomical object passes into the field of view of the pixel, thereby increasing the high voltage in that pixel, then the pixel is turned off [36]. This can be done automatically based on the pixels anode current, and is generally anticipated in the case of bright stars (with an apparent magnitude less than 6) crossing the field of view.

For the muon analysis, it is important to quantify any possible bias in the reconstruction occurring due to increased numbers of pixels turned off in the field of view. This helps to decide where to place a quality cut on the number of broken pixels occurring. In the case of too many broken pixels, then an alternative muon efficiency estimation should be used, such as using the value obtained from data on other regions of the sky from the same night.

To this end, a MC study was performed to check variation of the reconstructed muon efficiency with the number of broken pixels in the camera. A randomly assigned broken pixel mask was applied to each camera in the MC, for various broken pixel levels. Additionally, the effect of a missing drawer (group of 16 pixels) was also investigated (see figure 3.23). An entire drawer may be switched off due to electronics problems, which can occur during camera configuration. It is worth noting that the majority of such low-level single pixel or drawer problems occur on a run-wise or night-wise basis, and are usually speedily resolved. Figures 3.24 and 3.25 show the effect of increasing amounts of broken

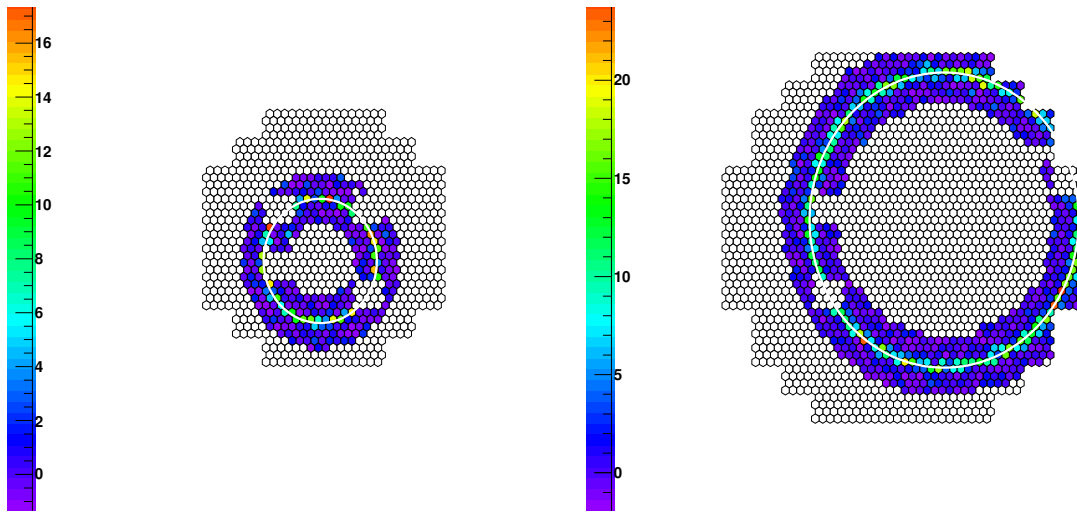


Figure 3.23: Monte Carlo camera muon event images with missing drawers, from a mask applied in the Monte Carlo study, shown for one of the H.E.S.S. I telescopes (left) and CT5 (right).

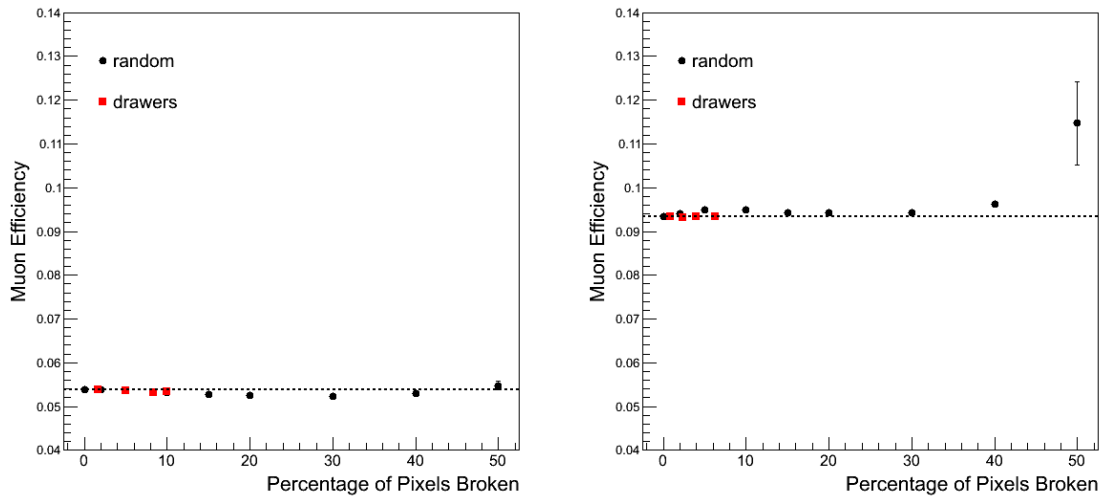


Figure 3.24: Effect of increasing amounts of broken pixels on the reconstructed muon efficiency, for both randomly distributed broken pixels (“random”) and for broken drawers (“drawers”), shown for CT1 (left) and for CT5 (right). The muon efficiency is seen to remain mostly stable with higher percentages of broken pixels.

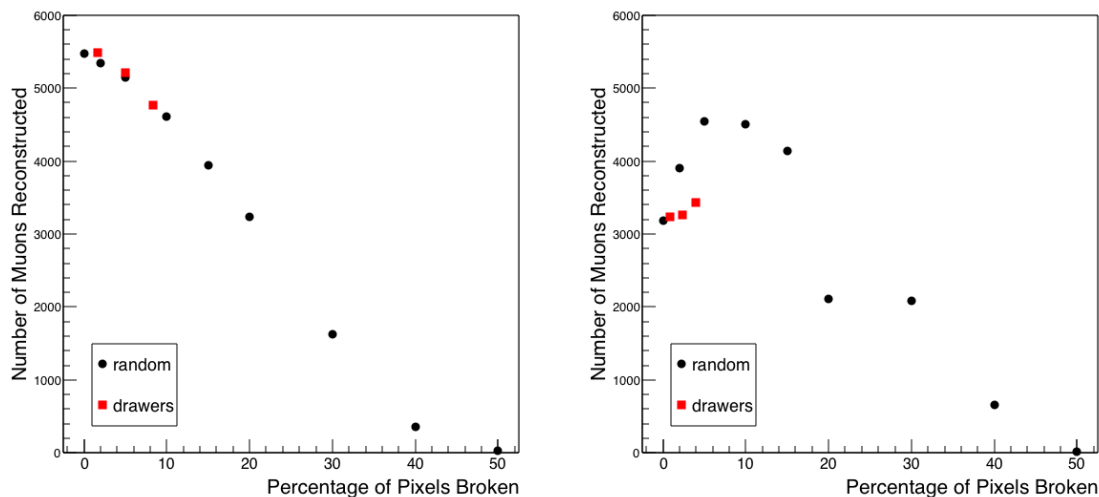


Figure 3.25: Effect of increasing amounts of broken pixels on the number of muons passing cuts, shown for CT1 (left) and CT5 (right), for broken pixels randomly distributed (“random”) and for broken drawers (“drawers”), clusters of 16 pixels. The number of events passing cuts increases initially for CT5 with more broken pixels - see text and figure 3.26.

pixels on the reconstructed muon efficiency and on the number of muon events passing cuts respectively. This algorithm is shown to be remarkably robust against broken pixels for the H.E.S.S. I telescopes, with little deviation seen up to 30% broken pixels. For CT5, the algorithm is reasonably robust also up to $\sim 30\%$ broken pixels, although clear deviations become apparent beyond this level.

As can be seen in figure 3.26, with increasing levels of broken pixels, the number of events passing the cut on the number of pixels in the image decreases as expected. As the cut on average number of neighbouring pixels is an upper limit (see table 3.1), with increasing broken pixels the number of events passing this cut actually increases initially for CT5, as the lower average number of neighbouring pixels differs, whilst the reconstructed ring parameters remain almost exactly the same for low amounts of broken pixels. This is also clearly seen in figure 3.25, where the number of muons increases more rapidly for randomly distributed broken pixels than for broken drawers, due again to the average distribution of pixels included in the image.

3.6.5 Dependence on Environmental Parameters

Monte Carlo (MC) were produced for muons under a variety of different environmental conditions, such as for varying wind speeds. The MC wind speed parameter is treated as equivalent in practice to the amount of aerosols present in the atmosphere. With increasing MC wind speed, the level of aerosol content increases, thereby increasing the likelihood of scattering of Cherenkov light. In regular data taking, the true wind speed alone has a negligible effect on the muon efficiency. This effectively means that the Cherenkov emission corresponding to different sections of the muons flight path no longer reach the telescope coherently; indeed, some of the emission may be scattered away from the mirror entirely. Consequently, the light intensity recorded in the camera for higher wind speed (aerosol content) is less than in the case of zero average wind speed, or no

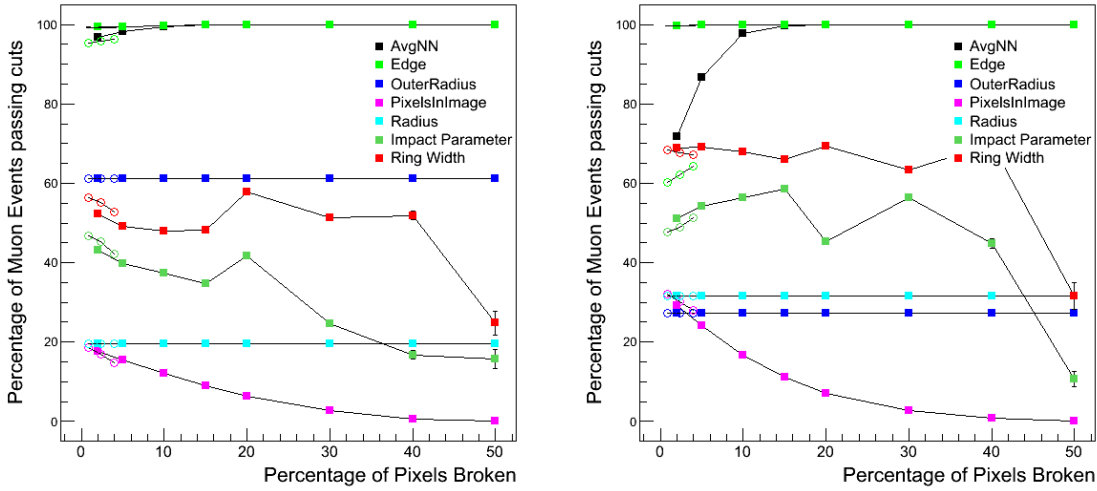


Figure 3.26: Effect of increasing amounts of broken pixels on the number of muons passing cuts, shown for CT1 (left) and CT5 (right). Solid points correspond to randomly distributed broken pixels, whilst open circles correspond to broken drawers (clusters of 16 pixels).

aerosols present, and the optical efficiency is underestimated. This effect is only seen for wind speeds above $\sim 10 \text{ ms}^{-1}$, as shown by figure 3.27. (Although not affecting the muon calibration, it is worth noting that under normal data taking conditions the wind speed does not exceed $\sim 7 \text{ ms}^{-1}$; wind speeds above 15 ms^{-1} are considered unsafe for data taking.) Rather than wind speed, measurements of the level of aerosols present in the atmosphere is better monitored by the Cherenkov Transparency Coefficient [38]. This parameter, which also depends on the telescope trigger rate and the camera gain, provides a means of quantifying the haziness of the atmosphere to Cherenkov light.

In a similar manner, the muon efficiency is seen to reduce under high humidity conditions ($\gtrsim 80\%$) as shown in figure 3.28. Again, this is due to the scattering of Cherenkov radiation (and/or the muon itself) by water droplets in the air. Although water droplets are continually present, the higher the humidity, the further the light is scattered, as it encounters water droplets more often. There is no significant variation of muon efficiency with atmospheric pressure or temperature (figure 3.28).

3.6.6 Cosmic Ray Primaries

Although MC studies are usually done with dedicated muon simulations, for which all primary particles are muons and typically do not decay before reaching the camera; in practice, all muons triggering IACTs originate from air showers initiated by hadronic primary particles. Often these muons are produced in the first few interaction vertices as the air shower develops, and may scatter far from the shower axis. In fact, due to the stereoscopic trigger of the smaller telescopes of the original H.E.S.S. array, this guaranteed that all muons recorded in the data were accompanied by a hadronic shower which triggered at least one of the other telescopes. With the monoscopic trigger of CT5, it is also possible to trigger on and record single muon events.

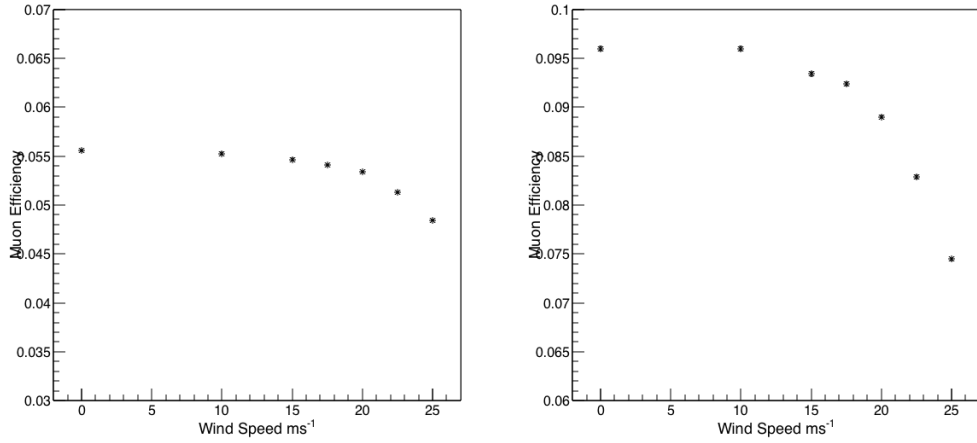


Figure 3.27: Muon Efficiency in CT1 (left) and CT5 as a function of wind speed (equivalent to the level of aerosols in the atmosphere). Results are from MC with the same input efficiency at all wind speeds (88% for CT5). Note that the wind speed rarely exceeds $6\text{-}7\text{ms}^{-1}$ under normal data taking conditions, whilst the aerosol content is monitored by the Cherenkov Transparency Coefficient [38].

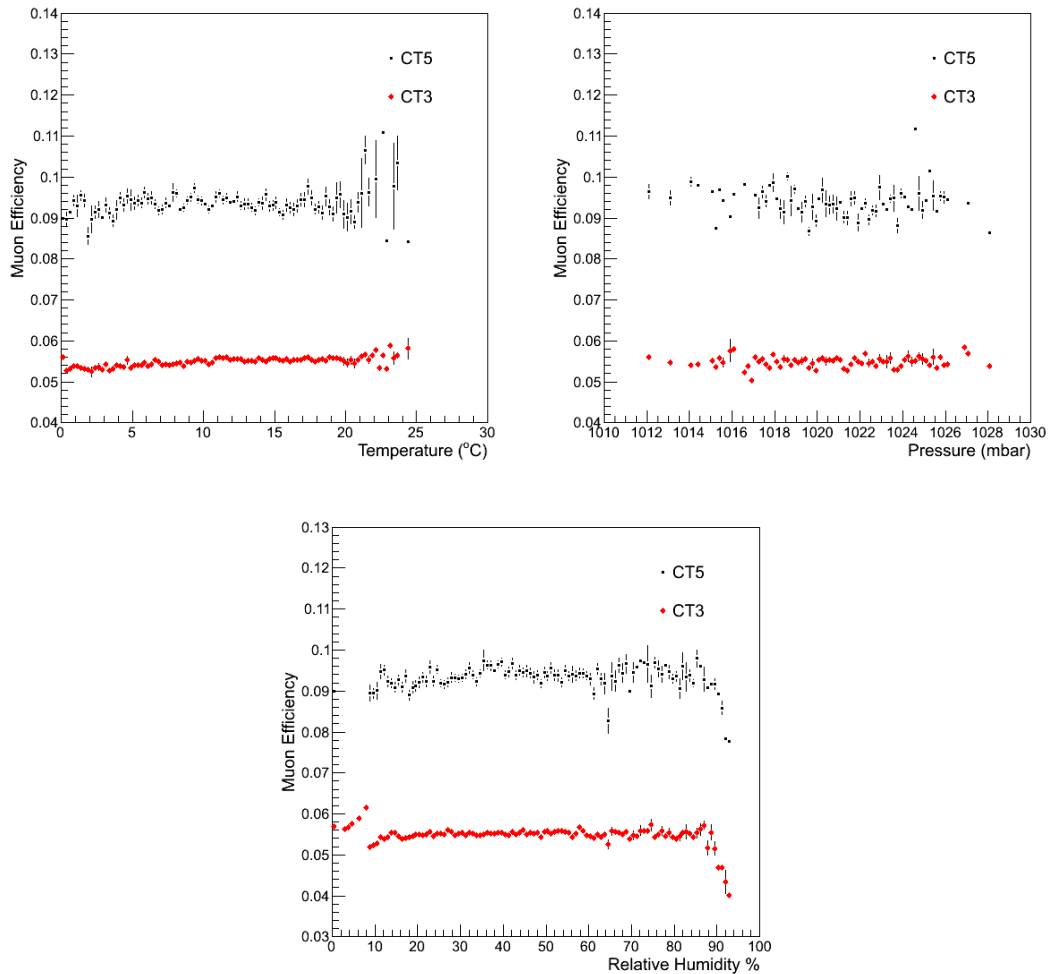


Figure 3.28: Top: Variation of muon efficiency with atmospheric parameters - no significant dependence of the muon efficiency on temperature (left) or atmospheric pressure (right) is seen. Bottom: the muon efficiency can be seen to drop when the relative humidity rises above $\gtrsim 80\%$.

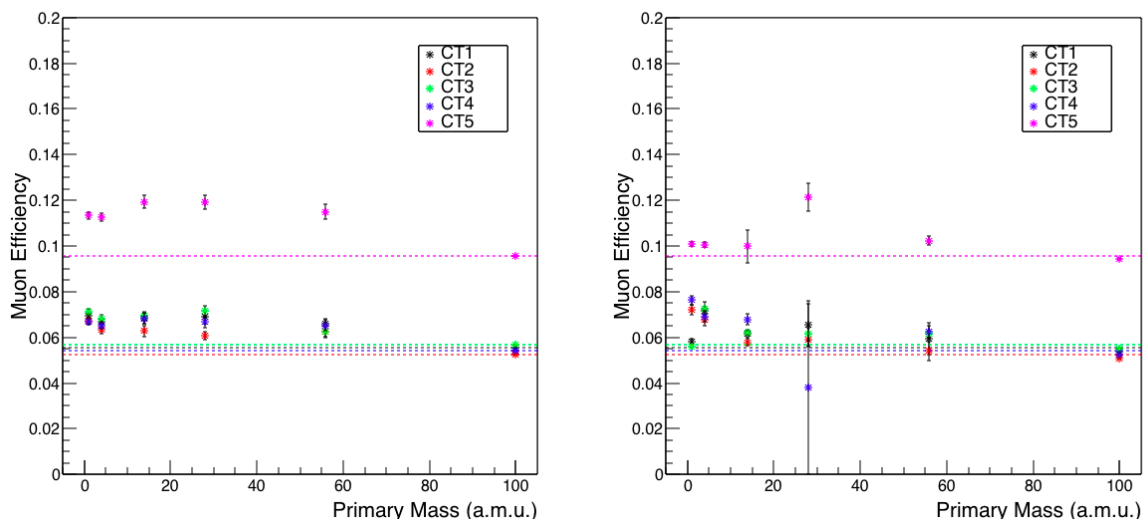


Figure 3.29: Muon efficiency with mass of Cosmic Ray primary particle from MC. The mean value, as traditionally used, is reasonably stable for the cosmic ray primaries, albeit slightly shifted to higher values. A similar trend is seen when using the Gaussian fit, although more consistent with the value obtained from dedicated muon simulations. The corresponding muon efficiency is plotted at a primary mass of 100 a.m.u. for clarity. Other primary particles used in the simulations were (from lowest to highest mass): protons, helium, nitrogen, silicon and iron.

Therefore, it is necessary to check for any possible bias arising between the MC single muons and muons resulting from later stages of shower development. The muon efficiency calibration algorithm was performed on MC for various cosmic ray primaries, and the results are shown in figure 3.29. The mass of the cosmic ray primary is given in atomic mass units (a.m.u.), however for clarity, the corresponding efficiency obtained from single muons is plotted at 100 a.m.u.. In general, the muon efficiency from heavier primary particles seems to be higher than that obtained on dedicated muon simulations, although the variation with increasing mass is reasonably flat.

The increased muon efficiency seen with simulations of hadronic showers is due to contamination of the image from Cherenkov light due to the parent shower. Although the image may be cleaned based on the location of the muon ring from the circle fit, it is still likely that some light from the parent hadronic shower overlaps with the muon ring (see figure 3.3). As this leads to an increase in the total light, the resulting muon efficiency is then shifted to higher values. A possible approach to mitigate this effect is to consider the total charge in the image outside of the muon ring; if this value is higher than the noise level, it may signify contamination from a parent hadronic shower. Alternatively, a simultaneous fit of a Hillas ellipse (see chapter 2) and a muon ring to the image could be performed; the Hillas ellipse would help to locate the contribution from the parent shower. Pixels falling within this ellipse could then be treated as “broken” and not included in the muon efficiency fit. Further studies would be required to verify that this reduces the effect.

MC phase	CT1	CT2	CT3	CT4	CT5	Start	End
1	100	100	93	100	-	01/01/00	26/05/04
1b	70	70	70	70	-	25/05/04	03/07/07
1c	60	54	60	60	-	03/07/07	27/04/10
1c1	60	54	85	60	-	27/04/10	17/10/10
1c2	60	72	78	60	-	17/10/10	14/04/11
1c3	75	70	75	53	-	14/04/11	12/11/11
1d	70	70	70	70	-	12/11/11	31/12/12
2a80	70	70	70	70	80	31/12/12	...
2b0	69.6	65.0	70.6	67.3	98.3	01/01/13	01/06/13
2b2	63	60	65	62	88	01/06/13	22/05/14
2b3	57.2	58.2	57.1	54.9	79.5	22/05/14	04/11/14
2b4	68	65.8	61.7	63.7	77.9	08/11/14	...

Table 3.2: Monte Carlo muon phases describing the optical efficiency over time. New phases are typically defined corresponding to significant hardware changes, such as mirror recoatings. Changes in the CT5 optical efficiency have a more significant effect on the analysis, such that simulations may need to be produced more often/corresponding to smaller changes. Phase 2a80, produced prior to the new muon algorithm, is now obsolete. Phases 2b0-4 were defined by the new muon algorithm.

3.7 Application to Data Analysis

The muon efficiency is used both for monitoring the overall degradation of the telescopes optical efficiency and for correcting the energy reconstruction within the data analysis chain. This energy reconstruction is done based on a set of lookup tables, generated from Monte Carlo (MC) considered to accurately represent the current state of the system. Following significant hardware changes, or significant changes in the muon efficiency over time, a new set of MC is produced. Each new set of MC with a separate optical efficiency configuration is termed a muon phase. From dedicated muon simulations within each MC set, a reference muon efficiency value is determined by performing the muon efficiency calibration on this MC. As part of the calibration chain, the muon calibration is performed prior to the data becoming available for analysis. This enables an efficiency value to be found for each run of data. The ratio of this run-wise muon efficiency value to that obtained in the most recent set of MC defines a correction factor. This correction factor is then applied directly to the energy reconstruction, such that the energy of a given event is: muon correction factor \times energy obtained from MC lookup tables (based on the event reconstruction, see chapter 2).

This procedure is done for each telescope individually. Each MC phase uses an input telescope efficiency; this is an arbitrary value, as a percentage of the nominal (100%) efficiency, where 100% = design specifications. Hence it is possible for a telescope to have $> 100\%$ optical efficiency as seen in the early CT5 data. Correction factors < 1.0 are common depending on the MC set (where the muon efficiency from data is greater than that simulated).

Table 3.2 lists the MC phases of the H.E.S.S. experiment; the use of the muon efficiency in defining these phases is outlined in more detail below.

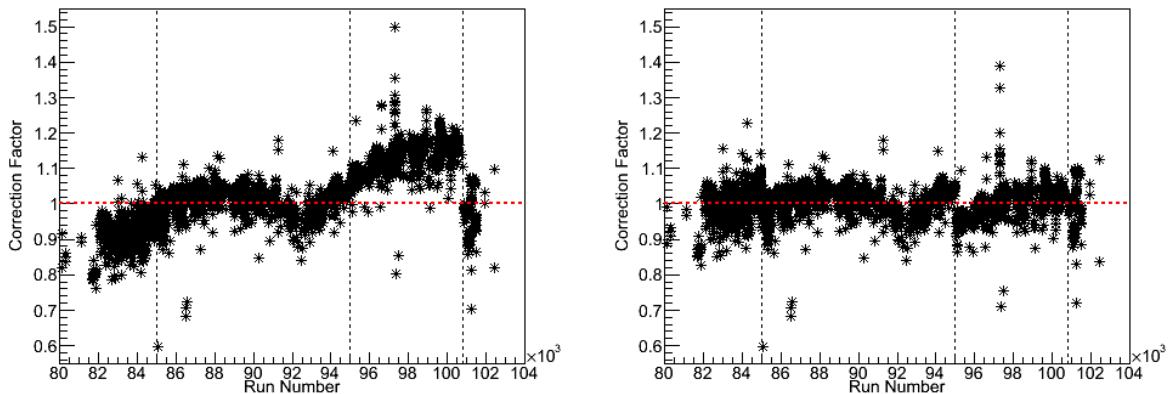


Figure 3.30: Muon Efficiency correction factor over time for CT4, shown prior to (left) and post (right) definition of new muon phases. The vertical dashed lines correspond to transitions between the newly defined phases: 2b0, 2b3 and 2b4. These phases are shown to better describe the system, with correction factors remaining stable around 1. This procedure is done in a similar fashion for all telescopes.

3.7.1 Definition of Muon Phases

Typically, the need for a new muon phase is established by considering any relevant hardware changes and/or the current value of the muon correction factor. If the muon correction factor differs by $> 10\%$ from 1.0, then a new MC phase is advisable. In the case of CT5, this tolerance may be somewhat reduced (see section 3.7.2). The input values required for a new MC phase are defined in an iterative manner, proceeding as follows.

Rather than matching the efficiency exactly to the values at the start of a new MC phase, it is advisable to match them to the average for the time period under consideration. This can be clearly defined retrospectively, by fitting a constant over the given time range. However, if the new MC phase is anticipated to cover an extended period of future data, then the adopted values are conservatively a few percent ($\sim 2 - 3\%$) lower than the current true value, in anticipation of some natural degradation in the optical components performance.

Firstly, the mean correction factor over the time period under consideration is obtained; this is most easily done by fitting a flat line of $y = C$, a constant value, to the plot of correction factor over time (such as that shown in figure 3.30). This correction factor was obtained from the current reference set of MC, call it MC_0 . The adjustment required to the input telescope optical efficiencies $\varepsilon(MC, CT_X)$ in set MC_0 to return the correction factor to 1.0 again is found via $\varepsilon(MC_0, CT_X) \times 1./C(MC_0, CT_X)$. A set of test MC (MC_t) is produced based on these values, with telescope optical efficiencies $\varepsilon(MC_t, CT_X)$ as input. For the dataset and time period under consideration, the correction factors with respect to the new set (MC_t) are found.² In an iterative approach, the mean correction factor of this dataset with respect to MC_t is tested again for agreement with 1.0; if the remaining discrepancy is $\gtrsim 2 - 3\%$, the process is repeated with the input values adjusted accordingly for the next test.

In practice, a new set of input values are usually converged upon within 2-3 iterations. This then enables a new set of MC to be produced; with corresponding lookup tables as required for the analysis.

²Note that this changes the reference values in equation (3.2.1). The muon efficiencies obtained on data remain the same - no reprocessing of data is required.

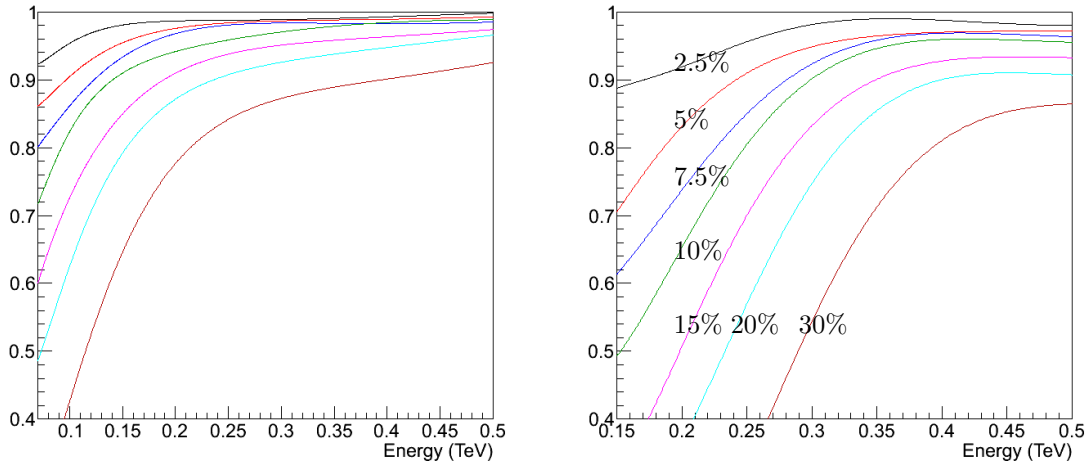


Figure 3.31: Ratio of the effective area for correction factors of varying amounts with respect to no correction factor. From black through to brown, the curves correspond to degradations with respect to the Monte Carlo reference of 2.5%, 5%, 7.5%, 10%, 15%, 20% and 30% respectively. Shown in the case of a CT5 mono (left) and stereo hybrid (right) analysis (R.D. Parsons, private communication).

3.7.2 Influence on the Effective Area

Whilst the muon efficiency is used to correct for single event energy estimates, the reduction in optical efficiency also leads to changes in the instrument response function which are not so easily accounted for. These may cause systematics in the spectral reconstruction. A set of dedicated simulations were produced to investigate the change in effective area with the optical efficiency correction factor for the H.E.S.S. II. Figure 3.31 shows the ratio of the effective area as a function of energy for each set of simulations to that with no optical efficiency correction, with curves corresponding to degradations of up to 30%. As can clearly be seen, this can lead to large systematics at low energies for optical efficiency correction factors above $\sim 5\%$. The recommendation following this small study was to ensure that MC phases are produced more often for H.E.S.S. II, aiming to keep the correction to $< 5\%$ as far as possible.

3.7.3 Statistical Variation

Traditionally, the muon efficiency values are determined separately for each observation run (~ 28 minutes) within the Heidelberg standard calibration chain (used in this work), whereas the French standard calibration chain find an average value per period of data taking (~ 28 days). In the former case, the run-wise muon efficiencies seem to be subject to some statistical variation on top of the overall time evolution (figure 3.32). In the latter case of monthly values, the period-wise muon efficiency progresses in a step-wise manner, where it can be seen that the correction factor is typically underestimated at the start of the month and overestimated by the end.

A compromise between these two options is to make use of a night-wise muon value. This option takes the average muon efficiency values for runs taken within 12 hours either side of the run start time. If less than 5 valid runs are found within this time period, then the search is extended by 24 hours again in each direction, until sufficient runs with valid muon efficiency values are found.

The root mean square distribution of the night-wise muon efficiency values found with this

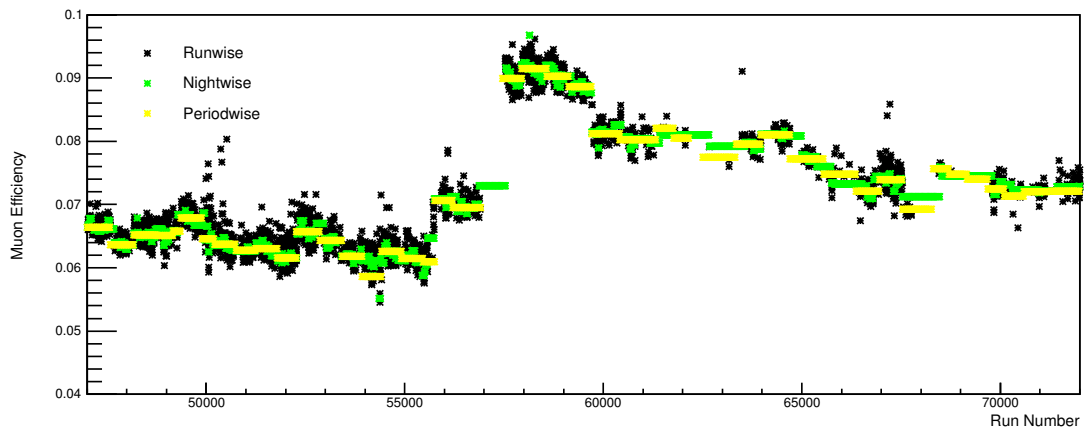


Figure 3.32: Evolution of muon efficiency (CT3) shown for run-wise, night-wise and period-wise averaged values. Statistical variation and anomalous values (due to short runs or weather conditions) are clearly reduced by night-wise averaging, whilst period-wise is a more crude approximation.

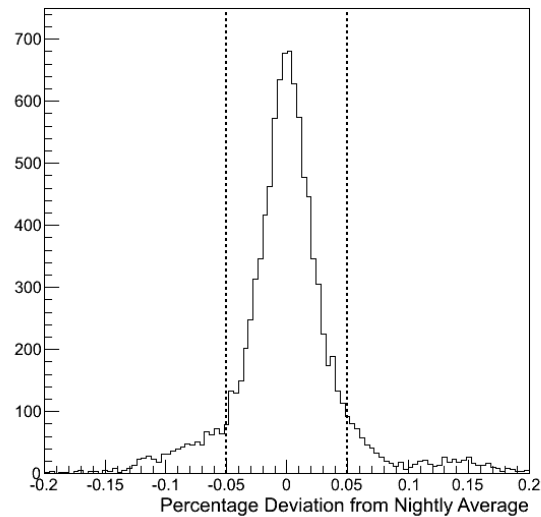


Figure 3.33: Variation of run-wise values around the nightly average. The variation is mostly at a level of $< \pm 10\%$; the majority of the deviation can be attributed to statistical variation (shown here for CT1). Systematic effects such as truncated runs, hardware issues and adverse weather contribute to the tails of the distribution.

approach is shown in figure 3.33. As the distribution seems to be mostly confined to $< 5\%$, we can conclude that there is some inherent statistical variation in the run-wise muon values around the mean, which can be mitigated with this approach.

Use of this option is recommended in cases where there are known issues with the data - for example, poor environmental conditions (such as high humidity or aerosol content) or camera issues (such as many broken pixels) which may affect the muon calibration result (see section 3.6.4). Eventually, this option should become standard practice; however, care must be always be taken with very new sets of data, as the nightly average will change if not all data taken in a given night is calibrated ready for analysis.

3.7.4 Conclusions on Muon Analysis

Optical efficiency calibration for IACTs using muons has long been established as a robust and versatile method [59]. Major benefits of the procedure are that, for current experiments with IACTs similar to the size of the H.E.S.S. telescopes, muons are contained within the data itself. Also, muons are a natural calibration source, subject to the same instrument characteristics as the Cherenkov showers initiated by γ -rays and, through the last $\sim O(1 \text{ km})$, to the same atmosphere. In this sense, muon calibration is very much a real-time calibration; being contemporaneous with the data, it also mitigates any bias due to gaps between dedicated calibration measurements, and is complementary to the use of external devices. Different approaches towards muon calibration have been adopted by each of the major IACT experiments currently in operation. In contrast to the algorithm adopted here, alternatives include a TMVA approach or use of a Hough transform; pattern recognition algorithm for identifying ring images in the data as used by the VERITAS collaboration [65]. However, we have found that our algorithm typically performs accurately and robustly on the number of muons identified, such that no need for these additional algorithms is foreseen [69].

3.8 Muon Calibration in CTA

Versatile and generic algorithms such as that presented here will be necessary in the near future of ground-based γ -ray astronomy, as the field transitions from dedicated single-type experiments to expanded multi-type arrays such as CTA, comprising many different telescope and camera types. However, for the current telescope specifications, the mirror dish shapes only have minor deviations from a circular shape, such that the analytical formula for distance traversed across a circular mirror dish, equation (3.1.7), may be used without considerable loss of accuracy (see figure 3.34). Nevertheless, instead of the analytical formula given in equation (3.1.7), the aforementioned mirror interpolation approach (section 3.4.2) was retained for these telescopes, using a large number of points to define the circle. Moreover, in the analysis of camera images, it may be expected that a 2D log-likelihood fitting procedure as outlined in section 3.4 would continue to provide improved reconstruction over a χ^2 fit to the 1D azimuthal intensity profile, especially in the case of broken pixels. In section 3.6.4 it was shown that the muon efficiency remained stable with up to $\sim 40\%$ broken pixels, in contrast to the $\sim 10\%$ found with the previous H.E.S.S. algorithm [59].

To this end, simulations of on-axis muons for CTA telescopes were run for four different telescope types; single dish LST, MST and SST, and also a Schwarzschild-Couder type dual dish SST. The LST, MST and Davies-Cotton SST single dishes are comprised of many hexagonal

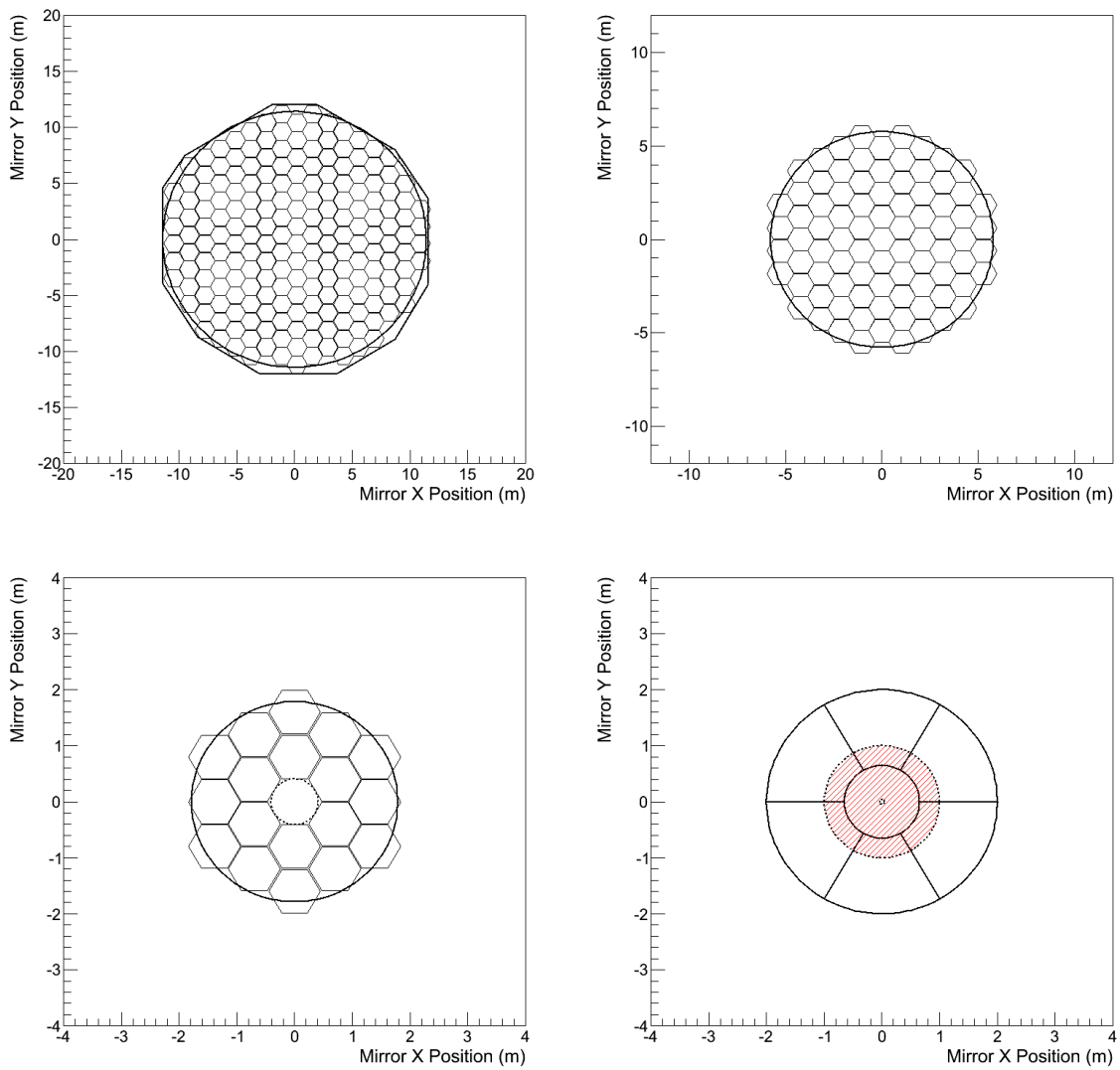


Figure 3.34: CTA mirror dishes, for (clockwise from top left) LSTs, MSTs, Schwarzschild-Couder SSTs and Davies-Cotton SSTs. A circle approximation (scaled to match the total mirror area) is a good approximation to the dish shape in all cases; the largest deviations being shown for the LST. The secondary mirror of the Swarzschild-Couder SST (bottom right) is shaded in red.

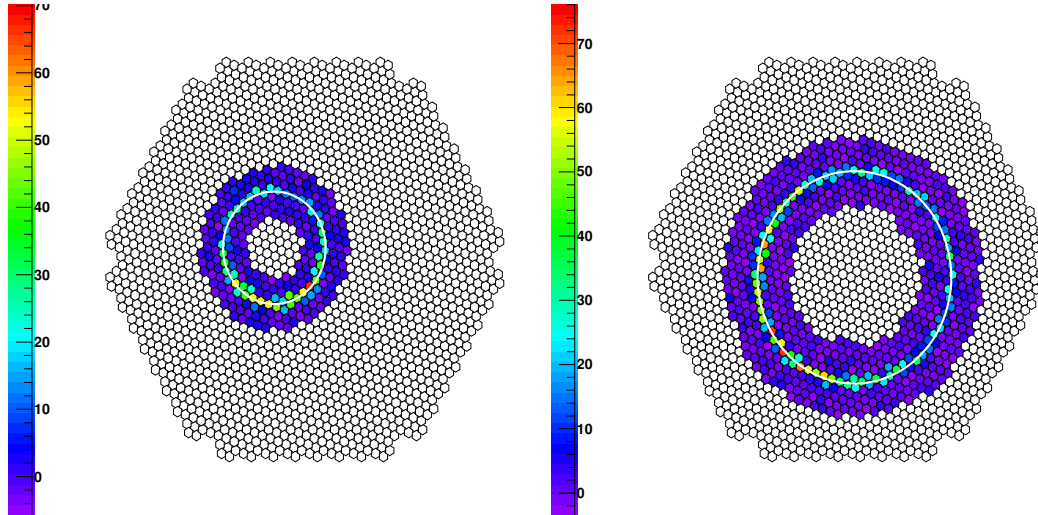


Figure 3.35: An example simulated muon event in an MST (left) and an LST (right). Although the cameras are differently shaped to the H.E.S.S. cameras, this does not affect formation or parameterisation of the ring images. The centres of the muon rings are offset from the camera centres, corresponding to muons inclined to the telescope axis (see figure 3.1).

facets, whilst the dual mirror Schwarzschild-Couder SST has a primary mirror comprised of 6 facets and a single facet secondary mirror. In order to analyse the muon images in the CTA telescopes, new mirror dish descriptions for each telescope type were required to be included. For all of these telescopes, the reflector dishes can be approximated by a circle without considerable loss of accuracy, as shown in figure 3.34. Aside from this, very few changes to the muon efficiency reconstruction algorithm were required, only some optimisation of the cut values for each type (taking into account the size of the camera and reflector dish). Despite the change in the shape of the camera, parameters describing the muon images do not differ greatly between telescope types, as seen by comparing the muon images in figure 3.35 to figure 3.11. An example azimuthal profile for an LST is shown in figure 3.36.

Considerably more thought is required, however, for the case of a dual mirror telescope. There are two possible approaches, the azimuthal profile for one of these is shown in figure 3.38, and the resulting distributions of muon efficiency in figure 3.39. The first approach is to treat the secondary mirror as a large hole, as no light from the muon can pass through the mirror (see figure 3.34). This approach, however, neglects the fact that the light must reflect off both mirrors in order to reach the camera (see figure 3.37). The second approach, is to add the chord across the primary mirror (less the hole in the primary mirror) to the chord across the secondary mirror (less the hole in the secondary mirror) to account for the modification to the azimuthal light profile due to both mirrors. In this case, however, to avoid overestimating the total number of photons, the chord must be multiplied by a coefficient β , to account for the reduction in light due to blocking by the secondary mirror before the light reaches the primary mirror.

$$\beta = \frac{A_p - (A_s - A_{sh})}{A_p - A_{ph}}, \quad (3.8.1)$$

where A_p , A_s , A_{ph} and A_{sh} are the areas of the primary and secondary mirrors (with radii R and R') and the areas of the inner dish holes respectively (see figure 3.34). The effect of this second approach on the azimuthal distribution of light around the muon ring is, for a muon aligned with the telescope optical axis yet offset from the mirror centre, to effectively fill in the part of the azimuthal distribution which would otherwise dip due to the light blocked by the secondary

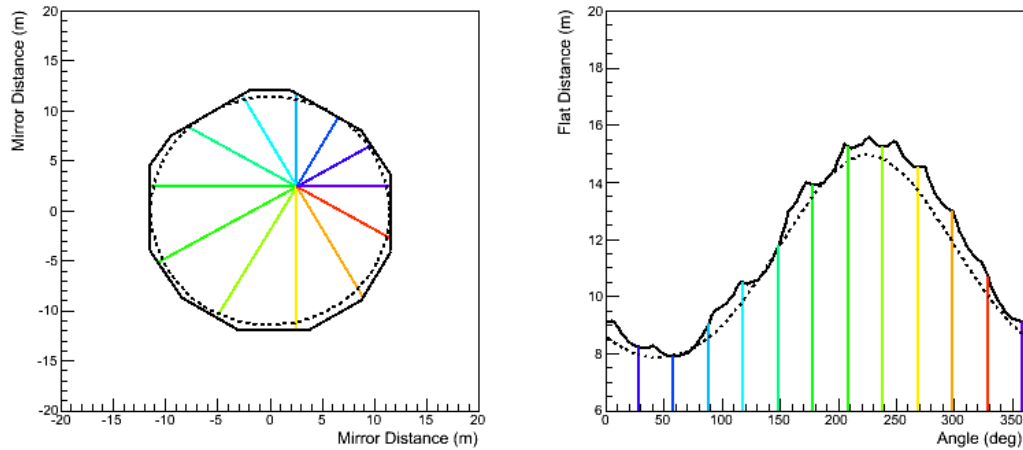


Figure 3.36: Left: The proposed mirror dish for an LST of CTA can be well approximated by a circle (dotted line), with only minor deviations. Right: The effect of using an interpolation (solid line) leads to only minor alterations in the 1-dimensional profile of integration distance with azimuthal angle. (Compare to figures 3.8 and 3.9). An example muon with an impact position offset from the mirror centre is chosen to illustrate the asymmetrical effect on the 1-dimensional profile.

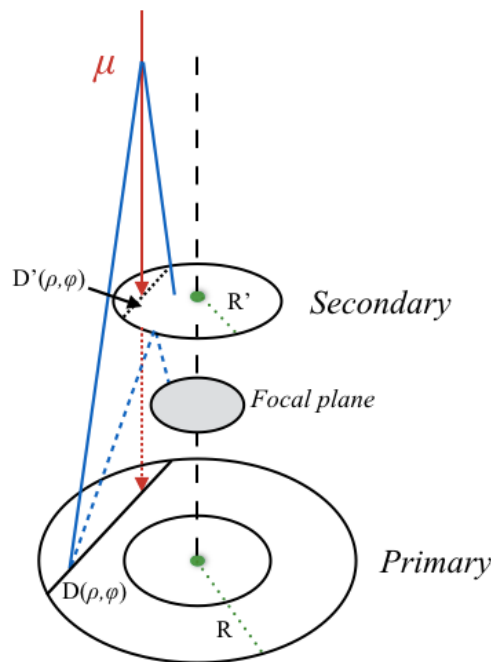


Figure 3.37: A muon passing through the secondary dish of a dual mirror telescope has a considerable proportion of the light blocked by the secondary mirror (radius R'). Cherenkov light reaching the camera must reflect off both mirrors (dashed blue line). The total contribution to the image intensity then has to include the chord across the primary and secondary reflector dishes, (D and D' respectively) along which all reflected light reaches the same point in the camera. After passing through the secondary mirror, the muon may continue to produce Cherenkov light in front of the camera (between the secondary mirror and the focal plane), considered to be a second order effect.

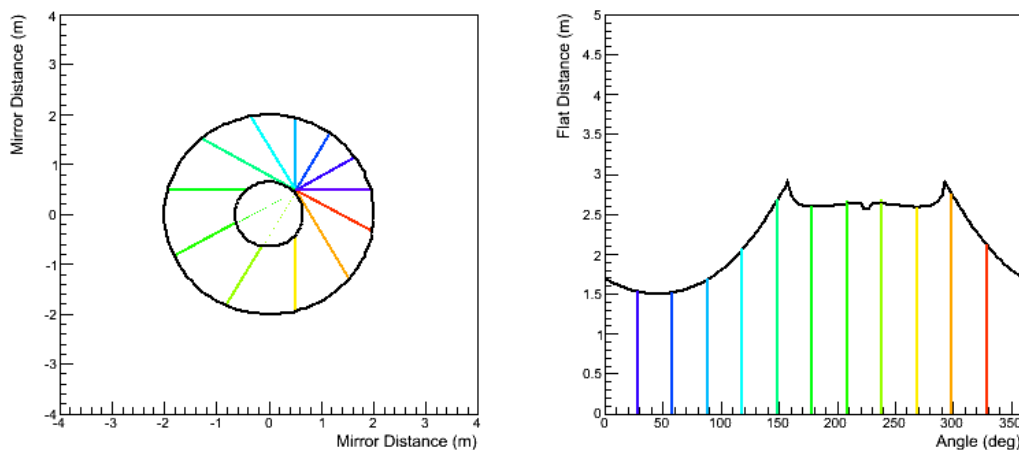


Figure 3.38: Variation in distance traversed across both mirrors of the dual mirror telescope with azimuthal angle, shown in the case of an on-axis muon (offset from the mirror centre, left). Right: The effect of including the distance traversed by the light across the secondary mirror is to reduce the depth of the dip induced by the hole of the primary mirror. Only the primary mirror is shown on the left.

mirror, or due to a hole in the centre of the reflector dish, as was seen for the H.E.S.S. telescopes in figures 3.8 and 3.9. This is shown in figure 3.38, although for clarity only the primary mirror is shown on the left hand side; the slight dip due to the hole in the secondary mirror can still be identified. Figure 3.39 shows the resulting distributions of muon efficiency in the case that the effect of the secondary mirror is treated in the same way as a hole (left) and where the chord across both mirrors is taken into account (right). The distribution is clearly much more in line with the expected near normal distribution (figure 3.13) when the total across both mirror dishes is used; in this case the reduction in light due to the secondary mirror is taken into account by equation (3.8.1).

Additional considerations include the amount of light emitted between the secondary and primary mirrors if the muon travels through the secondary mirror (figure 3.37). This contribution is, however, likely to be negligible for two reasons; firstly, the distance travelled by the muon during its passage between the two mirrors is a small fraction of the total distance; and secondly, the small opening angle of the Cherenkov light cone may result in a large proportion of this light being lost through the hole in the primary mirror for muons passing near the centre of the dish. Another aspect to consider is that, the shadow of the secondary mirror may move away from the centre for off axis inclined muons; as long as the shadow remains fully over the primary mirror, this is only a second order consideration, as the overall reduction in Cherenkov light will be the same as that given by equation (3.8.1). The issue of the shadow of the secondary mirror leaving the primary mirror dish is only relevant for high inclinations, as explained in the Appendix, section B.

The selection cuts used for the CTA telescopes, listed in table 3.3, followed broadly those used for the H.E.S.S. telescopes as summarised in table 3.1, with the same discriminatory parameters being used. Those cut parameters which were characteristic of the ring image itself rather than the telescope, such as the ring radius r , outer radius r_o and ring width Δr remained more or less the same between telescope types; other cuts which were more dependent on properties of the telescope and camera, such as the number of pixels N_{pix} and the impact parameter ρ needed adjusting. In particular, for sufficient muon events on the dual mirror SST, it was found

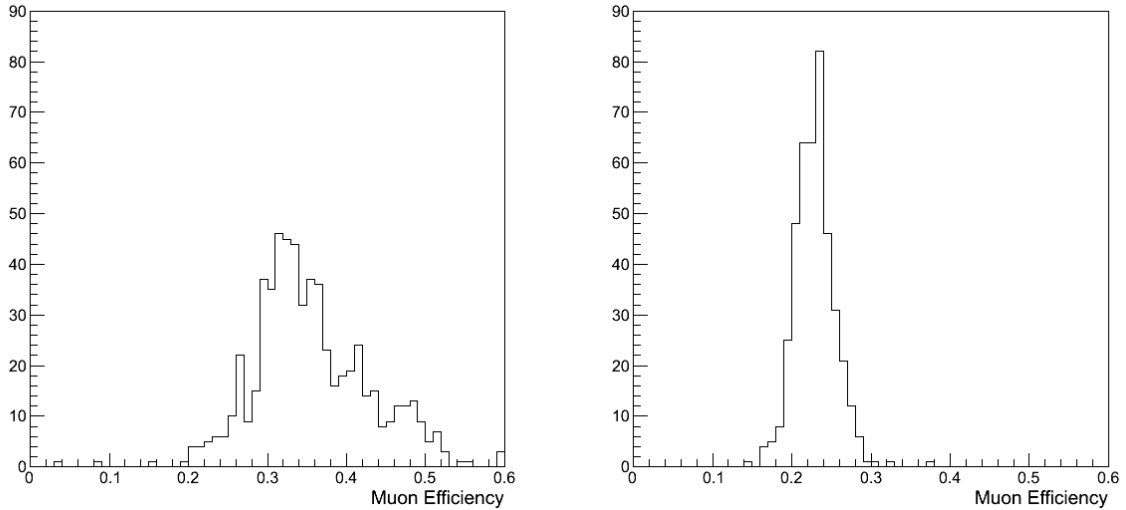


Figure 3.39: Distributions of the reconstructed muon efficiency using two different approaches for treatment of the secondary mirror in the case of a dual mirror Schwarzschild-Couder SST. Left: treating the secondary mirror as a large hole. Right: summing the chord traversing both mirrors, but normalising by a factor accounting for shadowing of the primary mirror by the secondary (equation (3.8.1)).

necessary to loosen the cuts on Δr and ρ somewhat.

3.8.1 Performance for CTA

As per figure 3.15, the major test of the muon reconstruction is that the correction factor found from Monte Carlo of the telescopes at a degraded optical efficiency is linear with the expected correction. As well as the reference MC at the nominal telescope optical efficiency (arbitrarily 100%), MC of the CTA telescopes was also produced at degraded mirror reflectivities of 80%, 60% and 40%. The resulting linearity plot is shown in figure 3.40, and demonstrates encouragingly that the muon reconstruction algorithm performs well on several different types of telescope, even without investing significant effort into cut optimisation. The small telescopes are both seen to deviate from linear at significantly degraded optical efficiencies. However, this is partly expected

Selection	Cut Parameter	LST	MST	SST-dc	SST-gct
Preselect	N_{pix}	> 100	> 30	> 5	> 5
	N_{brkpix}	< 50	< 70	< 70	< 70
	N_{edgepix}	< 30	< 10	< 10	< 10
	$\langle NN \rangle$	< 3.5	< 3.5	< 3.5	< 3.5
	$r(^{\circ})$	$1.1 - 1.4$	$1.0 - 1.5$	$1.0 - 1.5$	$1.0 - 1.5$
	$r_o(^{\circ})$	$0. - 1.7$	$0. - 2.$	$0. - 2.$	$0. - 2.$
Postselect	$\Delta r(^{\circ})$	$0.04 - 0.08$	$0.04 - 0.08$	$0.04 - 0.08$	$0.03 - 0.1$
	$\rho(\text{m})$	$0.5 - 14.$	$0.5 - 6.4$	$0.3 - 2.5$	$0.5 - 4.$

Table 3.3: Muon selection cuts used for the CTA telescopes. Based on the cuts used for the H.E.S.S. telescopes listed in table 3.1, the number of pixels and the impact parameter cuts were adjusted for the mirror and camera sizes of the different telescopes. The cuts were somewhat loosened for the dual mirror SST-gct.

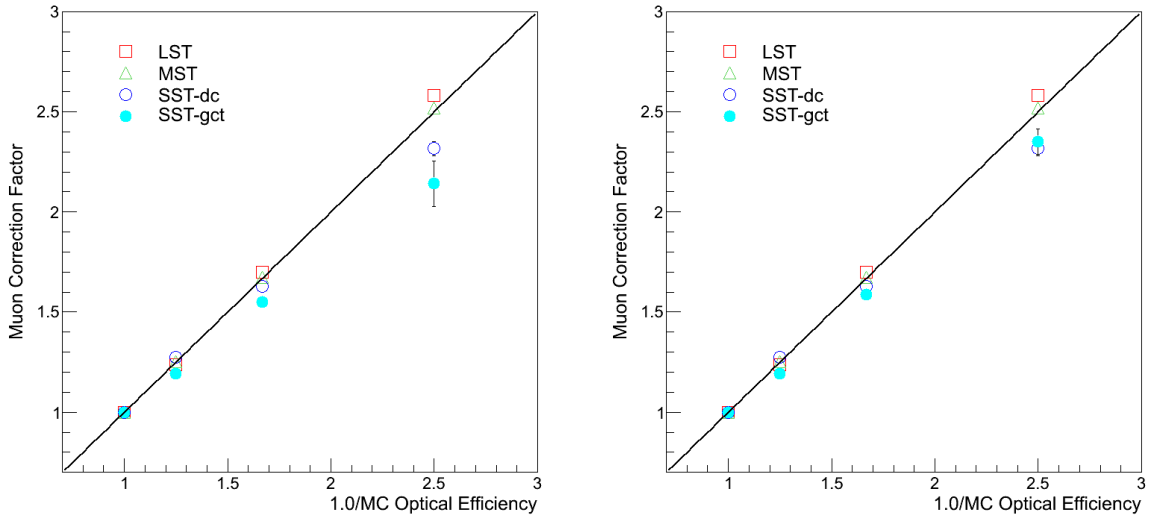


Figure 3.40: The muon reconstruction algorithm performs well on simulations of CTA telescopes at 100%, 80%, 60% and 40% optical degradation. The correction factor recovered is linear with the expectation down to low reflectivities for all telescope types, with some minor deviation at large degradations for the smallest telescopes. Left: treating the dual mirror SST using the first approach (effect of the secondary mirror is like a hole). Right: treating the dual mirror SST using the second approach of adding contributions from both mirrors to the azimuthal profile (but accounting for the factor (3.8.1)). The second approach shows improved linearity.

due to the lower triggering rate of muons and the high energy sensitivity of the SSTs, such that at low optical degradations they will be biased towards triggering on the highest energy muons, leading to an over-estimation of the telescopes optical efficiency and consequently an under-estimation of the required correction factor. As monitoring of the telescope optical efficiencies is expected to be performed regularly and routinely within CTA, the occurrence of a correction factor of more than 50% is unforeseen.

The number of muons passing cuts for all telescopes is shown in figure 3.41. As was the case for the H.E.S.S. telescopes in figure 3.26, with decreasing efficiency the number of muons passing cuts decreases for the SSTs. The least muons are found for the dual mirror SST, expected due to the large amount of shadowing by the secondary mirror. Fewer muons passed cuts in the LSTs than for the MSTs, due to a cut on the outer radius of the fitted circle (requiring that the images are well-contained) and a cut on the average number of neighbouring pixels in the cleaned image. For the H.E.S.S. telescopes, a value of this parameter < 3.5 well describes a circle; however, this cut has not been optimised for the finer pixelisation of the CTA cameras. The trend seen in the LSTs and MSTs, of a slightly increasing number of muons passing cuts with decreasing efficiency is again due to the neighbouring pixels cut; with fewer pixels remaining after image cleaning, more of the images have a lower average number of neighbouring pixels, hence more images pass this cut, which tends to dominate over cuts on other variables, such as the image size (see also section 3.6.4).

The number of muons increases for the single mirror SSTs at 80% efficiency due to more muons passing the ring width cut at degraded efficiencies; fainter pixels towards the edge of the muon ring fail the threshold cut, leading to a thinner ring overall.

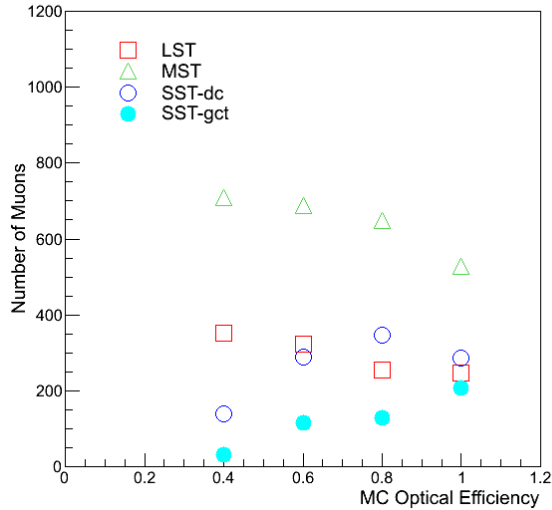


Figure 3.41: The number of muons passing cuts decreases with optical efficiency degradation as expected for the small telescopes. The cut on the average number of neighbouring pixels has a strong effect on the LST and MSTs (see main text).

3.9 Conclusions on Muon Calibration

Development of calibration methods, particularly in the early stages of a new experiment, is key to a robust data analysis and reliable physics results. For IACT based experiments, such as H.E.S.S. and CTA with different telescope types and sizes, flexible and generic algorithms applicable to several different detector types are currently of increasing importance.

As a natural calibration source, subject to the same detector effects as γ -ray events, muons offer a robust approach towards optical efficiency calibration, free from additional sources of uncertainty (such as a systematic bias) which may be introduced by an external calibration device. Although there is an intrinsic discrepancy in the Cherenkov light spectrum originating from muons and from γ -ray events, due to their relative production altitudes; between the atmosphere and the detection, the light undergoes the same treatment within the detector. The discrepancy in the light spectrum between muons and γ -ray events was shown to be a second order effect for the H.E.S.S. experiment, whilst for CTA (currently in the development stage), various methods (such as adding a filter window) are foreseen to ensure that the spectrum received at camera level is approximately the same between both event types (figure 3.6).

In effect, alongside physics results, muons may be considered a calibration signal obtained “for free” in the data, as part of the hadronic background. Although H.E.S.S. retains all of the triggered events (at least at the initial stage) for future data analysis, for CTA, the rate of spurious triggers due to an unwanted background of hadronic cosmic ray events is predicted to be overwhelming, making it impractical to save information about all triggering events. Instead, a trigger-level decision on whether or not an event appears γ -like is expected to be implemented. Whilst this is a good approach to reducing the amount of incoming data, a potential side effect is the loss of candidate muon events. Studies within CTA on the expected muon trigger rate for each telescope and camera type are ongoing; the option of a separate dedicated muon trigger optimised towards ring-like events is also being explored. This is mostly relevant for the SSTs, which would otherwise not trigger on sufficient muons in a stereo mode trigger alone.

On both H.E.S.S. II and CTA, the new muon algorithm presented in this chapter shows

improved performance over previous algorithms, with continued linearity out to large optical efficiency corrections (figures 3.15 and 3.40). Particularly relevant is the good performance demonstrated on telescopes of multiple types, primarily achieved through the improved mirror area description and the 2-dimensional log-likelihood fitting approach used (sections 3.4.2 and 3.4.3).

Within CTA, significant effort has been expended into studying the expected trigger rate with degradation for muons, as well as for dedicated muon trigger signals. This will help ensure that methods for recognising γ -ray showers and rejecting hadronic background do not additionally reject muon events. The well-known discrepancy in the Cherenkov light spectrum produced by muon events and γ -ray showers could lead to a bias in the muon correction, especially if the degradation rate of components of the telescope-camera system varies as a function of wavelength (see figure 3.6). Although this effect was previously shown to be of second order for the H.E.S.S. experiment, for some of the alternative and more sensitive detector components under consideration for CTA, studies have shown that this effect could be more pronounced [70]. To mitigate this effect, the possibility of adding a thin filtering window on silicon based photomultipliers within CTA is being explored, to remove all emission occurring below a wavelength of 300 nm. This only serves to underline the regard with which muon calibration, as a method using a natural source of Cherenkov light, is held.

Although viewed primarily as a calibration source, there is potential for some basic physics measurements of the properties of incoming muons, such as measurement of the muon energy spectrum. This can be obtained by exploiting the relation between the muon energy and the radius of the ring produced (figure 3.4), and relaxing the cut on the ring radius (table 3.1). For the H.E.S.S. experiment, for every \sim hundred ring-like events recorded in one telescope, (or a few hundred in CT5) there are $\sim O(0 - 3)$ ring-like muon events which are recorded simultaneously in more than one telescope. Attributing these events to the same hadronic shower, due to their timing and directional coincidence, the rate of such coincident muon triggers may be an interesting indication towards the composition of cosmic rays. CTA, with a much larger number of telescopes, is better suited to make such a measurement; however, care must be taken to avoid a bias due to the selection of near complete rings. The optimisation of triggers for γ -ray astronomy may prohibit such a measurement, whilst other experiments dedicated towards cosmic ray detection are better suited to investigations such as these.

As a general principle, calibration of detectors based on the data is a good guide towards treating the detector response equally in the case of both signal data and calibration data, thereby mitigating systematics. In the next chapter, a second approach towards optical efficiency calibration, also following this general principle, is explored.

4 Cross Calibration using Event Images

4.1 Telescope Cross Calibration

Ensuring consistency between telescopes and avoiding systematic biases due to individual telescopes is a particular challenge for telescope arrays. To this end, it is important to ensure robust inter-telescope calibration is performed. Consistency checks become particularly relevant in arrays where the telescopes differ significantly in technology, size, age, or other system components. A robust, independent calibration to compare telescope performance would therefore be an important addition to the current suite of calibration tools.

Telescope response efficiency is a measure of the proportion of the light emitted by a Cherenkov light shower that is recorded by the telescope. Quantitatively, it is the relation between the absolute light yield of the shower and the number of photoelectrons recorded in the camera, provided that the expected level of photoelectrons for a given shower has already been independently calibrated, such as via the calibration techniques outlined in chapter 2 [36]. As the light yield from a Cherenkov shower is intrinsically related to the energy of the initial γ -ray photon, any miscalibration consequently affects the energy reconstruction. The absolute value of the telescope response efficiency is determined through the muon ring calibration procedure [58], as outlined in the previous chapter.

A complementary method of calibrating telescope response efficiency, first demonstrated on the HEGRA array [71], is based on light yield from Cherenkov showers. This approach utilises comparisons between telescopes within an array to gain a measure of the relative efficiencies, and is further developed in this chapter. In the following, inter-calibration refers to use of the procedure between telescopes of the same kind, whilst cross calibration refers to calibrating across telescopes of different types and sizes. In section 4.2 the inter-calibration principle is outlined, which requires careful event selection. After appropriate events are selected, the telescope response efficiency may be probed directly using the recorded image amplitude in photoelectrons (‘image size’), or indirectly by using the reconstructed shower energy.

With the advent of H.E.S.S. II, it became increasingly important to develop calibration methods applicable to telescopes of differing types. This cross calibration tool is applied to H.E.S.S. phase I and in a modified form to H.E.S.S. II, whilst considerable further development was necessary for adaptation to CTA. With ever increasing variety in IACT arrays, methods such as this cross calibration tool offer a way of ensuring consistency between all telescopes.

4.2 Intercalibration using Cosmic Ray Event Images

Cross calibration of the response efficiency of IACTs within telescope arrays is accomplished through pair-wise comparisons between telescopes. We define an asymmetry parameter $a_{i,j}$ for

Parameter	Cut value
Image Size	> 80 pe
Stereo Angle ^a	$> 15^\circ - 25^\circ$
Reconstructed Energy ^b	$\gtrsim 1$ TeV
Angle to Shower Axis	$< 0.7^\circ$
Telescope Multiplicity	> 3

Table 4.1: Event selection cuts used for the cross-calibration procedure, following those used in [71]. *a*: The stereo angle was adjusted according to the zenith angle of the observations. *b*: The reconstructed energy cut was found from the event distribution itself; the 1 TeV value is a conservative value applied in the rare case that the fit failed, typically due to low event statistics or systematic issues.

such comparisons between telescopes i and j , where

$$a_{i,j} = \frac{x_i - x_j}{x_i + x_j}, \quad (4.2.1)$$

and x is an appropriate quantity; independently measurable by each individual telescope. In order to ensure such comparisons are fair, contributing events are restricted to those which should generate identical responses in the telescopes through a set of selection cuts as defined in section 4.2.1 (see also table 4.1). Typically, these are events well above trigger threshold, falling roughly equidistant between the two telescopes. As leptonic showers generally develop such that the light yield is approximately isotropic at a given radial distance from the shower core, this calibration may be performed after basic γ /hadron selection and without stringent cuts being required. In principle, a large proportion of hadronic showers also with an approximately uniform radial light distribution at sufficiently large impact distances and for low primary particle mass, can also be used for cross calibration. The fundamental requirement is simply that two telescopes receive on average the same amount of Cherenkov light, resulting in a large number of events available for this calibration and reducing statistical uncertainties.

4.2.1 Event Selection

To ensure that the amount of Cherenkov light received by each telescope is approximately the same, suitable images are classified as those from events which fall halfway between two telescopes, and with an image size well above threshold. For this calibration approach, basic selection cuts as shown in table 4.1 are used, such that the shower events used in the reconstruction are those for which identical responses in two telescopes may be expected. Values quoted in table 4.1 are default values, which may need to be adapted according to observation conditions (such as zenith angle) and as the overall absolute efficiency of the system degrades over time.

The ‘‘stereo angle’’ (see table 4.1) is the difference in orientation of the Hillas ellipses in the two telescopes (figure 2.8 in chapter 2). By requiring the stereo angle to be above a minimum threshold, this restricts the events to be at less acute angles to the line of equidistance between the two telescopes. This effectively selects events closer to the telescope pair and nearer to equidistance. The minimum ‘‘stereo cut’’ threshold was adjusted according to the zenith angle θ_z of the observations, varying as $15^\circ + 10 \cos(\theta_z)$, such that the cut becomes less stringent towards smaller zenith angles. The reasoning for this is simply that the stereo angle tends to be larger for events at smaller zenith angles, and too stringent a cut tended to remove too high a proportion of the events unnecessarily.

The energy cut was imposed to avoid potential biases near threshold, yet the energy threshold is known to vary as a function of zenith angle. In practice, the energy cut value is found based on a fit to the distribution, explained in more detail in section 4.3.2. A conservative fallback value of 1 TeV for the energy threshold was assigned in the case that the fit to the distribution of event energies failed; typically this only occurred for poor statistics or data sets affected by systematic issues. The rather high threshold was imposed to ensure the threshold region is avoided for most relevant zenith angles. In practice, any hard cut on the energy prior to forming the event distribution could lead to a bias, with one telescope preferentially triggering on showers exhibiting upwards fluctuations close to threshold. The reconstructed energy cut can be found from the distribution for all telescope pairs, yet is especially important for cross calibration between differing telescope types such as the H.E.S.S. II configuration, a topic addressed in section 4.3.

A telescope multiplicity of at least three telescopes were required to trigger on a shower event. However, for pair-wise comparison of telescopes, only the two telescopes under consideration may be used in the shower event reconstruction. The inclusion of more telescopes in the shower reconstruction, which are not being used in the pairwise measurement, may introduce a bias in the reconstructed parameters. For example, the reconstructed direction may be skewed and/or energy affected by the information from extra telescopes. Although information from more telescopes provides a better overall shower reconstruction, for this application, it renders the results no longer indicative of a direct comparison between two telescopes. For each individual event, however, the shower reconstruction may be repeated for all possible telescope pair combinations (from those telescopes which triggered on the event).

4.2.2 Image Size Approach

Particle air showers occurring equidistant between two telescopes should be seen with the same image intensity in each telescope. Imposing a set of cuts as outlined above to ensure only events for which this is true are included, enables a direct comparison of image size to be made between two telescopes.

The image size is a direct probe of the telescope efficiency, as it is a measure of how much charge has been collected. The asymmetry in the image size a_s and in the reconstructed core distance a_d is calculated using equation (4.2.1) for each event on which multiple telescopes triggered. For each telescope pair, the asymmetries are collected in a two-dimensional histogram of the image size asymmetry against the asymmetry in the reconstructed core distance, as shown in figure 4.1. To restrict the histogram to near equidistant events, a stringent cut on the distance asymmetry a_d of:

$$|a_d| < 0.05 + (0.1 \cos(90 - \theta_z)) \quad (4.2.2)$$

is applied, such that the cut is relaxed towards larger zenith angles θ_z . After cutting in the distance asymmetry, the mean of the remaining size asymmetry distribution may be used as a measure of the difference in response efficiencies of the two telescopes (see figure 4.1).

The values of these mean asymmetries $a_{i,j}$ can then be found for each telescope pair; given that each telescope thereby participates in multiple pair measurements, the system of unknown parameters is over-determined. A χ^2 minimisation using equation (4.2.3) is performed to find values for the response efficiency coefficients, c_i, c_j for all telescopes i, j .

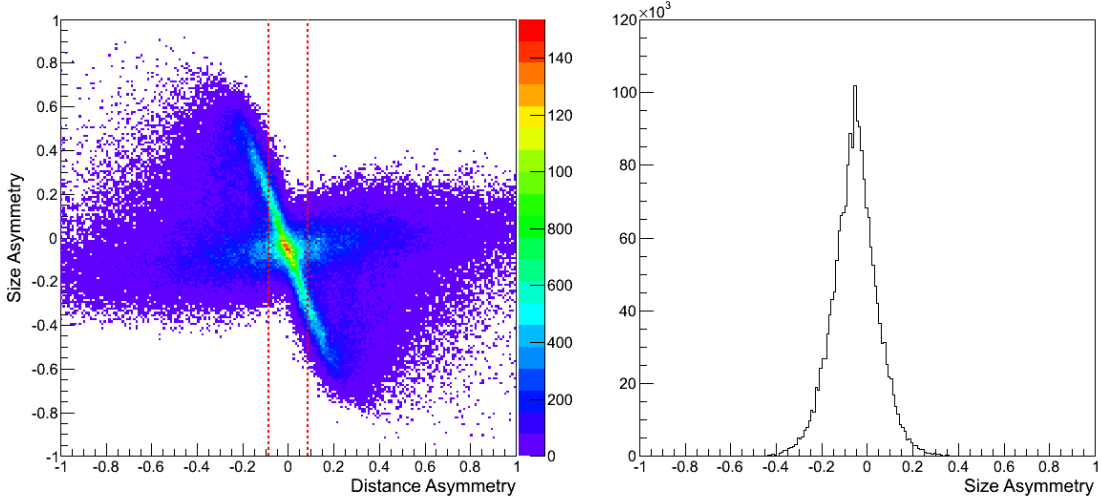


Figure 4.1: Monte Carlo histogram of image size asymmetry against distance asymmetry (left) features a horizontal and anti-linear component. Cutting on the absolute value of the distance asymmetry, $|a_d|$ (as shown by dotted lines) leaves a symmetric distribution of size asymmetries (right), the mean of which is a measure of the response efficiency asymmetry between two telescopes.

$$\chi^2 = \sum_{j>i}^N \frac{\left(a_{i,j} - \frac{c_i - c_j}{c_i + c_j}\right)^2}{\sigma_{i,j}^2} \quad (4.2.3)$$

where $\sigma_{i,j}$ is the error on the asymmetry measurement. Solving this equation system hence enables the relative response efficiencies of the individual telescopes to be found. Normalisation of the relative efficiencies found by this calibration may be done in one of three ways: (a) relative to a single telescope; (b) by defining the average efficiency as equal to a constant (e.g. 1.0); or (c) by rescaling such that the average relative response efficiency is equal to the average muon efficiency for a given data set. If all variations between telescopes have been perfectly accounted for elsewhere in the calibration chain (see chapter 2), then this method would produce a 1:1 response ratio between telescopes. Any residual discrepancies may be found using this technique and either corrected for, or used to indicate systematics elsewhere in the calibration.

There are two contributing components to the histogram of the image size and core distance asymmetries shown in figure 4.1; a horizontal and an anti-linear component. It was previously shown [72] that these two components, as demonstrated in figure 4.2, are separated by a cut in the reconstructed distance from the telescope to the shower core, made at the Cherenkov light pool radius, approximately 125 m. Within the Cherenkov light pool generated by an air shower, the light intensity distribution is approximately flat [73] (see also the Appendix A.3). Hence when both telescopes fall under this light pool (distance to the event, $d_i, d_j \lesssim 125$ m), they undergo equal illumination, resulting in a low image size asymmetry regardless of the asymmetry in distance. This gives rise to the horizontal component in figure 4.2. Outside of the Cherenkov light pool, with shower core distance to the telescopes $d_i, d_j \gtrsim 125$ m, the anti-linear relation occurs as expected; when the event occurs closer to one telescope than the other, the image size in that telescope is larger, and vice versa. The remaining, minor components contributing to the histogram in figure 4.1 are from events for which only one telescope had a core distance $d \lesssim 125$ m; these events fall between the anti-linear and horizontal components. This characteristic size of ~ 250 m diameter for the Cherenkov light pool applies for zenith angles around 20° ; the projected

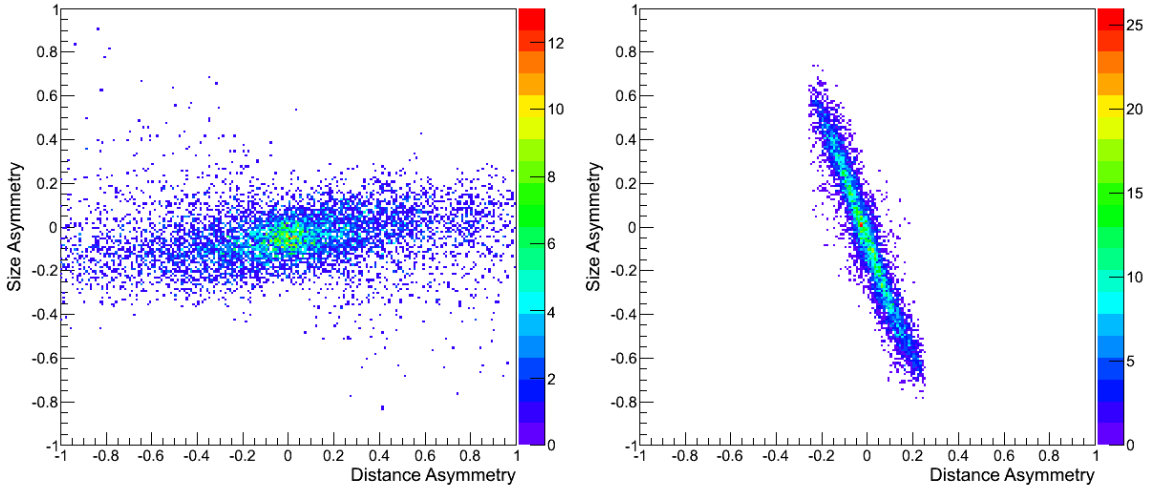


Figure 4.2: Two main components contribute to the Monte Carlo event distribution in a histogram of image size asymmetry against core distance asymmetry (at 20° zenith angle). A horizontal component is due to events with a core distance, $d \lesssim 125$ m in both telescopes (left) and an anti-linear component arising from events with $d \gtrsim 125$ m in both telescopes (right).

size of the Cherenkov light pool on the ground increases with increasing zenith angle due the shower geometry (see Appendix A.3).

4.2.3 Reconstructed Energy Approach

The reconstructed energy of a particle shower falling equidistant between telescopes can be used to form an alternative (though related) asymmetry parameter to the image intensity. Any two telescopes observing the same shower should ideally give the same energy estimate, as other systematics should be taken care of earlier in the calibration and analysis chain. This approach, previously investigated in [72], is heavily reliant on the accuracy of the energy reconstruction. In using this variable, we assume that the same image size in two telescopes of identical construction would lead to the same reconstructed energy. The validity of this assumption is discussed later in this chapter.

In a similar way to section 4.2.2, telescopes are compared pair-wise to construct an overall system of equations. When using the energy asymmetry procedure to cross calibrate through comparisons of reconstructed energy, it is important to impose a safe energy cut, such that the calibration uses only the region within which the energy histogram distribution is symmetric. Examples of the histogram distributions for energy asymmetry (between two telescopes) against $\log_{10}(E(\text{TeV}))$ (shower energy, reconstructed using both telescopes) are shown in figure 4.3. In the case of two telescopes with the same mirror area, the distribution is clearly symmetric, centred around the mean energy asymmetry value. Rather than an absolute cut-off at the minimum energy threshold of the two telescopes, the distribution can be seen to taper slightly such that at the lowest energies the energy asymmetry tends towards zero. This is interpreted as follows: near to threshold, the telescopes tend to trigger on brighter shower images, and are biased towards upwards fluctuations in the Cherenkov light, tending to over-estimate the shower energy. Close to threshold, large asymmetry values are only possible if both telescopes trigger on the shower and one telescope records the shower event at a higher energy than the other. Hence,

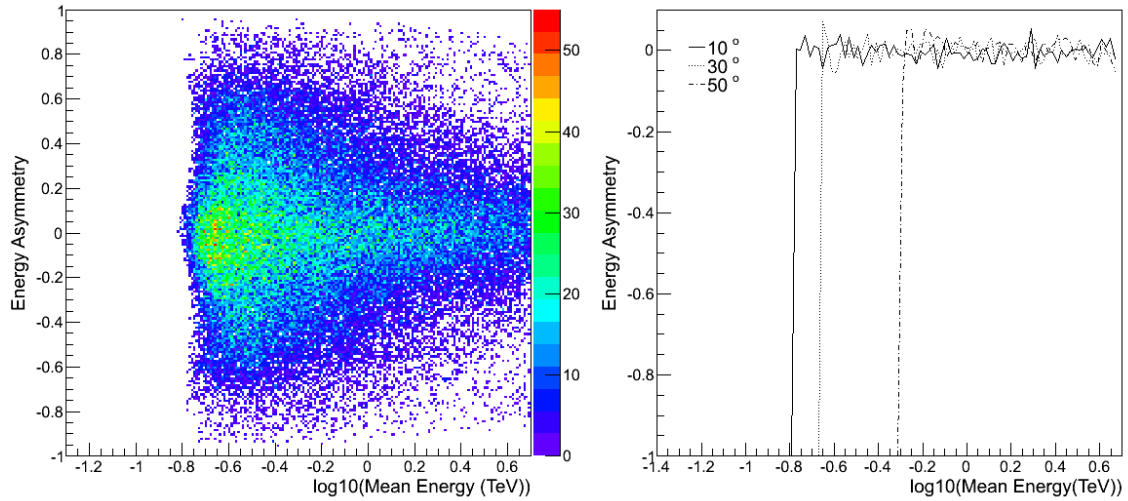


Figure 4.3: Left: Monte Carlo histogram of energy asymmetry as a function of shower energy, for two telescopes of the same mirror area. There is a mild tapering seen towards the energy threshold of the telescopes. Right: Energy asymmetry bias as a function of shower energy for two telescopes of the same mirror area. Zenith angles of 10° , 30° and 50° are shown; at larger zenith angles, the energy threshold shifts to higher energies.

for large asymmetry values, the overall mean energy for the telescope pair must lie further above the minimum energy threshold, and the distribution tends towards higher mean shower energies at larger asymmetries in the threshold region.

Although it has been assumed that, for two telescopes of identical construction, the same image size would lead to the same reconstructed energy, an additional complication arises since the energy reconstruction is based on a set of Monte Carlo lookup tables which already encode an estimate of the telescope efficiencies. This renders the energy inter-calibration an indirect probe of the telescope efficiency, as it instead probes the correction back to the reference efficiency used in generating the relevant set of lookup tables. The effect this has on the calibration results is clearly demonstrated in figure 4.4, showing how the results of the energy cross calibration are shifted with respect to the image size results depending on the set of lookup tables used. For each set, a different ratio between the reconstructed energy and image size cross calibration results is found. Agreement between the two methods is obtained only when all telescopes are simulated with the same optical efficiency (70 % of the nominal design value in figure 4.4). Therefore, for an unambiguous relative energy cross calibration to be obtained, a set of Monte Carlo lookup tables for which all telescope response efficiencies have the same value would be required.

4.2.4 Monte Carlo Linearity

The ability of this calibration method to recover the MC input telescope optical efficiencies is demonstrated in figure 4.5. Three MC phases with different combinations of optical efficiency were tested. For each set, the relative values obtained from the cross calibration are normalised to the average optical efficiency of the telescopes in each phase as follows. By keeping one telescope fixed to a relative efficiency of 1.0 in the minimisation of equation (4.2.3), a relative efficiency value per telescope is obtained. The average relative efficiency is then set equal to the average of the Monte Carlo telescope efficiencies, such that the system is normalised to the Monte Carlo values. This system normalisation is achieved by rescaling the telescope relative efficiencies by

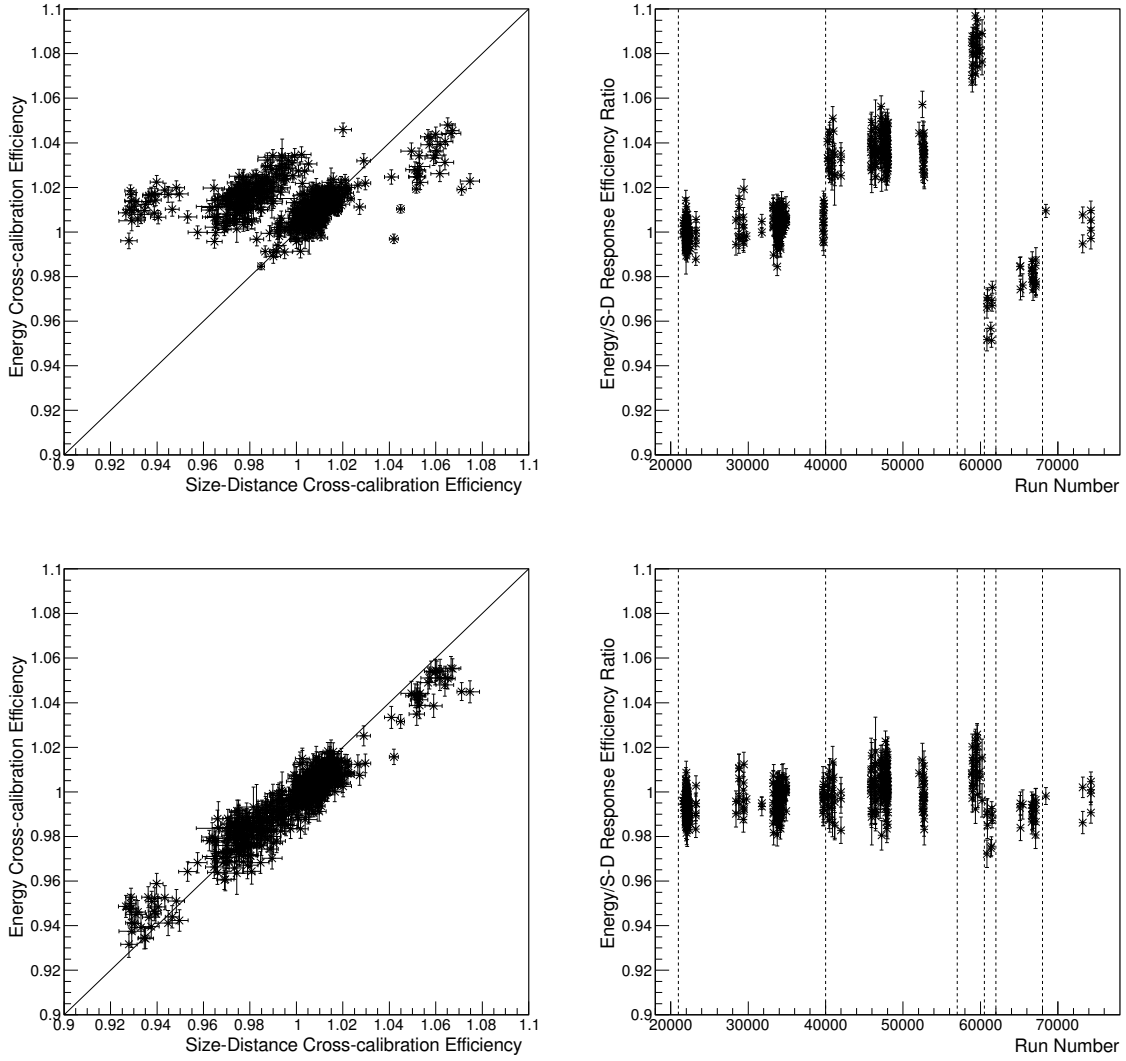


Figure 4.4: Correlation of the energy and image size (size-distance) inter-calibration response efficiencies, results shown for CT2 over time (or equivalently, run number), as found from H.E.S.S. I PKS 2155-304 data (a bright extragalactic γ -ray point source). There are clear discrepancies seen (left), which occur systematically within specific periods, as shown by the evolution of the ratio of the two approaches over time (or equivalently, run number, right). Shifts in the value of the ratio clearly coincide with changes in the set of Monte Carlo lookup tables being used (dashed lines). When ensuring the same set of Monte Carlo lookup tables is used throughout (with near uniform telescope efficiencies, phase 1b in table 3.2) the two approaches show good agreement (below), with a near constant unity ratio.

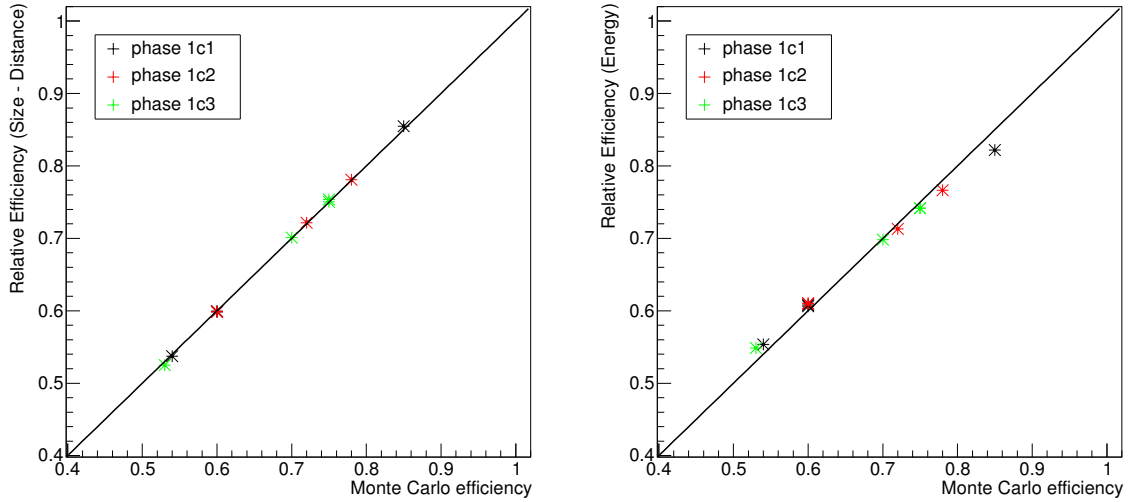


Figure 4.5: Test of the cross calibration approach on MC, with both the image size (left) and reconstructed energy (right) methods. Phases correspond to table 3.2 in chapter 3. Good linearity is seen with both methods, although a slight bias occurs as expected towards the extremes of the relative efficiencies obtained via the reconstructed energy method.

the ratio of the means,¹ enabling the linearity of the efficiencies obtained by the cross calibration method to be checked.

It can be seen that good linearity is obtained with both the image size and reconstructed energy approaches; however, in the case of the reconstructed energy, there is some deviation from linear seen at the highest and lowest energies. This is to be expected due to a slight energy bias when using energy lookups with flat optical efficiencies, which may be significantly different from the true values at extremes of the range probed. This may be solved with the use of an iterative approach, whereby, based on the results of a first pass of the calibration, the corresponding lookup tables are regenerated to match the recovered optical efficiency values. The procedure is then repeated; previous biases would be reduced by a better match of the lookup tables to the true optical efficiency values.

4.3 Application to Telescopes of Multiple Sizes

Additional considerations have to be taken into account when cross calibrating between telescopes of different sizes and types, such as found in the second phase of H.E.S.S. and as is also foreseen with the Cherenkov Telescope Array (see section 4.6). For this purpose, the two approaches of using the absolute image size and the reconstructed energy were developed further.

4.3.1 Adaptation of Image Size Approach

The different telescope mirror areas (600 m^2 to 100 m^2 in H.E.S.S. II) lead to intrinsically different total charge in photoelectrons recorded by the telescopes for the same light intensity. That is, for the same shower occurring equidistant between two telescopes of different mirror area, there is a systematic difference in recorded image size. This leads to a shift in and compression of the

¹That is, the ratio of the mean recovered relative efficiency to the mean Monte Carlo efficiency

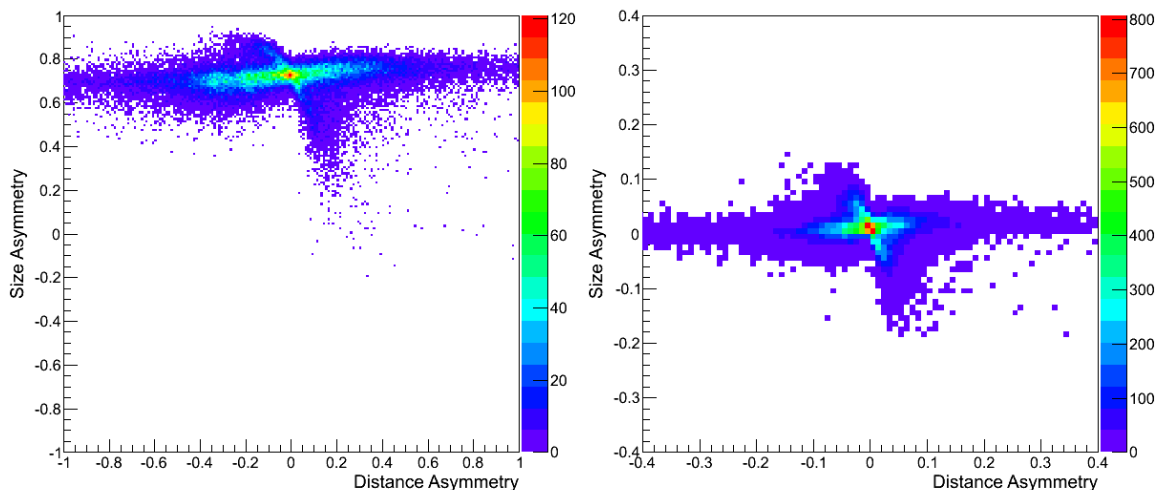


Figure 4.6: Monte Carlo size distance histogram between two H.E.S.S. telescopes (CT5 and CT1) of 600 m^2 and a 100 m^2 mirror area respectively. Left: the distribution has clearly been shifted from that in figure 4.2.2. Right: the image size in CT5 has been rescaled using an expected size ratio from simulations. This rescaling was performed using the logarithm of the image sizes, such that the distribution appears squashed, as well as shifted back to be centred on zero.

distribution found by the size-distance asymmetry procedure of section 4.2.2, as shown in figure 4.6.

Reliable understanding of the expected difference in image size is required in order to apply this procedure to telescopes of multiple sizes. One possibility is to find the expected image size ratio from Monte Carlo studies, which is accounted for predominately by the ratio in the mirror areas of the two telescopes; yet the variation in image size with mirror area is non-linear. For the distribution shown in figure 4.6, the average image size ratio was found to be around 5. By rescaling the image sizes in CT5 by this size ratio, the distribution could be brought to the expected shape, shown in figure 4.1. However, as the rescaling was performed using the logarithm of the image sizes, image size axis is somewhat reduced in figure 4.6. This ratio will also change over time, due to the changing optical efficiencies and with other secondary factors also contributing. These include the different materials used for the mirror coating and variation in the camera component technologies between telescopes which can lead to differing optical efficiency degradation rates, as well as other less well investigated effects which may contribute higher order terms to the variation. Whilst many of these factors are calibrated using this approach, decoupling which effects are accounted for by the expected size ratio from those effects contributing to the calibration results is a challenging enterprise.

If the Monte Carlo optical efficiencies of the telescopes are not equal, then the expected size ratio obtained from Monte Carlo intrinsically encodes and accounts for the expected optical efficiency discrepancy. In the cross calibration between telescopes of the same size described in section 4.2.2, it was implicitly assumed that the expected size ratio between telescopes is always 1. In principle, the image size approach with rescaled image amplitudes between telescopes of multiple sizes is just as valid as between telescopes of the same size; however, this approach tended to produce biased results, as will be demonstrated in chapter 5. As the image size recorded by a telescope varies non-linearly with energy and mirror area, an alternative approach was sought for cross calibration, adapting the reconstructed energy approach of section 4.2.3.

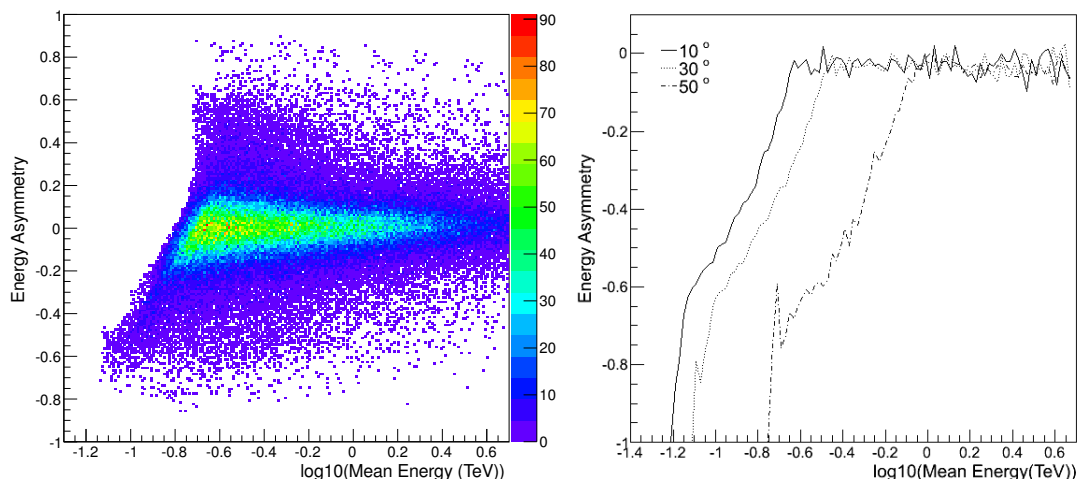


Figure 4.7: Left: Monte Carlo histograms of energy asymmetry as a function of shower energy, for CT5 and CT1, two telescopes of different mirror areas. There is clearly a biased region at the low end of the distribution. Right: Energy asymmetry bias as a function of shower energy between CT5 and CT2, obtained from Monte Carlo. Zenith angles of 10° , 30° and 50° are shown; at larger zenith angles, the unbiased region shifts to higher energies. See figure 4.3 for comparison.

4.3.2 Adaptation of Reconstructed Energy Approach

Applying this technique to the H.E.S.S. II array, it can be shown that the relative efficiencies of the four H.E.S.S. phase 1 telescopes are reliably recovered using the size-distance asymmetry procedure as outlined in section 4.2.2. The energy asymmetry procedure also recovers satisfactorily the correction to the muon efficiency from that stored in the Monte Carlo lookup tables (as discussed previously in section 4.2.3). Whereas for the image size calibration in principle all shower events can be used, as the lookup tables for energy reconstruction are created based on γ -ray events, the energy reconstruction for hadronic events performs poorly, due to the inherent fluctuations in hadronic showers and difficulties in recovering the full shower behaviour. Hence the systematic accuracy of the procedure is best when performed after γ /hadron selection cuts, which help to improve the accuracy of the energy reconstruction by ensuring that only γ -like events are used.

When comparing the reconstructed energy of the fifth telescope to that of one of the four telescopes of the original array, the calibration must be taken only from within the region for which the energy ranges of the two telescopes overlap. The histogram distribution in this case is shown in figure 4.7, where there is clearly a biased region which occurs near the energy threshold of telescopes, caused by the telescopes being intrinsically biased towards triggering on local upwards fluctuations in the showers.

For events reconstructed with an energy falling comfortably within the energy range of the fifth larger telescope, this telescope accurately reconstructs the energy. When operating in stereo hybrid mode (required for the calibration), another telescope seeing the event will reconstruct the energy within its detectable energy range. If the energy is just below threshold, the mere fact that the smaller telescope has seen the event is sufficient for its energy to be over-estimated and reconstructed within its energy range.

This leads to a biased region in energy, near the low energy threshold of the smaller telescopes, within which the energy asymmetry is skewed. As the biased region is heavily zenith angle dependent, one possible approach is to use a set of Monte Carlo lookup tables recording

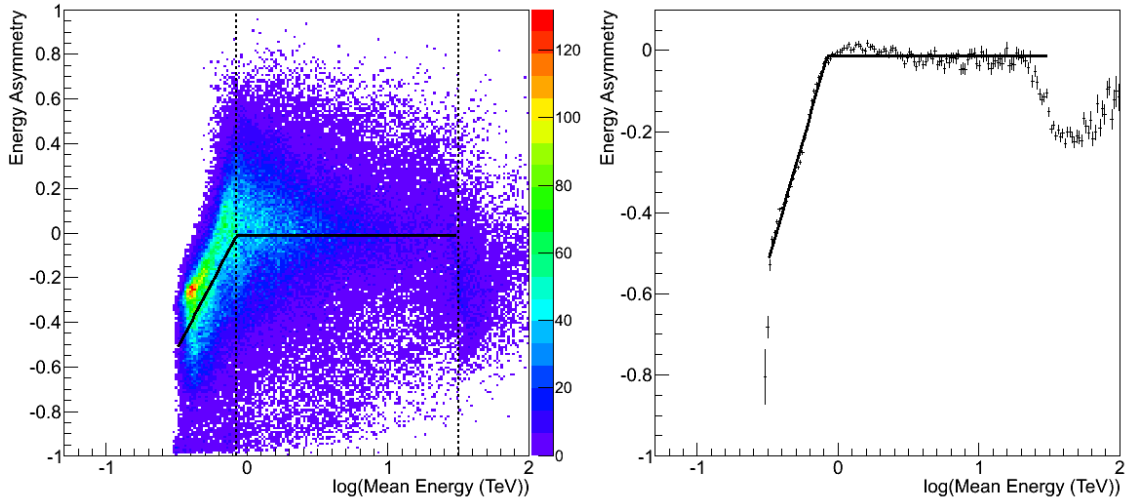


Figure 4.8: Histogram of energy asymmetry against the reconstructed shower energy (above) for pair-wise shower reconstruction by CT5 and CT1 on Crab Nebula data from 2014. There is clearly a biased region beyond the CT1 threshold, which may be located by fitting the histogram profile with energy (below) with equation (4.3.1). A similar biased region is seen at high energies, due to CT5 underestimating the shower energy. The fit function and location of the cut thus obtained are overlaid on the histogram.

this bias, from which the energy required for a safe cut may be extracted. The bias occurs at the same energy for all particles, if reconstructed under the assumption of being a γ -like shower. The variation of this zenith angle dependency of this energy bias is shown in figure 4.7 between telescopes of the H.E.S.S. II array. As the instrument threshold is not only zenith angle dependent, but will also vary with environmental conditions and the overall telescope-camera system optical efficiency itself, there will be slight variation in the location of the biased region over time.

Due to this zenith angle dependent energy asymmetry bias, a safe energy threshold cut needs to be defined, removing the biased region and beyond which the energy asymmetry histogram may be treated as symmetric. Rather than finding this cut from lookup tables based on zenith angle, it is possible to determine this cut from the data itself, as shown in figure 4.8. The location of the bias threshold may be easily found from the profile of the histogram with energy (figure 4.8), by fitting the simple function:

$$y = \begin{cases} mx + c & (x < b) \\ mb + c & (x > b) \end{cases} \quad (4.3.1)$$

where b is the location of the safe energy cut and c is roughly the value of the asymmetry $a_{i,j}$ between the telescopes. From figure 4.8, it can also be seen that there is a second biased region occurring at high energies. In similar fashion to the low energy bias, this occurs for high energy events due to the shower being well reconstructed by the smaller telescopes, yet under-estimated by CT5. However, this biased region is not accounted for in equation (4.3.1), as the high energy statistics are far lower such that this region does not influence the fit as strongly. Nevertheless, a safe energy cut at the high end is forcibly imposed at $E = 30$ TeV ($\log_{10}(E(\text{TeV})) \approx 1.5$). If this fitting procedure fails (due to low statistics, for example), then a safe default minimum energy cut value of $E = 1$ TeV ($\log_{10}(E(\text{TeV})) = 0$) is used.

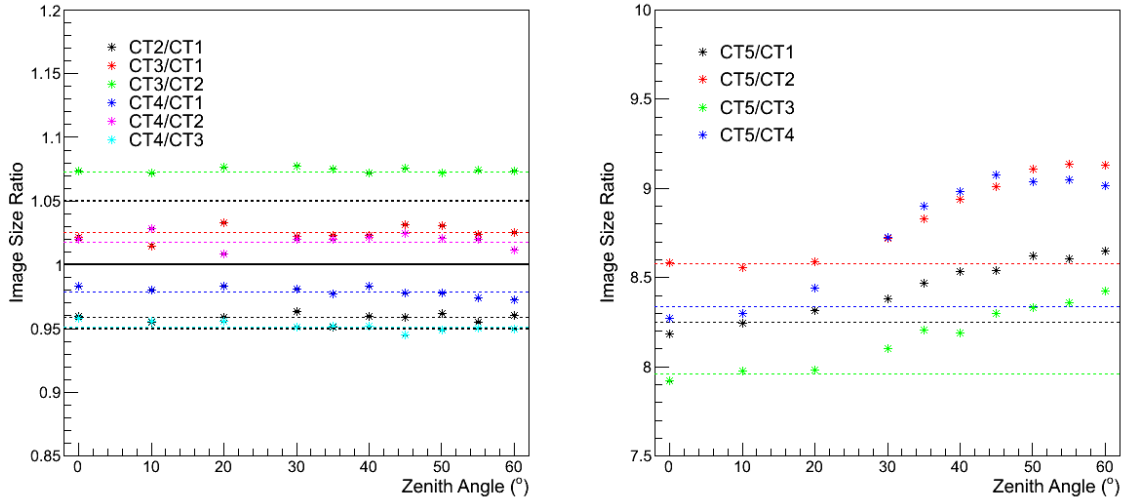


Figure 4.9: Ratio of image sizes between telescopes as a function of zenith angle. Left: the ratio is stable across all zenith angles for CT1-4, as indicated by the dashed lines showing the average ratio. Right: the ratio of image sizes between CT5 and each of CT1-4 increases with increasing zenith angle beyond 20°. Dashed lines indicate the average of the first three points.

4.4 Variation with Zenith Angle

Given the known dependence of both the energy threshold and the projected area of the Cherenkov light pool for a given shower with zenith angle, possible variation of the cross calibration results with zenith angle was investigated using Monte Carlo. Although towards higher energies the energy threshold of the instrument increases, the ratio of the image sizes between telescopes was expected to remain more or less constant; this was indeed found to be the case for the H.E.S.S. I telescopes of the same size, although some scatter around the mean size ratio was seen (figure 4.9).

In contrast, the ratio of the image sizes between CT5 and CT1-4 was found to increase with increasing zenith angle, as shown in figure 4.9. A ratio of $\sim 8 - 9$ arises from a combination of the ratio of the reflector dish areas and the optical efficiency differences. The changing ratio with zenith angle can be understood from figure 4.10, where the image size in photoelectrons is plotted as a function of the reconstructed energy. It can be seen that the relation is linear, as expected; however, the gradient of the linear fit is steeper for CT5 than for CT1-4. Therefore, as the shower energy increases, so the image size increases more rapidly for CT5 than for CT3, leading to an increased ratio between the image sizes seen in the two telescopes. The increasing size ratio with zenith angle is then due to the increased energy threshold. Consequently, an average size ratio used to correct for the differences between CT5 and the H.E.S.S. I telescopes is sufficient at first order, yet will be biased towards low energies due to the higher number of events, and the true ratio will deviate from this as a function of energy.

Nevertheless, the results of both the image size and the reconstructed energy cross calibrations are mostly stable with zenith angle on this Monte Carlo (see figure 4.11). The image size results for CT5 are slightly above 1 for all zenith angles; this is due to the expected size ratio being obtained from Monte Carlo with CT5 simulated at 80% and CT1-4 at 70% of their nominal values respectively. The set of Monte Carlo used for this study, however, is phase 2b2 (as defined in table 3.2 of chapter 3) which comprises a different set of simulated efficiencies.

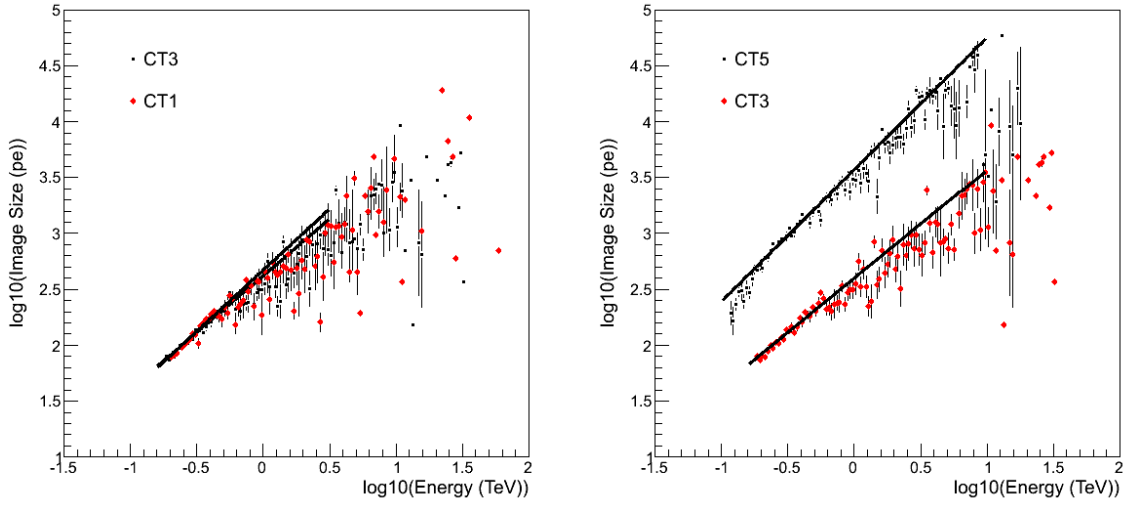


Figure 4.10: Left: For two H.E.S.S. I telescopes, the linear relation between the shower image size and reconstructed energy has approximately the same slope. Right: The image size against shower energy has different slopes for CT5 and the H.E.S.S. I telescopes, such that a single image size ratio does not apply uniformly to the whole energy range. The linear fit tends to be weighted towards higher statistics and lower energies.

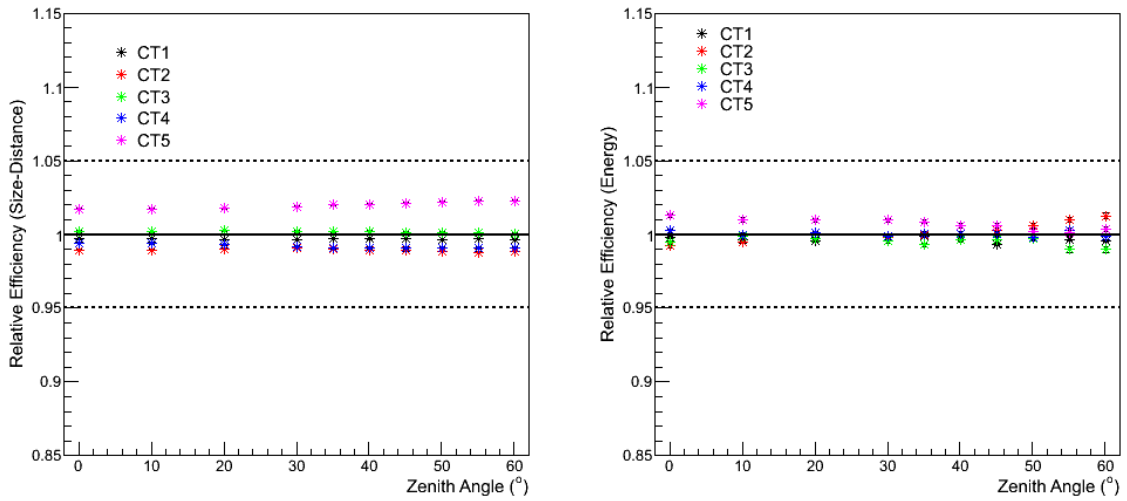


Figure 4.11: Left: The results of the image size cross calibration are mostly stable with zenith angle, although CT5 is systematically offset from unity, due to the expected size ratio being obtained from a set of Monte Carlo with different simulated optical efficiencies to those used in this study. Right: The energy cross calibration results change slightly with increasing zenith angle due to the changing energy threshold, however the effect is at the $\sim 1 - 2\%$ level.

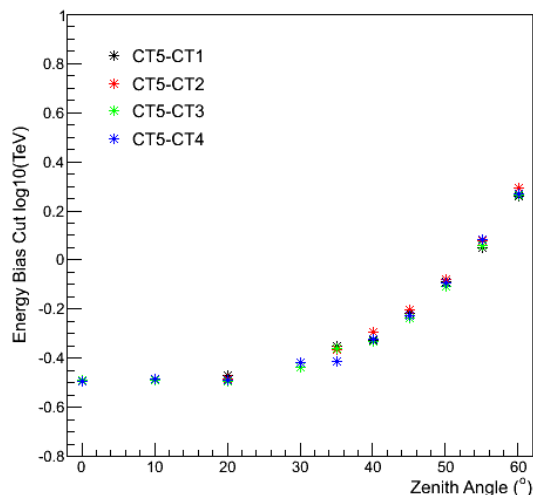


Figure 4.12: Above zenith angles of $\sim 30^\circ$, the energy bias cut shifts towards higher energies with increasing zenith angle. This is a consequence of the increasing energy threshold (see also figure 2.13 of chapter 2).

There is a slight trend seen in the energy cross calibration results for CT5 decreasing with increasing zenith angle in figure 4.11; this is again due to the changing energy threshold of the observations, yet the overall systematic effect on the results is at the $\sim 1 - 2\%$ level. This effect is seen most explicitly in the changing energy bias cut with zenith angle (figure 4.12). Above zenith angles of $\sim 30^\circ$, the energy bias cut increases noticeably; with increasing energy threshold, the location of the bias also shifts. As the bias is essentially a threshold effect, occurring due to the preferential triggers on upward shower fluctuations close to the smaller telescopes, this bias shifts to higher energies as the threshold changes (see also figure 2.13 of chapter 2).

4.5 Conclusions on Cross Calibration with H.E.S.S.

Sound knowledge of imaging atmospheric telescope response efficiencies is important for reliable energy reconstruction. The per telescope response efficiencies are calibrated using the well established muon ring calibration procedure [58], whilst the efficiencies may be calibrated between telescopes in a relative manner as outlined in [71]. Here, an adaptation of the latter technique has been presented, enabling individual telescope coefficients to be recovered. This technique can also be used to monitor the relative degradation rates between telescopes. In order to extend the method to multi-size arrays, several additional factors must be taken into account. The inter-calibration technique as originally proposed makes a direct comparison of the image size between two telescopes, when selecting events with shower cores equidistant to the two telescopes. Whilst the image size is affected by broken pixels, tail cuts and Night Sky Background effects, it is generally found to be a robust procedure between telescopes of the same size. To calibrate between two telescopes of differing mirror area, the approach can be adapted with the use of an expected size ratio obtained from Monte Carlo, however, this ratio varies with event energy. A suitable alternative variable to the image size is the telescope reconstructed energy, however due to the differing energy ranges, one must take care to avoid a biased region near the energy threshold of one of the telescopes.

Whilst performing the energy cross calibration, if the Monte Carlo lookup tables being used do

not have the same efficiency value for all telescopes, care must be taken with the interpretation. The relative optical efficiencies recovered in this case will refer to the differences above and beyond those already incorporated into the lookup tables being used.

After taking these considerations into account, the energy cross calibration relative efficiency values correlate with those found via the image size asymmetry values and with the muon efficiency parameters at the few percent level. This cross calibration procedure may be used as a cross-check on the muon efficiency parameter, and is particularly relevant for calibrating efficiencies between elements of a multi-size array. Interplay of the muon and cross calibration procedures is covered in more detail in chapter 5. As muons and γ -ray air showers have differing intrinsic wavelength dependencies of the Cherenkov light distribution, one of the major advantages of this calibration procedure is that it intrinsically finds the optical efficiency of the telescope at the appropriate wavelength, thereby negating any biases arising from achromatic degradation of telescope components.

The main advantage of comparing telescopes in a pair-wise manner is the many independent measurements. As the number of telescopes grows, the number of telescope pairs grows as $\frac{1}{2}N(N-1)$, such that the number of measurements far exceeds the number of unknown parameters (response efficiencies). The measurements are independent, as in each case the telescope combination used to measure a discrepancy for a particular shower is free of influence from the other telescopes in the array.

One key advantage of this calibration procedure is amount of data which can be used; comparisons between how two telescopes view the same air shower are independent of certain analysis quality cuts such that some runs which would otherwise be discarded (due to truncated data taking or a hazy atmosphere, for example) may be used. Additionally, the nature of the shower and of the primary particle is irrelevant to the image size cross calibration, such that hadronic as well as leptonic showers may be used.

4.6 Cross Calibration for the Cherenkov Telescope Array

The method of cross calibration of IACT optical response efficiencies as outlined earlier in this chapter is extendable to larger air shower physics experiments comprising multiple components and/or multiple detector types.

The physics agenda for CTA follows that of H.E.S.S., but is foreseen to lower the sensitivity threshold considerably, enabling more detailed studies of known sources as well as unprecedented new information.

In order for such an array to fulfil its potential, robust calibration procedures are mandatory. A key part of the calibration chain is knowledge of the optical throughput efficiency, which is expected to be provided absolutely using the muon calibration as outlined in chapter 3, and relatively using the cross calibration as already demonstrated on H.E.S.S.. For CTA, two aspects of the calibration need to be considered - calibration of the elements of each subsystem² of a given type (intercalibration) and calibration of those subsystems to each other (cross calibration). Both aspects will be addressed in the following sections.

This approach has been demonstrated to achieve a few percent accuracy on H.E.S.S., and

²A “subsystem” comprises all telescopes in the array of the same type (not an arbitrary subset of telescopes); hence there are as many subsystems as telescope types.

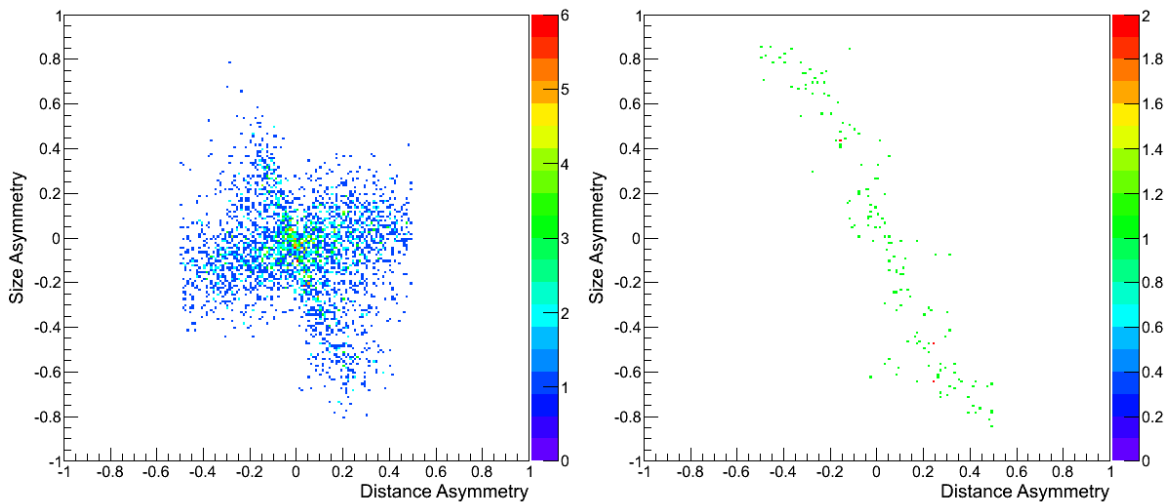


Figure 4.13: Histograms of size asymmetry against distance asymmetry for two large telescopes (LSTs) at 100 m separation (left) and two small dual mirror telescopes (sc-SSTs) at 330 m separation (right) in a potential CTA array layout. The horizontal component is no longer present for the sc-SSTs at larger separation distance.

therefore has the potential to also reach this level on CTA, fulfilling the CTA performance goal of 5% systematic uncertainty on the absolute intensity of Cherenkov light at each telescope [74].

4.6.1 Intercalibration using Image Size

The image size asymmetry against distance asymmetry relation was found to behave similarly to that seen between the H.E.S.S. telescopes. For γ -ray showers, there are two major contributing components; a horizontal component, corresponding to those events for which the core distance to both telescopes is $\lesssim 125$ m; and an antilinear component, corresponding to events with the core distance to both telescopes $\gtrsim 125$ m. As explained previously in section 4.2.2, this is due to the intrinsic shape of the lateral Cherenkov light distribution from an EAS. Within the Cherenkov light pool, the light distribution is approximately flat, giving rise to the horizontal component of the histogram, whilst the drop in light beyond the shoulder of the Cherenkov light pool corresponds to the anti-linear component (see also appendix A.3).

Subsequently, as the telescope separation distance increases, so the prominence of the horizontal component decreases; for telescope separations $\gtrsim 200$ m, the horizontal component is essentially not present, as seen for the small dual mirror telescopes (sc-SSTs) in figure 4.13.

There are two possible approaches to using the image size asymmetry against core distance asymmetry to recover the optical efficiency asymmetry of the two telescopes. One is the approach of section 4.3.2 within the context of H.E.S.S., where a cut on the distance asymmetry is imposed and the resulting distribution projected onto the size asymmetry axis (figure 4.1). The mean of this projection can then be interpreted as a measurement of the mean size asymmetry between two telescopes - this is shown for the large telescope (LST) histogram of figure 4.13 in figure 4.14. A Gaussian fit to this projection was found to perform well in the case of low statistics or unoptimised cuts (no cuts were applied to the distributions in figures 4.13 and 4.14). A second approach, more relevant in the case of large telescope separation distances (typically above 250 m), is to fit the profile of the anti-linear component with a straight line; the intercept of this line with a distance asymmetry of zero then provides a measure of the residual size asymmetry

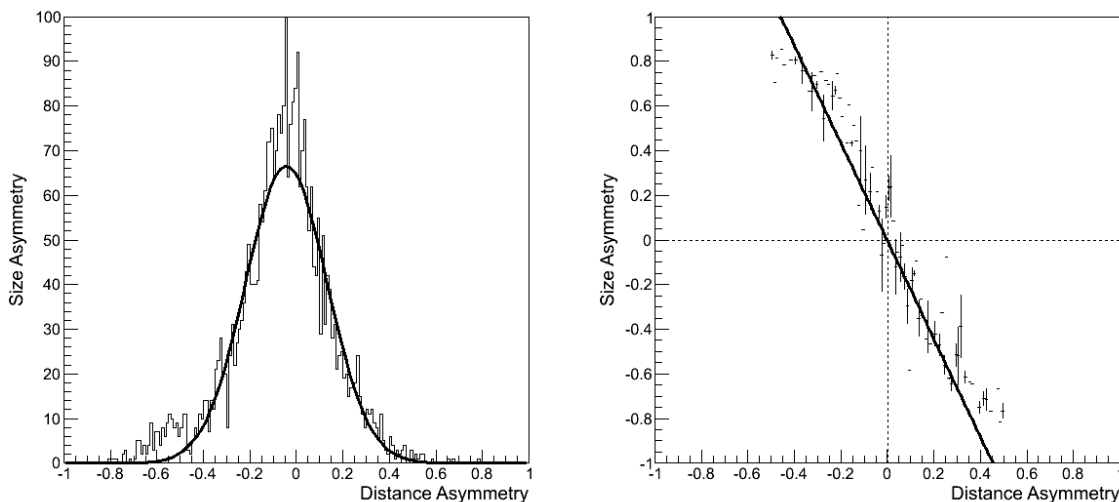


Figure 4.14: Left: for nearby telescopes, the mean size asymmetry is obtained from the projection of the distribution in figure 4.13 along the y -axis. A Gaussian fit could be used in place of a weighted mean, in the case of low statistics or unoptimised cuts (no cuts to the distribution were applied here). Right: Between telescopes at large separation distances, the overall image size asymmetry may be recovered from the histograms via a fit to the anti-linear component, rather than the mean as in figure 4.1), obtained via the profile along the x -axis. The value of the intercept obtained in the fit can be interpreted as a measure of the overall size asymmetry between the two telescopes.

and hence also the optical efficiency asymmetry between the two telescopes (illustrated in figure 4.14).

4.6.2 Intercalibration using Reconstructed Energy

Whilst comparison of image sizes directly is possible for telescopes of identical specifications, in the case of CTA with multiple telescope types, the variation in image size with hardware is more complex, especially near trigger threshold. Although use of an expected size ratio (obtained from simulations) may be considered, this approach suffers considerably from low statistics and random fluctuations for telescope separations exceeding the radius of the Cherenkov light pool $\sim O(100 \text{ m})$.

Instead, the proposed approach is to use the reconstructed shower energy as an alternative to the image size, as beyond the biased threshold region all telescopes should agree on the shower energy.³ This approach was adopted for H.E.S.S. in section 4.2.3, the key principles of the calibration remain the same here.

4.6.3 Cross Calibration Principle

The cross calibration principle for CTA follows that outlined in section 4.2 for H.E.S.S.. Shower events triggering multiple telescopes are reconstructed by each telescope pair separately. The variation in reconstructed energy between two telescopes is quantified by the use of an asymmetry parameter, a_{ij} :

$$a_{ij} = \frac{E_i - E_j}{E_i + E_j}, \quad (4.6.1)$$

³A cut on the energy bias could be imposed to ensure that the threshold region is avoided (see section 4.3.2).

where E_i and E_j are the energies reconstructed by telescopes i and j individually. From the image size and reconstructed distance, a per telescope energy estimate and uncertainty is obtained from a set of lookup tables. In the case of two telescopes of the same type, the energy asymmetry distribution is symmetric; however, when comparing telescopes of different types a biased region occurs near the trigger threshold of the smaller telescope. The location of a safe bias cut to remove the biased region can be found from the distributions for each pair separately, following the method outlined in section 4.3.2, or by imposing a hard energy cut for pair measurements across telescopes of different types. However, the asymmetry measurements between pairs of different types were found to exhibit larger scatter, due to the lower remaining statistics, and a systematic offset with respect to measurements between telescope pairs of the same type. Hence measurements of the energy asymmetry are only made between telescopes of the same type.

The overall asymmetry a_{ij} and its uncertainty σ_{ij} between two telescopes is determined by the weighted mean and uncertainty of all available event-wise energy asymmetry estimates, weighted by σ_{ij}^{-2} . This energy asymmetry is interpreted as corresponding to the intrinsic optical efficiency asymmetry of the two telescopes, with all other factors contributing at a negligible level.

Measurements for the optical response asymmetry between two telescopes are made for all pairs of telescopes of the same type. For each system of N telescopes, the number of pairs available is $\frac{1}{2}N(N-1)$. However, in the case of large arrays, a limit on the separation distance of telescopes between which measurements are made needs to be imposed. Once the telescope separation distance exceeds the typical Cherenkov light pool diameter, the reconstruction performance drops off with increasing distance; the much lower rate of events triggering both telescopes leads to lower statistics, such that comparisons between telescopes at large separation distances are impractical. Nevertheless, with a cut on separation distance the majority of telescopes within an array still participate in multiple asymmetry measurements a_{ij} , such that the system of unknown parameters (response coefficient c_i per telescope i) is overdetermined. These response coefficients can therefore be recovered via a χ^2 minimisation procedure for all valid pairs up to N telescopes:

$$\chi^2 = \sum_{i=1, j>i}^N \frac{\left(a_{ij} - \frac{c_i - c_j}{c_i + c_j}\right)^2}{\sigma_{ij}^2}. \quad (4.6.2)$$

This minimisation procedure is performed on each subsystem of telescopes of a given type separately. An example system of measurements for a given telescope is depicted schematically in figure 4.15.

During the minimisation, one telescope is arbitrarily kept fixed in order to remove free parameters due to the overall system scaling factor. As all measurements are made in a relative sense between telescope pairs, the telescope-wise optical response efficiencies obtained for each telescope subsystem may be normalised after minimisation in a second step outlined below.

4.6.4 Monte Carlo Studies

As a test of the method outlined above, Monte Carlo (MC) simulations were performed using the second CTA production configuration of CORSIKA/*sim_telarray* [75]. One of the candidate Southern sites for CTA was simulated with γ -rays at 20° zenith angle. From these simulations, two potential array layouts, 2A and 2B were selected as depicted in figure 4.16, incorporating different telescope types, spacings between telescopes and optimisations, with layout 2B optimised for higher energies than layout 2A. Both layouts have similar LST and MST configurations, whilst the SST design and configuration differs. In the case of layout 2A, the SSTs have 7 m

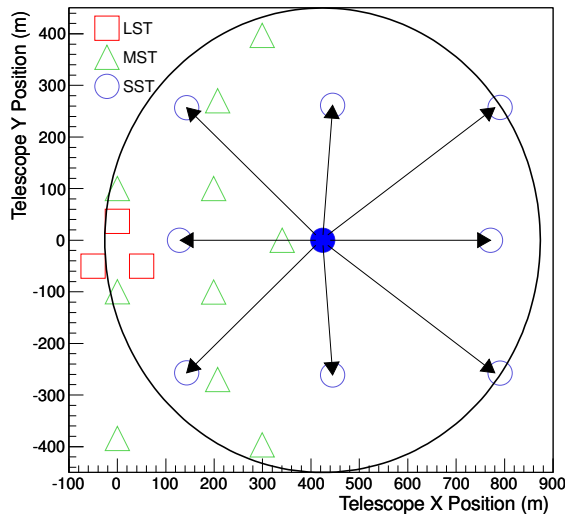


Figure 4.15: Part of a CTA array layout. For a given telescope (filled in circle), asymmetry measurements are made with all other telescopes of the same type falling within a certain radius.

diameter mirrors and Davies Cotton optics [76] (DC-SST), whereas the SSTs in the 2B array layout are of Schwarzschild-Couder optical design [77] with a 4 m diameter primary mirror and a 1 m diameter secondary mirror (SC-SST) and cover a wider ground area in order to maximise the effective area at the highest energies. However, it should be noted that whilst development of the DC-SST for CTA has progressed on to telescopes of 4 m diameter rather than the 7 m diameter of layout 2A, this does not affect the conclusions on the applicability of this method for either intercalibration or cross calibration to multi-type IACT arrays (although cut optimisation for different layouts is required).

All telescopes were randomly assigned optical response efficiency values according to a Gaussian distribution with a mean response efficiency of 70% nominal value and a standard deviation of 10%, limited to values $\leq 100\%$. Gamma ray initiated air showers originating from 20° zenith angle were subsequently simulated according to an E^{-2} energy spectrum over an energy range of $\sim 5 \text{ GeV} - 500 \text{ TeV}$.

These simulated events were reconstructed separately by all independent same type telescope pairs as outlined above using a CTA baseline Hillas analysis (see also section 2.5.2) [78]. The reconstruction was performed using a set of lookup tables based on all telescopes having 70% optical efficiency.

Measurements were made between all telescope pairs with separation distances $d_{ij} < 300 \text{ m}$, enabling many cross-checks (table 4.2). For the SSTs, which are spread over a larger area (figure 4.16), the allowable telescope separation was increased to $d_{ij} < 350 \text{ m}$ for the 7 m DC-SSTs of array 2A, and to $d_{ij} < 450 \text{ m}$ for the 4 m SC-SSTs of array 2B, permitting cross-checks in the outermost regions of the array.

To ensure that the shower events used for the calibration are treated in a consistent manner, are sufficiently above threshold to avoid instrumental effects and that measurement biases are minimal, a set of good quality cuts were defined as outlined in table 4.3.

Additionally, weak background cuts on the image shape were imposed; only events with values of the mean reduced scaled width and mean reduced scaled length less than 2 were included (see also section 2.5.2) [78]. These are scale parameters characterising images from multiple telescopes

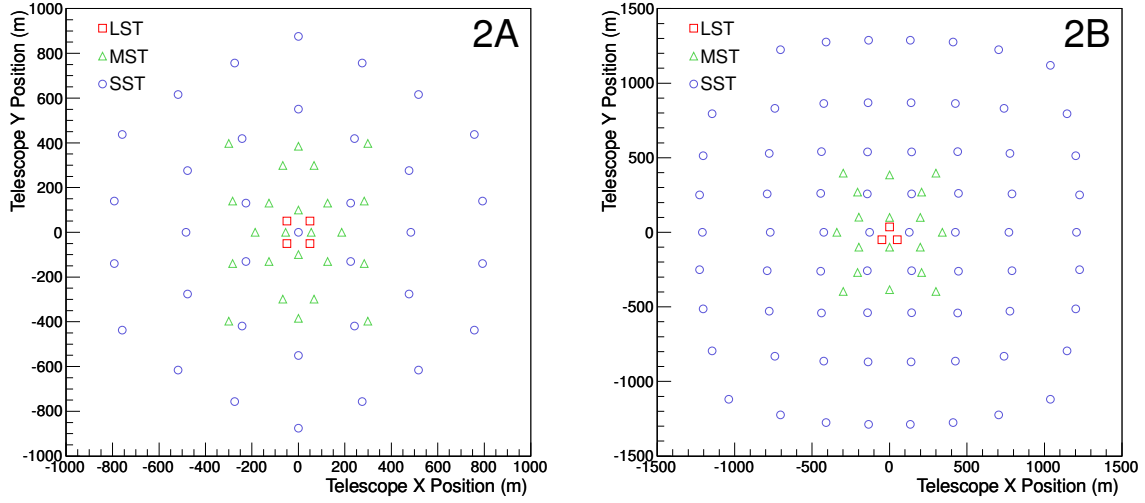


Figure 4.16: Array layouts used in the MC studies performed, with number of telescopes and primary mirror diameters as follows. Left: Layout 2A comprising 63 telescopes; 4 LSTs (23 m), 24 MSTs (12 m) and 35 DC-SSTs (7 m). Right: Layout 2B comprising 93 telescopes; 3 LSTs (23 m), 18 MSTs (12 m) and 72 SC-SSTs (4 m).

Array	Subsystem	Telescopes	Telescope Pairs
2A	LST	4	6
	MST	24	100
	DC-SST	35	78
2B	LST	3	3
	MST	18	37
	SC-SST	72	183

Table 4.2: Number of telescopes and of telescope pairs suitable for asymmetry measurements for each telescope type subsystem.

Parameter	LST	MST	DC-SST	SC-SST
Image Size (pe)	93	90	79	29
Tail Cuts (pe)	9,12	8,11	6,9	3.7,5.5
Total image pixels	5	4	3	4

Table 4.3: Event selection cuts used for the cross calibration procedure. All values quoted are minimum thresholds (see [78]), determined for the central energy range according to telescope dependent properties. The tail cuts image cleaning retains all pixels with photoelectron charge greater than the upper threshold and neighbouring pixels with charge greater than the lower threshold.

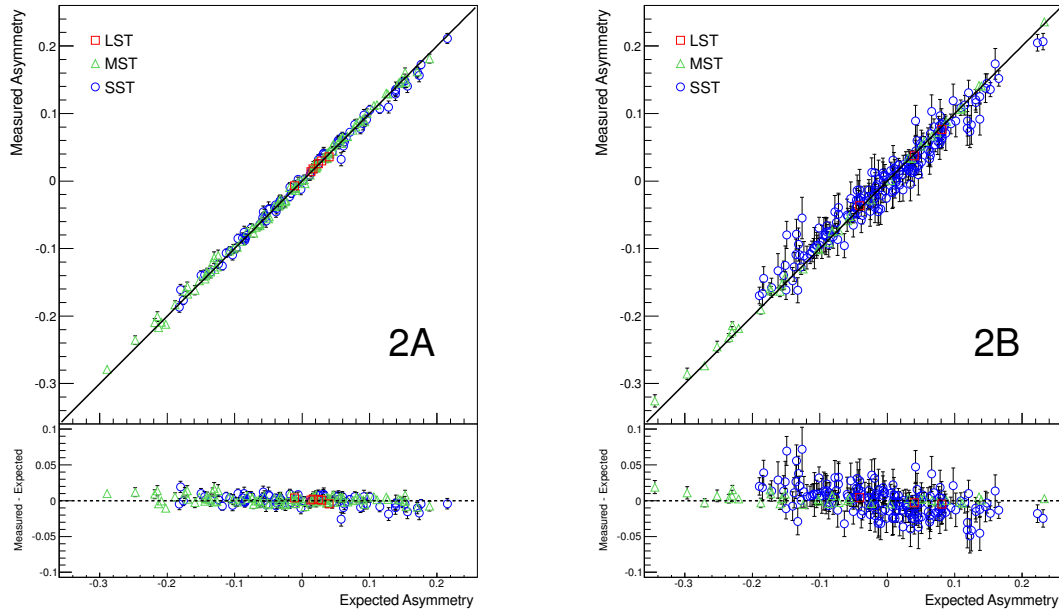


Figure 4.17: Measured asymmetries against the expected values calculated from the preassigned optical efficiencies, for the array layouts 2A (left) and 2B (right). Shown for all telescope pairs with pairs between LSTs shown in red, between MSTs in green and between SSTs in blue. Measurement errors are typically of the order of the marker size $\sim O(0.005)$, noticeably increased (to $\sim O(0.01)$) for SST pairs in the outermost regions of layout 2B. A black, solid line defines the case of perfect agreement.

in stereoscopic observations; these were calculated separately for each pair of telescopes which triggered on a shower event. All shower events were required to trigger at least two telescopes.

4.6.5 Simulation Results

Asymmetry Correlation

Independent asymmetry measurements were made between all telescope pairs in each subsystem passing the separation distance cut, as summarised in table 4.2.

Excellent agreement between the obtained reconstructed energy asymmetry and the true expected response efficiency asymmetry (the asymmetry of the preassigned telescope mirror reflectivities) is demonstrated in figure 4.17, verifying that the reconstructed energy is a valid alternative variable to the image size and does indeed probe the telescope response asymmetry. This correspondance may, however, be affected in the case of non-linear systematics affecting the Monte Carlo reference. Larger errors are consistently obtained for the smaller 4 m SSTs in layout 2B than for the 7 m SSTs in layout 2A, especially for telescope pairs at larger separations in the outermost regions of the array, where the event rate (and hence statistics) is particularly low. Correspondingly, there are fewer events triggering both telescopes due to the increased telescope separation distance, causing lower statistics and larger measurement errors.

At large asymmetries some small bias was found, mainly within the MST subsystem, as seen particularly for layout 2B in figure 4.17; on further investigation, these pairs involved one of two MSTs located centrally to the array layout with randomly assigned mirror reflectivities of 49% and 100% of nominal, quite far from the mean of 70% used in the lookup tables. Consequently, energy asymmetry distributions produced with these telescopes were slightly biased due to the

20%–30% discrepancies in optical throughput efficiency involved. This bias would be reduced in the case of an iterative approach. Nevertheless, the overall correlation between the true optical efficiency asymmetry and the measured energy asymmetry is excellent.

Subsystem Minimisation

The individual telescope response efficiencies were found using the aforementioned procedure, assuming that all telescopes had a response efficiency of 70% as starting points for the minimisation of each subsystem. For the minimisation, performed using MINUIT [68], one telescope was arbitrarily kept fixed, to avoid ambiguities due to the uncertainty in the overall scaling factor of the system. This restriction is later lifted, as outlined below.

In order to cross calibrate the entire array, the relative normalisation between the telescope type subsystems is required. As the minimisation of each subsystem was performed in a relative manner, the average response efficiency per subsystem was defined to be equal to 1.0 and the telescope-wise relative response efficiencies were correspondingly rescaled. The reciprocal of these rescaled efficiencies gave a per telescope correction factor, which was applied to the per telescope energy estimates in order to correct for the differences in efficiencies as found from the minimisation. Subsequently, the relative normalisation between the telescope subsystems were obtained as follows.

Scaling Factors between Subsystems

Events detected by two different telescope types, with at least two telescopes of each type triggered, were selected. These showers were reconstructed separately by each telescope type subsystem, with all telescope energy estimates corrected for efficiency variation within each subsystem as outlined above. The mean ratio of the event-wise subsystem energy estimates, obtained by a Gaussian fit to the distribution accumulated from the same data set, provided the scaling factors sf_{LM} and sf_{MS} , between the LST/MST and MST/SST subsystems respectively.

As the two different array layouts comprise different combinations of telescopes with differently assigned efficiencies, as well as different SST types, the average true efficiency of the various telescope type subsystems does not remain the same. The scaling factors adjust for this, and are indeed seen to differ for the same scaling (such as LST/MST) between the two array layouts.

Due to the requirement of multiple telescopes of each type triggering in all events used to determine the scaling factors, there remains a systematic bias towards events near the centre of the array (and also towards lower energies, with a correspondingly higher event rate). Consequently, the scaling factors, sf , found from the Gaussian fit more closely match the mean efficiencies of centrally located telescopes than those at larger distances. To account for this, the scaling factors are modified by the ratio of the average telescope relative response efficiency to the average weighted by telescope participation.

$$sf_{LM} \rightarrow sf_{LM} \times \left(\frac{\sum_i^{N_M} \varepsilon_i N_i}{\sum_i^{N_M} N_i} \right), \quad (4.6.3)$$

where the sum is over all telescopes i in a given subsystem up to the total number of telescopes in that subsystem N_M , for each telescope with efficiency ε_i which triggered on N_i events. Equation (4.6.3), shown for the LST/MST scaling factor sf_{LM} , is used analogously for the MST/SST scaling factor (sf_{MS}).

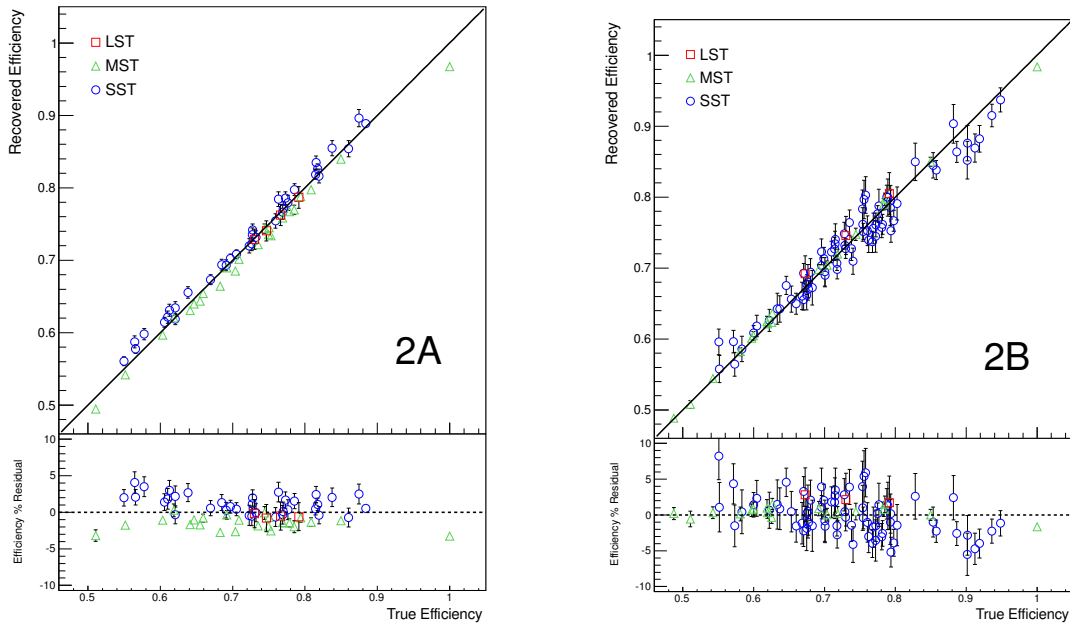


Figure 4.18: Telescope response efficiencies obtained post minimisation compared to the initially assigned values. Results correspond to the 2A array layout (left) and the 2B array layout (right). Measurement errors are typically $\lesssim O(0.02)$ and are statistical only, with percentage residuals shown below. A black, solid line defines the case of perfect agreement.

Using these scaling factors to scale the response efficiencies obtained for the LST and SST subsystems to the MST subsystem yielded the overall relative LST response efficiencies of all telescopes within an array.

Recovered Efficiencies

The agreement obtained between the assigned and recovered telescope response efficiencies with this cross calibration procedure (after relative normalisation of telescope subsystems) is shown in figure 4.18, with the RMS of the residuals for different array layouts and telescope subsystems stated in table 4.4. For the purposes of illustration, the mean recovered efficiency was set to the mean true preassigned efficiency; in practice, as long as the calibration procedures and simulations are self-consistent, the absolute value of this normalisation is not necessary for telescope cross calibration.

In obtaining this level of precision, 35×10^6 γ -ray events were simulated, with $O(1 \times 10^5)$ events triggering the array and $O(4 \times 10^4)$ events passing cuts for both array layouts. This corresponds to approximately 10 or 13 hours of data for array layouts 2A and 2B respectively, on a source with 10% of the γ -ray flux of the Crab Nebula (over the energy range 50 GeV – 100 TeV), adopting a spectrum for the Crab with index $\Gamma = 2.39 \pm 0.03$ and flux at 1 TeV $I_0 = 3.76 \pm 0.07 \times 10^{-11} \text{cm}^{-2} \text{s}^{-1} \text{TeV}^{-1}$, as measured by the H.E.S.S. experiment [40]. Accordingly, the sparser 2B array layout optimised for the rarer events at the high end of the energy range, requires longer to collect similar suitable calibration event statistics to the more compact 2A array layout.

Although there was a small bias seen at large asymmetries for some MST pairs, this did not adversely affect the resulting overall calibration, as demonstrated by the excellent agreement shown in figure 4.18. Some slight bias is seen for those telescopes with particularly high or low

Array Component	2A	2B
LSTs	0.2%	0.5%
MSTs	0.9%	0.7%
SSTs	1.2%	2.8%
Full array	1.7%	2.5%

Table 4.4: Root Mean Square percentage residual for different arrays and components after simulations corresponding to approximately 10 hours (2A) or 13 hours (2B) of data on a source with 10% of the γ -ray flux of the Crab Nebula (over the energy range 50 GeV – 100 TeV), adopting a spectrum as measured by the H.E.S.S. experiment [40]. These percentage residuals are calculated for each subsystem independently. The full array value corresponds to figure 4.18, after all subsystem scaling factors have been applied.

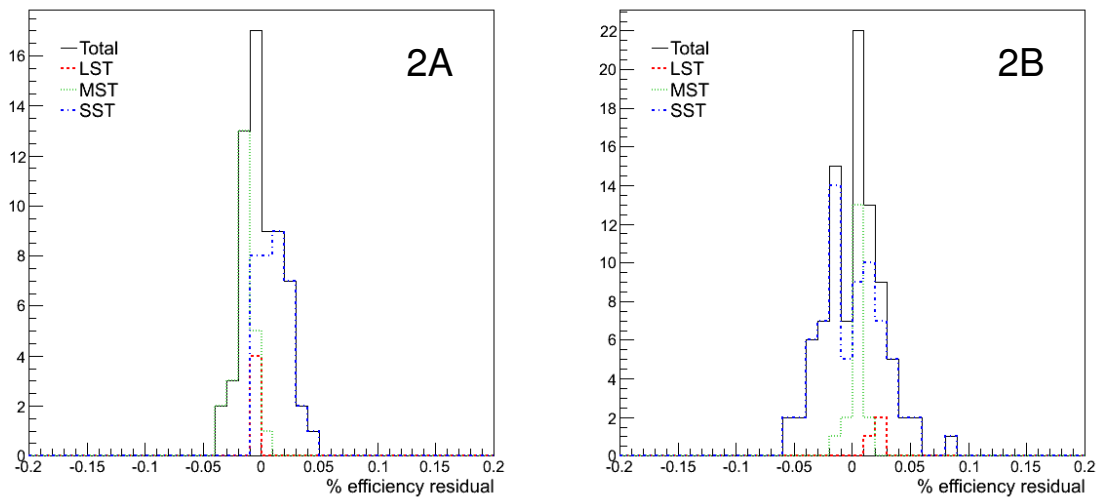


Figure 4.19: Distribution of the residuals in the recovered optical efficiencies as shown in figure 4.18, more clearly illustrating the slight bias remaining between subsystems and the spread. Left: For the 2A array layout, the MST and dc-SST subsystems show systematic shifts to negative and positive residuals respectively. Right: In the 2B array layout, the spread of sc-SSTs is much broader than for the dc-SSTs of layout 2A. Whilst both the MST and SST subsystems are well centred on zero, the LSTs exhibit a slight shift.

efficiencies; this is due to reconstructing the event energy from lookup tables with all telescope efficiencies set at 70% of nominal value, quite far from the true value in these extreme cases; representing deviations $\sim O(20\%)$ in optical efficiency. Nevertheless, good performance is seen for all telescopes within this range. In practice, this calibration would be performed in an iterative manner, with lookup tables generated based either on telescope efficiencies obtained with a first pass attempt, calibration from the previous month or from a muon calibration, thereby reducing the influence of these biases. The calibration and maintenance of reference values, especially in the case of run-wise simulations, would be essentially continuous, such that large discrepancies should not routinely occur.

Additionally, a small systematic bias in the scaling between telescope subsystems is also seen in figure 4.19, despite adjusting the scaling factors for being more heavily weighted towards telescopes in more densely packed regions of the array. This is particularly apparent for the 2A array layout on the left of figures 4.18 and 4.19, where the recovered MST efficiencies lie systematically below the true values with negative residuals, yet the recovered dc-SST efficiencies are systematically above the true values with positive residuals.

In the case of the 2B array layout, larger scatter was seen in the SSTs than for 2A, due partly to the reduced mirror size (4 m in comparison to 7 m), but also due to the wider separations between SSTs reducing the stereo trigger rate and event statistics. Nevertheless, a precision of $< 3\%$ is still achieved on these SSTs, with the MST subsystem calibrated to $< 1\%$ and the LST subsystem precision level limited by a systematic offset from the scaling ratio. As expected, a higher level of accuracy is achieved with the more compact 2A array than for 2B, due to the larger event statistics occurring with lower telescope separations. With the amount of γ -ray showers used for this calibration, the remaining systematics in the method are already the dominating factor in the level of precision obtained. From figure 4.19, it can clearly be seen that all telescopes are individually calibrated to $< 10\%$ with this method, the majority to $< 5\%$. This meets the CTA performance goal of 5% systematic uncertainty on the individual telescope measurement of the absolute Cherenkov light intensity [74], whilst the SSTs may struggle to achieve this with alternatives such as the muon calibration.

4.6.6 Other Studies

Cross Calibration on Hadronic Background

All results presented here so far are for γ -ray events only, whereas in practice IACT arrays suffer from a huge hadronic background. To mitigate this, γ -hadron separation procedures are routinely performed, such as the use of image shape cuts. In practice, no γ -hadron separation is perfect, and, especially in the case of observations of faint, transient or as yet undetected sources, the capability to perform the cross calibration on low γ -ray content (or diffuse γ -ray) data is highly relevant. Corresponding proton simulations were run using the same telescope configurations; assuming that the hadronic background follows the Cosmic Ray spectrum, these corresponded to an observing time of just a few seconds.

Applying shape cuts based only on information from the two telescopes being compared in each pair measurement results in the selection of γ -like subshowers, in which case systematics from the poor performance of the energy reconstruction dominate. In a more realistic background rejection scenario, shape cuts are applied based on information from all triggered telescopes to select γ -like hadronic showers. This improved background rejection leaves just $\sim O(10^{-3})\%$ of 7.95×10^9 simulated events passing cuts. Despite this, encouraging results were obtained, with a precision of 11% (13%) obtained for the MST subsystem of layout 2A (2B), whilst for the LST (much better background rejection) and SST (much lower trigger rate) subsystems, meaningful conclusions on the efficiency cross calibration could not be drawn from the surviving statistics. Better precision could in principle be obtained from hadronic events, if the energy reconstruction is done based on lookup tables generated from hadronic simulations. Despite this, encouraging correlation in the asymmetries was seen, as shown in figure 4.20. The residual RMS on the hadronic simulations (no γ -ray showers) is quoted in table 4.5.

Simulating sufficient hadronic background to achieve the same level of precision as that quoted for γ -rays in table 4.4 is currently prohibitively expensive in computing time and memory. However, once data taking with the first CTA telescopes commences, the overwhelming hadronic background will provide ample opportunity for a thorough characterisation of this procedure prior to its final implementation on the full array. The image size asymmetry procedure as outlined in [71], may also be used as an additional cross-check.

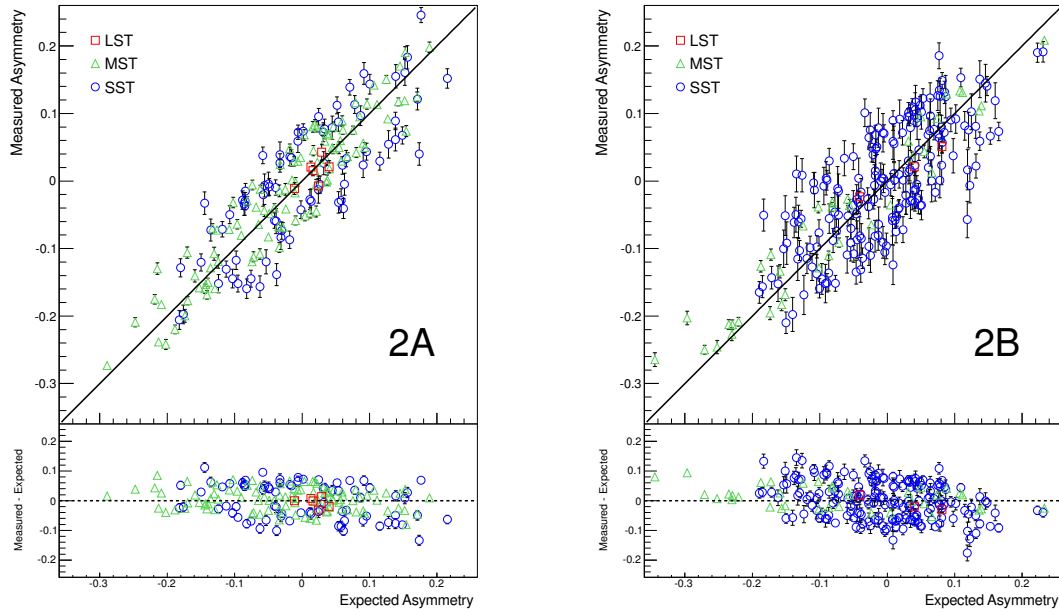


Figure 4.20: Measured asymmetry against expected asymmetry as per figure 4.17, except for the case of hadronic simulations only. A larger spread of asymmetries is seen as expected, especially for the SSTs.

Array Component	2A	2B
LSTs	1.3%	2.7%
MSTs	11.7%	12.8%
SSTs	25.0%	30.2%
Full array	21.3%	27.9%

Table 4.5: Root Mean Square percentage residual for different arrays and components after hadronic simulations as described in section 4.6.6 (compare to table 4.4).

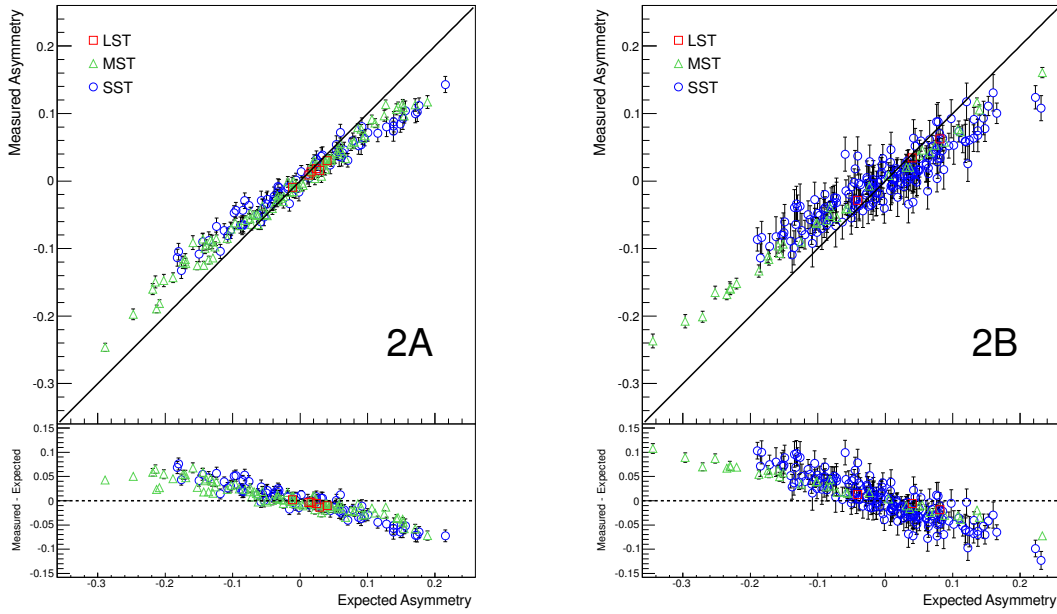


Figure 4.21: Measured asymmetry against expected asymmetry as per figure 4.17, except for the case of a distance dependent bias in the energy reconstruction applied. The change in slope from perfect agreement clearly indicates the presence of a biased energy reconstruction.

Systematically Biased Energy Reconstruction

The robustness of the algorithm also needs to be tested under realistic cases, such as the performance in the presence of systematic biases. To investigate the effects of a biased energy reconstruction on the performance of this calibration algorithm, a distance, $d(\text{m})$ dependent energy bias ($E \rightarrow E \times (200/d)$) was imposed. This had the effect of considerably overestimating the energy of showers near to the telescope, and underestimating the energy of showers falling further away. Retaining all other cuts as previously defined, the resulting distribution of measured against expected asymmetries between telescope pairs is shown in figure 4.21.

Essentially, the trends shown in figure 4.21 are unsurprising; if the energy reconstruction is biased, then the bias propagates through the reconstruction chain to the results from the cross calibration, which are biased to the same degree and in the same sense. (That is, they are underestimated at high efficiencies, corresponding to high energies and impact distances $\gtrsim 200$, and overestimated at low efficiencies, corresponding to low energies and nearby events $\lesssim 200$.) It is important to note that in this test no additional cut on the energy bias was imposed, instead this applied bias was treated as an unknown systematic of the reconstruction. The residual RMS on this biased MC is quoted in table 4.6.

Iterative Calibration Approaches

In practice, one could envisage using information from a first pass calibration to correct for discrepancies between the true telescope efficiency and that simulated, in order to reduce the mismatch in reconstructed energies. This may be done by implementing a per telescope correction factor, which corrects the single telescope efficiency back towards the mean efficiency of all telescopes. Reconstructed energies E_t then become modified such that:

$$E_t \rightarrow E_t \times \frac{\varepsilon_{\text{avg}}}{\varepsilon_t}, \quad (4.6.4)$$

Array Component	2A	2B
LSTs	0.9%	1.6%
MSTs	3.9%	5.7%
SSTs	5.0%	6.4%
Full array	4.7%	7.3%

Table 4.6: Root Mean Square percentage residual for different arrays and components after simulations as described in section 4.6.6 with an energy bias applied (compare to table 4.4).

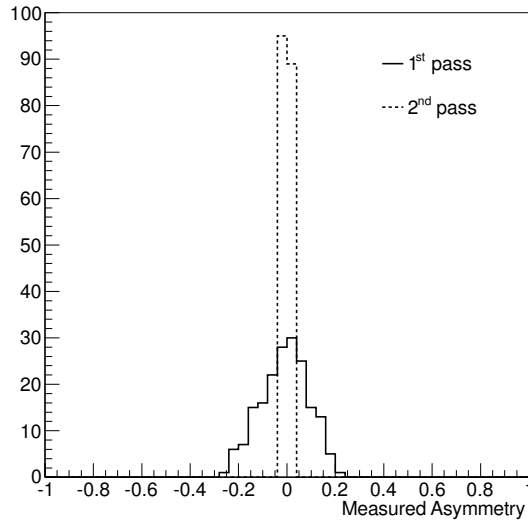


Figure 4.22: Distribution of measured telescope pair energy asymmetries from a first pass of the cross calibration, and from the second pass using a per telescope correction factor, given by equation 4.6.4. The energy estimations adjusted for optical efficiency variation in the second pass drastically reduce the spread of energy asymmetries.

where ε_t is the individual telescope efficiency found from the first pass minimisation, and ε_{avg} is the average of all telescope efficiencies found from the first pass. This correction accounts for the differences in telescope optical efficiencies, and should reduce the energy asymmetry seen between different telescope pairs. Figure 4.22 shows the reduction in measured energy asymmetry after applying a correction as shown in equation 4.6.4 based on the recovered telescope efficiencies.

4.6.7 Conclusions on Cross Calibration for CTA

Cross calibration of telescope response efficiencies through the use of γ -ray images has been shown to be a robust approach enabling an independent calibration of many different hardware technologies. Relative calibration through pair-wise comparisons ensures that multiple independent measurements over-determine the system of unknown parameters, leading to an overall precision at the 1% – 3% level after reasonable data collection times. This is within the CTA performance requirements on the telescope optical efficiency calibration for all telescope types [74]. A slight bias was seen in energy asymmetry measurements involving telescopes with efficiencies quite far (up to 30%) from the mean value used in the lookup tables. However, this was not seen to bias the response efficiencies recovered from this calibration procedure significantly. This level of discrepancy between the true telescope response efficiency and the reference value in

the lookup tables is unlikely to be encountered in practice, as regular monitoring should ensure that telescope response efficiencies remain fairly well known, with lookup tables being produced as required to more closely match the telescope parameters. From section 4.6.5, a tolerance level of $\sim \pm 20\%$ is implied; yet experience with H.E.S.S. (section 3.7.2) has found a more conservative tolerance level of $\sim \pm 5\%$ for H.E.S.S. II ($\sim \pm 10\%$ for H.E.S.S. I).

This method is capable of testing linearity under various intensities and intrinsically uses the correct input light spectrum, whereas the received light yield from muons is tied to that of a minimum ionising particle and has a slightly different Cherenkov light spectrum due to the difference in the production altitude of the Cherenkov light (see also chapter 3). Application of this method to data taken under various zenith angles and observing conditions would help eliminate possible angular or wavelength dependencies of the response coefficients.

Further studies of the robustness of this approach could include various realistic scenarios of systematics (already the limiting factor in the level of precision obtained), such as a gradient in response efficiencies over an array, or of varying telescope optical throughput efficiency degradation rates. Situations involving biases due to the performance of the energy reconstruction can also be imagined, the influence of which merits further investigation. As the response efficiencies recovered via this procedure are relative, it is envisaged to be used alongside the other calibration methods. Regardless of final implementation, this cross calibration procedure offers an ideal complement to the muon calibration for the next generation Cherenkov Telescope Array. In principle, such a method could be applied to other air shower physics experiments comprising multiple detector types situated at the same site.

The contents of this section 4.6, with the omission of sections 4.6.1 and 4.6.6, have been separately published at [79].

5 Complementarity of Optical Efficiency Calibration Methods

In chapters 3 and 4, two different methods of optical efficiency calibration for IACTs were presented. Both methods achieve this calibration from the data itself rather than requiring additional hardware, mitigating any systematic uncertainties arising from external calibration devices. This chapter will address the issue of complementarity of the two methods, covering their respective advantages and disadvantages, and outlining how they may be envisaged to operate in harmony with one another.

The difference in the wavelength distribution of Cherenkov light produced by muons and by γ -rays (see figure 3.6 in chapter 3) is a key motivator for use of the cross calibration approach. As the latter is done using γ -ray events themselves, it intrinsically uses the correct wavelength distribution for calibrating the γ -ray energy scale. Nevertheless, the muon calibration is invaluable as a means of absolute calibration of IACT optical efficiencies, given that the cross calibration approach is only permissible in multiple telescope systems. Indeed, the cross calibration can be expected to perform better with increasing numbers of telescopes, permitting more independent measurements between telescope pairs.

Whilst the cross calibration is a robust approach for relative calibration of individual telescopes in array systems, it lacks an absolute normalisation which must be given independently. In the case of no additional information, this normalisation may be provided either by setting the efficiency value for one telescope to 1 as a reference, measuring all other telescope efficiencies relative to that reference; or by arbitrarily normalising such that the average efficiency of the system is equal to 1 (methods (a) and (b) in section 4.2.2). The former approach would be appropriate in case of interest in the relative degradation rates of individual telescopes and/or of identifying problematic outliers. The latter approach would be more appropriate if the cross calibration is primarily used for correcting the relative efficiencies of individual telescopes, in a sense “flat-fielding” the array in a manner analogous to flat-fielding of the camera (see section 2.4.1). In practice, however, the difference is only a matter of how the mean is defined.

A possible third approach (method (c) in section 4.2.2) is to normalise to the average muon efficiency parameter; the telescope efficiencies obtained via the two methods may then be checked for agreement. Perfect agreement would be indicated by a best fit line with gradient of 1, however an additional consideration is that the optical efficiency of the telescope may vary chromatically (as a function of wavelength), which may lead to an otherwise unaccounted for discrepancy between the efficiencies found using the two methods.

Cross calibration is a useful probe of how well the reference set of Monte Carlo (MC) or of lookup tables for the energy estimation reflects the actual status and condition of the array. Absolute degradation in the optical efficiency of an entire system of telescopes is better monitored by the muon calibration. If, instead of arbitrarily normalising the system average to 1 it is normalised to the average muon efficiency after cross calibration, then the level of agreement

between the two can provide an indication of the systematic uncertainties remaining on the optical efficiency calibration.

5.1 H.E.S.S. Optical Efficiency Calibration

The evolution of the optical efficiency of the H.E.S.S. array is described by a series of MC phases, each of which encodes an optical efficiency value for each telescope. For each phase, a set of corresponding lookup tables for the analysis is produced (see chapter 2). Typically, these are redefined only when there is a substantial change in the optical efficiency, $\sim O(5 - 10\%)$, although the second phase of the H.E.S.S. array is more sensitive to these changes due to the large difference in the rates of change of the CT5 and CT1-4 efficiencies, as well as the corresponding change in effective area (see section 3.7.2). As the optical efficiency acts as a global scaling factor in equations (2.4.2), it is sensitive to changes in many different system components. Reasons for defining new MC phases have previously included: recoating of telescope mirrors, adjustment of the camera gains, cleaning of the camera Winston cones and after a period of general degradation. A new MC phase was required following the mirror recoating of each individual telescope, as the lookup tables are sensitive to the status of the overall array, not just individual telescopes.

The optical efficiency found for each run from the muon calibration is used to define a correction factor back to the relevant MC phase, as described in section 3.2.2, which is applied to the event-wise energy estimates for that run. This is because the energy estimates are taken from the lookup tables which were generated assuming certain values for the optical efficiencies. If the optical efficiency obtained from the muon calibration for the current run differs from the simulated efficiency in the relevant MC, a correction needs to be applied, which is assumed to be linear (generally a good assumption, see figure 3.15). This calibration method is applied as standard within the H.E.S.S. analysis chain.

The cross calibration method is relatively new to H.E.S.S., and was not historically applied as part of the standard analysis chain. Instead, it can currently be run independently generating run-wise output for future reference (such as checking for improvements with new MC phases), or it can alternatively be run as part of any analysis as a diagnostic cross-check.

5.1.1 Correlation of the Muon Efficiency with Image Size Cross Calibration

As the muon efficiency is calculated based fundamentally on the pixel charges, independent of any lookup tables, it is expected to correlate with the relative efficiencies as found from the image size cross calibration. This latter method, described in section 4.2.2, returns a system of relative efficiency values with a mean of 1 (method (b) by default). In order to compare the output of the two methods directly, the mean muon efficiency for each run is used to scale the relative response efficiencies found by the cross calibration, such that the results are normalised to each other (method (c)).

These two approaches should correlate, as was shown in section 4.2.4 in chapter 4 on MC and as is shown in figure 5.1 on H.E.S.S. data taken on the Crab Nebula. The correlation is shown to be slightly off for the H.E.S.S. phase II data, which is unsurprising given the challenge of comparing the image sizes between different telescope sizes. As the image size is rescaled by an expected ratio in pair comparisons with CT5, it may be that this expected ratio (found from MC) is no longer accurate for the time period under consideration.

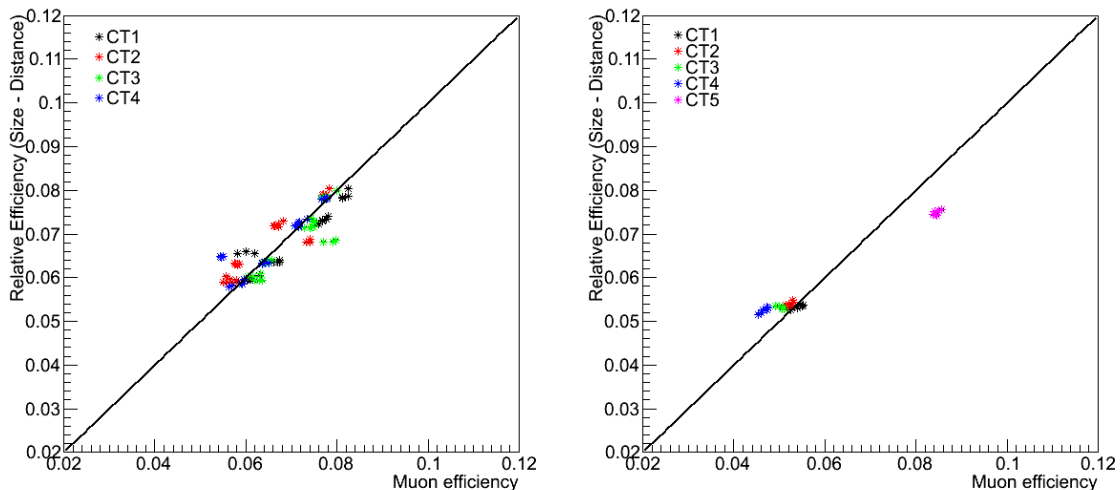


Figure 5.1: Optical Efficiency recovered using the cross calibration with image size and the muon calibration approaches from Crab Nebula data taken with H.E.S.S. during the first (left) and second (right) phases of the experiment.

5.1.2 Combination of the Muon Efficiency with Reconstructed Energy Cross Calibration

Under standard analysis procedures, the relative efficiencies obtained from the reconstructed energy cross calibration would not necessarily be expected to correlate with the muon efficiency. Discrepancies between the reference MC and the muon efficiency are accounted for by the muon correction factor, as described in section 3.2.2. This correction factor is then applied to all energy estimates of the individual telescopes prior to calculating the asymmetry in the reconstructed energy. Therefore, as the cross calibration is essentially based on the mean energy asymmetries, any pronounced differences between telescope efficiencies should already be accounted for. If the system of relative efficiencies is normalised such that the mean is 1 (method (b)), then the per telescope relative efficiencies obtained should also be compatible with 1. Figure 5.2 shows the spread of relative efficiencies obtained using the reconstructed energy cross calibration around a constant value with run number (error bars are statistical).

Deviation from a flat system of efficiencies may indicate that the muon efficiency based correction factor does not adequately account for all aspects of the variation between telescopes. Alternatively, it may indicate the presence of systematic uncertainties in the energy cross calibration procedure. Systematics may arise due to atmospheric effects (such as haziness), observational effects (such as high zenith angle) or as a result of miscalibration elsewhere in the analysis and calibration chain. In this case, the cross calibration was run on data taken on the Crab Nebula, which is at a high zenith angle for H.E.S.S. observations. This increases the energy threshold for these observations with respect to other objects (see section 4.4), also reducing the energy range available for the cross calibration, leading to a higher level of intrinsic scatter and a potential bias of the results towards high energies.

Uncertainties due to the muon efficiency and correction factor applied may be reduced by use of a nightly averaged muon efficiency value, an approach described in section 3.7.3. Implementing a night-wise muon correction factor instead of a run-wise value reduces the spread in the H.E.S.S. I results to deviations of less than 5%, whilst only making a marginal difference to the H.E.S.S. II results. This may be due to other systematic effects arising due to the comparison between CT5

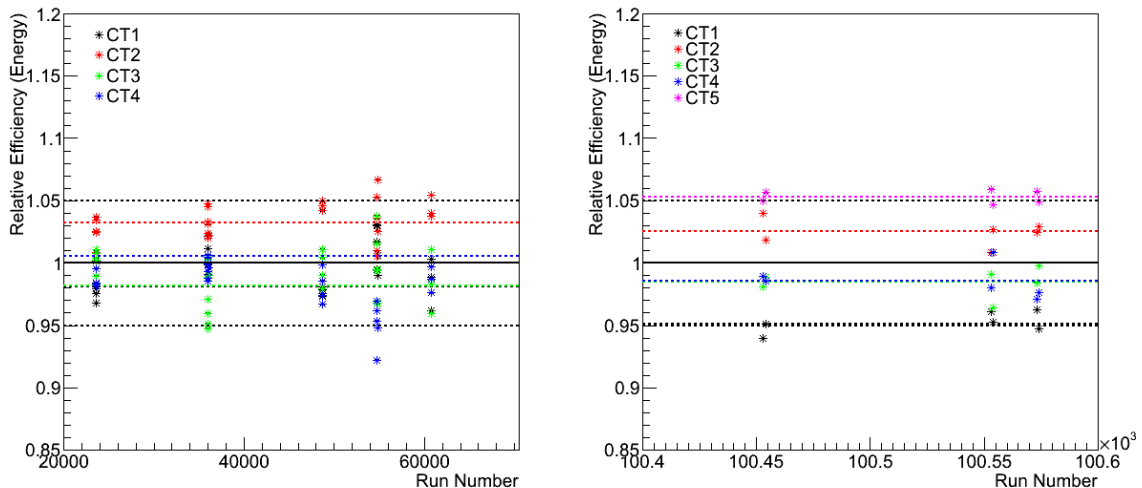


Figure 5.2: Results of the energy cross calibration over time (shown as run number of the data). After applying the muon efficiency correction factors, all telescope relative efficiencies should be within agreement of 1. To guide the eye, black lines are drawn at 0.95, 1.0 and 1.05, coloured lines are drawn corresponding to the mean relative efficiency for each telescope.

and CT1-4 telescopes dominating over effects due to the muon efficiency calibration only. Such effects could include the large optical efficiency discrepancy between the MC and the data in this time period. The MC used for this analysis was optimised for a period approximately six months before this data was taken, whilst in the meantime, the camera gains had been adjusted, leading to a known shift of 10 % or more in the optical efficiencies. This issue should be addressed with an updated set of MC, dedicated to this time period, with optical efficiencies better matched (see figure 3.30 of section 3.7).

Performing the reconstructed energy cross calibration on the same dataset but with a set of MC better matched to the true optical efficiencies, the overall spread of the relative efficiencies between the telescopes is clearly reduced in figure 5.3 from figure 5.2. With the exception of CT2, the relative efficiencies are all compatible with 1 to within a few percent. As the time period corresponding to this dataset falls towards the end of the time covered by this MC, the optical efficiencies were matched to the average over the time period, such that slight deviations are not unexpected. For CT2, it is likely that the true optical efficiency is somewhat degraded with respect to the reference, such that a relative efficiency greater than 1 is obtained. Additionally, the high zenith angle of these Crab observations may contribute some systematics in the energy cross calibration. Approximately one month after this data was taken a camera maintenance campaign to clean the Winston cones of CT1-4 improved their optical efficiencies by roughly 5-10%, and a new set of MC was defined to match this.

5.1.3 Reversal of the Implementation

A useful exercise to check the functionality and implementation of the two cross calibration approaches is to reverse the implementation. That is, that the muon efficiency based correction factor is applied directly to the image size rather than to the reconstructed energy. One would then expect that the variation in relative efficiencies obtained using the image size approach are in agreement with a constant, and that the relative efficiencies obtained via the reconstructed energy approach would correlate with the muon efficiency. A major caveat of this approach,

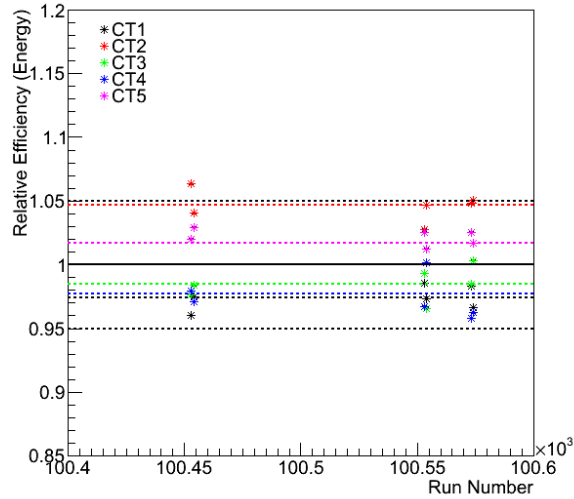


Figure 5.3: Energy cross calibration on the same dataset as in figure 5.2, but using an updated muon phase to better match the true optical efficiencies. The overall spread of coefficients has clearly been reduced. Lines are drawn to guide the eye in the same manner as in figure 5.2.

however, is that the correction applied in this manner is inherently nonlinear. Image size is typically calculated after image cleaning, such that pixels with low amplitude signals lying below the cleaning threshold do not contribute to the image size. Quantifying the magnitude of the lost contribution is nigh-on impossible without the use of more advanced fitting techniques. This is also dependent on the telescope optical efficiency, as well as the quantum efficiency of the individual pixels.

Figure 5.4 shows the spread of relative efficiencies obtained using the image size approach around a constant value with run number. For H.E.S.S. I, the spread is significantly less than for the energy cross calibration approach. This is unsurprising, as this comparison is semi-independent of all systematic uncertainties arising from the MC, using only information from the raw image. For H.E.S.S. in its second phase, however, the agreement is worse, due predominantly to the different reflector dish sizes of CT5 and CT1-4, which lead to a large difference in intrinsic image size. This is partly accounted for in pair-wise comparisons between CT5 and one of CT1-4 by scaling the image size of one telescope by the expected size ratio, as described in section 4.3.1. Nevertheless, the aforementioned caveat of the non-linear scaling of the cleaned images to the true image size could affect comparisons between different sized telescopes more significantly than comparisons of like with like.

With no muon efficiency correction factor applied to the reconstructed energy estimates, the agreement with 1 would be expected to significantly degrade, as seen in figure 5.5. In the absence of the muon correction, the expectation is that the relative efficiencies obtained by the reconstructed energy cross calibration approach correlate with the muon efficiencies. However, due to the fact the the energy estimates are taken from a reference set of lookup tables generated from MC, these energy estimates already compensate for a certain level of inter-telescope variation. The two methods can only be expected to correlate fully in the case that the efficiencies of all telescopes in the MC used to generate the lookup tables have the same value (no inter-telescope variation). For H.E.S.S. I, such a set of MC exists, with all telescope efficiencies set to 70 % of the nominal value. Using this MC set, there is indeed correlation between the two approaches, as seen in figure 5.6. For H.E.S.S. II, there is no such set of MC; all of the available

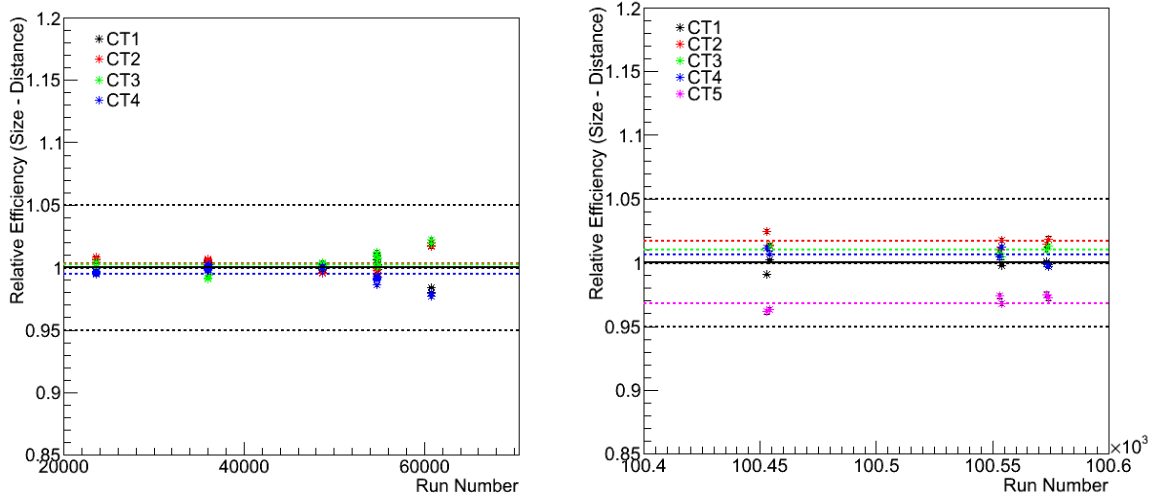


Figure 5.4: Applying the muon correction to the image size rather than reconstructed energy, the cross calibration results should be within agreement of 1 for all telescopes. The results are improved over the energy cross calibration for H.E.S.S. I. For H.E.S.S. II, the performance was comparable.

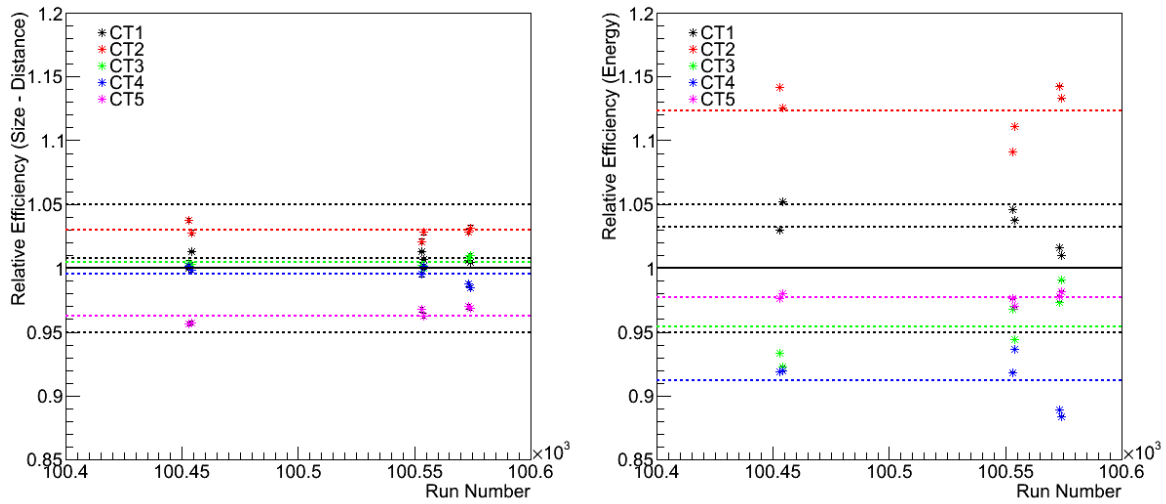


Figure 5.5: Results of the cross calibration with no muon correction applied. Left: the image size cross calibration (with reversed implementation) seems to still perform comparatively well. Right: the energy cross calibration performance is significantly degraded to that shown in figure 5.2.

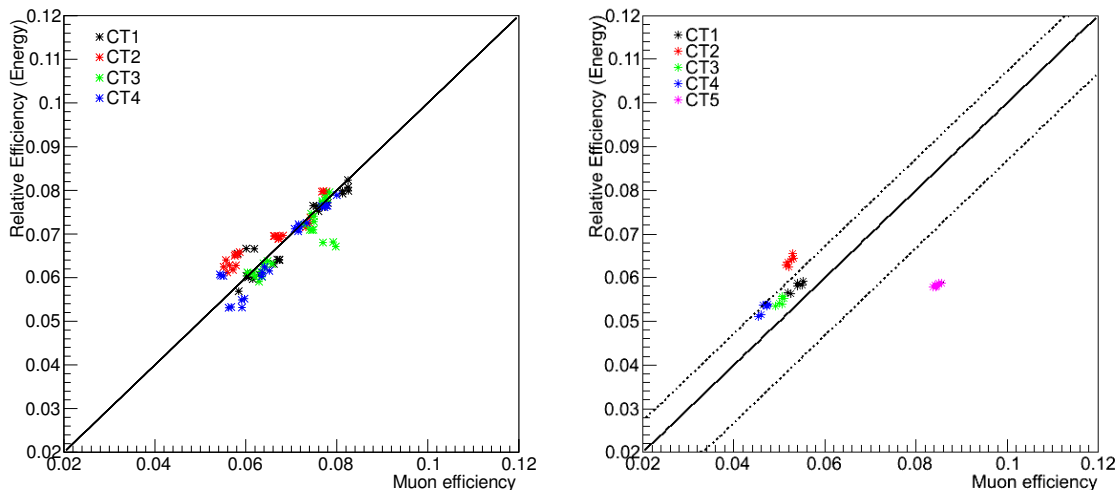


Figure 5.6: Optical Efficiency recovered using the cross calibration with reconstructed energy and the muon calibration approaches from Crab Nebula data taken with H.E.S.S. during its first (left) and second (right) phases of operation. No muon correction was applied to the reconstructed energies. The expected level of deviation due to the MC reference optical efficiencies not being the same for all telescopes in phase 2 is indicated by the dashed lines, for CT4 (above) and CT5 (below).

sets account for variation between the telescopes - this is partly due to the difference in age of the CT5 mirrors with respect to the mirrors of CT1-4, as the older mirrors of CT1-4 are significantly more degraded than those of CT5, such that there is no real need within the standard analysis for a MC set with all telescope efficiencies set to the same value. The expected deviation due to the variation already accounted for by the MC is shown by two dashed lines, for CT4 and CT5, falling above and below the reference $y = x$ line respectively. Additional deviation may arise for the same reasons as outlined in section 5.1.2; that the reference values of the telescope efficiencies as stored in the MC are quite far from the true values for this time period. This issue should be resolved with a better matched set of MC, as described in section 3.7. The remaining offset of CT5 seen in figure 5.6 is of roughly the same order as that seen for the same dataset with muon correction applied in figure 5.1.

5.2 Scheme for CTA Optical Efficiency Calibration

Studies presented in sections 3.8 and 4.6 have demonstrated how both the muon calibration and cross calibration methods correlate with expectation in dedicated Monte Carlo studies for CTA. However, the issue of whether the results from the two calibration methods can be expected to correlate with each other depends on the implementation. As the calibration scheme for CTA is currently under development, with details of the implementation not yet finalised, a possible approach towards practical application of these two major optical efficiency calibration methods in conjunction with each other is discussed below.

5.2.1 Implementation of Calibration Methods

In practice, the implementation of correction factors in CTA is to be avoided. One would hope that regular monitoring with both approaches will ensure that corrections are not required, or are only minor. During the commissioning phase of CTA, a reference set of Monte Carlo may be

required. Discrepancies between this reference set and the true status of individual telescopes should be identifiable on a short timescale with the muon calibration. As the size of the array grows, discrepancies between MC and data affecting the whole system can be monitored using the cross calibration. One may easily expect that newer telescopes, added later, will typically have higher optical efficiency values than those installed earlier, which will have already started to degrade before the newer telescopes are added. Depending on how the array is constructed, this may lead to a bias in the form of a gradient in optical efficiencies across the array, or of one particular telescope type being systematically offset (at higher or lower optical efficiencies) than other telescope types. The latter case may also occur due to differences in the material components used for different telescope types, which may degrade at different rates.

By the time the full array is in operation, the current state of each telescope and of the array as a whole should be known and understood to a reasonable degree of precision. For each run of data taking, the state of the array during that run will be simulated precisely. An appropriate suggestion for the processing of a given observation run with respect to the optical efficiency is as follows:

1. Initial calibration, image cleaning and first pass image identification is performed.
2. The muon calibration is performed on tagged muon events.
3. If the muon calibration shows a discrepancy with the known optical efficiencies (from previous data) for each telescope, these are adjusted.
4. The image size cross calibration is performed on γ -like events simultaneously to steps 2 and 3, for each telescope type separately, to check the optical efficiencies found.
5. The observation run is then simulated with these optical efficiencies as input.
6. The energy cross calibration is performed per night, or per run on bright sources. Any systematic offsets between telescopes or telescope types is identified.
7. If significant offsets are found, the run is re-simulated. Otherwise, minor adjustments are made for the next run or the next night.

In this manner, both large systematics and multiple simulations should be avoidable. After the commissioning stage, provided the cross calibration is performed regularly, any necessary changes should be minor, as illustrated by the difference in root mean square residuals of telescope optical throughput efficiencies following a first and second pass of the cross calibration procedure, shown in figure 4.22.

5.3 Further Applications

5.3.1 Calibration of Other Parameters using Muons

Depending on the specifics of the experiment, use of muons may be expanded beyond the global telescope-camera system optical efficiency. Over a longer period of time, sufficient muons may be observed to provide some coverage over the whole camera. With knowledge of the efficiency from each event and the pixel participation within each image, the mean reconstructed efficiency per pixel may be used for a flat-fielding measurement. That is, it should become noticeable whether the mean efficiency obtained for images containing a particular pixel deviates significantly above

or below the mean across all pixels. This has been demonstrated previously with H.E.S.S. in [59] and [62], however, the approach cannot compete with existing devices for flat-field measurements, and serves to offer a useful cross-check. Due to the cuts implemented on muon events to ensure that they are well contained within the camera, regions of the camera towards the centre or the edges would be poorly covered by muon events. Using this approach for flat-fielding on data would be better achieved with standard γ -ray events.

MAGIC, another IACT experiment, also utilises muon events for optical efficiency calibration. They assume the point spread function (PSF) of the instrument to be the dominant effect contributing to changes in the muon ring width, with natural contributions (such as variation in the refractive index and scattering) expected to remain approximately constant over time (see section 3.1.2). As the width of the muon ring is a free parameter of the fit, monitoring of this parameter provides information about the PSF of the instrument. Nevertheless, H.E.S.S. does not use the fitted ring width for this purpose, assuming that the dominant effects affecting the ring broadening remain intrinsic to the shower, namely ionisation losses and multiple Coulomb scattering, with the PSF contributing to second order.

With CT5, the time of maximum of the Cherenkov light pulse within the 16 ns integration window is also recorded. It is known that signals from muon events peak earlier and have a narrower distribution than signals from gamma-ray showers. The FACT collaboration, which uses SiPMs for which the degradation rate is much slower than that of standard PMTs, use muons primarily for timing calibration. Efforts in exploiting this information for image cleaning have started within the H.E.S.S. collaboration, and similar approaches may be of significant interest to CTA, where the expected data rate is much larger, such that methods of reducing data to times or regions of interest at trigger level are important.

5.3.2 Cross Calibration of Other Variables

The underlying principle, of comparisons of an invariant parameter between telescopes, may be extended to other applications (see appendix A). These include calibration of the overall rate of Cosmic Ray events, of the telescope pointing precision and of the event timing accuracy, which are outlined in sections A.1, A.2 and A.4 respectively [80, 39]. Additionally, pairwise comparisons between telescopes enable measurements of the Cherenkov light pool radial distribution to be made, as done for H.E.S.S. in section A.3 [73].

6 The Pulsar Wind Nebula HESS J1825-137

6.1 Introduction to Pulsar Wind Nebulae

6.1.1 Supernovae and Neutron Stars

Stars such as the sun generate their energy output from nuclear fusion within their cores, providing thermal energy and pressure which supports their massive size against inwards collapse, maintaining a state of hydrostatic equilibrium. Initially, this process is almost entirely fusion of Hydrogen into Helium. However, eventually the supply of Hydrogen within the stellar core dwindles, the rate of stellar fusion decreases and the star cools and contracts. The contraction of the star increases the temperature and pressure of the core again, until the conditions are sufficient to start nuclear fusion of Helium into Carbon and Oxygen within the core. During the contraction, gravitational potential energy is released, heating up the star and igniting Hydrogen burning in a shell layer around the core [2, 8].

Stars of similar mass to the sun will become red giants at later stages in their evolution, which have an expanded, convective envelope. Eventually, the outer envelope of the red giant is lost in a series of shell flashes or pulsations, leaving just the degenerate core behind. This dense core is supported against collapse by electron degeneracy pressure for core masses up to $\sim 1.4M_{\odot}$ (the Chandrasekhar limit).

Massive stars of around $8-40M_{\odot}$ have sufficiently high core temperatures and pressures, that nuclear fusion of heavier elements continues beyond Helium. Burning of Carbon, Oxygen and Silicon ignites sequentially, continuing in a series of concentric shells (along with the production of many other nuclei), ultimately generating a predominantly Iron core. With increasing nuclear mass, the amount of energy released in the fusion process decreases, such that burning occurs more rapidly to provide sufficient energy output to internally support the star. Hence the time required for a star to use up the available fuel also decreases, to a timescale of just days for Silicon burning to complete. As Iron has the highest binding energy per nucleon, nuclear fusion beyond Silicon is energetically unfavourable and the mostly Iron core grows.

At this stage, photons produced in earlier fusion reactions in the core have sufficient energy to disintegrate the heavy nuclei back into protons and neutrons. It becomes energetically favourable for free electrons, which had previously provided the electron degeneracy pressure supporting the star from collapse, merge with the protons to form neutrons, producing neutrinos in the process. These neutrinos are able to carry significant amounts of energy away from the core, due to their low interaction rate and huge number. Due to the vast reduction in the electron density, the pressure in the central core is lost and the core collapses inwards faster than the speed of sound (p.534 [2]). The abrupt slowing of the collapse as the core becomes supported by neutron degeneracy pressure sends shockwaves into the outer layers of the star. This, together with the energy deposited by the neutrino interactions in the dense infalling material during the collapse,

is sufficient to cause a supernova explosion. In this type of core-collapse supernova, the outer layers are thrown off by the shockwaves, leaving just the core behind. The extent to which this collapse continues depends on the mass of the progenitor star. Heavy stars with initial masses $\lesssim 25 M_{\odot}$ generally leave remnants supported by neutron degeneracy pressure, termed neutron stars; incredibly dense objects (similar to that of an atomic nucleus) composed primarily of neutrons. The neutron star surface is mainly comprised of heavy nuclei, electrons and ions; the neutron interior is likely to be primarily free neutrons, protons and electrons, in some superfluid or relativistic state. However, the core composition of neutron stars remains highly uncertain, with exotic particle mixtures comprising pions and kaons or quark matter being likely.

For the most massive stars, even neutron degeneracy pressure (and strong force repulsions) are insufficient to stop the inwards collapse, which would continue to form stellar mass black holes.

During the collapse process of Neutron star formation, both the angular momentum L and the magnetic flux Φ_B of the star are conserved, $L = \text{const.}$ and $\Phi_B = \text{const.}$, where the angular momentum varies with the moment of inertia I and rotation speed ω as $L = I\omega \propto R^{-2}$, and $\Phi_B = BR^2$ is a function of the magnetic field strength B . Consequently, as the radius R and size of the object dramatically decreases during the collapse, so too does the rotation period, with a correspondingly dramatic increase in the rotation speed ω and the magnetic field strength B .

The existence of Neutron stars as compact stars produced in supernova explosions was first predicted by W. Baade and F. Zwicky in 1934; at the same time, they also coined the term supernova, and postulated that such supernova explosions are a plausible origin for the acceleration of energetic cosmic rays [81, 82]. Current understanding remains in line with this; neutron stars have been discovered near the centre of supernova remnants, and supernova are still believed to be a major source of energetic cosmic rays. The first neutron star discovery, however, came in the form of a pulsar, more than 30 years after neutron stars were first predicted.

6.1.2 Pulsars

Pulsars were discovered as regular pulses in radio signals, by Jocelyn Bell and Antony Hewish in 1967, the first pulsar detected being PSR B1919+21 with a period of 1.337 s [83].¹ Until that moment, no such precise and fast pulsating objects in astrophysics were known. The majority of pulsars have periods of between 0.25s and 2s although a population of millisecond pulsars (with periods $\sim O(10^{-3})$ s) also exists. Pulsars are now understood to be rapidly rotating Neutron stars, due to two key pieces of evidence; if their density was less than similar to that of a Neutron star, then the object would disintegrate at the observed rotation speeds; additionally pulsars have been found at the centres of nearby supernova remnants, encouraging their interpretation as the remains of massive stars.

At the time of formation, however, the supernova ejecta and subsequent collapse process typically does not proceed uniformly in all directions, resulting in the Pulsar acquiring a net drift away from its original birth site. From the proper motion of the pulsar on the sky (change in apparent position with time), the transverse velocity of this drift can be obtained if the distance to the pulsar is known, although typically the component of the pulsars motion along the line of sight is not known, such that although the absolute velocity cannot be determined, the measured velocity forms a lower limit.

¹Hewish was later awarded the 1974 Nobel prize for the discovery of pulsars, jointly with Martin Ryle for his contributions to radio astronomy [84].

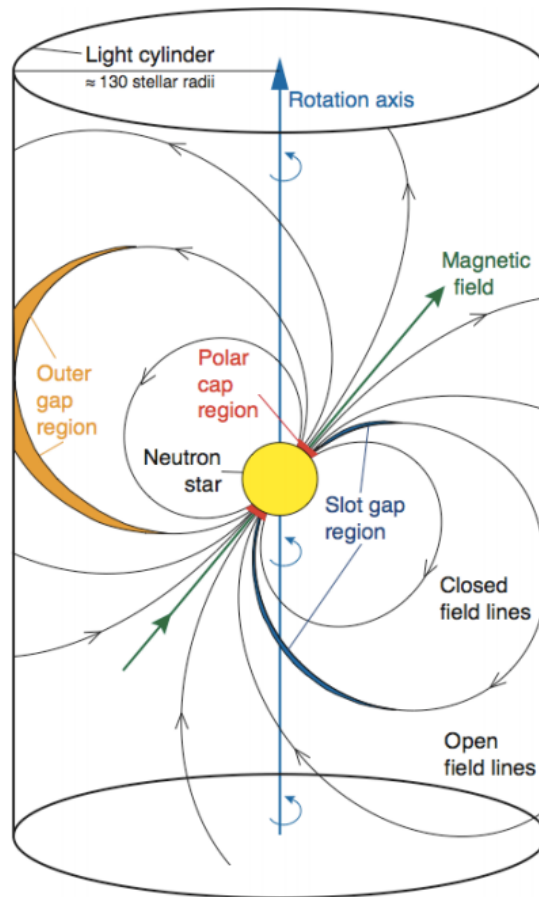


Figure 6.1: Schematic of a pulsar showing its magnetic field lines, with the magnetic field and rotation axes misaligned. Particles accelerated along the open field lines may escape at the light cylinder, at which they would have to travel at the speed of light to continue co-rotating with the Neutron star (figure taken from [85]).

Pulsar Models

The characteristic pulsed signals, from which pulsars get their name, are generally attributed to jets of emission, originating from the poles of the pulsars magnetic field, swinging past the Earth. As the pulsar rotates, the lines of magnetic field rotate with it and the rotating magnetic field will generate an electric field on the surface. Charged particles near the surface are accelerated by the electric field and become trapped by the strong magnetic field, confined to travel along the magnetic field lines only. As these charged particles move, synchrotron and curvature radiation is produced as explained in chapter 1, leading to beams of electromagnetic radiation along the magnetic field axes. Due to the misalignment of the magnetic field and rotation axes, the direction of the beamed emission changes as the pulsar rotates, leading to a pulsed signal being detected as these beams pass in the direction of Earth. The stronger the magnetic field, the more tightly aligned the emission is to the magnetic field lines; this has an observational consequence in the form of strong linear polarisation of the electromagnetic radiation from pulsars.

As the pulses of emission travel across space, the various frequencies of emission become dispersed in time, with the amount of dispersion experienced depending on the average density of free electrons, ρ_e , in the intervening medium. The greater the distance travelled and the electron density, the greater the dispersion, making the dispersion measure, DM a useful tool for estimating the distances to pulsars. The distance to a pulsar d can be calculated by integrating the electron density distribution over the path travelled by the light l :

$$\text{DM} = \int_0^d \rho_e dl , \quad (6.1.1)$$

where DM is in units of $\text{m}^{-3} \text{ pc}$.

Over time, the pulsar gradually slows down by losing rotational energy, primarily through the generation of a relativistically moving and magnetised wind. The rate of rotational energy loss is quantified by the spin-down luminosity, \dot{E} :

$$\dot{E} \equiv 4\pi^2 I \frac{\dot{P}}{P^3} , \quad (6.1.2)$$

where I is the moment of inertia of the pulsar, P its spin period and \dot{P} the period derivative (change in period over time). This spin-down luminosity gradually reduces over time t from an initial value \dot{E}_0 , evolving on a timescale τ_0 as:

$$\dot{E}(t) = \dot{E}_0 \left(1 + \frac{t}{\tau_0} \right)^{\frac{n+1}{n-1}} , \quad (6.1.3)$$

where n is the braking index, so called due to its characterisation of the reduction in the spin frequency Ω over time, $\dot{\Omega} = -k\Omega^n$, with constant of proportionality k . Generally, only the most powerful pulsars with $\dot{E} \gtrsim 10^{36} \text{ erg s}^{-1}$ tend to have associated TeV emitting nebulae that are detectable with the sensitivity of current instruments.

The age of the pulsar system is given in terms of P and \dot{P} by:

$$\tau = \frac{P}{(n-1)\dot{P}} \left[1 - \left(\frac{P_0}{P} \right)^{n-1} \right] , \quad (6.1.4)$$

where P_0 is the initial spin period at the time of formation, typically unknown. Assuming a value of $n = 3$ for the braking index, corresponding to energy loss purely by magnetic dipole radiation, the characteristic age, τ_c , of a pulsar can be estimated as :

$$\tau_c \equiv \frac{P}{2\dot{P}} , \quad (6.1.5)$$

assuming that $P \gg P_0$, which is not strictly true for young pulsars. Measured values of the braking index n typically lie in the range $2 - 3$, showing that the magnetic radiation may be more complex than purely dipolar, and is potentially not the only contribution to the spin-down [86]. In the case that the pulsar has a dipole magnetic field, the surface magnetic field strength can be estimated as:

$$B_p \equiv 3.2 \times 10^{19} (P\dot{P})^{1/2} \text{ G} , \quad (6.1.6)$$

with typical values for pulsars hosting PWNe falling around $\sim 1 \times 10^{13} \text{ G}$ [86].

Goldreich and Julian argued that due to the presence of this strong magnetic field on the pulsar surface, a strong electric field is generated, the parallel component of which is much stronger than the gravitational force at the surface, such that it is able to pull charged particles away from the surface [87]. This forms a particle plasma around the pulsar, within the closed magnetic field lines forming the magnetosphere.

Close to the pulsar, the plasma of charged particles co-rotates with the pulsar and the magnetic field lines. However, with increasing distance the particles must travel at ever greater speeds in order to keep up with the pulsars rotation. The distance at which the particles would have to travel at the speed of light to continue co-rotating is termed the light cylinder radius (see figure 6.1).

The location at which the emission from the pulsar originates is still a matter of debate, though generally thought to be due to the acceleration of electrons by strong electric fields in locations of reduced particle charge density. Three such locations identified as among the most suitable are: near the neutron star surface close to the magnetic pole; along closed magnetic field lines away from the poles yet close to the surface; or at the edge of the magnetosphere, where the magnetic field lines cease to be closed within the light cylinder. In the first two regions, the reduced particle density is due to the strong acceleration of particles along the magnetic field lines, whilst in the latter case the reduced density is due to particle escape beyond the light cylinder. Models pertaining to these three locations are referred to as ‘polar cap’, ‘slot gap’ and ‘outer gap’ models respectively (see figure 6.1) [88, 89, 90].²

At the light cylinder boundary the magnetic field lines become open, and the accelerated particles are able to drift away from the pulsar along the open field lines, yet retaining some of the magnetic field, leading to the formation of a highly magnetised supersonic particle wind.

6.1.3 Pulsar Wind Nebulae

Formation

Pulsar wind nebulae form in the environment around a pulsar from the particle wind leaving the pulsar environment as outlined above.³ At the time of the pulsars formation, the supernova ejecta moves outwards, shocking the interstellar medium and slow supernova ejecta, whilst the pulsar continues to travel with the drift velocity acquired at its birth. Particles escaping from the light cylinder region as part of the supersonic pulsar wind form a termination shock in the surrounding region, where medium is less dense, having been effectively evacuated due to the supernova forward shock (see figure 6.2).

As the supernova forward shock progresses, it gradually sweeps up a mass equivalent to its own, slowing down in the process and entering the so-called Sedov phase. At this stage, whilst

²These models were first proposed by Sturrock in 1971, Arons in 1983 and Cheng in 1986 respectively. See [91] for a recent review.

³See [86] for a review of the current understanding of Pulsar Wind Nebulae.

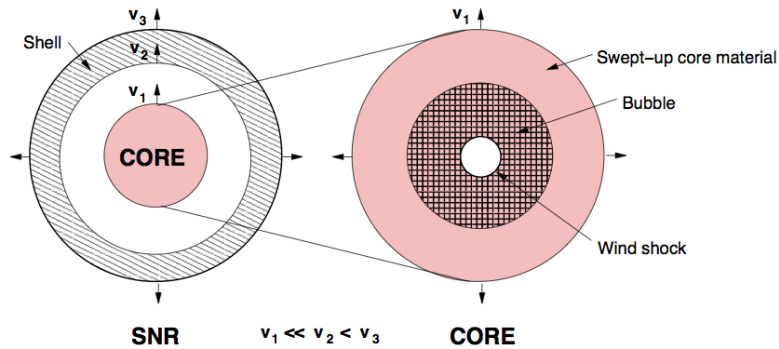


Figure 6.2: Schematic of an SNR/PWN complex system. The SNR shell expands outwards, with inner and outer edges travelling at speeds of v_2 and v_3 respectively, whilst the core material expands outwards at speed v_1 . The PWN is fully contained within the SNR bubble, the outer edge of the pulsar wind forming a shock in the SNR ejecta [92].

the supernova forward shock continues to progress outwards into the ambient medium, a reverse shock forms as the ejecta are decelerated, and starts to move inwards, back towards the birth location of the pulsar, reaching the centre of the SNR explosion in a time

$$t \approx 7 \left(\frac{M_{ej}}{10M_{\odot}} \right)^{5/6} \left(\frac{E_{SN}}{10^{51} \text{ergs}} \right)^{-1/2} \left(\frac{n_0}{1 \text{cm}^{-3}} \right)^{-1/3} \text{ kyr} , \quad (6.1.7)$$

where M_{ej} is the mass ejected in the supernova explosion of energy E_{SN} , and n_0 is the number density of the ambient gas [86, 92].

Meanwhile, the particles from the pulsar wind are accelerated at the wind termination shock, undergoing diffusive shock acceleration, gaining energy on each shock crossing (see section 1.2.1 of chapter 1). The energetic particles (mostly electrons) start to form a nebula in the immediate surroundings; at this stage, the typical particle energy within the nebula is much greater than that of a particle in the pulsar wind, and a pulsar wind nebula bubble gradually grows.

After a certain time, the reverse shock from the supernova will meet the pulsar wind nebula, leading to a crushing effect. As the reverse shock tends to return earlier from higher density regions of the ambient medium than from lower density areas, this can lead to an irregular, distorted nebula shape. Crushing of the pulsar wind nebula is accompanied by a corresponding increase in the magnetic field, causing an increase in the synchrotron energy losses of the particles, causing the highest energy electrons to lose energy more rapidly. The crushing also causes an increased pressure in the region; when this pressure surpasses that of the reverse shock, the PWN rapidly expands again. PWN systems will typically undergo several reverberations before the shock strength fades.

As the supernovae shock dissipates and reverberations cease, the pulsar wind nebula continues to form around the current position of this pulsar; by this stage, due to the pulsars net drift velocity and asymmetric crushing effects, the nebula may be significantly distorted and offset from the current pulsar position and the original site of the supernova explosion.

Relic Nebula

In older systems, the pulsar is typically found to one side or offset from the nebula, due to its continuing proper motion, potentially leaving the original pulsar wind nebula and forming a new one around its current position, after the passage of the reverse shock. The particles in the

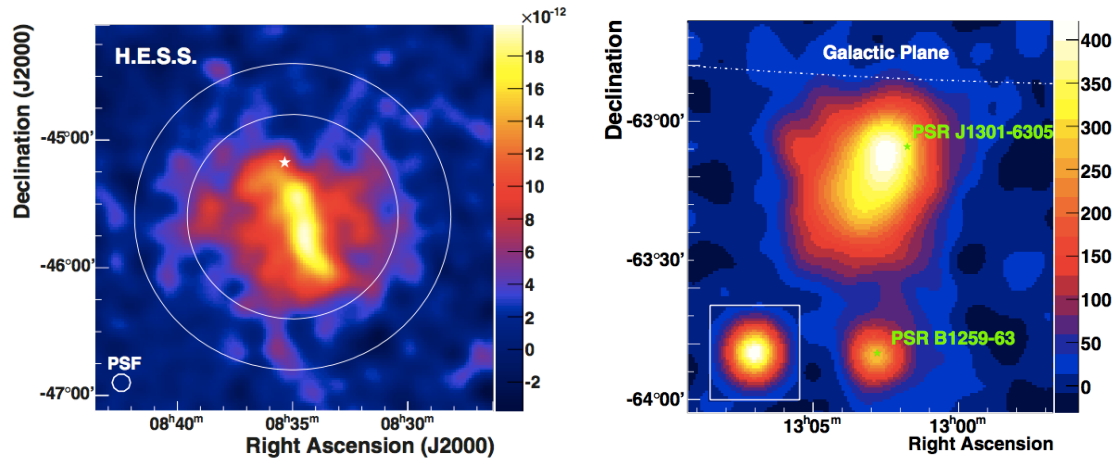


Figure 6.3: Left: Surface brightness map of the Vela X nebula as seen at TeV energies by H.E.S.S. (at a distance of 0.29 kpc). The system appears offset with respect to the pulsar position, marked by a star. As a guide to the angular extent of the nebula, circles at radii of 0.8° and 1.2° respectively are overlaid. Right: Excess counts map of HESS J1303-631, also offset with respect to the pulsar PSR J1301-6305 (at a distance of 6.6 kpc). The binary system PSR B1259-63 is also visible within the field of view. Figures taken from [93, 94].

pulsar wind nebula have synchrotron cooled, such that X-ray emission is no longer prominent. However, Inverse Compton producing particles typically have less energy than that required for synchrotron emission in X-rays, and Inverse Compton scattering continues to take place after the energy has dropped below that required for synchrotron emission.⁴ Therefore, the nebula continues to produce TeV emission long after the X-ray emission has faded away, typically leading to a much larger apparent size at TeV energies than in X-rays. Gradually, as the particles are transported away from the pulsar and continue to cool over time, even the TeV emission reduces. The final picture is then of a large, irregularly shaped nebula, with a pulsar to one side or offset from the TeV emission. With increasing distance from the pulsar, the original particles will have lost energy due to their cooling losses, the high energy emission consequently reducing and the spectrum becoming softer (a greater proportion of low energy emission). This leads to a signature energy dependent morphology of evolved pulsar wind nebulae systems, which has been detected by H.E.S.S. in three systems: HESS J1825-137, Vela X and HESS J1303-631 (see figure 6.3) [95, 93, 94].

TeV Observations of PWNe

Despite pulsar wind nebulae accounting for the largest proportion of galactic objects in the TeV sky, there remain many unanswered questions relating to their formation and evolution [34]. Of the overall population, current studies are just grazing the tip of the iceberg in terms of exploring the pulsar population at VHE (see figure 6.4). Further studies should help to clarify the nature of the primary acceleration mechanism (polar cap or outer gap), the complex interactions of the particles with the magnetic fields and the local environment, and probe substructure variation due to the particle population across the nebula. In this work, the source exhibiting the strongest known example of energy dependent morphology and the first PWN to be detected with this property at TeV energies, HESS J1825-137, is explored in detail with deep H.E.S.S. I observations

⁴Inverse Compton scattering occurs between the energetic particles and photons of the surrounding ambient medium, including contributions from starlight, dust and the CMB.

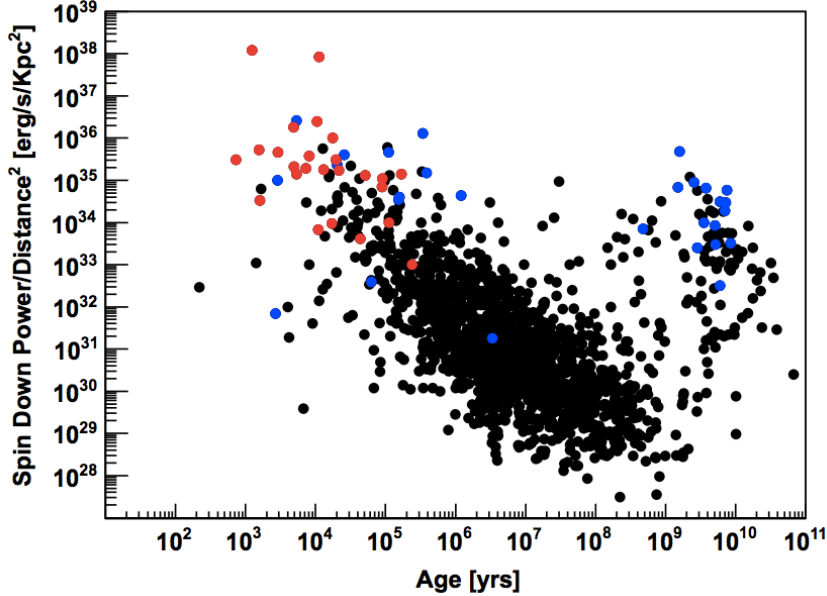


Figure 6.4: Radio pulsars from the ATNF catalog plotted as a function of their spin-down power (equation (6.1.3)) and age [96]. As of 2013, pulsars already detected by IACTs are shown in red, those detected by the Fermi-LAT γ -ray satellite in blue. Figure taken from [97].

and with the enhanced energy range of the H.E.S.S. II array.

6.2 Introducing HESS J1825-137 and its Field of View

The Galactic plane of the Milky Way is rich with TeV sources, including many point-like sources such as binary stellar systems, as well as supernova remnants and pulsar wind nebulae with extended morphology, making regions along the galactic plane of great interest to study. However, the density of sources along the Galactic plane is such that emission from one source may appear to overlap with emission from other sources nearby on the sky yet offset along the line of sight. As the sensitivity of experiments increases with time and with technological developments, weaker sources become detectable, increasing the density of known sources in each region and exacerbating the issue. Consequently, Galactic regions can be complex to analyse, and the field of view around HESS J1825-137 is no exception (see figure 6.5).

The pulsar PSR B1823-13 (RA: 18 26 13.175, Dec: -13 34 46.8) believed to power HESS J1825-137, is a young pulsar (spin-down age 2.14×10^4 yr) with a spin-down power of 2.8×10^{36} erg s $^{-1}$ and a period of 0.1015 s, discovered in 1986 [96]. The pulsar, situated at a distance of 4.12 kpc, was found to have a transverse velocity of 455.67 kms $^{-1}$, corresponding to a proper motion of $\mu_\alpha = (23.0 \pm 2.5)$ mas yr $^{-1}$ and $\mu_\delta = (-3.9 \pm 3.1)$ mas yr $^{-1}$, following a trajectory as shown in figure 6.6 [98]. ROSAT observations revealed the presence of an extended nebula around the pulsar in 1996 (confirmed by XMM-Newton in 2003), comprising both core and diffuse emission, making this object a prime target for TeV observations [99, 100]. However, targeted observation campaigns by HEGRA (2002) and Whipple (2005) only yielded upper limits, and although a nearby source was found by EGRET (1999), the nature of this source remained unidentified [101, 102, 103].

Previous upper limits were unconstraining in comparison to the sensitivity afforded by the

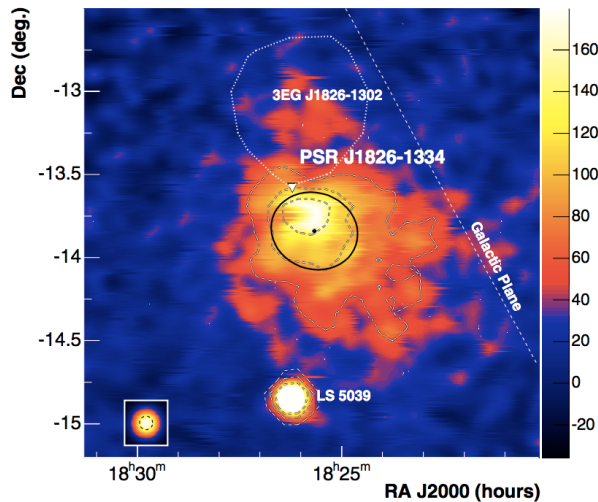


Figure 6.5: Excess sky map from the 2006 H.E.S.S. analysis [95]. The psf of the instrument is shown in the inset. HESS J1825-137 is largely extended and in close proximity to the galactic plane, such that the presence of other sources within the field of view (the binary system LS 5039 and the as yet unidentified source HESS J1826-130) is unsurprising.

first H.E.S.S. Galactic plane survey and HESS J1825-137 was discovered as part of this survey in 2005 [104]. In this first study at TeV energies, it was already found that the TeV size was much greater than the size of the X-ray nebula, implying that the electron population had already synchrotron cooled, with ongoing Inverse Compton emission responsible for the continuing TeV emission, much as described in section 6.1.3. The centroid of the emission was also found to be significantly offset from the pulsar position, and the overall morphology was found to be reminiscent of that expected in the case of supernova expansion into an inhomogeneous medium, with reverse shocks returning at different times from different regions of the nebula. At this stage, a much steeper drop in emission towards the North of the pulsar than across the Southern extent was already becoming apparent.

A more in-depth analysis was published in 2006, which clearly revealed the presence of energy dependent morphology in the system, the first time this had been discovered at TeV energies [95]. Using spatially resolved spectra, the spectral index was seen to soften with increasing distance from the pulsar, implying that the population of electrons in the nebula had travelled and cooled out to larger distances. With the electrons at the largest distance from the pulsar also being the coolest and showing the softest spectrum, these were interpreted as the oldest electrons in the system. Alongside a softening of the spectrum, an equivalent measure of the same physical property is the decreasing size of the nebula with increasing energy. Multiple mechanisms could account for this trend; three possibilities were previously discussed in [95]. These were: radiative cooling of electrons as they propagate away from the pulsar causing energy loss; energy dependent transport mechanisms such as diffusion or advection; and variation in the electron injection spectrum over time. It was also found that in order to explain the energy stored in the electrons, a higher pulsar spin-down luminosity was required than that measured today; implying that the spin-down luminosity of the pulsar must have been higher in the past, and could not have remained constant.

Both advective and diffusive transport scenarios could be used to explain the observed source size variation with energy and brightness variation with distance. Distinguishing between the two scenarios is challenging, and a combination of advection and diffusion is likely to be ultimately responsible. Given that the spin-down luminosity of the pulsar is expected to have been higher

in the past, this would have corresponded to stronger magnetic fields in the region, affecting both the acceleration and cooling timescales [95]. The energy dependent source size is a strong indication that the energetic particle population is mostly electrons, or that the emission is electron dominated.

At the time of writing, approximately 10 years since the last H.E.S.S. study [95], the dataset has again increased markedly, enabling further in-depth studies of the spectral variation over a larger region than was previously possible. Additionally, the addition of CT5 to the H.E.S.S. array has considerably lowered the energy threshold of the experiment, opening up a new energy regime to explore below the ~ 270 GeV threshold of the previous analysis. With increasing livetime, the high energy statistics are also significantly improved. Exploring the pulsar wind nebula with the strongest known energy dependent morphology with an enhanced energy range and sensitivity is therefore an opportunity to uncover more of the properties of the nebula environment and to study particle transport and cooling mechanisms in more detail.

There are two prominent TeV sources in close proximity to HESS J1825-137, namely the binary system LS 5039 to the South, and the unidentified hard spectrum source HESS J1826-130 to the North. LS 5039 is an X-ray binary, microquasar system, most likely comprised of a normal star orbiting around a compact companion, either a neutron star or a stellar mass black hole. Its spectrum exhibits a 3.9 day orbital modulation, and it appears point-like on the sky [105]. Along with HESS J1825-137, it was discovered as part of the first H.E.S.S. Galactic plane survey in 2005 [106]. HESS J1826-130, by contrast, is a hard spectrum source, and was revealed by sky maps made in different energy bands, where above 5 TeV the source is clearly distinguishable from HESS J1825-137. The true physical nature of this source, however, is as yet unknown [107]. Possible scenarios include an independent PWN located at $\sim 1 - 2$ kpc, or a physical association to the HESS J1825-137 region.

6.3 Analysis of Currently Available H.E.S.S. Data

At the time of writing, there is an extensive dataset available on this region, amounting to some ~ 400 hours of livetime spread over 11 years; approximately 6 times the ~ 67 hour dataset used in the most recent publication [95]. However, the data including CT5 (available as part of regular data taking since 2013) only amounts to ~ 15 % of this. Whilst it is possible to analyse data from 2013 onwards including CT5 with telescopes CT1-4 only, the converse (adding CT5 to pre 2013 CT1-4 data, before CT5 became operational) is obviously not possible. Therefore, it was decided to proceed with two complementary analyses; an analysis of the full available dataset with CT1-4, and an analysis of the data including CT5 using stereo triggered events (see chapter 2). For both analyses, the template-based ImPACT analysis was used, which shows improved sensitivity and performance over the Hillas parameter based analyses previously used (see section 2.8) [47, 54].

The data were selected using quality cuts to remove data affected by known hardware issues. An analysis of the CT5 data using mono-triggered events was also performed, permitting a lower energy threshold whilst also subject to larger inherent uncertainties; results from the mono analysis are only presented where relevant. These two analyses and their corresponding datasets will be referred to in the following as analyses (datasets) A and B respectively (see table 6.1). Results presented in the following sections will also be compared to the results of the 2006 publication [95] for compatibility and consistency checks.

As explained in chapter 2, when collecting data on a specific object or region of the sky,

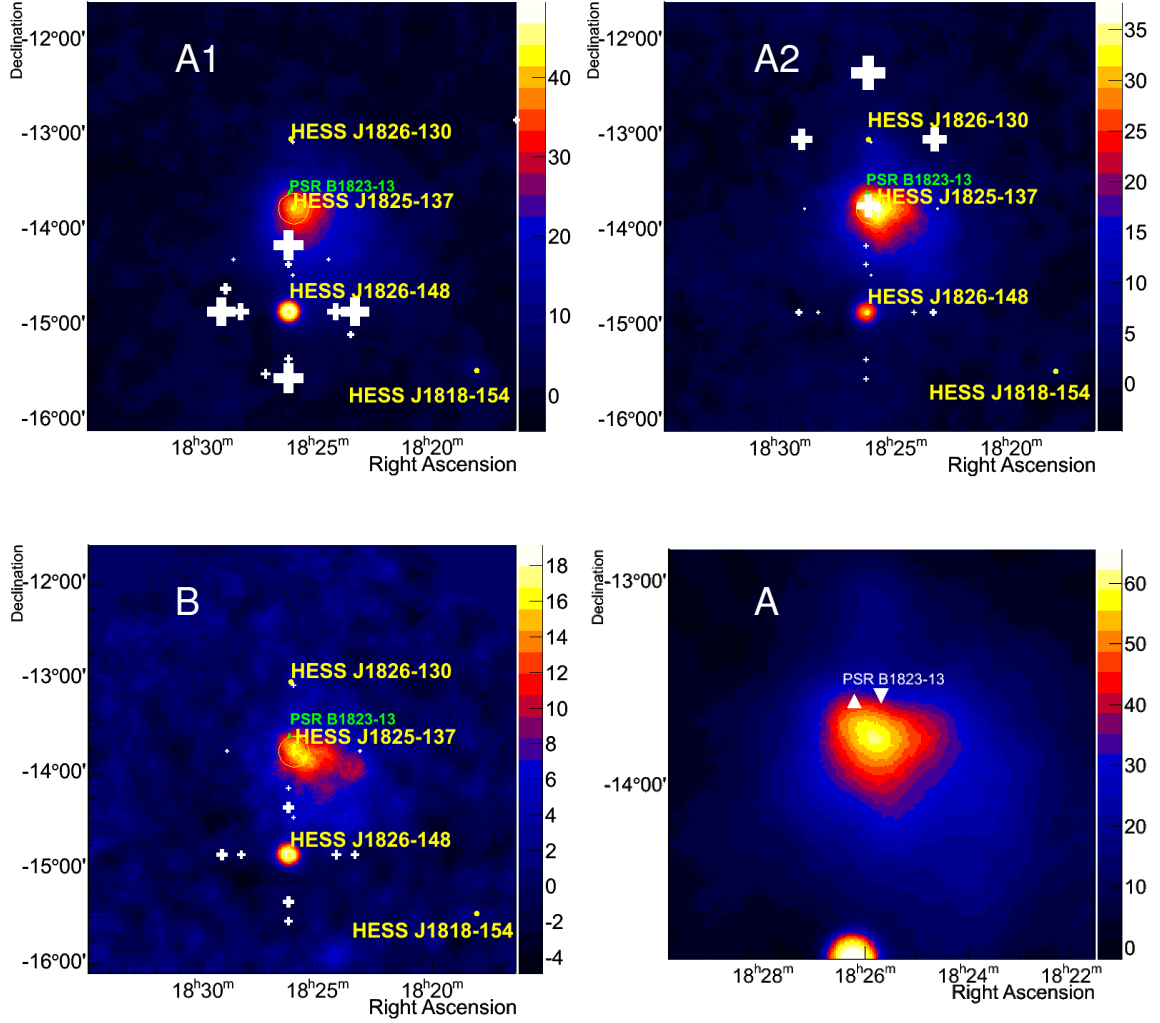


Figure 6.6: Positions at which data was taken on the HESS J1825-137 region (see table 6.1). The size of the marker corresponds to the amount of data taken at each position. Above: Positions corresponding to dataset A taken in the H.E.S.S. phase I (left, A1) and phase II (right, A2) eras. Below: Positions corresponding to dataset B (left), dominated by a campaign of observations of the binary system LS 5039 to the South. In all cases, the observation positions are overlaid on a significance map obtained from that dataset. Also shown is the extrapolated birth position (downwards triangle) determined from its proper motion and age, and current location (upwards triangle) of the pulsar PSR B1823-13, overlaid on a zoomed-in view of the central region using the full dataset A (right, A1+A2).

Dataset	Start Date	End Date	Telescopes	Number of Runs	Live Time (h)
A1	16/05/04	17/08/12	CT1-4	380	162
A2	09/07/13	12/08/15	CT1-4	332	142
A (= A1+A2)	16/05/04	12/08/15	CT1-4	712	304
B	09/07/13	12/08/15	CT1-5	83	38

Table 6.1: The length and time period of each dataset used in the HESS J1825-137 analysis. Dataset A is a combination of A1 and A2, whilst dataset B comprises all data including CT5. The quoted livetime corresponds to that used for making a sky map; data quality selection cuts are typically more stringent for spectral analyses, leading to a reduced livetime corresponding to the spectra. Data is recorded in observation runs, typically of ~ 28 minutes length each, although some runs can be shorter.

observation positions are generally chosen to be offset from the source in question. This approach enables a background estimate to be taken from the opposite side of the camera to that where the source is located, yet under the same radial acceptance behaviour of the camera. Dataset A comprises data over a sufficiently long time period that the exposure is reasonably uniform over the region. Due to substantial changes in the software and calibration of the H.E.S.S. experiment, this dataset was further subdivided into data from the first and second phases of the H.E.S.S. experiment (datasets A1 and A2 respectively) for analysis purposes; the results were later re-combined forming dataset A. As can be seen in figure 6.6, A1 is composed of observation campaigns on HESS J1825-137 and on the binary system LS 5039 (or HESS J1826-148), whilst dataset A2 is dominated by observations of HESS J1826-130. Dataset B, comprising only data with CT5 available and hence by definition from 2013 onwards only, is rather unbalanced in exposure across the region, focused on the binary system LS 5039.

For dataset B (and A2), the optical efficiency calibration was done using the generic muon calibration approach developed for H.E.S.S. phase II, as outlined in chapter 3. As previously shown in chapters 3 - 5, matching the optical efficiency evolution of the telescopes is important to reduce biasing effects. Over the time period of both datasets there were substantial changes in optical efficiency, as listed in table 3.2; these were taken into account by the standard H.E.S.S. calibration chain in this HESS J1825-137 analysis. A cross check of this calibration is presented in the next section.

6.4 Cross Calibration

To check the optical efficiency calibration of these datasets, the cross calibration method outlined in chapter 4 was used. As previously explained, the relative telescope efficiencies obtained from the image size based cross calibration are expected to correlate with the muon efficiency values. The relative telescope efficiencies obtained using the energy cross calibration are expected to be consistent with 1 across all telescopes. This check was performed for both datasets A and B.

The cross calibration results for dataset A1 (CT1-4 in the H.E.S.S. phase I era) are shown in figure 6.7, and for dataset B (contemporaneous to dataset A2) in figure 6.8, with the interpretation of these plots covered in more detail in chapter 5. As can be seen, for both datasets, the relative efficiency coefficients obtained for all telescopes by the energy cross calibration method for each separate observation run lie broadly within a 5% – 10 % tolerance level. Comparing the relative efficiencies obtained via the image size cross calibration approach to the muon efficiencies obtained for these runs, the correlation is good for dataset A1, yet is seen to be biased for dataset B, with a lower relative response efficiency obtained for CT5 than the muon efficiency calibration would suggest. This occurs due to difficulties in performing the image size cross calibration between telescopes of differing specifications, particularly of differing mirror areas (see chapters 4 and 5 for more details).

The largest deviations in the energy cross calibration with dataset A1, around run number 65000 in figure 6.7, correspond to the time period when the mirrors of CT1-3 had been recoated, yet CT4 had a significantly degraded mirror with respect to the other three telescopes. This time period also accounts for the largest deviations from linearity in the right hand plot of figure 6.7. The image size based cross calibration performs well for telescopes of the same size, and illustrates this effect with CT4 more clearly in figure 6.9, demonstrating that these larger deviations are due to the large optical efficiency differences and non-linear effects between telescopes of different types, rather than due to mismatches in the MC per se.

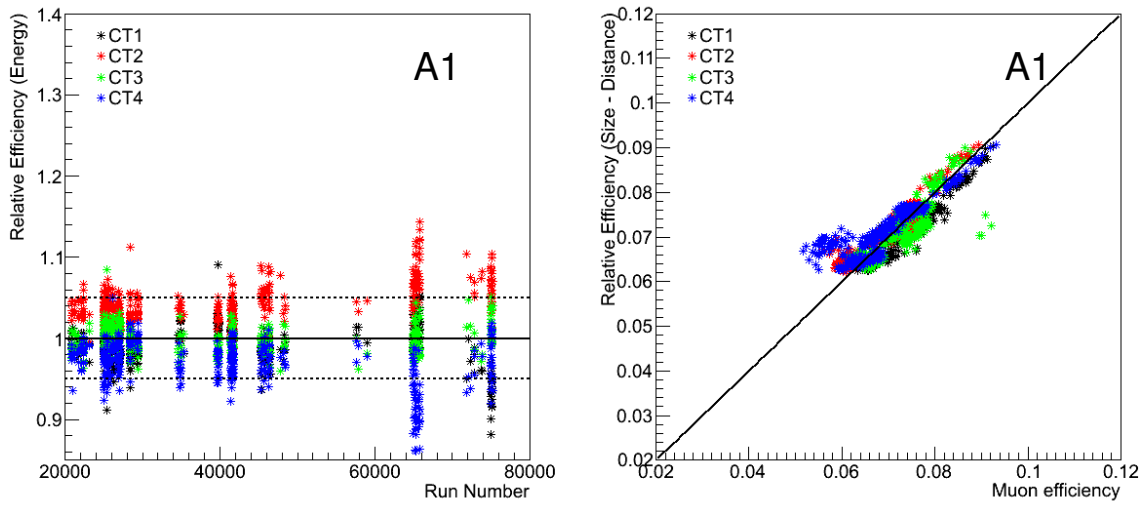


Figure 6.7: Results of the cross calibration on dataset A1. Left: the relative efficiencies obtained via the reconstructed energy approach lie generally within the acceptable tolerance level, except for a time period during which CT4 was significantly degraded with respect to the other telescopes. Right: correlation of the image size based relative efficiencies with the muon efficiency values. The few large outliers correspond to the time period of considerably degraded CT4.

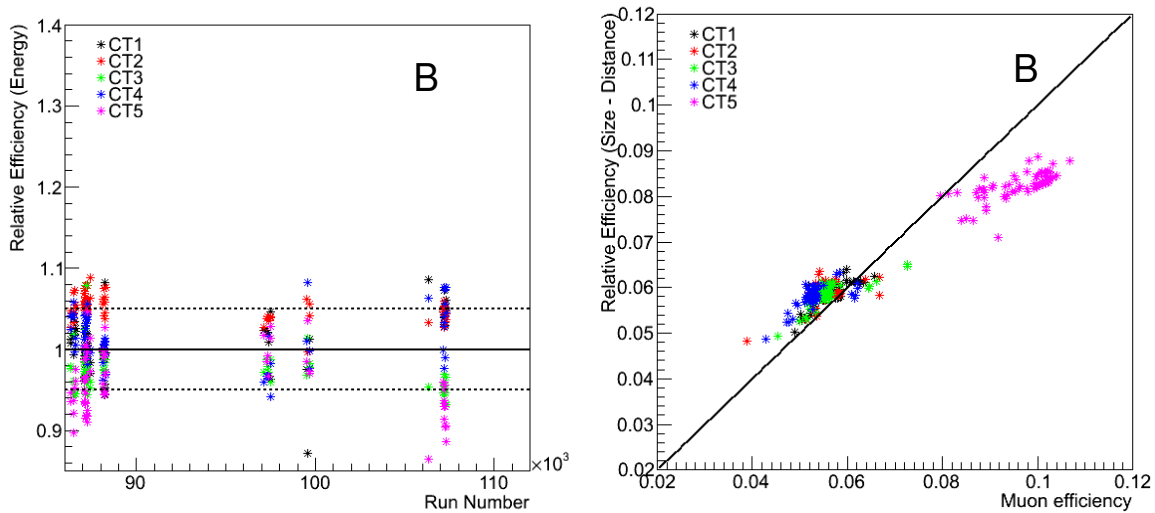


Figure 6.8: Results of the cross calibration on dataset B. The reconstructed energy approach (left) shows that the coefficients lie broadly within the 5% – 10 % tolerance level permissible for analyses. Whilst the image size approach (right) shows a bias with muon efficiency for CT5, this is a known issue arising from the image size scaling ratio for CT5 being found for a different time period, and unoptimal for this dataset, such that non-linear deviations inherent in the procedure have a significant effect.

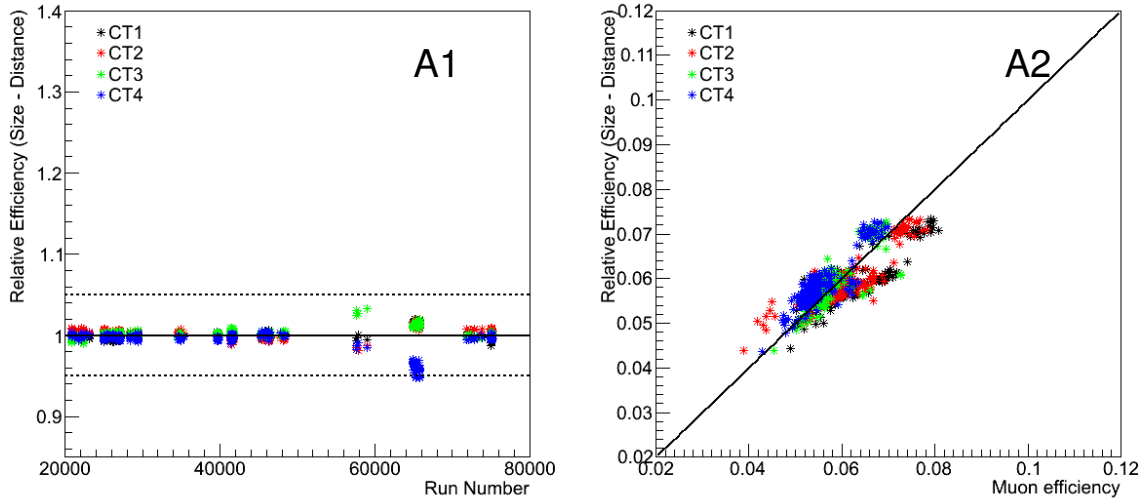


Figure 6.9: Verifying the results of figures 6.7 and 6.8. Left: the image size cross calibration demonstrates that the period of large variation seen in figure 6.7 is indeed unusual in the H.E.S.S. history, with a larger dispersion seen at similar run numbers (~ 65000). Right: with dataset A2, the correlation between the image size coefficients and the muon efficiency is good over the same time period as dataset B, showing that the bias observed in figure 6.8 is due to inherent difficulties in the image size procedure between CT1-4 and CT5.

Dataset A2 covers the same time period as dataset B, yet utilises only CT1-4, providing a useful check of the cross calibration in this time period. As figure 6.9 shows, the image size relative efficiency coefficients are well correlated with the muon efficiencies in this time period when CT5 is removed from the analysis. This verifies further that the observed bias in figure 6.8 arises due to the expected size ratio used to adjust the image size estimates being found from a set of Monte Carlo optical efficiencies quite far from those matching this dataset; more details are outlined in chapters 4 and 5.

In conclusion, only mild deviations, within the bounds of expectation, were found by performing the cross calibration checks on the datasets used in the analysis of HESS J1825-137. The results of the preceding analysis may be deemed trustworthy, with the understanding that data taken during periods of large deviations across elements of a telescope array, such as the period of low CT4 optical efficiency in dataset A1, or of high CT5 optical efficiency towards the start of dataset B, must be handled properly by the analysis. It is worth re-iterating at this stage that the cross calibration results presented here were performed on a run-wise basis within H.E.S.S. (each point corresponding to ~ 28 minutes of data taking). The performance, particularly of the energy cross calibration, may be expected to improve with averaging over the observations of a whole night, to mitigate any loss in calibration performance due to a restricted energy range at large zenith angles. A nightly average value for the muon efficiency, as described in chapter 3, would reduce the variation in this parameter, used for normalisation, whilst in the case of CTA, the increased number of available telescope pairs would significantly enhance the precision of the cross calibration procedure.

6.5 Morphology and Sky Maps

HESS J1825-137 is a highly extended object in the TeV γ -ray sky, making it challenging to analyse. Due to the angular extent of the TeV emitting nebula on the sky, the emission tends

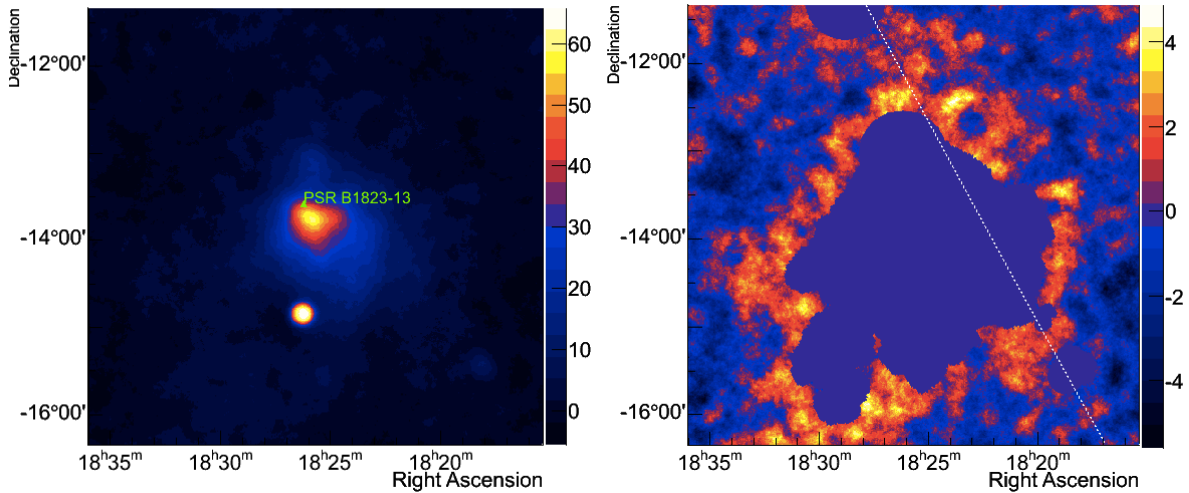


Figure 6.10: Left: Significance map of the HESS J1825-137 region, using the full available energy range with dataset A showing the pulsar PSR B1823-13. Right: Exclusion regions used in the HESS J1825-137 analysis; the plane of the Milky Way is indicated by the white dashed line. These are the small version of the exclusion regions used for the H.E.S.S. Galactic Plane Survey (HGPS); more comprehensive than the default non-HGPS regions, yet less than the standard HGPS regions, due to the coverage of this region in datasets A and B centred on this field of view [107].

to fill a large section of the field of view of the telescopes,⁵ restricting the available regions from which a background estimate can be taken (see section 2.6).

Due to the asymmetric and extensive nature of the emission, a set of exclusion regions larger than the default regions was used, as defined according to the H.E.S.S. Galactic Plane Survey (HGPS) [107]. In this case, the background estimation was made using an adaptive version of the ring background method outlined in section 2.6 [49]. That is, that the size of the inner ring radius is varied around the source in order to take into account the size of the exclusion regions in different directions, with a minimum radius of 0.8° . The ring thickness was kept fixed for this analysis, at 0.5° , to ensure the off region area used is large with respect to the on region, helping to minimise fluctuations in the background statistics. The maximum outer ring radius used was 1.8° , restricted by the camera field of view. Small scale variation of the parameters was found not to affect the analysis, and the background was well normalised. The exclusion regions used are shown in figure 6.10. The test position used for the location of the peak emission from HESS J1825-137 was the centre of gravity from the previously published H.E.S.S. analysis; $18\text{h } 25\text{m } 41\text{s}, -13\text{d } 50' 21''$ [95].

Looking at the excluded significance map (figure 6.10) one can see that there are positive areas of emission at the $\sim 4\sigma$ level in the map. In the case of perfectly excluded emission, a Gaussian fit to the excluded significance distribution would have a mean, μ compatible with zero and a width of $\sigma = 1$. However, the excluded significance distribution in figure 6.11 has a mean $\mu = -0.2 \pm 0.4$ and width $\sigma = 1.5 \pm 0.3$, slightly above 1, showing that these positive regions are not accounted for by the exclusion regions and are above background fluctuations. These regions occur near to the edge of the exclusion regions, suggesting that the leaked emission present in the region can be attributed to HESS J1825-137. Although this is the most likely explanation, inherent Galactic diffuse emission near the Galactic plane or a contribution from weaker, as yet undetected background sources cannot be ruled out.⁶ However, due to the coverage

⁵CT1-4 and CT5 have fields of view of $5.^\circ$ and 3.2° respectively (see chapter 2).

⁶This Galactic diffuse emission has also been significantly detected by H.E.S.S. [108].

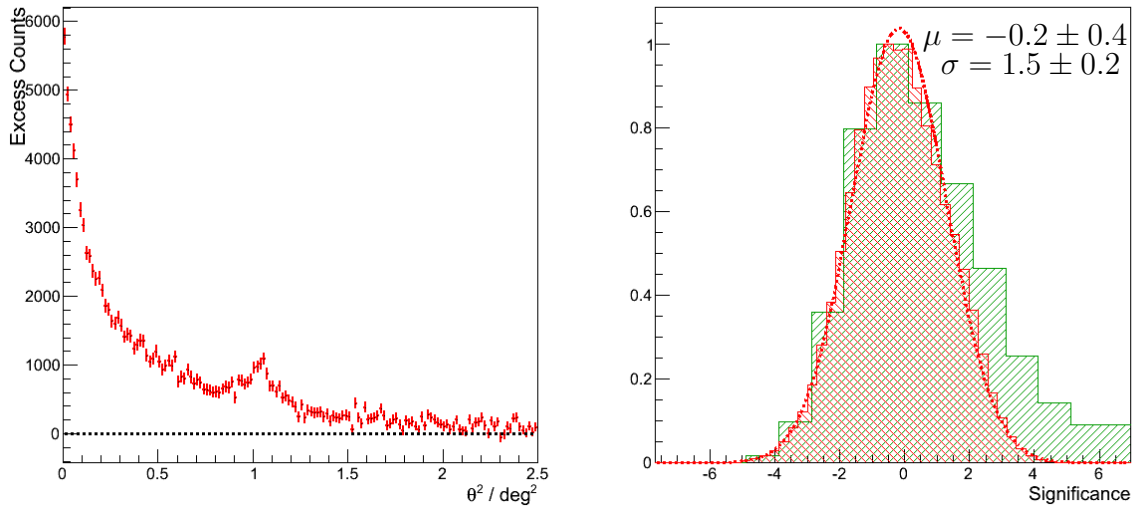


Figure 6.11: Left: Distribution of excess counts with angular distance from the peak of the emission. Significant emission is seen to extend out to large angular distances from the emission peak (centre of gravity position taken from [95]), with a second peak seen at $\sim 1^\circ$ due to the binary system LS 5039. Right: Significance distribution after exclusion - there is clearly a small excess of positive significance, implying that some of the significant positive emission has not been excluded.

of the region in this dataset, larger exclusion regions severely restrict the area available for background estimation. The current exclusion regions therefore provide an adequate balance between excluding all significant emission and providing sensible areas for background estimation.

Sky maps of the region are shown in figure 6.10 using both dataset A with CT1-4 only and in figure 6.12 using dataset B with CT1-5 respectively. As can be seen, the morphology of the object broadly agrees between the two datasets, although the centre of the source appears much more significant in dataset A due to the more extensive dataset and consequently higher sensitivity. The apparent size of the nebula is also much smaller for dataset B than for dataset A, as the areas of weaker surface brightness have not yet become significant above background at larger radial distances from the pulsar. In figure 6.12, the peak of the emission is also seen to be slightly further to the South in the mono analysis than in the stereo analysis; this is likely to be due to the different energy ranges and sensitivities of the analyses, with the peak emission at lower energies occurring further away from the pulsar.

A secondary effect contributing to the apparent difference in size could be due to the choice of exclusion regions used. Figure 6.13 shows the exclusion regions used for dataset B, which are noticeably smaller than those used in figure 6.10. Using the larger exclusion regions appropriate for dataset A was found to introduce systematic artefacts into the maps of dataset B (due in part to the lower sensitivity, see table 6.1), whereas with the smaller exclusion regions used here, the background was well normalised (right hand side of figure 6.13).

However, as the background estimation is taken from regions outside of those excluded, it may be that large areas of weak surface brightness, just around the threshold of the sensitivity of dataset B, enter into the background estimation such that some emission from HESS J1825-137 is removed as part of the background. This would also contribute to a lesser apparent size such as that seen between figures 6.10 and 6.12; the issue will be addressed in more detail in section 6.7.

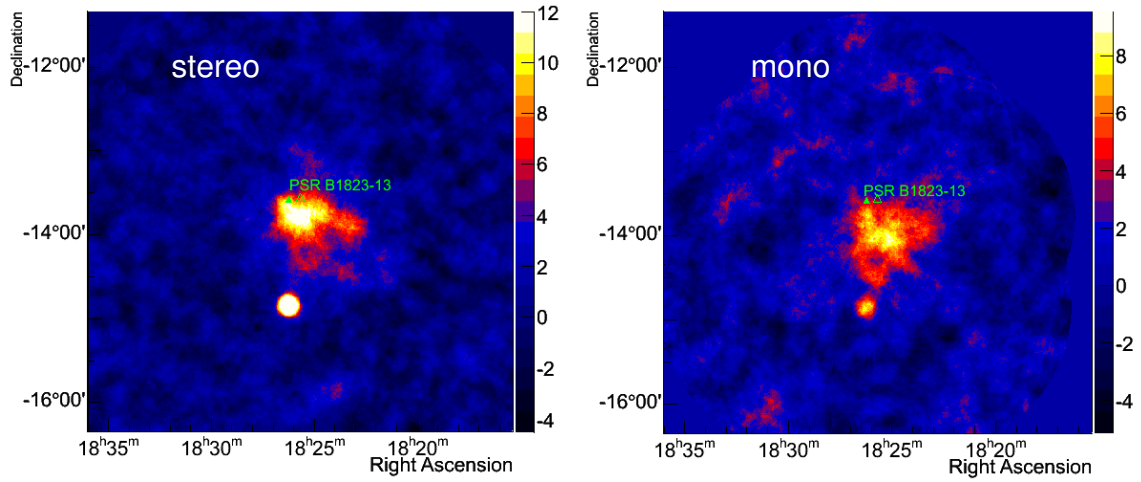


Figure 6.12: Significance maps made from dataset B, using a stereo analysis with CT1-4 (left) and a mono analysis of CT5 only (right). The peak emission appears to be further from the pulsar in the mono analysis, potentially due to the different intrinsic energy ranges.

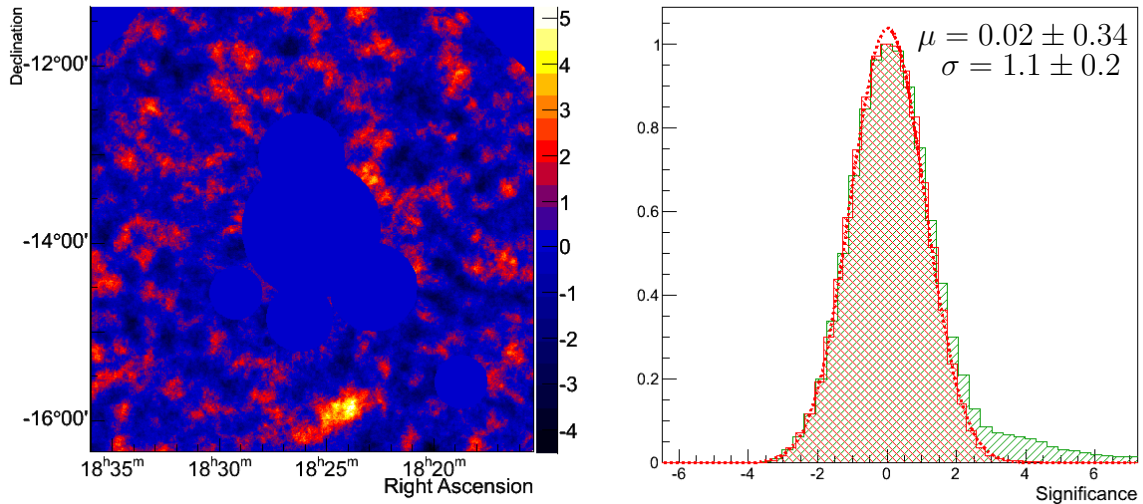


Figure 6.13: Left: Excluded significance map of HESS J1825-137 using a stereo analysis of dataset B; the exclusion regions are smaller than those in figure 6.10 to avoid introducing systematic in the low statistics data. There is an $\sim 4\sigma$ artefact visible in this map, not seen in dataset A, which is likely to be an instrumental effect. Right: The excluded significance distribution has a mean compatible with zero and a width σ compatible with 1, indicating that the significant emission is well accounted for by these exclusion regions.

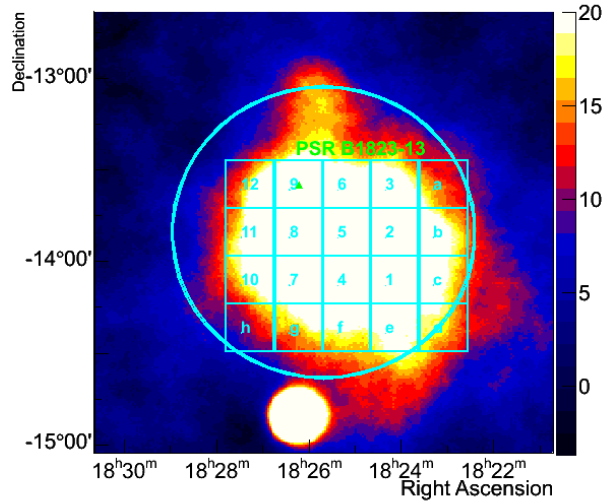


Figure 6.14: Significance map saturated at 20 sigma, showing the box-shaped regions used for spectral extraction. Regions 1-12 were used in [95] and are also used in the analysis of dataset B, whilst regions a-h are only significant in the extensive dataset A and are hence included in this analysis only. Box 9 is centred on the current location of the pulsar PSR B1823-13. Also shown is the 0.8° radius area used for the whole region spectrum as defined in the 2006 publication [95].

6.6 Spectral Analysis

A spectrum of the full region was taken, using a spectral extraction region of 0.8° radius, around the peak of the emission as illustrated in figure 6.14. The background estimation in this case was performed using the reflected region method, as opposed to the ring background method used in construction of the sky maps (see chapter 2). Due to the different data quality cuts used for spectral analyses and the sizes of the on regions (from which the spectrum is taken), the livetime of the data is typically shorter than that of the sky maps. Additionally, runs are required to contain both the on region and sufficient area for an off region to be defined (from which a background estimation can be taken), such that runs centred on unsuitable observation positions are omitted (for example, falling on the peak of the nebula emission, see figure 6.6). For datasets A and B, the spectral livetimes corresponding to table 6.2 were 232 and 18.7 hours respectively. The spectral analysis procedure is described in more detail in section 2.10 of chapter 2. The energy range of the spectral fit for each dataset and parameters of the fit are given in table 6.2.

Whilst the spectrum is consistent with a power law model, the best fit is provided by a power law with exponential cut-off in the case of dataset A, and by a log parabola shaped fit for dataset B. However, the log parabola preference for dataset B is only marginal over a power law with exponential cut-off. Shaped models were also preferred over a power law fit in the 2006 published analysis [95]. The fitted indices obtained for dataset B are generally harder than those of dataset A; this is potentially coupled with the higher flux at 1 TeV seen in dataset B. The exponential cut-off found is consistent between dataset A and the 2006 analysis, yet was considerably lower in dataset B (~ 10 TeV as opposed to ~ 30 TeV). However, the spectrum clearly shows much larger uncertainties at high energies in dataset B than for the other analyses, such that the fitted exponential cut-off is likely to be affected by lower statistics in the high energy data (due to the lesser livetime). This is also reflected in the reduced energy range of the analysis, hence one

Dataset	Fit Model	Index	Fit parameters	Flux (1 TeV)	χ^2
A	power law	2.43 ± 0.01	-	1.85 ± 0.02	132.8/27
A	log parabola	2.42 ± 0.01	$\beta = 0.032 \pm 0.007$	1.91 ± 0.02	107.43/26
A	exp cut-off PL	2.34 ± 0.02	$E_c = 36.5 \pm 6.3$ TeV	1.90 ± 0.02	76.5/26
B	power law	2.33 ± 0.03	-	2.48 ± 0.08	69.0/42
B	log parabola	2.31 ± 0.03	$\beta = 0.13 \pm 0.03$	2.97 ± 0.13	36.2/41
B	exp cut-off PL	2.09 ± 0.06	$E_c = 10.6 \pm 2.8$ TeV	2.78 ± 0.11	40.2/41
'06	power law	2.38 ± 0.02	-	1.90 ± 0.04	40.4/15
'06	log parabola	2.29 ± 0.02	$\beta = -0.17 \pm 0.04$	2.10 ± 0.04	14.5/14
'06	exp cut-off PL	2.26 ± 0.03	$E_c = 24.8 \pm 7.2$	2.10 ± 0.05	15.1/13

Table 6.2: Parameters of a spectral fit to a single extraction region covering the majority of the emission, as shown in figure 6.14. Three fit models were used: power law, ($I_0 E^{-\Gamma}$); log parabola ($I_0 E^{-\Gamma + \beta \log E}$); and a power law with an exponential cut-off (exp cutoff PL, $I_0 E^{-\Gamma} \exp(-E/E_c)$). The fitted energy range was [0.18, 91.] TeV for dataset A, and [0.20, 68.] TeV for a stereo analysis of dataset B. The flux at 1 TeV was measured in units of ($10^{-11} \text{ cm}^{-2} \text{ s}^{-1} \text{ TeV}^{-1}$). Values corresponding to the 2006 analysis correspond to the energy range [0.27, 35.] TeV and are taken from [95].

can expect the discrepancy to resolve with increased exposure of dataset B. The area used for spectral extraction is shown in figure 6.14.

6.6.1 Spectral Map

Division of the region of significant emission into small, equally sized regions was an approach adopted in [95] to probe spectral variation across the PWN. Initially, in the 2006 analysis 12 boxes were defined as illustrated in figure 6.14, with a size of $0.26^\circ \times 0.26^\circ$; these were used for spectral extraction with both current analyses. However, due to the small size of the extraction region, the uncertainties on the obtained parameters of the spectral fit are rather larger than would be obtained for larger regions encompassing more emission. The original set of 12 regions could be further enhanced for dataset A, by the addition of 8 extra boxes (labelled a-h in figure 6.14) covering the emission region, although the flux contribution here is much lower.

One key advantage of dividing the emission region into boxes in this manner, is that the region is more evenly sampled and no apriori assumptions are made about the spectral variation and nature of the emission. A power law was fit to the spectrum obtained from each box separately, and the variation of fit parameters with distance from the pulsar was explored. A key finding, illustrated in figure 6.16, is that the power law index clearly increases with increasing distance from the pulsar, and the flux above 1 TeV clearly decreases. Using dataset A, the strength of the correlation between these parameters, as shown in figure 6.16, was evaluated using the Pearson correlation coefficient r . The power law index and distance were found to have $r = 0.80 \pm 0.10$, whereas the flux and distance were anti-correlated, with $r = -0.75 \pm 0.02$.

Mild exceptions to this trend can be seen in the measured flux in regions 10-12; this may be interpreted through one or a combination of effects. Considering the birth location of the pulsar and its trajectory over time (see figure 6.6) in relation to the current position, regions 10-12 lie mostly ahead of the pulsar; it is possible that the particles responsible for the emission have not been transported to these areas in the same way as for other regions (e.g. 9, 8, 6, 5). The significantly lower flux of regions 10-12 than that which would be expected at this distance indicates that the particle population is considerably less in number. A change in energy distribution of the particle population would manifest itself in a changed spectral index. One possible cause of this would be that the time taken for particles to reach regions 11 and

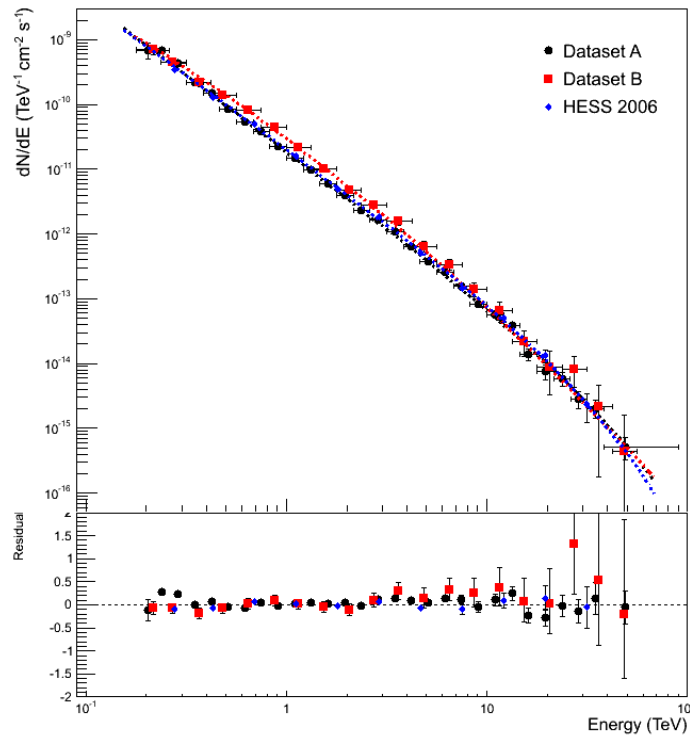


Figure 6.15: Spectra taken with datasets A and B from a 0.8° radius around the HESS J1825-137 centre of gravity from [95], to match the region used for spectral extraction in 2006 (see figure 6.14). The published spectrum from 2006 is also plotted. Dataset A agrees well with the previous publication, whilst the flux is visibly higher in dataset B at $E \lesssim 5$ TeV, a fact reflected in table 6.2. Residuals were calculated for each analysis with respect to the best fit model, either an exponential cut-off power law or a log parabola.

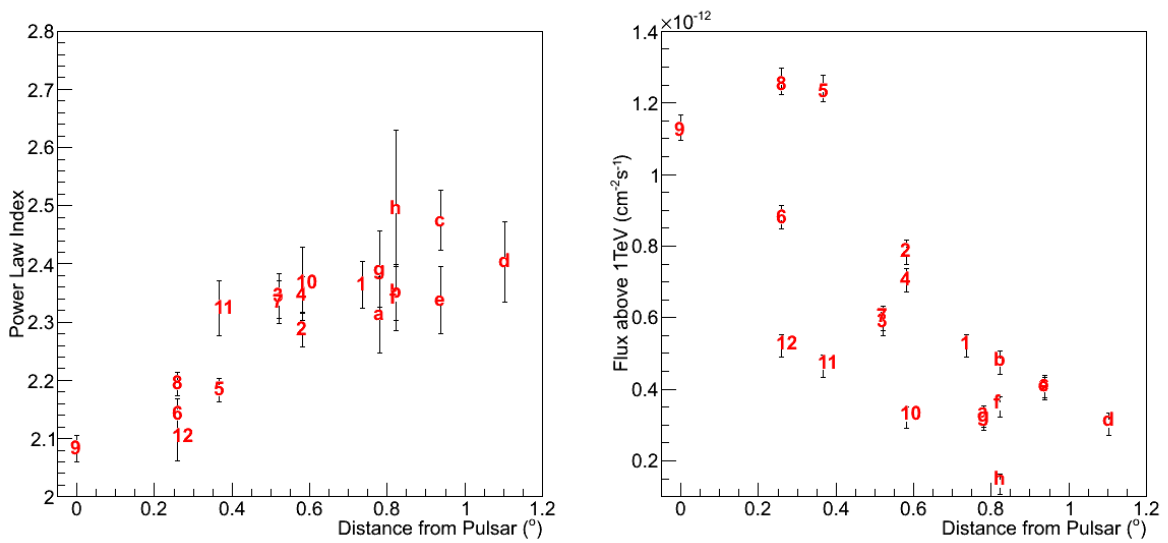


Figure 6.16: Variation in spectral index and flux with distance, obtained from dataset A. With increasing distance from the pulsar, the spectral index of the power law fit clearly increases (becoming softer, left) and the flux drops off (right).

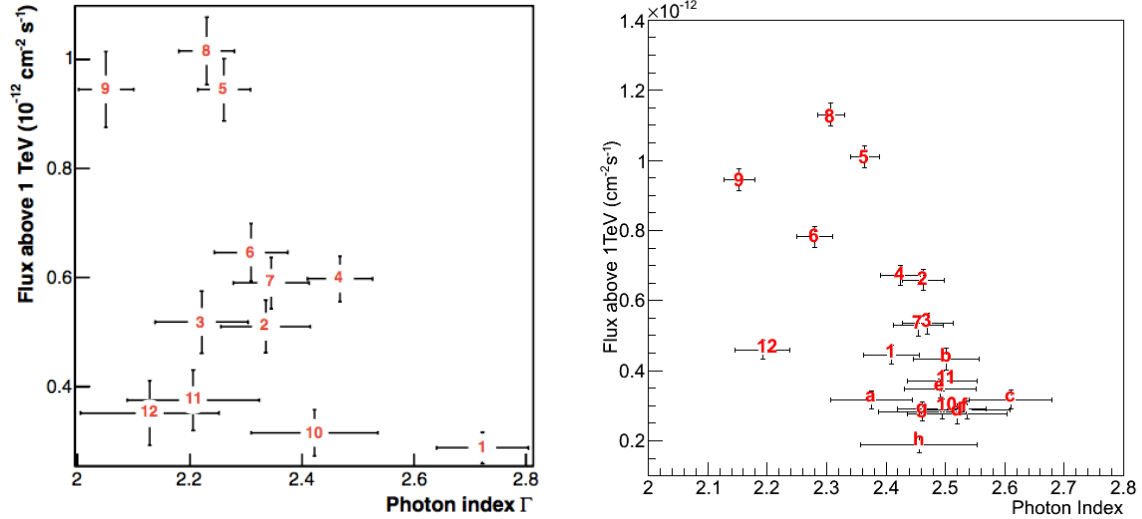


Figure 6.17: Flux above 1 TeV against photon index, as published in [95] (left) and as obtained in the re-analysis of dataset A (right). The two quantities appear to be anti-correlated, likely a result of their common dependence on the distance from the pulsar.

12 is either longer or requires more particle energy than that of other nearby regions (e.g. 8 and 9). Alternatively, there may be variations in the ambient medium, such as material density or magnetic field strength, which block the particles from moving into these regions. Lastly, a contribution from projection effects and the 3D geometry of the system may also play a role.

The resulting power law index is a trade-off between only the most energetic particles reaching this region by having sufficient energy to travel the necessary distance (presumably along an indirect path), and the energy losses that must have occurred along the particles trajectory to that location. That the measured indices for these regions 10-12 do not lie too far from the general trend, indicates that this trade-off approximately cancels out, although the slightly lower power law index for region 12 (than regions 6 and 8 at the same distance, see figure 6.16) suggests that the high particle energy requirement dominates slightly over losses incurred. Conversely, the higher index for region 11 than region 5 at the same distance indicates that the particles have suffered more losses.

Variation of the photon index with flux above 1 TeV was also explored. In [95] a mild anti-correlation of the two parameters was claimed (correlation coefficient of $r = -0.46 \pm 0.14$); this is supported by the new analysis, which found a correlation coefficient of $r = -0.6 \pm 0.1$ for dataset A (with an increased number of spectral regions). Increasing photon index corresponds to cooling of the particles, such that a larger proportion of the emission shifts to lower energies. For a flux measurement above a fixed threshold (1 TeV), the flux will decrease for a cooled particle population. Figure 6.17 shows that the flux and spectral index are anti-correlated, mostly likely a consequence of their distance dependence, although again, region 12 provides the largest deviation from the trend.

6.6.2 Spectral Softening

To explore the spectral softening with increasing radial distance from the pulsar in more detail, a series of wedge-shaped spectral regions were defined centred on the pulsar and increasing in radius towards the South. Whereas in [95] a constant opening angle was used (figure 6.18), and

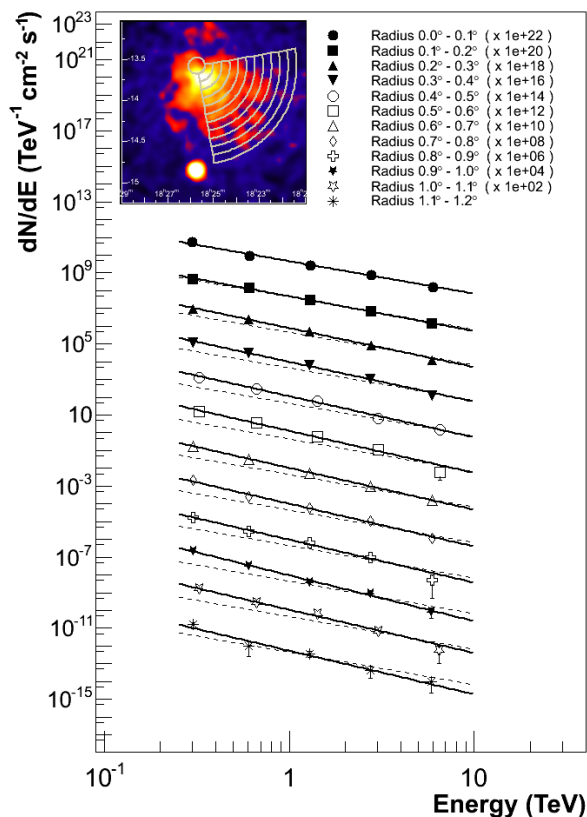


Figure 6.18: Spectra extracted from wedges in [95], demonstrating the softening of the spectrum with increasing distance from the pulsar (in the energy range [0.27,35.]TeV). For each wedge, the flux normalisation is offset by an arbitrary factor for clarity. The slope of the innermost wedge is indicated by a dashed line as a reference.

the innermost regions were extended in [109] to cover the emission out towards LS 5039,⁷ for this analysis the extent of the wedges were redefined to better match the emission. Additionally, the width of the spectral extraction regions was doubled with respect to the previous analysis, to account for the reduced size of dataset B and for the poorer PSF of the H.E.S.S. II analysis.

Figure 6.18 succinctly captures the key result of [95]; with the innermost region spectral slope as a reference, the spectral softening with increasing distance, reflecting the shift in distribution of the parent particle population, is clearly present.

A re-analysis of dataset A using a set of thin spectral wedges with opening angle corresponding to the original analysis, is shown in figure 6.19, with the spectral slope information summarised by the power law index. This analysis found agreement with the analysis done by [110] in 2011; the discrepancy found when using the same dataset may be due in part to improvements in the background modelling and analysis techniques over the intervening period, which improved the accuracy of the energy (and hence also the spectral) reconstruction.

Spectral Ring analysis

As was shown in section 6.6.1, the pulsar PSR B1823-13 appears to be the source powering the nebula emission, with the spectral variation across the region seeming to be linked to the

⁷This involved an arbitrary scaling of the flux based on the ratio of the areas of the original H.E.S.S. analysis regions to the extended regions for modelling purposes; no re-analysis was performed.

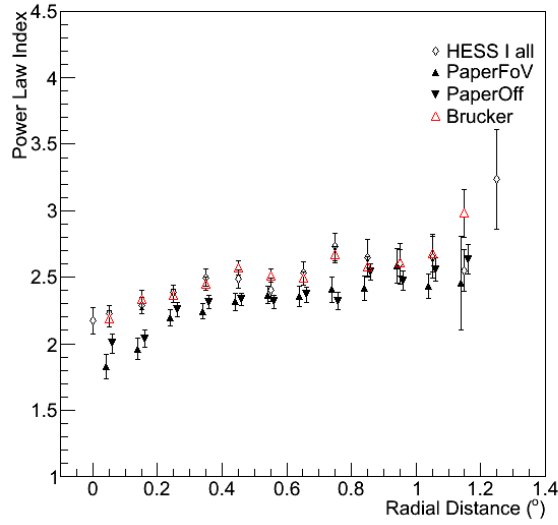


Figure 6.19: Change in power law index with distance from the pulsar. For the same dataset and wedge regions (shown in the inset of figure 6.18), the current analysis of all of 0.1° thick wedge regions separately (labelled “HESS I all”) agrees more with the 2011 re-analysis by Julia Brucker ([110], labelled “Brucker”) than with the 2006 publication [95]. Two different background estimation methods were used in the 2006 analysis, namely the Field of View and Off-data methods; results corresponding to these are labelled “Paper FoV” and “Paper Off” respectively.

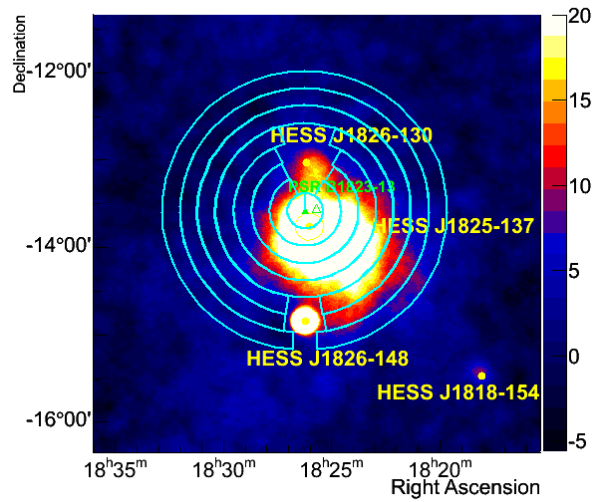


Figure 6.20: A series of ring-shaped regions of 0.2° radius each were defined, extending out to 1.6° radius from the pulsar. These regions are overlaid on a significance map of the region, saturated at 20 sigma. Masks were applied to remove the emission from the overlapping H.E.S.S. sources LS 5039 (0.2° radius mask) and HESS J1826-130 (0.3° radius mask).

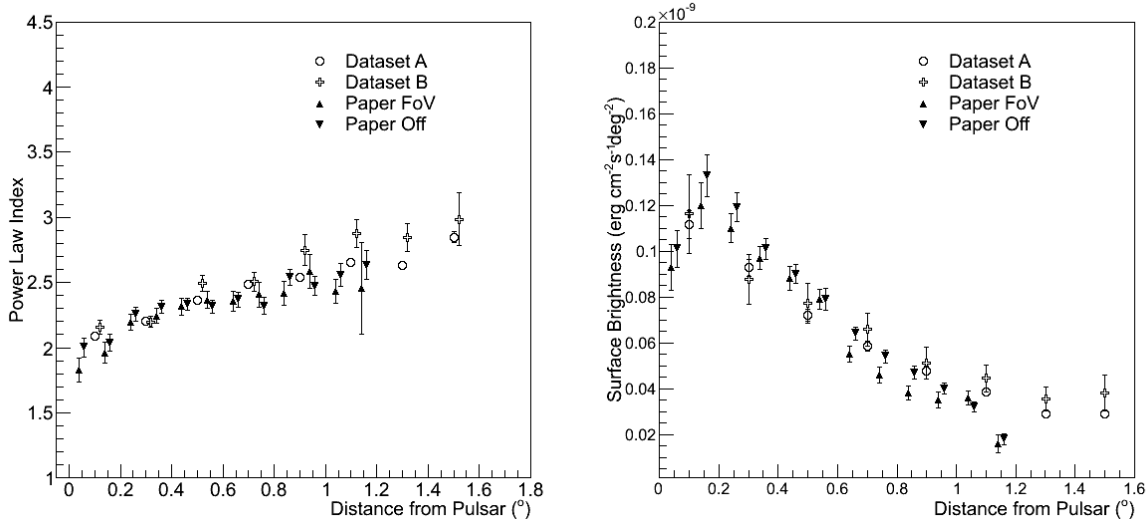


Figure 6.21: Results of a spectral analysis of the ring-shaped regions around the pulsar for both datasets A and B, shown with the results published in [95]. The results from [95] corresponding to the Field of View and Off-data methods are labelled “Paper FoV” and “Paper Off” respectively. Left: power law index with distance from the pulsar. Right: surface brightness with distance from the pulsar. With increasing distance from the pulsar, the spectral index softens and the surface brightness reduces, after peaking a short distance away from the pulsar.

pulsar. To investigate further the observed variation in spectra with distance from the pulsar as presented in section 6.6.1, a series of ring regions of 0.2° width were defined as shown in figure 6.20, and spectral analyses were performed for each of these ring-shaped regions. Essentially these are full rings, yet were constrained to avoid contamination from the other sources in the field of view. The results of a power law fit as a function of distance from the pulsar are shown in figure 6.21.

Figure 6.22 displays these results analogously to figure 6.18. With increasing distance from the pulsar, the spectral index of a power law fit clearly softens, implying a reduced high energy component to the emission, or equivalently a relative increase in the proportion of lower energy emission. In the same range, the surface brightness also exhibits behaviour similar to that seen in the 2006 H.E.S.S. published analysis. The peak brightness occurs a short distance offset from the pulsar, before then decreasing with increasing radial distance. The surface brightness values from analyses of both datasets are largely in agreement with the published values.

Using full ring regions for spectral extraction reduces possible biases arising from unaccounted for emission at larger azimuthal angles, or from selectively omitting part of the significant emission, as may be the case from the map inset in figure 6.18. However, this may also lead to a large contribution from background emission being summed around the ring.

Spectral Wedge Analysis

In order to better trace the emission (largely towards the South) and to ensure that the results of figure 6.21 are not biased by large regions of weak emission, a set of spectral wedges were defined with a fixed opening angle, based on the observed spread of significant emission around the azimuthal profile of the full radial extent (see figure 6.23). To characterise the distribution of the emission with azimuthal angle, the location of the minima were found by using a weighted moving average. The distribution to the whole region (from 0° to 1.6° radius) was found to be well described by a Gaussian distribution between the minima of the excess profile, as shown

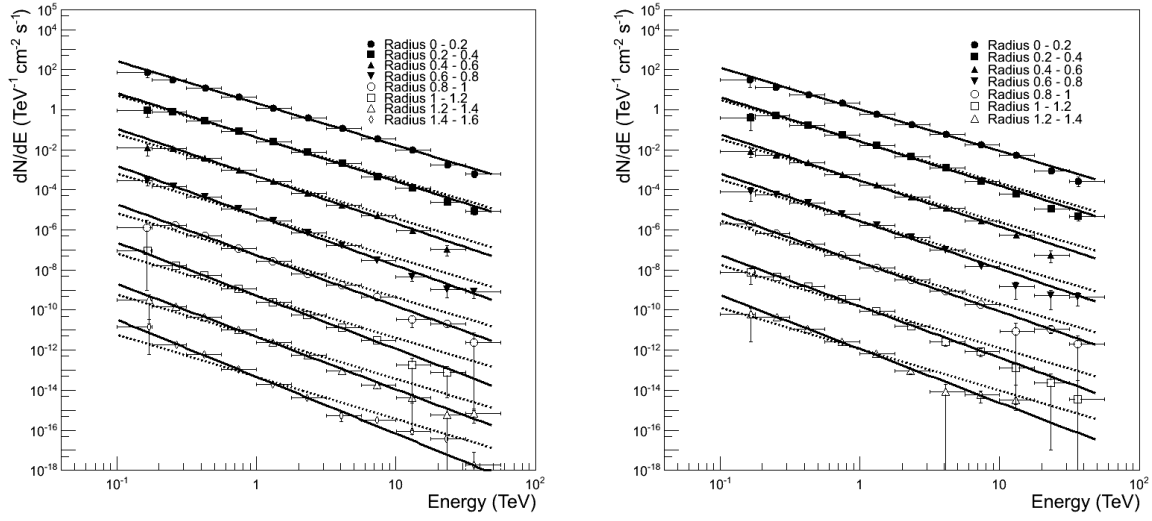


Figure 6.22: Overlaid spectra (from dataset A) with increasing radial distance; the spectra for each region are offset by an arbitrary flux scaling, to contrast with figure 6.18 (note the larger energy range encompassed by this analysis). Left: spectra extracted from ring-shaped regions around the pulsar. Right: spectra extracted from wedges with a fixed opening angle (emission beyond 1.4° was not significant in this case). The level of softening is in agreement in both cases.

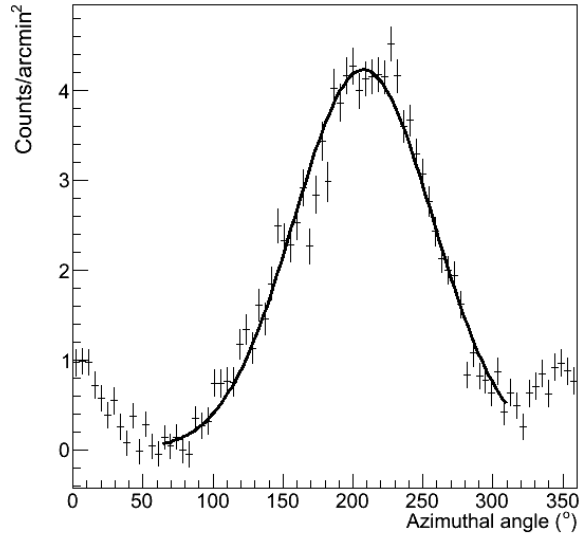


Figure 6.23: Azimuthal profile (from dataset A) for all emission extending from the pulsar out to 1.6° radius (equivalent to the area covered by all rings in figure 6.20), measured anticlockwise from 0° , defined to be in the direction of positive declination. Masks were applied to remove the other sources in the region, as shown in figure 6.20. The distribution is well described by a Gaussian between the excess minima.

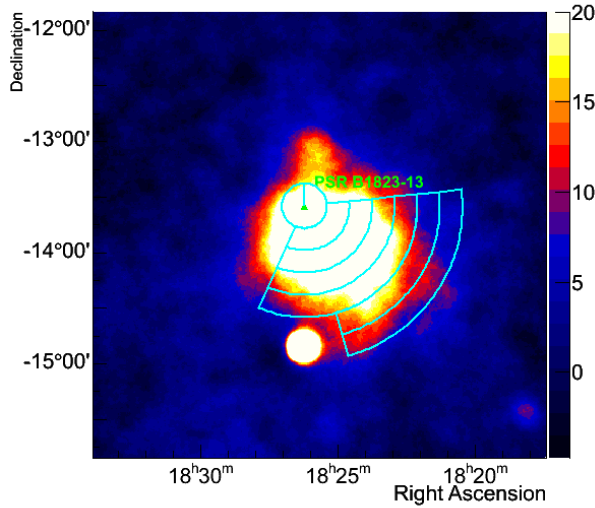


Figure 6.24: Significance map showing regions for spectral extraction using wedges centred on the pulsar out to 1.4° . The opening of the wedges were redefined with respect to [95], to better match the distribution of significant emission. A region at 1.4° offset from the pulsar, but 180° opposite to the spectral regions was also tested.

in figure 6.23. One advantage of this approach is to avoid integrating spectra over large areas of background emission at larger radial distances, thereby reducing the overall contribution of background emission to the spectral fit. Due to poor statistics, the innermost region was kept as a full circle as used in section 6.6.2, and the emission can be seen to extend in all azimuthal directions close to the pulsar (see figure 6.24). At large radial distances, however, this opening angle was constrained by the presence of LS 5039 to the South. The results of a spectral analysis of these regions are shown in figures 6.22 and 6.25.

In figure 6.25, it can be seen that for the wedge-based analysis the index softens as expected and as seen from the ring analysis; however, for dataset B the index remains more or less flat. This is at least partly due to the low significance of the dataset in the stereo analysis beyond $\sim 0.6^\circ - 0.8^\circ$, which can be seen from the maps in figure 6.12. The spectral measurement in these regions may be dominated by few, high energy events, leading to the harder measured indices; however, given the large uncertainties, these measurements all lie within $1 - 2 \sigma$ of the values obtained from dataset A and the 2006 publication.

The surface brightness appears to be slightly greater than previously measured for dataset A, yet lower for dataset B. This may be interpreted as follows: for the spectral wedges as defined in 2006, the opening angle was fixed for all radial distances, missing a significant component of the nebula emission at radial distances closer to the pulsar than LS 5039, yet also incorporating a larger area of insignificant emission towards the Northern and Eastern sides at larger radial distances. As the wedge opening angle has been redefined here to better match the emission, more of the significant emission and less of the insignificant region has been included; as such, it is unsurprising that the surface brightness is generally higher than the previous values for dataset A. Additionally, at larger radial distances, although the opening angle is then reduced with respect to the previous analysis, the increased livetime of dataset A enables low flux regions to become significant above background, also contributing to enhance the measured surface brightness.

Conversely, figure 6.25 also shows a reduced surface brightness in the dataset B analysis with respect to the previous values, especially at larger distances. This could be an artefact of the

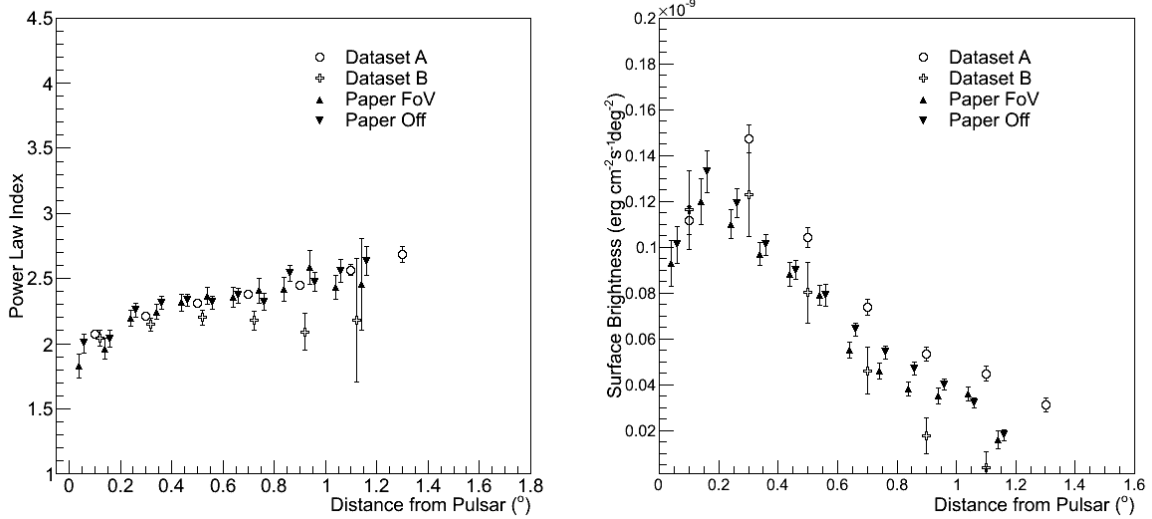


Figure 6.25: Results of a spectral analysis of the fixed opening angle wedge-shaped regions around the pulsar with both datasets A and B. The results from [95] corresponding to the Field of View and Off-data methods are labelled “Paper FoV” and “Paper Off” respectively. Left: power law index with distance from the pulsar for both datasets. Right: surface brightness with distance from the pulsar, shown with the results published in [95]. See also figure 6.21.

analysis sensitivity; given the reduced exposure of dataset B with respect to dataset A and that used in [95], large, low surface brightness components of the nebula may not yet be significant above the background emission. Nevertheless, the surface brightness should remain more or less compatible within statistical uncertainties for the innermost regions, and this is generally seen to be the case. In figure 6.25, the measured indices of the power law fits to dataset B are also harder than those found for dataset A, consistent with the interpretation of only the high energy part of the emission being significant above background in this shorter livetime dataset. No significant flux variation with time was seen over the entire period of observations.

The emission was also found to extend further than was previously detected, with spectral extraction up to 1.4° away from the pulsar being possible (1.6° in the ring-shaped region analysis). To verify that this extension was still part of the PWN emission, a test region at the same radial distance 180° opposite to this region was also used for spectral extraction. In this region, no known VHE sources exist (although being located close to the Galactic plane, the presence of significant amounts of Galactic diffuse emission and/or unresolved sources below the sensitivity limit of current instruments is also possible). This region was found to be non-significant and consistent with background, verifying that the extension to 1.4° away from the pulsar contains significant emission and is presumably still part of the PWN. In the ring analysis of section 6.6.2, measurements were also possible in the $1.4^\circ - 1.6^\circ$ band; however, as the distribution of emission across the ring width is not measured by the spectral analysis, a firm extent out to $\gtrsim 1.4^\circ$ only is established. At the distance of 4.12 kpc away (measured distance to the pulsar) this extent corresponds to a true size of nearly 100 pc. More detailed extent measurements are made in the next section.

Plausible models for the origin of this softening and a multiwavelength view of PWN HESS J1825-137; providing a more complete understanding of this source, are outlined in the following chapter.

6.7 Morphological Analysis

6.7.1 Azimuthal Emission Profiles

The distribution of emission in the nebula was profiled as a function of azimuthal angle in figure 6.23. Azimuthal angle was measured anticlockwise around the pulsar from 0° , defined to be in the direction of positive declination. The excess distribution between minima was well described by a Gaussian, implying that there is a preferred axis for the distribution and flow of energetic particles from the pulsar into the nebula, with some spread either side of this.

To better characterise how this distribution varied with increasing radius, the azimuthal distributions for each of the rings used for the spectral analysis of section 6.6.2 as shown in figure 6.20 were found, and a weighted moving average was used to find the location of minimum emission within the ranges of $0^\circ - 180^\circ$ and $180^\circ - 360^\circ$. Between these two minima, the excess distribution was fit by a Gaussian. In cases where it was found to give a better description of the profile (lower χ^2 of the fit), an asymmetric Gaussian distribution was used instead. Examples of these azimuthal distributions and their fits are shown in figure 6.26 for dataset A only, the statistics for dataset B being insufficient to allow measurements over such a wide range of radial distances.

From these fits, it was found that the spread of the emission reduces with increasing radial distance, whilst the peak of the emission remained roughly similar. The weighted average value of the Gaussian mean was found to agree with a linear regression of the Gaussian mean positions, at a value of $216.0^\circ \pm 0.6^\circ$. This angle was used to define the major axis of the emission emanating South of the pulsar. The position of the peak emission appears to shift slightly in azimuth angle as a function of distance. Whilst this may have a physical origin, with the exception of the innermost region, the $\sim 10^\circ$ azimuthal range in peak position could well be accounted for within systematic uncertainties.

As shown in figure 6.27, not only does the position of the mean shift with radial distance, but also the level of spread (as indicated by the standard deviation of the Gaussian fit) reduces. Three possible scenarios that could account for this feature are as follows: firstly; the physical spread of the particles responsible for the TeV emission is less at larger distances (possibly indicating that the flow of particles in the nebula was more channelled in the past, or that only the most energetic particles reached these distances). Secondly; at large radial distances, there remains an undetected population of older particles at larger azimuthal angles which have since cooled below the threshold for the production of TeV photons by Inverse Compton scattering. Finally; the particle transport via diffusion or advection differs parallel and perpendicular to the major axis of the nebula emission. The mean of the Gaussian fit to the innermost ring is considerably different from those of the outer regions. This is probably related to the larger azimuthal spread seen in this region closest to the pulsar than in the outer regions.

From the azimuthal distributions, the major axis of the TeV emission was defined as outlined above; using the mean of the Gaussian fits. The minor axis of the emission was subsequently defined to be perpendicular to this.

6.7.2 Slice Emission Profiles

In [95], a 2D Gaussian was fit to the morphology of the PWN over the entire energy range (to the maps as shown in figure 6.28). The major and minor axes of this 2D Gaussian fit, were used for excess slice extraction in a range of energy bands, as outlined in section 6.7.3.

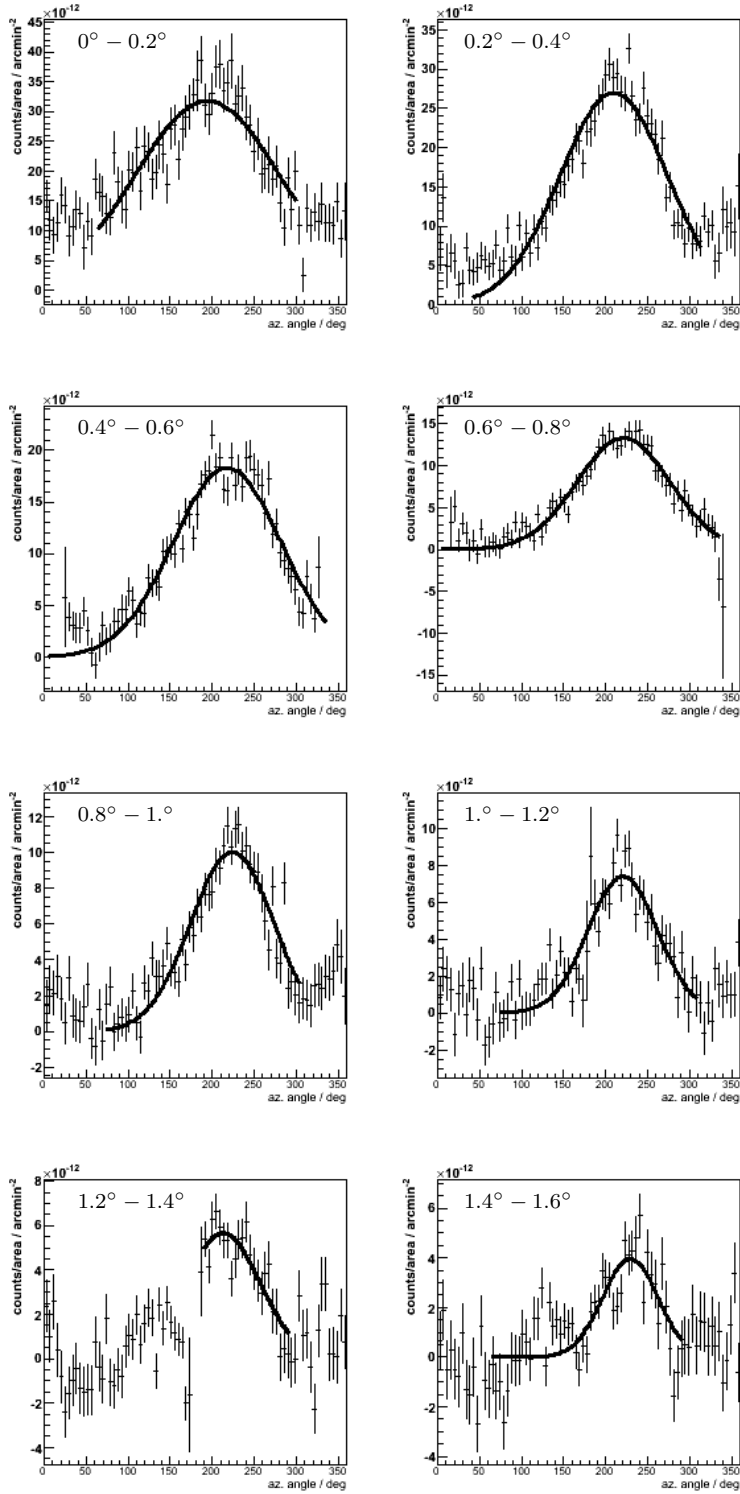


Figure 6.26: Azimuthal profiles of the (acceptance corrected) excess distribution around the pulsar as a function of radius (using dataset A). From left to right (and top to bottom), the profiles correspond to bands of increasing radial distance. In the innermost band (top left, $0 - 0.2^\circ$) the emission is seen to be rather broad, extending to all ϕ around the pulsar. Region $0.2^\circ - 0.4^\circ$ (top right) is one of the asymmetric Gaussian cases (implying more emission towards the South). From $0.4^\circ - 0.8^\circ$ (second row) there is an absence of emission around $340^\circ - 10^\circ$ due to the masked region over HESS J1826-130. In region $1.2^\circ - 1.4^\circ$ (bottom left) the fit is constrained by the subtracted emission from the location of LS 5039 at $\sim 160^\circ - 180^\circ$, which also accounts for a dip in flux/increased uncertainties at this point in the neighbouring regions $1.0^\circ - 1.2^\circ$ and $1.4^\circ - 1.6^\circ$; although there is little significant emission remaining in this outermost region (bottom right).

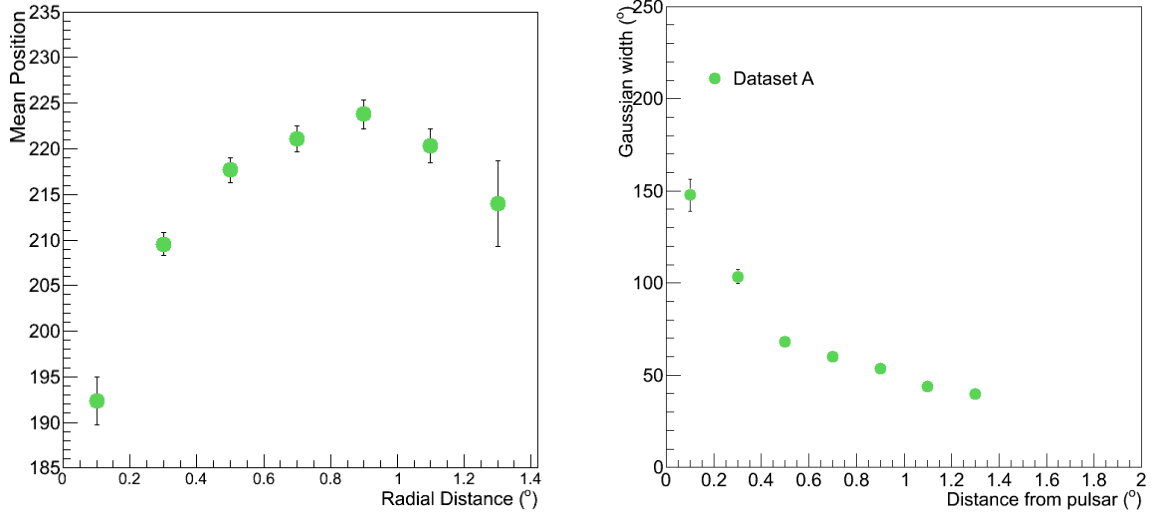


Figure 6.27: Left: Mean of the Gaussian fit to the azimuthal excess profiles shown in figure 6.26 as a function of radial distance. The position seems to shift with increasing distance. Right: azimuthal spread (standard deviation of the Gaussian fit) as a function of radial distance. With increasing distance, the spread appears to reduce.

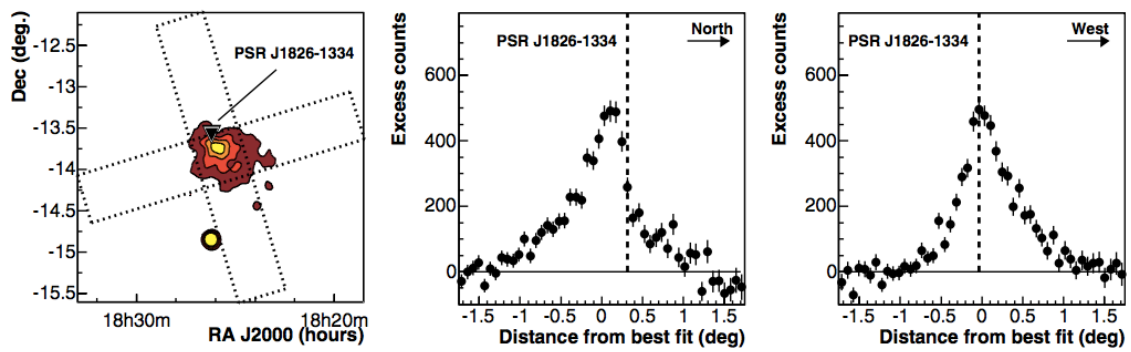


Figure 6.28: An excess map from [95], showing the slices used for extraction of the excess (along the major and minor axes of a 2D Gaussian fit), and the distribution of excess along those slices in relation to the centre of gravity, situated at $0.^\circ$ offset) and the pulsar position (marked with a dashed line). The excess emission can be seen by eye to extend to $\sim O(1.^\circ)$ towards the South.

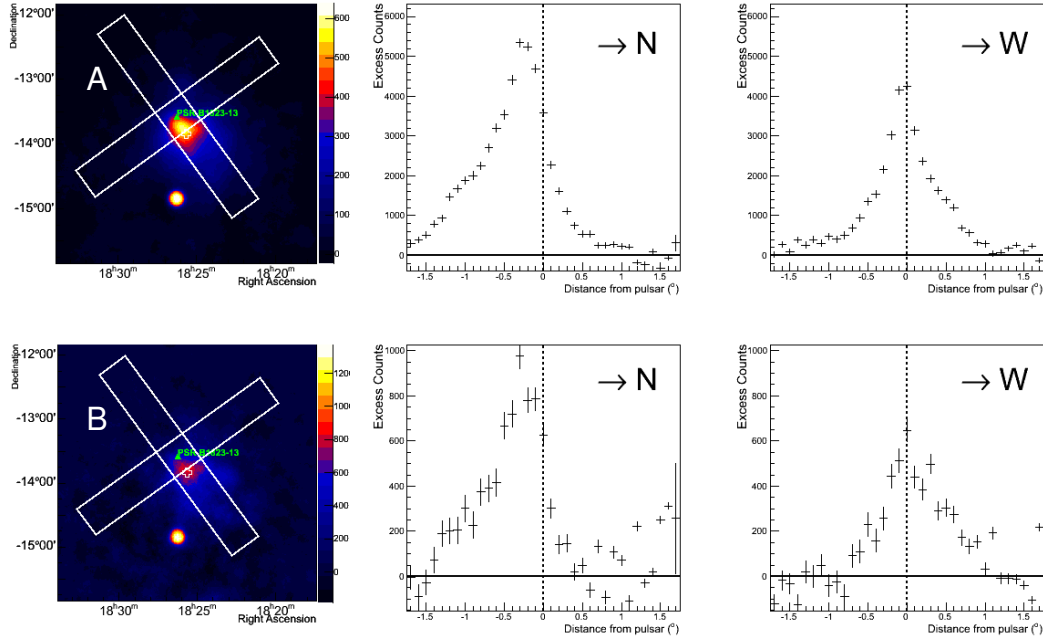


Figure 6.29: Slices taken along the major and minor axes from the excess map, centred on the pulsar position (indicated by a dashed line), with dimensions $3.5^\circ \times 0.5^\circ$. The emission peak is clearly offset to the South of the pulsar, with the emission extending out to $\sim 1.5^\circ$ from the pulsar. In contrast, the emission drops off extremely steeply from the emission peak towards the North of the pulsar. South and West are orientated towards lower values of declination and right ascension respectively. Shown for datasets A (above) and B (below, stereo analysis).

Slices were taken from the excess map along the major and minor axes of the emission as determined from the azimuthal profiles, with dimensions $3.5^\circ \times 0.5^\circ$. These slices are shown for datasets A and B in figure 6.29, with the position of the pulsar indicated by a dashed line. Along the North-South direction, the steepness of the drop in emission towards the North is reproduced, whilst the emission towards the South seems to extend further in dataset A than was previously seen in figure 6.28. Dataset B, however, is just half the length of the previously published analysis and is partially statistics limited as well as affected by fluctuations, such that the apparent extent is considerably less. In all cases shown in figures 6.28 and 6.29, there appears to be a change in slope of the emission towards the South, becoming less steep and broader from around -0.7° to -1.0° offset from the pulsar. This changing slope could be an indication of multiple components to the emission.

A Gaussian provided a poor fit to the excess distribution along the slice, although this was improved slightly by an asymmetric Gaussian fit. This is particularly due to the increased steepness of the distribution from the peak of the emission towards the pulsar position. Along the East-West direction, the emission is less peaked, such that the fitted full width at half maximum is typically broader than along the North-South direction. In general, these profiles are consistent with the picture of a pulsar wind continuously injecting particles into the nebula towards the South and away from the North, such that the particle population spreads out preferentially in this direction; with spreading along the East-West direction (corresponding to the azimuthal spread) occurring gradually over time. This propagation direction and spread is perpendicular to the proper motion of the pulsar across the sky (the extrapolated birth location of the pulsar is indicated by an upwards triangle in figure 6.6). The steep drop observed towards the North could be due to a combination of physical effects (such as asymmetric crushing by a reverse shock

from the progenitor supernova) and projection effects, especially as the component of the pulsars velocity along the line of sight is not known. Corresponding profiles of the excess emission made in different energy ranges are provided in the appendix C.

6.7.3 Energy Dependent Morphology

The spectral analyses in section 6.6.2 have shown the spectrum of TeV γ -ray emission to vary across the nebula; correspondingly, morphological variation of the nebula with energy is also expected, and was demonstrated in [95]. Within the scenario of a changing spectral index with increasing distance from the pulsar, one would expect that the extent of the nebula would also change as a function of energy. Harder spectral indices closer to the pulsar imply that there is more high energy emission present here than in the outer regions of the nebula with softer measured spectral indices. Given the known energy dependent morphology of this source, maps of HESS J1825-137 were taken across a range of energy bands, to further explore how the extent of the emission varied with energy. To investigate this property, the region was mapped in 8 energy bands; < 250 GeV; $250 - 500$ GeV; 500 GeV – 1 TeV; $1 - 2$ TeV; $2 - 4$ TeV; $4 - 8$ TeV; $8 - 16$ TeV and > 16 TeV.

Radial Profiles

The major and minor axes as defined from the azimuthal profiles were used to divide the nebula and surrounding region into independent areas for characterising the extent, as shown in figure 6.30. Taking the minor axis passing through the pulsar position, the region was divided into Northern and Southern halves; the radial profile of the (acceptance corrected) excess distribution showed in both cases decreasing excess counts with increasing distance. The peak of the emission is, however, offset towards the South of the pulsar. The Southern region could be further subdivided into two quadrants, A and B, by splitting along the major axis of the emission; however, this was not done for the Northern region, as the level of emission was far less significant and did not extend to as large radial distances.

In order to measure the radial extent of the nebula in each energy band, an approach using the radial profile, extending from the current pulsar position, was adopted. Figure 6.30 illustrates the region extracted in each energy band; a mask of 0.2° radius was applied over LS 5039 (HESS J1826-148) and of 0.3° radius over HESS J1826-130, to avoid contamination of the profile of the excess nebula emission, which could affect the extent measurement. When making measurements of the extent of emission, it is particularly important to ensure that any asymmetries in the relative exposure of the dataset to different regions of the sky have been taken into account. This is done by dividing the excess profiles by the acceptance profiles, which provide the number of expected γ -ray events at a particular position given the exposure and sensitivity of the dataset, thereby effectively correcting for this effect.

From figure 6.31, it can be seen that the emission does not drop away from the pulsar directly, but rather that the peak emission is roughly flat out to $\sim 0.2^\circ$ radial distance, after which the emission starts to drop. The extent of the emission was characterised by fitting a polynomial to the radial profile, in the range $0.2^\circ - 2.4^\circ$, using the formula:

$$y = \begin{cases} a(r - r_0)^n + c & (x < r_0) \\ c & (x \geq r_0) \end{cases}, \quad (6.7.1)$$

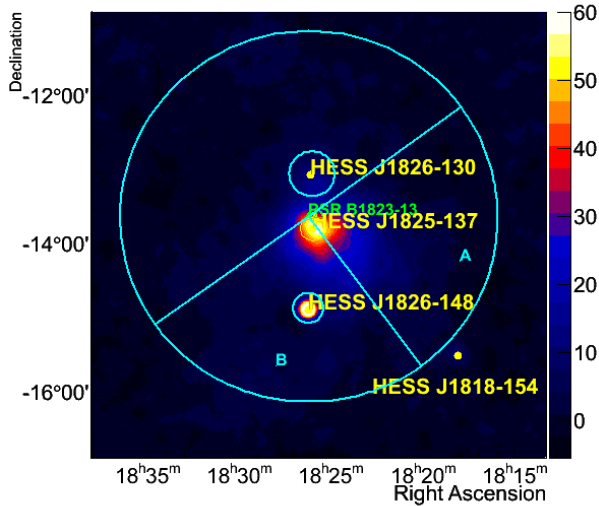


Figure 6.30: Significance map of HESS J1825-137 showing the regions used for characterising the extent of the nebula. The North-South divide is taken along the minor axis of the emission as determined by the azimuthal profiles, and passing through the pulsar position. The Southern region was also further subdivided along the major axis into two quadrants, labelled A and B. Also shown are the masked regions around two other H.E.S.S. sources falling within these regions; emission from within the masks over LS 5039 (HESS J1826-148) and HESS J1826-130 were subtracted from the radial profiles.

such that with increasing r , the emission decreases out to a distance r_0 at which it assumes a constant value, c . Whilst the parameter a simply provides the overall normalisation, the fitted value of r_0 characterising the extent, was found to be highly sensitive to the order of the polynomial n , with r_0 increasing strongly with increasing n as shown in figure 6.32. To mitigate this effect and to characterise the extent in a more robust manner, a moving average was used to find the location and value of the peak of the emission. The radius at which the fitted function dropped to a fixed fraction of the peak value (e.g. 10%, r_{10}), was then used as an alternative measure of the nebula extent. In contrast to r_0 , the parameter r_{10} was found to be robust against the order of the polynomial n (figure 6.32), and the fixed fraction radius was used to characterise the emission in all energy bands, with $n = 3$ chosen arbitrarily.

The radial profile of the emission could be equally well described by an exponential function, as well as the polynomial given in equation (6.7.1). Rather than using 10% of the peak flux as outlined above, the distance at which the flux reduced to 50% of its peak value (i.e. the full width at half maximum, FWHM) was adopted to measure the extent. As can be seen from figure 6.31, at the 10% flux level, the measurement is entering a regime dominated by noise, rendering the measurement less reliable than taking the FWHM. Furthermore, the FWHM is a more stable measure of the extent which should remain robust against effects due to the livetime of the dataset in the case of approximately Gaussian distributed emission. This is particularly important given that the peak location also shifted closer to the pulsar with increasing energy, such that the range of the fit gradually changed from $0.2^\circ - 2.4^\circ$ in the lowest energy bands (figure 6.33), to $0.^\circ - 2.4^\circ$ at high energies (figure 6.34). Both polynomial and exponential functions were used to fit the radial profiles and estimate the nebula size, as the true size should be independent of the fit model used. As well as a useful cross check, this also provides an estimate of the systematic uncertainties. The distance at which the fitted function evaluated to half of the peak value was found to be consistent between the polynomial and exponential fits.

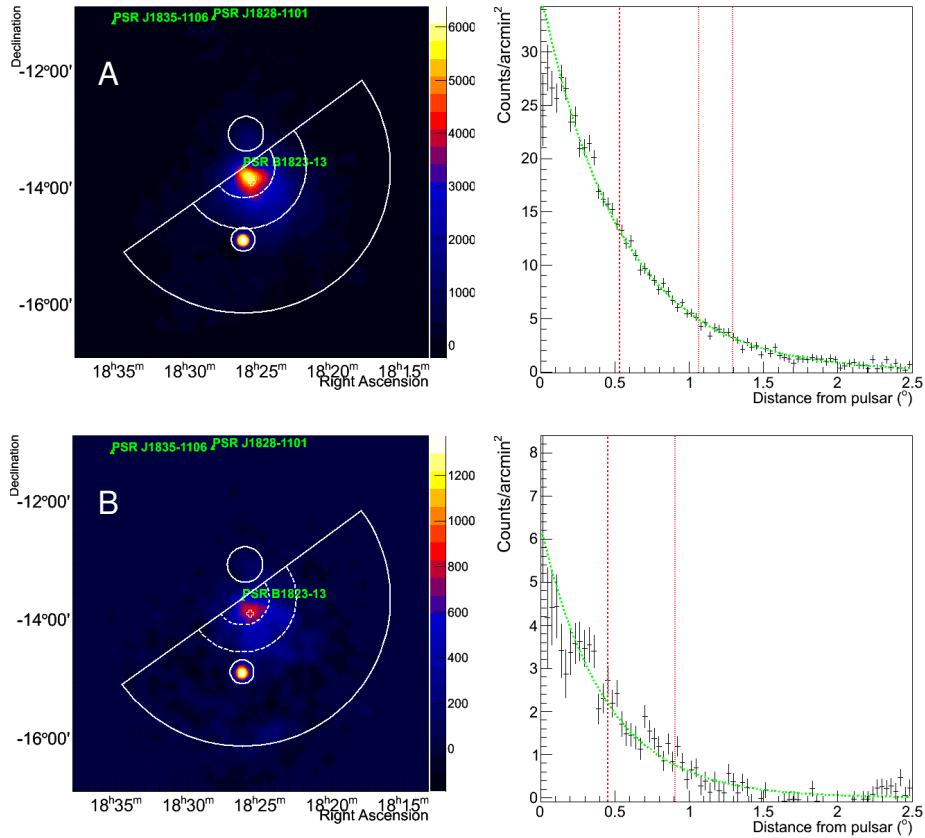


Figure 6.31: A semi-circular region (left), with the pulsar at the apex and a mask applied over LS 5039, was extracted from the excess maps to form a radial profile of the emission (right), shown here for the full energy range with dataset A (above) and for dataset B (below). The radial profile was fitted by a polynomial (equation (6.7.1)) to characterise the extent of the emission. Dashed and dotted lines mark the FWHM, twice the FWHM and (for the high statistics dataset A) the radial distance at which the emission drops to 10 % of the peak value respectively.

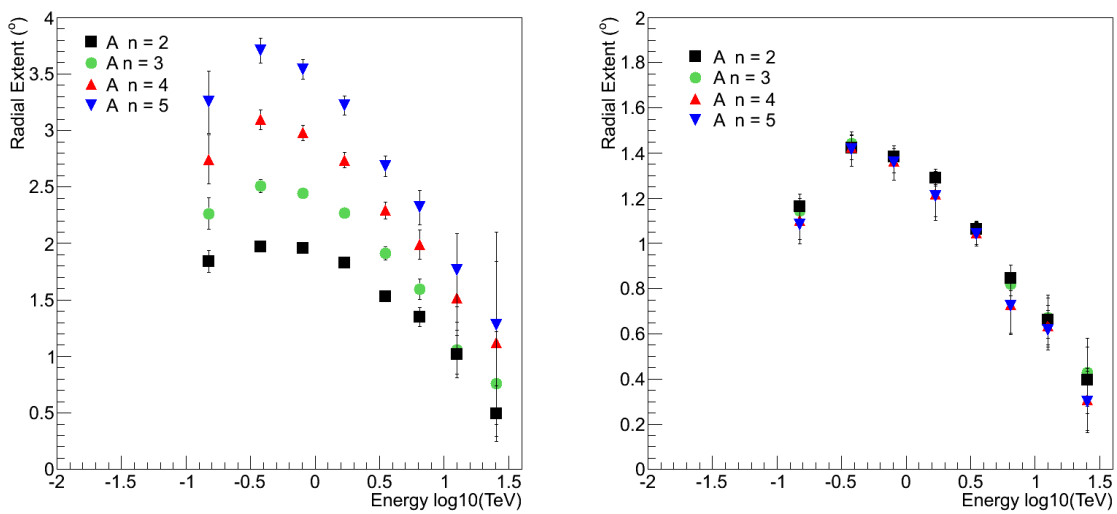


Figure 6.32: Left: radial extent with energy using the fitted value of r_0 from equation (6.7.1). Right: radial extent with energy using r_{10} ; the radius at which the fitted function drops to 10 % of the peak of the emission. The latter approach, of measuring the radius where the emission reaches a fixed fraction of the peak, is found to be robust against the order of the polynomial.

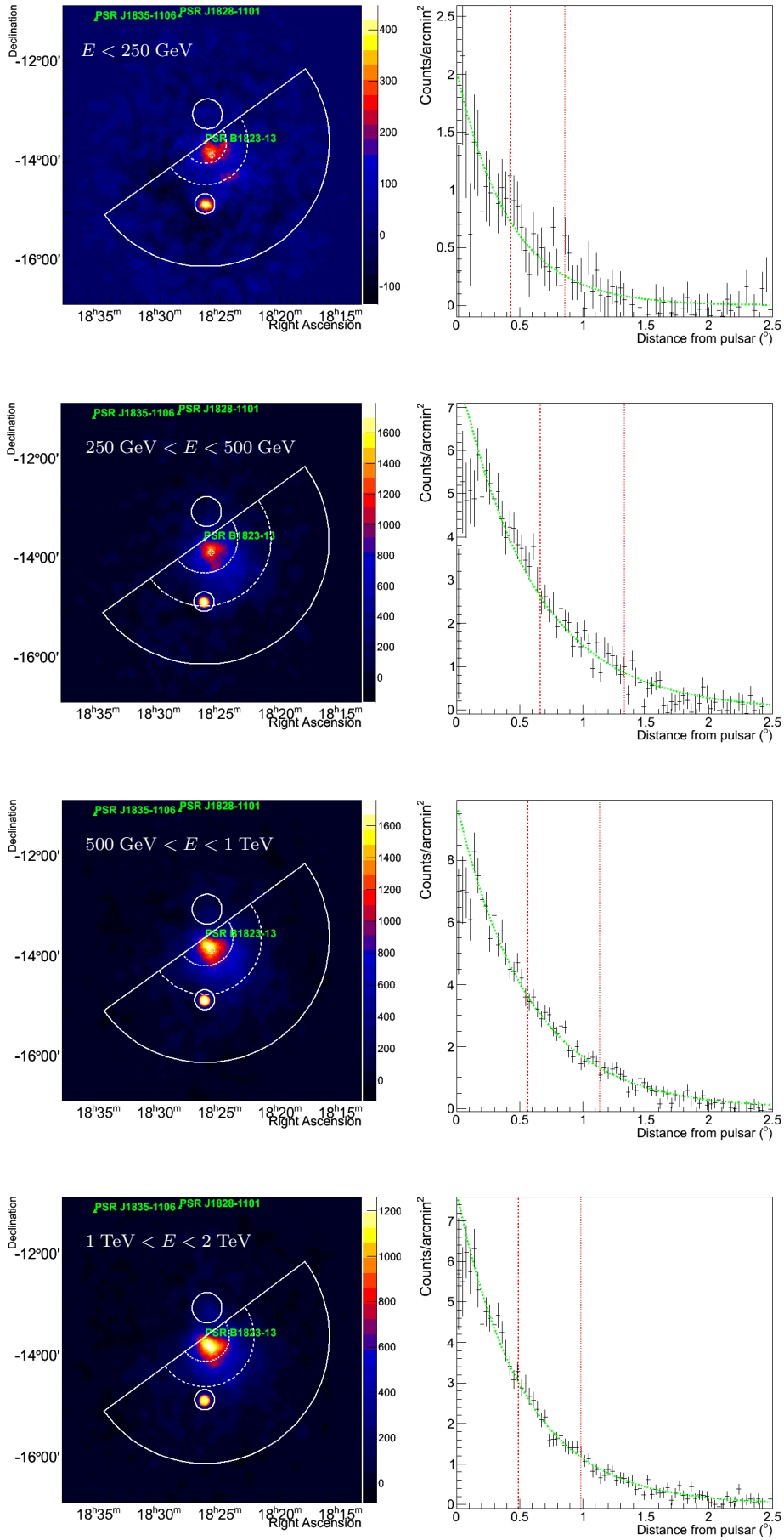


Figure 6.33: Excess sky maps and radial profiles of the emission made with dataset A in four energy bands below 2 TeV.

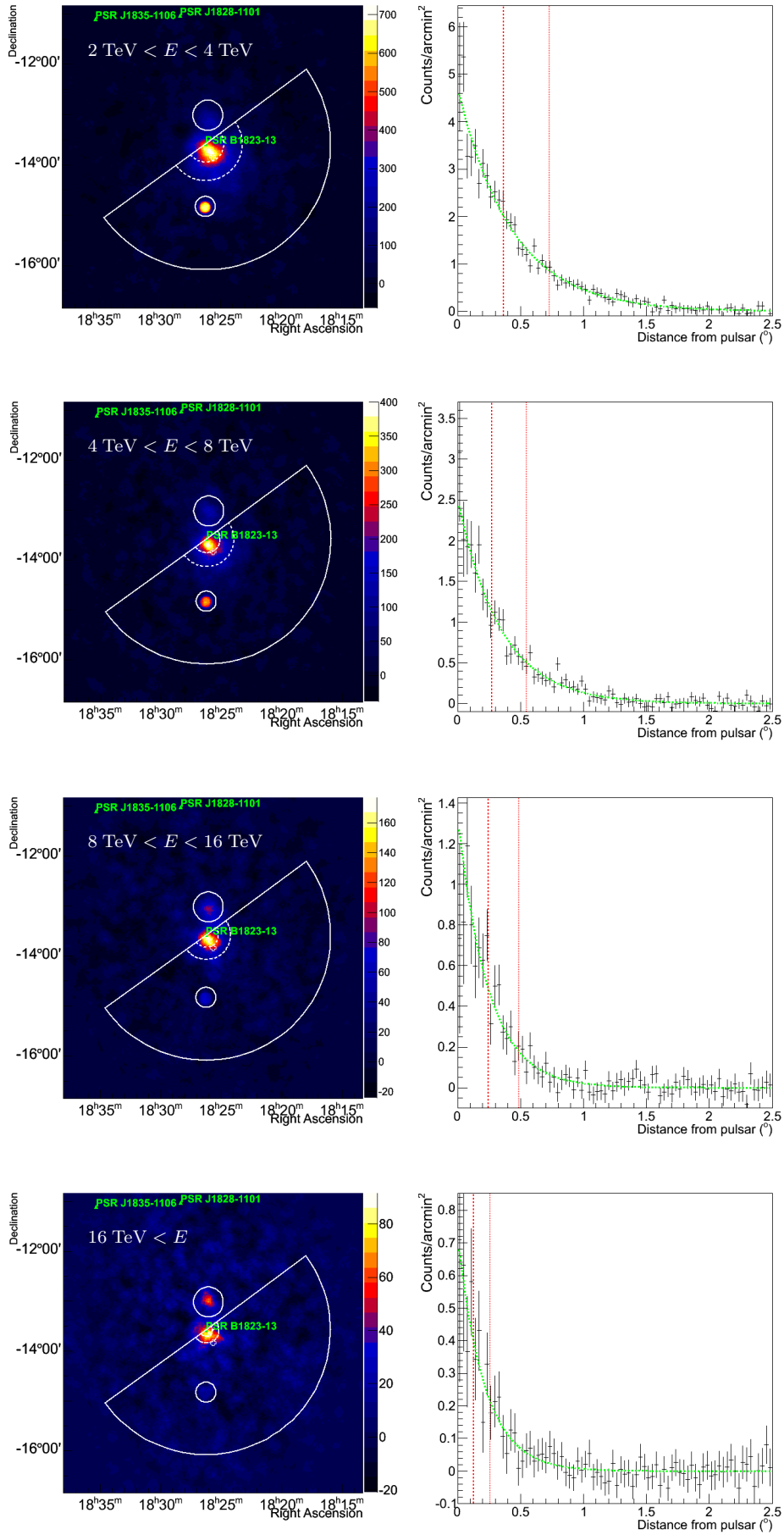


Figure 6.34: Excess sky maps and radial profiles of the emission made with dataset A in four energy bands above 2 TeV.

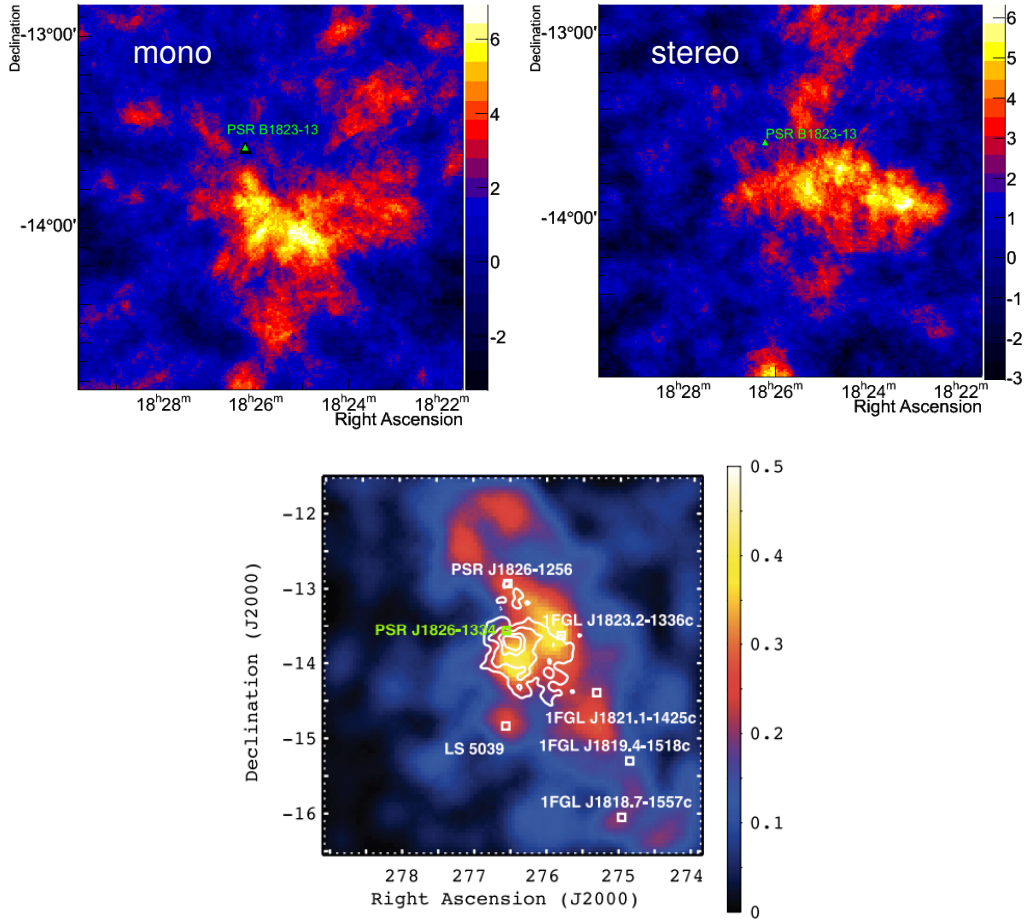


Figure 6.35: Above: H.E.S.S. maps below 250 GeV made from dataset B using mono (left) and stereo (right) analyses respectively. Below: counts map from the Fermi-LAT above 10 GeV; the instrument is sensitive in this analysis to the energy range 100 MeV - 300 GeV. The overall distribution of the low energy emission is consistent between analyses, although statistics limited here in comparison to figure 6.33. Fermi-LAT map taken from [111]

View with the Extended Energy Range of H.E.S.S. II

With the introduction of CT5, the H.E.S.S. II array has improved sensitivity at lower energies, such that it is instructive to compare maps of the distribution of emission in the lowest energy bands between analyses. In comparison to the lowest energy map of figure 6.33, which shows more emission close to the pulsar, in analyses of dataset B, the emission seems to peak at larger radial distances from the pulsar (see figure 6.35). In the mono analysis (with the lowest energy threshold), this is seen to be further towards lower declination, whilst for the stereo analysis the distribution lies further towards lower right ascension. This could be either an instrumental effect, due to the poorer angular resolution of the CT5 mono analysis, or a physical effect, where there is indeed more emission at the lowest energies (to which only CT5 alone is sensitive) in the region towards lower declination. Comparing these maps to a counts map above 10 GeV from the Fermi-LAT satellite based instrument (which for this analysis was sensitive in the range 100 MeV - 300 GeV), the broad distribution of emission appears to be consistent with the lowest energies of the H.E.S.S. analysis; that is, largely offset from the TeV peak and the pulsar position.

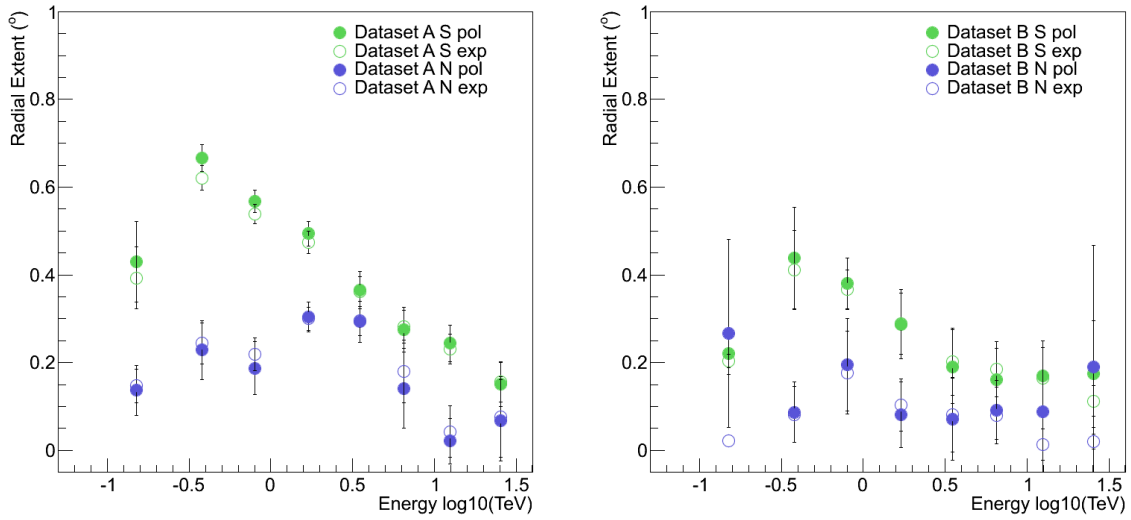


Figure 6.36: Radial extent (FWHM) as a function of energy, measured within the Northern and Southern regions as shown in figure 6.30. Shown for datasets A (left) and B (right); both the polynomial and exponential fits agree within errors in all cases. (Except for the lowest energy band in dataset B on the Northern side of the pulsar, where the fit failed due to poor statistics.)

Radial Extent with Energy

Figure 6.36 shows the measured extent (FWHM) using both procedures within the Northern and Southern regions as a function of energy, for both datasets A and B. The nebula appears smaller on the Northern side, which exhibits some mild change in extent with energy. On the Southern side, however, there is a strong dependence of the nebula extent with energy; the implications of this are explored in more detail in chapter 7.

As seen in figure 6.36, the nebula extent appears to be smaller in dataset B than in dataset A. To check whether this effect is due to the different exclusion regions used for datasets A and B (see figures 6.10 and 6.13), dataset A was re-analysed using the exclusion regions otherwise used for dataset B. If the exclusion regions used were inadequate, then some significant emission may have formed part of the background emission, leading to significant emission being removed in the analysis and a reduction in the overall size. (The converse test, of using larger exclusion regions for dataset B, is ill-advised with the lower statistics and the smaller field of view of CT5, as it was found to introduce artefacts into the maps, especially in the case of separate energy bands.) This test is shown in figure 6.37. With smaller exclusion regions, the measured size from dataset A is indeed seen to reduce, yet still remains above the size measured in dataset B. Therefore, choices made at the analysis level are not solely accountable for the different measured sizes seen between the datasets.

If the fit well describes the data, then the full width at half maximum should be relatively robust against effects such as the total exposure time of the dataset, and the variation in acceptance across the field of view having been corrected for. However, if the emission has a long, comparatively low flux tail, and the noise in the dataset is large in low flux regions, then the fit can be affected by the presence of the noise (or equivalently, the absence of a tail). This can lead to a steeper fit than the true distribution, or, with low livetime, a less significant and consequently less well defined peak value and location. Also, as the peak increases, then whilst the magnitude of half of the peak value also increases, the spread will be larger, such that the true half of the peak value may correspond to a larger radial distance than previously (i.e. the

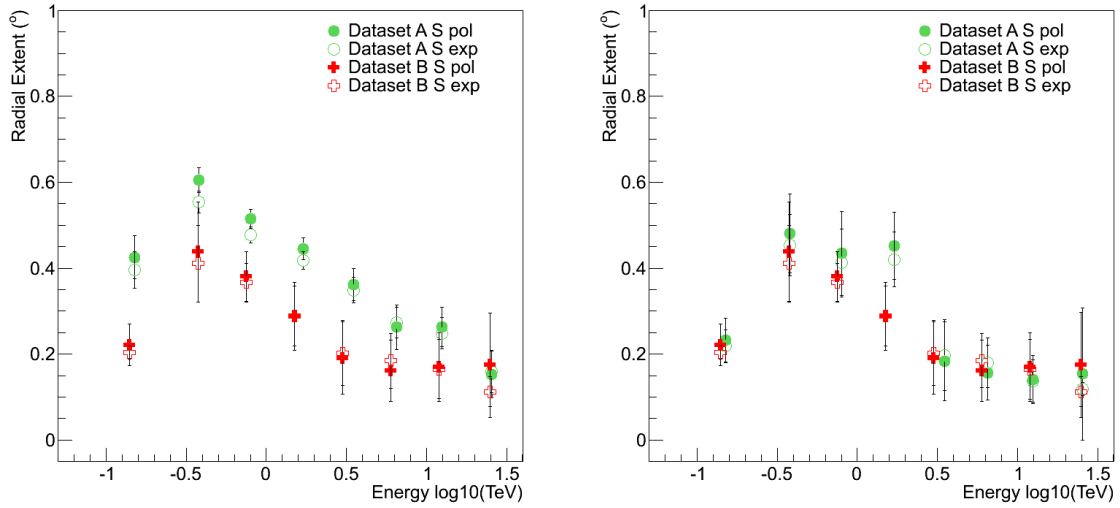


Figure 6.37: Left: Using the small exclusion regions of dataset B on dataset A, the extent reduces slightly with respect to figure 6.36, yet remains above the level seen by dataset B, such that differences between analyses are not solely accountable for the difference in measured extent. Right: Reducing dataset A (as analysed with the small exclusion regions used for dataset B) to 10% of its length, approximately the livetime of dataset B, the extent measurements were found to be well in agreement. This is a consequence of the large, low flux tail of the nebula being subsumed by noise in short livetimes, and of the non-Gaussian distribution of the emission.

relative flux increase may not be the same if the sensitivity to emission has markedly improved). Combined, these effects can lead to an underestimate of the true extent of the nebula in lower livetime datasets, where the fit and measured extent comprises only the brightest regions (as well as a secondary effect from the exclusion regions used for the analysis). This was indeed found to be the case; by taking a cross section of dataset A corresponding to approximately the same livetime as dataset B (and with the same exclusion regions), the extent measurements were then found to be in agreement, as demonstrated in figure 6.37.

Subdividing the Southern region into two quadrants along the major axis of the emission (see figure 6.30), it was found that the emission was more extended in quadrant A than quadrant B, as shown in figure 6.38. This is indicative of further asymmetries in the particle distribution and/or transport across the nebula.

Given the distance to the source of 4.12 kpc, a maximum extent of 1.4° as seen by doubling the FWHM extent, would correspond to a physical size of ~ 100 pc. This value is in rough agreement with the 1σ radius of 0.75° , found as part of the second Fermi-LAT catalogue of hard spectrum sources (2FHL) [112]. The implications of this measurement and some physical interpretation of figure 6.36 is given in chapter 7.

The detection of emission which is more compact at higher energies with a peak located closer to the pulsar position, is consistent with the current physical interpretation of injection of highly energetic electrons by the pulsar into the surrounding environment, which gradually spread out, by diffusion or advection, into the surrounding environment and cool down [95]. This cooling down accounts for the lack of high energy emission at larger distances from the pulsar, whilst the peak of the low energy emission is located farther out than the higher energy emission peaks. This is complementary to measuring this cooling via the softening of the spectral index; at larger distances from the pulsar, with less high energy emission and more low energy emission, the spectrum becomes softer.

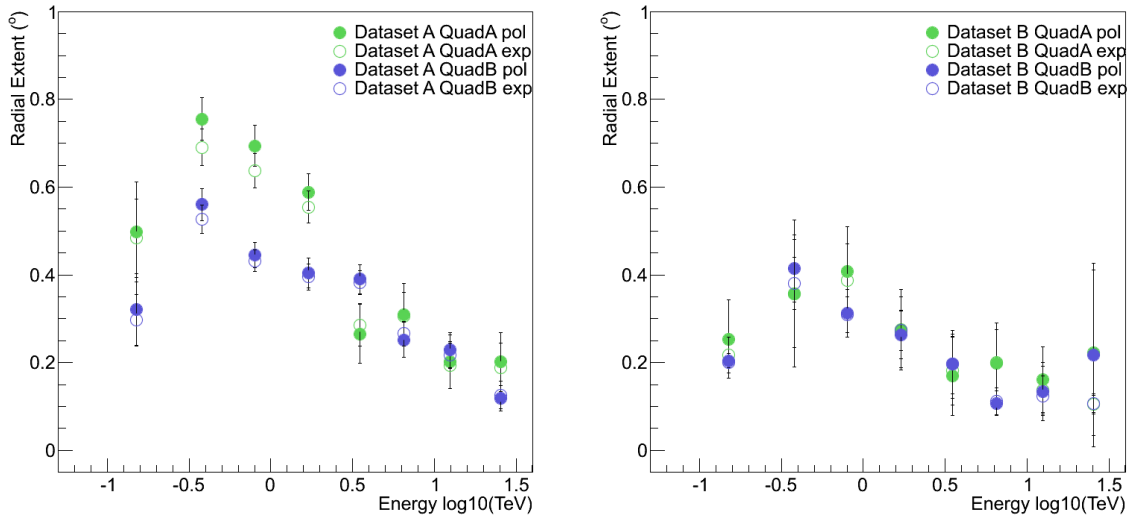


Figure 6.38: Radial extent of the nebula on the Southern side, divided into two quadrants, A and B, as shown in figure 6.30, and measured by datasets A (left) and B (right). The emission is clearly more extended in quadrant A than in quadrant B for both datasets.

6.8 Conclusions on Analysis of HESS J1825-137

Given the large angular extent of HESS J1825-137, despite its ~ 4 kpc distance, it offers considerable opportunity for in-depth studies of pulsar wind nebulae. The H.E.S.S. dataset, spanning over ten years of observations, lends itself to detailed studies of the spectral evolution of the particle population within the nebula, as well as of morphological studies of the particle distribution via the TeV γ -ray emission. For example, the steep drop in excess flux seen along the North-South direction at the pulsar position points towards a sharp physical boundary or projection effect occurring at this point. This could indicate the presence of a shock front, or that the pulsar is on the brink of leaving the nebula. Given the trajectory of the pulsar, however, apparently tangential to the edge of the nebula distribution, this implies that the ambient medium surrounding the pulsar varies significantly on either side of this transition boundary. Also, measurements of the changing extent with energy and of the spatially resolved spectra enable particle transport mechanisms and interior properties of the nebula to be constrained.

Further interpretation of the analysis results presented in this chapter, particularly in the context of multiwavelength observations and of various models of the formation and evolution of pulsar wind nebulae, will be presented in chapter 7.

7 HESS J1825-137 in Context

In order to fully interpret the analysis results of chapter 6, some context needs to be provided. Therefore, in this chapter an overview of previous observations of HESS J1825-137 and its pulsar PSR B1823-13 will be given in section 7.1, including observations in several wavelength bands besides γ -rays, and using γ -ray detectors complementary to IACTs. Sections 7.2 and 7.3 aim to provide some interpretation in a model-independent manner. Given the anomalously large physical extent of the PWN, transport mechanisms should be explored in more detail, and the implications of the measured extent and change in extent with energy are covered in section 7.2. By combining a H.E.S.S. VHE γ -ray analysis with a spatially coincident re-analysis of X-ray data, it is possible to map the magnetic field strength in the inner nebula, as will be shown in section 7.3. A brief review of approaches to modelling PWN, and of previous attempts at modelling HESS J1825-137 in particular, is given in section 7.4. To explore the global properties of the PWN, simple, one-zone models are applied in section 7.5 in an attempt to match the overall spectral energy distribution obtained by combining data from the Fermi-LAT and from the H.E.S.S. experiment. These models are constrained by measured quantities of the systems, and the resulting curves are compatible within the limits and caveats of such an approach. Possible future extensions to these models are outlined.

7.1 Multiwavelength Data

Previous observations of HESS J1825-137 and the associated pulsar PSR B1823-13 have been made across many different wavelengths, enabling a more complete picture of this object to be formed than can be achieved in just one wavelength band.

7.1.1 Radio, Infrared and Optical Data

A search for counterparts in archival data at lower wavelengths was done by [98] (to complement their X-ray analysis); with three plausible sources found in the radio regime. One of the radio sources (region A in figure 7.1) had a counterpart in the infrared; this emission was attributed to thermal radiation from dust and from nearby molecular clouds. A subsequent search for molecular clouds in the vicinity yielded a CO counterpart, its colocation identified via the distance estimate, derived from the velocity profile of the CO emission.

Molecular Clouds

A recent study of gas in the Interstellar Medium (ISM) around HESS J1825-137 (particularly towards the North) measured several different molecular gas tracers and investigated the possibility of an association between HESS J1825-137 and the hard spectrum source HESS J1826-130 towards the North [113].

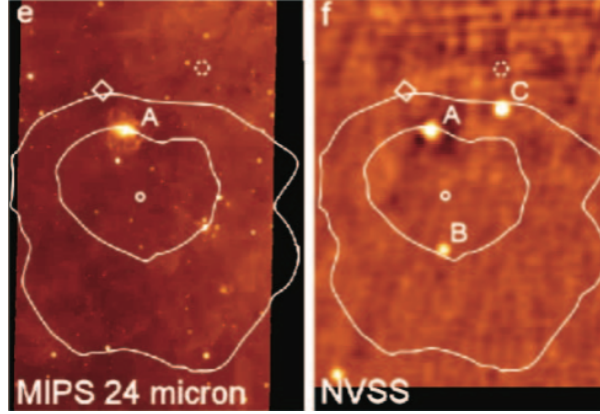


Figure 7.1: View of the HESS J1825-137 region in infrared (left) and radio (right) bands, with TeV contours from [95] overlaid. The infrared data at $24\ \mu\text{m}$ was taken from the *Spitzer* MIPS as part of the GLIMPSE survey, the radio data at 1.4 GHz from the NRAO VLA Sky Survey (NVSS). Solid and dashed circles indicate the current position and projected birth location of the pulsar respectively. Region A is present in both images. Figure taken from [98].

In particular, they probe the extent of $\text{CO}(1-0)$, $^{13}\text{CO}(1-0)$, CS, ammonia (NH_3) and $\text{H}\alpha$ in the region. In the case of the $\text{H}\alpha$ map, the presence of a rim of $\text{H}\alpha$ gas is seen at a radius of approximately 120 pc from the pulsar. This may be attributed to the outer shock region of the progenitor supernova of HESS J1825-137, which has remained hitherto undiscovered. The distance to this gas determined from the line of sight velocity is approximately the same as the distance to the pulsar PSR B1823-13 (P1 in figure 7.2). The observed radial distance of this rim from the pulsar is in agreement with the SNR radius predicted in a 2009 study on the implications of H.E.S.S. observations of the PWN Vela X and HESS J1825-137 [114].

In addition to the discovery of this SNR rim, [113] also identified the presence of several molecular clouds in the surrounding region, with a distance estimate in agreement with the dispersion measured distance of PSR B1823-1334. Of particular interest are the regions R1 and R5, situated to the North of HESS J1825-137, shown in figure 7.2. Region R1 in particular shows indications of turbulent gas, with several velocity peaks and wide velocity dispersion in $\text{CO}(1-0)$.

One possible interpretation of this region is that the SNR shock towards the Northern side of the pulsar was severely slowed down by the presence of the molecular clouds, accumulating large amounts of mass at the shock front and generating turbulent motion of the gas. At comparatively early times in the SNR evolution, due to the mass accumulation and slowing of the shock front in the molecular cloud, a reverse shock formed on the Northern side which returned back towards the pulsar. This reverse shock caused the PWN to become offset due to its passage through the nebula, leading to the observed highly asymmetric nebula. Continuous emission from the pulsar wind into the nebula was subsequently emitted in a preferentially Southerly direction.

An additional region towards the South of HESS J1825-137 (R6, also shown in figure 7.2) was found to have a broad spatial distribution of $\text{CO}(1-0)$ gas in the region, and may modify the morphology of the nebula in this region [113].

7.1.2 X-ray Data

In a manner analogous to that adopted by the VHE γ -ray analysis, previous analyses of X-ray data (by the satellite based XMM-Newton [100], Chandra [98] and Suzaku [115] telescopes) were able to extract spectral data from multiple regions, focusing on a core at the location of the pulsar and a more diffuse region extending further out. The first detection of X-ray emission was

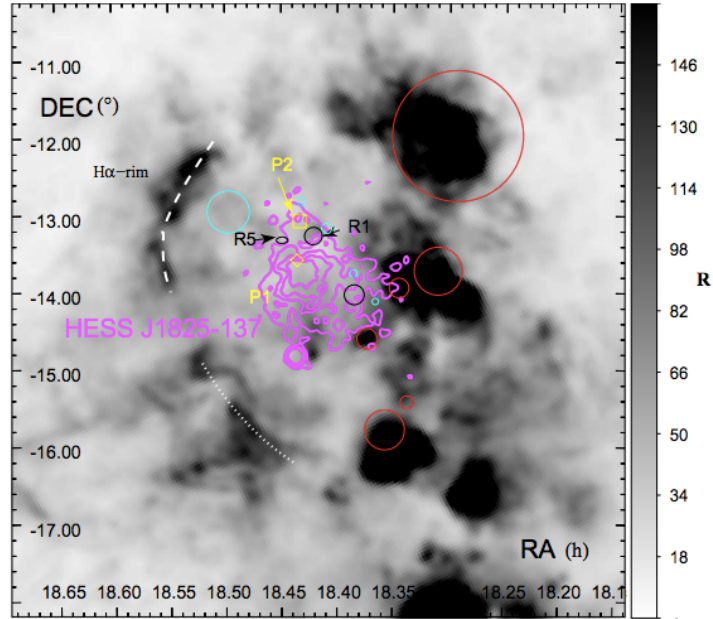


Figure 7.2: $H\alpha$ map of the HESS J1825-137 region, showing a ridge-like structure towards larger right ascension (indicated by the dashed white line), and clumps of $H\alpha$ emission corresponding to known HII regions towards lower right ascension values (indicated by red circles). The H.E.S.S. contours from 2006 [95] are overlaid in magenta, the locations of nearby molecular clouds are indicated by black circles, labelled R1 and R5 towards the North and region R6 towards the South. The pulsars associated with HESS J1825-137 and HESS J1826-130 are shown by yellow boxes and labelled P1 and P2 respectively. A tentative second $H\alpha$ SNR rim is indicated by a dotted white line. Figure taken from [113].

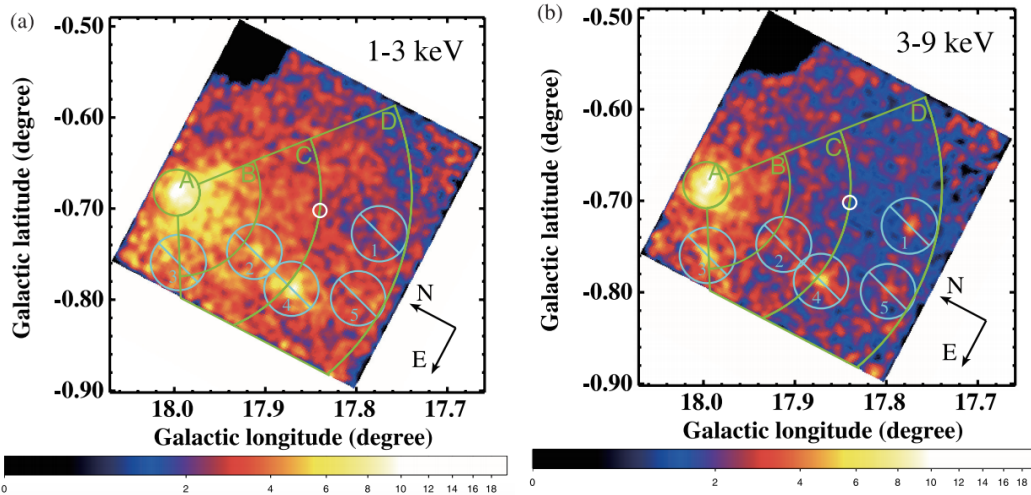


Figure 7.3: Suzaku maps of the HESS J1825-137 region in Galactic coordinates, showing the Suzaku field of view and the four regions A-D identified in the X-ray observations. Maps were made in two independent energy bands, 1 – 3 keV (left) and 3 – 9 keV (right). Also indicated are the locations of five point sources excluded from the analysis. Figure taken from [115].

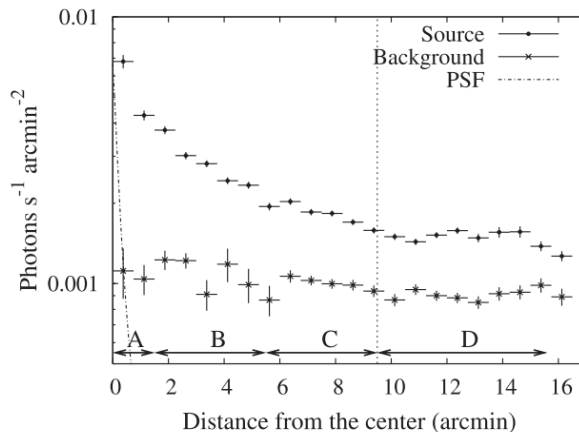


Figure 7.4: Radial profile of the X-ray surface brightness with distance from the pulsar, as measured by the Suzaku telescope, with regions A-D indicated. A dashed line indicates the peak of the VHE γ -ray emission, offset from the pulsar, as measured by [95]. Figure taken from [115].

found by ROSAT [99], where the existence of an extended nebula component to the emission was already apparent, and the similarity of the pulsars spin properties to the well studied Vela pulsar object and nebula was discussed. The XMM-Newton published X-ray analysis of this object also found that it was comprised of two components, a core region, 30 arcseconds across, and diffuse region extending 5 arcminutes towards the south, with distinct spectral features [100]. Following observations with the Chandra satellite, the existence of two components to the emission, a compact core and a diffuse component with distinct spectral parameters, was again verified. Suzaku detected emission in two further zones with increasing distance from the pulsar in addition to the previously identified core and diffuse regions (as defined by the Chandra and XMM-Newton analyses, see figure 7.3). The PWN is clearly extended in X-rays, with emission significantly above background out to a radius of 16 arcminutes, as shown in figure 7.4.

The spectral properties of both the core and diffuse components of the PWN as found by all three X-ray satellites are summarised in table 7.1. In all cases, the parameters are quoted for a power law (PL) model, (energy dependence of the emission varying as $\propto E^{-\Gamma}$) with fluxes corrected for interstellar absorption. The values quoted from the XMM-Newton and Chandra observations are for a fixed Hydrogen density of $1.0 \times 10^{22} \text{ cm}^{-2}$, whilst the Suzaku values are compatible with 1.0 for all regions, although lower values for the Hydrogen density are favoured at larger radial distances from the pulsar. Furthermore, the Suzaku observations found that a magnetic field of $7 \mu\text{G}$ for a single population of high energy electrons gave a good fit to a joint SED of the VHE γ -ray and X-ray data.

7.1.3 γ -ray Data

Aside from IACT based experiments, such as Whipple and HEGRA, whose observations resulted in upper limits which were unconstraining with respect to the H.E.S.S. sensitivity, observations of the region have also been carried out by complementary γ -ray experiments. Detection of HESS J1825-137 in the high energy γ -ray regime (100 MeV - 100 GeV) was achieved by the Fermi-LAT in 2011. Although a joint SED was presented, there was a gap at approximately the location at which the spectral peak is expected to occur changes (figure 7.5).

Since the publication of a Fermi-LAT analysis of HESS J1825-137 in 2011 [111], there have

Region	Experiment	PL index Γ	Flux (10^{-13} erg s $^{-1}$ cm $^{-2}$)	Energy range (keV)
Core	XMM-Newton	1.6 ± 0.1	2.9 ± 0.3	0.5 – 10
	Chandra	$1.33^{+0.11}_{-0.13}$	1.7 ± 0.1	0.5 – 8
Diffuse	XMM-Newton	1.9 ± 0.1	13 ± 2	0.5 – 10
	Chandra	1.87 ± 0.14	$4.5^{+0.3}_{-0.2}$	0.5 – 8
A (core)	Suzaku	$1.69^{+0.09}_{-0.07}$	13(17)	0.8 – 10
B (diffuse)	Suzaku	$1.97^{+0.09}_{-0.09}$	12(17)	0.8 – 10
C	Suzaku	$2.01^{+0.1}_{-0.1}$	12(17)	0.8 – 10
D	Suzaku	$1.94^{+0.12}_{-0.08}$	14(19)	0.8 – 10

Table 7.1: Fit parameters for a power law spectral fit to radial extraction regions used in the analyses by XMM-Newton [100], Chandra [98] and Suzaku [115]. The flux discrepancies seen between the analyses are due to differences in the spectral extraction regions and in the instrument PSF. Fluxes quoted for XMM-Newton and Chandra are unabsorbed values for a Hydrogen density of $\sim 1 \times 10^{22}$ cm $^{-2}$, whereas the Suzaku values are observed fluxes, with absorption corrected values in parentheses (for best fit Hydrogen densities).

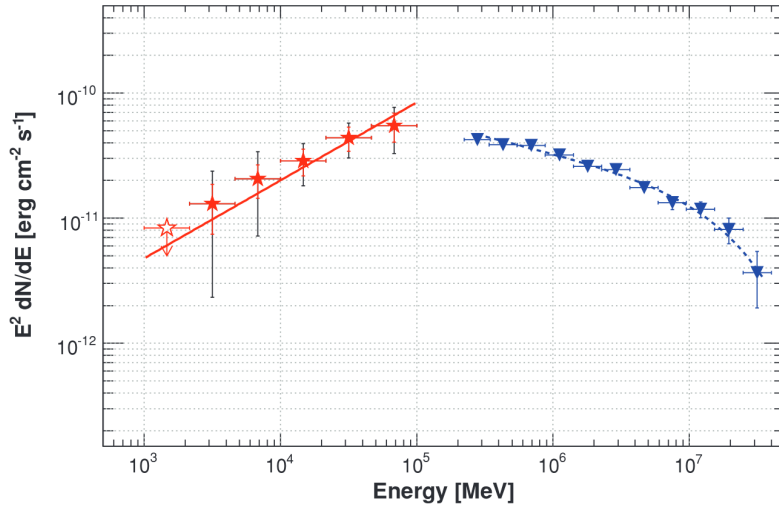


Figure 7.5: Joint spectral energy distribution from both the Fermi-LAT and H.E.S.S. experiments, taken from the 2011 Fermi-LAT publication [111]. The data are complementary; a spectral turnover is expected within the energy gap between the two experiments, at the location of the Inverse Compton peak. Since the publication of this spectrum, analysis improvements and the addition of CT5 to the H.E.S.S. array have enabled the Fermi-LAT and H.E.S.S. energy ranges to be extended, such that they now overlap [112].

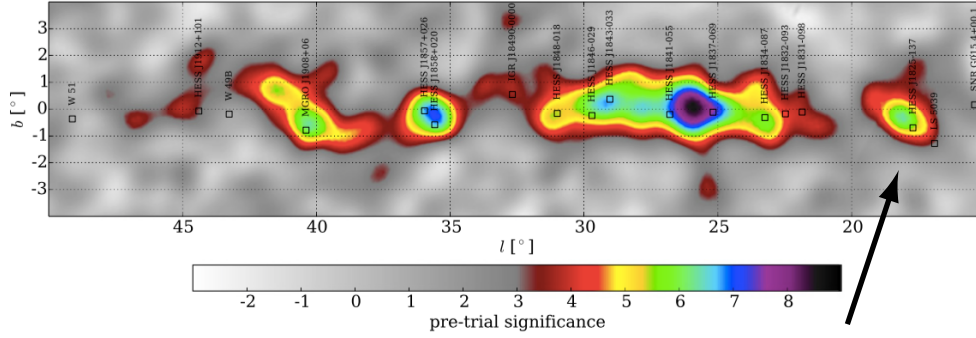


Figure 7.6: Significance map from a partial configuration (roughly one third) of the HAWC experiment during its construction, showing the Galactic centre region and the HESS J1825-137 field of view (indicated by the arrow). The peak position detected by HAWC is offset by about 0.5° from that of the H.E.S.S. position. Figure taken from [116].

been considerable improvements to the data analysis, enabling their energy range to be extended at the high end up to ~ 1 TeV [112]. Meanwhile, the construction of H.E.S.S. II and the corresponding gain in low energy sensitivity of the H.E.S.S. experiment, pushing the energy threshold down to $\sim O(30$ GeV), should permit considerable overlap of the two experiments with a re-analysis of the available data. An analysis of the H.E.S.S. II data was presented in the previous chapter, whilst a basic analysis of HESS J1825-137 was published as part of the 2FHL catalogue (the second catalogue of hard Fermi-LAT sources) in the 50 GeV - 2 TeV range [112]. This 2FHL analysis gave an angular extent of the PWN of 0.75° as the 1σ radius of a 2D Gaussian, with a spectral index of 1.89 ± 0.11 [112].

The HAWC experiment (High-Altitude Water Cherenkov Gamma-Ray Observatory) commenced data taking with a partial configuration (roughly one third) of the array in mid 2013, with completion of the experiment occurring in 2015 [116]. Water Cherenkov based experiments like HAWC are complementary to IACT observations; although they are more limited in terms of energy and spectral measurements, they have a less restrictive field of view (FoV) than IACTs, and as such are more suited towards the detection of large emission regions and to surveying the sky. As well as measurements of diffuse emission, this also makes such experiments suitable for measuring the size of large extended objects such as pulsar wind nebulae, particularly where they are larger than the IACT field of view.

In the TeV γ -ray Galactic plane as seen with a partial configuration of the HAWC experiment, a plausible counterpart for HESS J1825-137 was detected with a post trials significance of 5.4σ [116]. The best fit centroid of this object was located approximately 0.5° offset from that obtained in the H.E.S.S. analysis of [95], as shown in figure 7.6. Barring either or both experiments suffering from systematic errors in their pointing direction, one possible interpretation is that the emission from HESS J1825-137 extends over a far larger region than the H.E.S.S. field of view. In this case, large scale diffuse emission from the PWN will enter into the background estimate, such that some of the true emission is subtracted from the region and thereby leading to an underestimate in the true extent of the nebula. However, given that the low energy threshold of the HAWC experiment is around 1 TeV and that the offset is seen in the opposite direction from the known nebula extension, this scenario seems unlikely, whilst a more significant contribution from HESS J1826-130 at high energies cannot be ruled out.

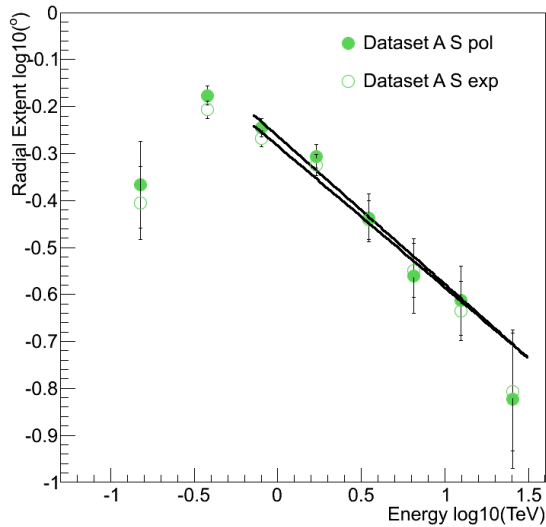


Figure 7.7: Change in extent with energy as explored in section 6.7.3, shown here in log space. The range of the fit was restricted to between 700 GeV and 30 TeV, corresponding to the expected turnover due to cooling and the transition into the Klein-Nishina regime (although the latter may occur at nearer 10 TeV). A linear fit to the data on the Southern side enables a plausible diffusion index and advection characterisation to be extracted.

7.2 Extent Measurements and Transport

Given the detected extension of the nebula over 100 pc, it is difficult to account for the propagation of electrons over such large distances via diffusion alone. An interesting result is the measurement of the changing extent of HESS J1825-137 with energy. Should energy dependent diffusion be the only influencing factor (with no cooling losses), particularly in the case of young PWNe, then the extent of the nebula would be expected to increase with energy, assuming that all particles were injected at a single instance in time. However, where cooling processes play a role, the nebula would be expected to become more compact at higher energies. Other transport mechanisms such as advection could also account for the final observed variation of nebula size with particle energy. The interplay of these transport and cooling effects would be expected to produce a maximum extent at a given energy, corresponding to the energy at which the particle cooling time is comparable to the age of the nebula. This is indeed seen in figure 7.7 (see also section 6.7.3 of the previous chapter), with a maximum extent of the nebula occurring in the energy band 500 GeV - 1 TeV.

Measurements of the radial extent were made with both a polynomial and an exponential fit in section 6.7.3, and the results of a linear fit to measurements of the Southerly nebula extent using both approaches are presented in table 7.2. The lower bound on the fitted range was determined from the timescale for cooling losses due to inverse Compton scattering, τ_{IC} , which is given by (in cgs units):

$$\tau_{IC} = \frac{\frac{3}{4}m_e^2}{\sigma_T c \epsilon_{CMB} E_e}, \quad (7.2.1)$$

where ϵ_{CMB} is the energy density of the CMB, m_e^2 the electron mass, σ_T the Thomson cross-section and c the speed of light. Rearranging for the electron energy E_e in erg, and setting the cooling timescale equal to the characteristic age of the pulsar (the plausible time over which electrons have cooled), an electron energy of ~ 11 erg (or ~ 7 TeV) is obtained. Electrons

with energies $E_e > 7$ TeV are mostly traced by photons with energies $E_\gamma > 700$ GeV, due to the average energy distribution of Inverse Compton scattered photons [117]. Hence a value of 700 GeV is taken for the lower bound (see also section 7.2.2 and equation (7.2.10) later).

The upper bound on the fit range can be estimated as corresponding to the transition from the Thomson into the Klein-Nishina regime. Within the Thomson regime, the average energy of scattered photons scales with the square of the electron energy, yet in the Klein-Nishina regime the electron loses a significant proportion of its energy on each scattering interaction [117]. The parameter Γ determines the Inverse Compton scattering regime:

$$\Gamma = \frac{4E_{CMB}E_e}{(m_e c^2)^2}, \quad (7.2.2)$$

where $E_{CMB} \approx 2.7kT$ is the energy of the CMB. The Thomson regime is relevant where $\Gamma \ll 1$, whilst $\Gamma \gg 1$ is relevant for the Klein-Nishina regime. The transition is therefore determined to take place at $\Gamma = 1$, which corresponds to an electron energy of $E_e \approx 100$ TeV, or $E_\gamma \approx 10$ TeV for scattering off CMB photons. However, as Klein-Nishina effects first begin to dominate for $\Gamma \gg 1$, and the exact transition point varies for different ambient photon fields, the maximum energy appropriate for the linear fit in figure 7.7 was allowed to be beyond the final point of the H.E.S.S. data (at ~ 30 TeV).

7.2.1 Diffusive Particle Transport

Under the assumption of diffusion and cooling losses, a linear fit to figure 7.7 at energies above the maximum extent yields the diffusion index directly. Taking the radial extent R to vary with the diffusion coefficient $D = D_0 E_e^\delta$ and the cooling timescale τ as:

$$R = \sqrt{2D\tau} \quad (7.2.3)$$

$$= \sqrt{2D_0 E_e^\delta \tau}, \quad (7.2.4)$$

and where the cooling losses for Inverse Compton scattering vary with energy as $\tau \propto 1/E_e$ in the Thomson regime, we obtain $R \propto E_e^{(\delta-1)/2}$. Given that the energy of γ -ray photons (E_γ) produced via Inverse Compton scattering interactions varies with the electron energy (E_e) as $E_\gamma \propto E_e^2$ (see equation (1.3.9) of chapter 1), the relation between R and E_γ relevant to figure 7.7 is:

$$R = k E_\gamma^{(\delta-1)/4}, \quad (7.2.5)$$

where k is a constant of proportionality. Hence from the fitted index α of the slope in figure 7.7 (where $R \propto E^{-\alpha}$), the strength of diffusion is obtained directly as $\delta = 4\alpha + 1$. The diffusion index δ typically lies in the range 0.3 – 0.6, with extremes of energy independent diffusion at $\delta = 0$, and of Bohm diffusion at $\delta = 1$. From a linear fit to $\log R$ against $\log E_\gamma$, the gradient of the fit yields the diffusion index directly, whilst the constant relates to the coefficient k .

	α	$\log k$	δ	β
S pol	-0.31 ± 0.04	-0.26 ± 0.02	-0.20 ± 0.16	0.6 ± 0.2
S exp	-0.30 ± 0.04	-0.28 ± 0.01	-0.24 ± 0.16	0.6 ± 0.2

Table 7.2: Parameters of a linear fit to the Southern (S) radial extent of the nebula with energy, as shown in figure 7.7. Results are shown for the extent as measured by using a polynomial fit (pol) and alternatively an exponential fit (exp) to the radial emission profile (see section 6.7.3 for details). Parameters δ and β are defined in equations (7.2.5) and (7.2.9) respectively. A nonsensical diffusion index of $\delta \approx -0.2$ is obtained, whilst the β values are relevant to the advection case (see sections 7.2.1 and 7.2.2).

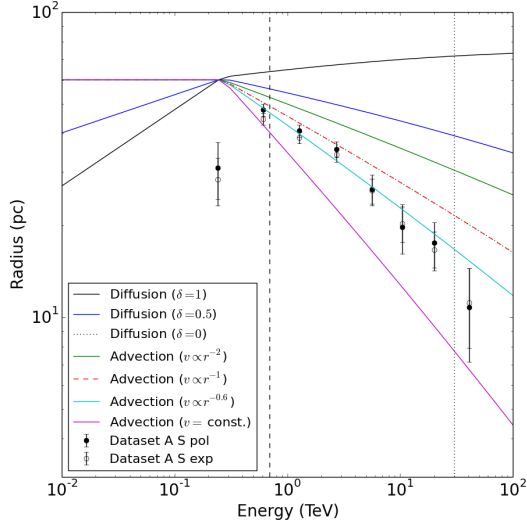


Figure 7.8: Plausible model gradients for various transport scenarios for the variation of radius with energy (under the assumption of steady-state flow with constant density). All lines are arbitrarily normalised to a size of 60 pc at 250 GeV. The vertical dashed line indicates the lower bound of the fit (~ 700 GeV), whilst the vertical dotted line at ~ 20 TeV indicates a plausible location for the transition into the Klein-Nishina regime.

The results of the fit are shown in table 7.2, and a nonsensical diffusion index of $\delta \approx -0.2$ was obtained; if the lower limit in the energy range is raised to 1 TeV, then the index obtained becomes less compatible with the diffusion scenario still, producing $\delta \approx -0.6$, such that a range of -0.2 to -0.6 incorporates some systematic uncertainty on the obtained index. The fitted index of ~ -0.2 obtained indicates that energy dependent diffusion as the dominant transport mechanism does not seem to be consistent with the steep change in extent as a function of energy.

To illustrate this more clearly, plausible gradients corresponding to various diffusion and advection scenarios are overlaid with the data points from figure 7.7 in figure 7.8. All curves were arbitrarily normalised to 60 pc at 250 GeV. The vertical lines indicate the lower bound of the fit range (at ~ 700 GeV) and the transition into the Klein-Nishina regime (at ~ 20 TeV). In deriving the indices listed in table 7.2, all points above the lower bound were included in the fit, and it was assumed that $E_\gamma \propto E_e^2$. However, in the Klein-Nishina regime the proportionality becomes linear $E_\gamma \propto E_e$, such that the gradient of the radius against energy plot may be expected to steepen. This is in accordance with the apparent steepening of the highest energy data point in figure 7.8.

Three diffusion scenarios corresponding to $\delta = 0, 0.5$ and 1 in equation (7.2.5) are shown in figure 7.8; all three lie above the data points with incompatible gradients, in accordance with the nonsensical value of $\delta = -0.2$ obtained from the linear fit. In order to normalise the different lines to a fixed size of 60 pc at 250 GeV (chosen arbitrarily), the parameter D_0 in equation (7.2.4) had to be adjusted for the different diffusion scenarios. For $\delta = 0, 0.5$ and 1 , the values of D_0 required for the normalisation were 2.6×10^{28} , 2.1×10^{26} and $1.7 \times 10^{24} \text{cm}^2 \text{s}^{-1}$ respectively. A possible alternative scenario, of advective transport, is outlined in the next section.

7.2.2 Advective Particle Transport

If, instead of diffusion, advection is assumed to be the dominant particle transport mechanism, then a relation between R and E_γ analogous to equation (7.2.5) can be obtained. During the particle outflow through the nebula, it is required that the equation of mass continuity is satisfied:

$$\frac{\partial \rho}{\partial t} + \nabla \cdot (\rho \bar{v}) = 0, \quad (7.2.6)$$

where ρ is the density of the particle flow and v the flow velocity. By also requiring a steady-state density profile $\dot{\rho} = 0$, then the flow must preserve:

$$\rho(r)A(r)v(r) = \text{const.}, \quad (7.2.7)$$

where $A(r)$ is the area through which the particles flow, and the radial dependence of $\rho(r)$, $A(r)$ and $v(r)$ is unknown. Assuming that the flow density ρ is not a function of the radius, then $v(r) \propto A(r)^{-1}$. Therefore, in the case of spherical symmetry, the area through which the flow travels is $A(r) = 4\pi r^2$, and the flow velocity $v(r) \propto r^{-2}$. The flow velocity variation with radius r can be parameterised as:

$$v = v_0 \left(\frac{r}{r_0} \right)^{-\beta}, \quad (7.2.8)$$

where r_0 and v_0 are the initial radius and velocity of the nebula respectively, and β describes the radial dependency required in order to yield a constant density profile. In extreme cases, β can take on values of 0 (for constant velocity expansion) or 2 in the case of spherical expansion. By separation of variables and integrating over all radii and up to the cooling time, one obtains the proportionality relation $R \propto E_e^{-\frac{1}{1+\beta}}$. Accounting for the relation between E_γ and E_e , this relation becomes:

$$R \propto E_\gamma^{-\frac{1}{2(1+\beta)}}, \quad (7.2.9)$$

such that the gradient of linear fit to figure 7.7 yields a value of β ; the values obtained in this case are quoted in table 7.2. The obtained index for the velocity variation with radius is $\beta \approx 0.6$, which is a significant dependence beyond the constant velocity case, approaching $\beta = 1$, which corresponds to flatter, more disc-like flow expansion (e.g. $A(r) = 2\pi r$).

Four plausible gradients corresponding to advection scenarios are overlaid in figure 7.8, representing the extreme cases of constant velocity flow throughout the nebula ($\beta = 0$), of spherically expanding flow ($\beta = 2$), a reference case of $\beta = 1$ and the case corresponding to the value of $\beta = 0.6$ obtained from the fit. As is apparent from the fit, the $\beta = 0$ and $\beta = 2$ extreme cases are both incompatible with the data, falling above and below the points respectively. The case of $\beta = 1$ follows exactly the same gradient as $\delta = 0$, corresponding to energy independent diffusion. The gradient of the advection model with $\beta = 0.6$, as obtained by the linear fit to the data points (see table 7.2), is again consistent with the data in figure 7.8. However, the exact positions at which this line crosses the points can be seen to deviate slightly with respect to figure 7.7. This is due to additional assumptions arising in forming the model lines, including the arbitrary normalisation of all curves to a size of 60 pc at 250 GeV, and the dependence of E_γ on E_e . This latter dependence was assumed to follow (within the Thomson regime):

$$E_\gamma = \frac{4\bar{\varepsilon}E_e^2}{9m_e^2c^4}, \quad (7.2.10)$$

taken from [117], where m_e is the electron mass and $\bar{\varepsilon}$ is the average energy of a photon in the ambient radiation field, taken here to be the average CMB photon energy, $\bar{\varepsilon} \approx 2.7k_B T$, with a

temperature of $T = 2.73$ K (and k_B is Boltzmann's constant). The factor of $1/9$ arises from the mean of the distribution of scattered photons, such that the average energy E_γ of photons scattered from an electron of energy E_e is approximately the value given by equation (7.2.10).

To normalise the different lines in the advection case, from equation (7.2.8), the required constant factor could be transferred onto a change in r_0 , the radius of the wind termination shock, or v_0 , the velocity of the flow at the termination shock. (The wind termination shock occurs roughly where the pressure of the pulsar wind becomes equal to the pressure of the surrounding medium, forming a rough definition of the start of the PWN.) The initial velocity at the termination shock, v_0 , was assigned a value of $c/\sqrt{3}$; for the cases of advection with $\beta = 1$ or 2 , adjusted v_0 required values greater than the speed of light, and therefore incompatible. A standard value of $r_0 = 0.1$ pc was adopted at first; for normalisation, this had to be adjusted to values of 0.03 pc, 0.5 pc and 4.4 pc for the cases of $\beta = 0.6$, 1 and 2 respectively, the latter value being somewhat large for typical wind termination shock radii. Whilst it cannot be distinguished whether the normalisation arises from changes to v_0 or r_0 , the subsequent values for r_0 and v_0 are both reasonable in the $\beta = 0.6$ case.

7.2.3 Improving Transport Model Trends

To improve the description of the scattered photon energy, the expected distribution of photon energies $f(\hat{E}_\gamma)$ can be taken into account, where \hat{E}_γ is the maximum scattered photon energy arising from an electron of energy E_e . The distribution function was taken from [117] and has the form $f(\hat{E}_\gamma) = 2\hat{E}_\gamma \ln \hat{E}_\gamma + \hat{E}_\gamma + 1 - 2\hat{E}_\gamma^2$; this is shown in figure 7.9. In this case, a maximum electron energy was chosen to take on the fixed value of 100 TeV. Three representative curves are shown in figure 7.9, corresponding to the cases of diffusion with $\delta = 0.33$, advection with $\beta = 0$ and advection with $\beta = 0.6$. In all three cases, the curve can be seen to drop off more rapidly towards the Klein-Nishina transition region, where the Thomson description used here ceases to accurately describe the interaction processes. By eye, the best match seems to be provided by the advection case with $\beta = 0.6$.

To normalise the three curves in figure 7.9, the diffusion curve took a coefficient of $D_0 = 10^{27} \text{cm}^2 \text{s}^{-1}$. In the constant velocity advection case, the velocity took on a value of $0.015c$, in agreement with that expected from a simple kinematical argument based on the size of the nebula, in order to account for particles at the outer nebula edge (i.e., $v = 100 \text{ pc}/\tau_c$, where τ_c is the characteristic age of the pulsar). For the fitted case of advection with $\beta = 0.6$, the velocity at the termination shock was assigned a value of $v_0 = 0.65c/\sqrt{3}$ for a fixed value of $r_0 = 0.1$ pc, although an alternative argument for a fixed v_0 and adjusting the inner radius is also valid.

Further improvements to the description shown in figure 7.9 would include using a variable maximum electron energy, depending on the energy of the γ -rays produced. In the diffusion case, this would have the effect of reducing the expected size, particularly at low energies, where reduction in maximum electron energy for the lower energy γ -ray photons corresponds to a smaller expected travel distance across the nebula for the same amount of time. Explicit inclusion of the expected Klein-Nishina behaviour above the transition region would improve the fitting of the reduction in size, beyond that expected from the linear trend, at the highest energies, without the steep drop present in figure 7.9. Additional data points at the lowest and highest energies would help to verify the transition into the Klein-Nishina regime and the reduction in size at lower energies. This latter behaviour is to be expected where the cooling time of the electrons responsible for γ -ray emission at these energies is longer than the age of the system, in the case of strong energy-dependent diffusion. Previously published Fermi-LAT measurements

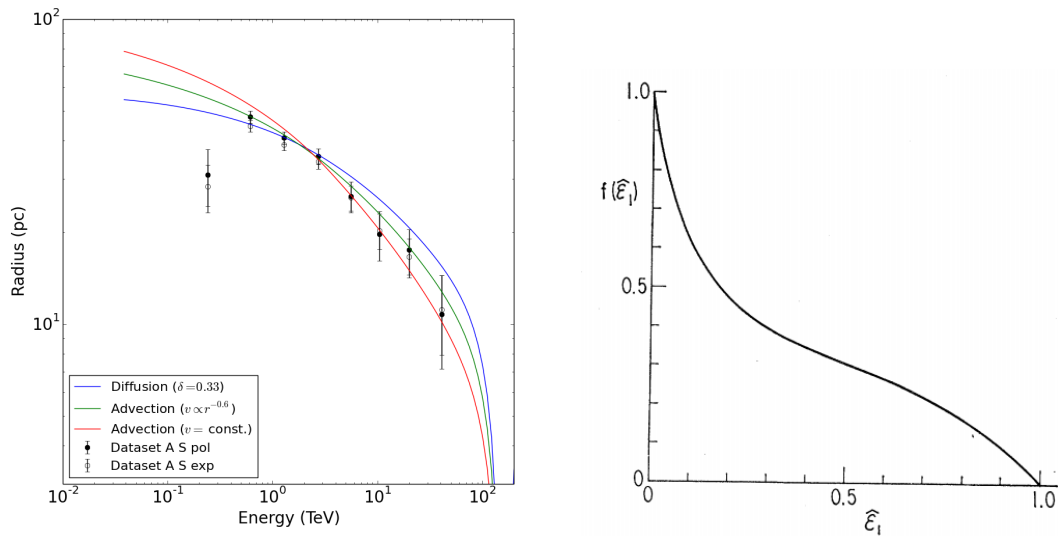


Figure 7.9: Left: Plausible model curves for different particle transport scenarios. In contrast to figure 7.8, the expected scattered photon distribution arising from Inverse Compton interactions is taken into account. By eye, the advection case with $\beta = 0.6$ is the most compatible. A steep drop-off occurs towards the end of the Thomson regime. Right: the distribution of scattered photons used for the model curves, figure taken from [117].

of the nebula size were not included, however, due to the differences in the parameterisation used. Whereas in the measurements of chapter 6 a fit to the asymmetric radial profile used, the Fermi-LAT measurements employed a symmetric Gaussian description for the whole nebula, centred on the peak emission.

A more realistic scenario would include a combination of diffusive and advective effects, possibly also with re-acceleration further out in the nebula. Complicating the situation still further, the magnetic field is also expected to change within the nebula as a function of distance and over time, affecting the particle energy losses and transport. To fully describe the transport mechanisms at work within the nebula, the magnetic field contribution should not be neglected. The magnetic field strength variation across the core emission is partially mapped in the next section, providing an insight into the varying conditions within the nebula.

7.3 Mapping the Magnetic Field

Coverage of the HESS J1825-137 in X-rays is provided by previous observations by the XMM-Newton [100], Chandra [98] and Suzaku [115] telescopes; further Suzaku observations after the 2009 analysis enabled a more extensive analysis of the region, done as part of [109]. The positions of the Suzaku observations of this region are shown overlaid on a H.E.S.S. map of the region in figure 7.10.

It was found that the Suzaku observations corresponded well with the boxes used for spectral extraction in section 6.6.1. Regions 4-9 were found to overlap with the X-ray observations made by Suzaku, each to a varying extent. In order to better match the Suzaku coverage of the region, and to reduce the introduction of systematic uncertainties unnecessarily, H.E.S.S. γ -ray and Suzaku X-ray spectra were extracted in each of five boxes matching the separated exposures taken in each of these regions. In addition to simplifying the X-ray analysis with respect to combining spectra from multiple regions and times, this also increased the area of the boxes

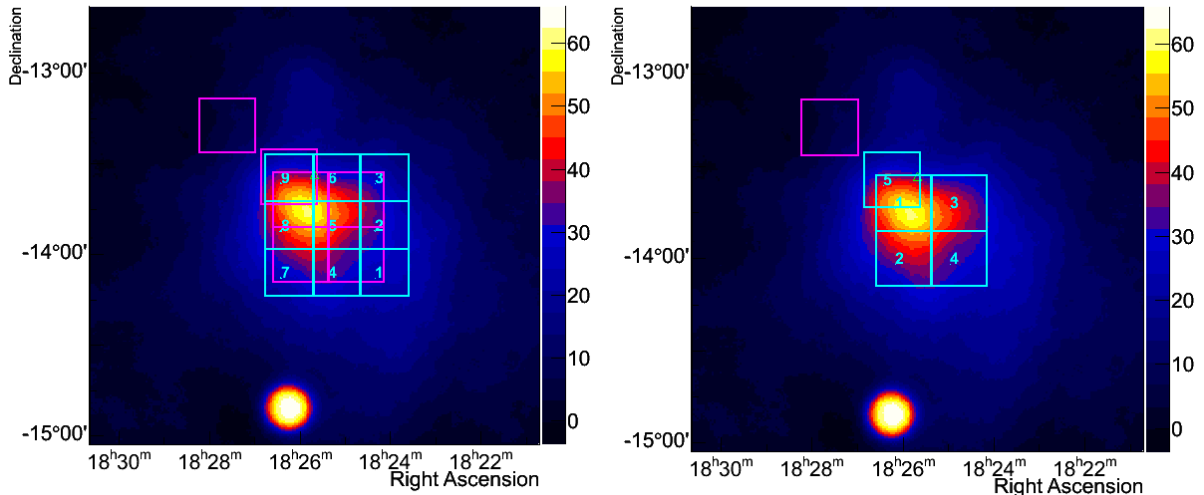


Figure 7.10: Left: Suzaku observation positions (magenta) overlaid with the overlapping box-shaped regions used for spectral extraction in section 6.6.1. Right: H.E.S.S. spectral extraction regions (cyan) defined to better match the Suzaku coverage of the region. These boxes will be referred to as boxes 1-5 hereafter. A H.E.S.S. spectrum was extracted corresponding exactly to each Suzaku observation, with the exception of the region used for background estimation.

from $0.26^\circ \times 0.26^\circ$ to $0.3^\circ \times 0.3^\circ$; thereby improving the statistics and reducing uncertainties in both the X-ray and TeV data. These matched boxes are shown in figure 7.10.

7.3.1 X-ray (Suzaku) Spectral Points

A re-analysis of the X-ray data from the Suzaku satellite was done by P. Eger, extracting spectra separately from each region defined in figure 7.10, to enable simultaneous fitting of the spatially coincident X-ray and TeV data. In each pointing, foreground X-ray point sources and calibration sources towards the edges of the field of view must be removed prior to a spectral analysis of the diffuse emission component from HESS J1825-137. This results in a reduced spectral extraction area for the X-ray analysis with respect to the full region, which must be accounted for in the flux estimates. The background estimation is taken from the dedicated region outside of the spectral boxes, also indicated in figure 7.10. X-ray emission is typically subject to significant absorption along the line of sight; to obtain the true unabsorbed flux, therefore, an assumption on the absorbing column density must be made. This may be kept fixed for all boxes, as one can reasonably assume that the line of sight absorption is the same across all regions of HESS J1825-137 (angular extent of $\sim 0.5^\circ$ on the sky across all boxes); however, should the absorption coefficient be under- or overestimated, this would result in an over- or underestimate of the flux respectively. This effect has a stronger influence towards the low end of the energy range. The integrated energy fluxes were provided in three energy ranges; 1-2 keV, 2-4 keV and 4-8 keV; for each box, except for an upper limit being obtained across the full energy range of 1-8 keV in the case of box 2 (see right hand side of figure 7.10 for the box labels). As the integrated flux points were derived under the assumption of a power law spectrum with a particular index Γ , the differential energy flux was required for forming a joint spectral energy distribution with the VHE data (both quantities having the same units of $\text{erg cm}^{-2} \text{s}^{-1}$). Therefore, the corresponding flux normalisation was obtained as follows. The X-ray flux points provided in each energy range;

$F_X(E_1 - E_2)$ corresponded to an integrated power law spectrum;

$$\begin{aligned} F_X(E_1 - E_2) &= \int_{E_1}^{E_2} E \cdot F(E) dE \\ &= N(E_0) \int_{E_1}^{E_2} E \cdot \left(\frac{E}{E_0}\right)^{-\Gamma} dE, \end{aligned} \quad (7.3.1)$$

where $N(E_0)$ is the desired flux normalisation at an energy E_0 , which was chosen to be the middle of the energy range under consideration, $E_0 = \frac{1}{2}(E_1 + E_2)$. It can be shown that the expression for the differential flux normalisation is then:

$$N(E_0) = \frac{F_X(E_1 - E_2)}{(E_2^{2-\Gamma} - E_1^{2-\Gamma})} (2 - \Gamma) E_0^{-\Gamma}. \quad (7.3.2)$$

The corresponding differential energy flux (at an energy E) could then be obtained from:

$$F(E) = N(E_0) \left(\frac{E}{E_0}\right)^{-\Gamma}, \quad (7.3.3)$$

however, for the SED one is free to choose the energy E at which $F(E)$ is evaluated, and hence one can choose $E = E_0$ for simplicity (such that $F(E_0) = N(E_0)$). Finally, the flux must be scaled by the ratio of the spectra extraction areas in γ -rays and X-rays; A_γ/A_X , to take into account the reduced extraction area used for the X-ray analysis (due to foreground and calibration sources). The integrated flux quantity $E^2 F(E)$ in $\text{erg cm}^{-2}\text{s}^{-1}$ is plotted together with the H.E.S.S. measurements in figure 7.11.

7.3.2 Fitting the Spectral Energy Distributions

By simultaneously fitting the X-ray and VHE γ -ray spectral measurements with a joint Synchrotron and Inverse Compton spectral energy distribution (SED), under the assumption that the emission is of leptonic origin (i.e. predominantly due to accelerated electrons), it is possible to make measurements of the magnetic field in different regions of the PWN, or to put constraints on the magnetic field strength where there is no significant X-ray emission. This was done for each of the regions shown in figure 7.10; with the X-ray data constraining the Synchrotron component and the VHE γ -ray data the Inverse Compton component, the flux ratio of the two components then provide an estimate of the magnetic field strength. The fit model used for this purpose did not include any evolution, but was rather a fit to the emission via both components assuming a broken power law particle distribution at that location. The fitted joint SEDs are shown in figure 7.11, and the results of the fit are given in table 7.3. The γ -ray index is found under the assumption of a power law spectrum.

Due to the asymmetric errors on the H.E.S.S. points, to treat these correctly in the minimisation, the following χ^2 formula was used [118]:

$$\chi^2 = \delta^2 \left(\frac{\sigma^{+3} + \sigma^{-3}}{\sigma^{+2}\sigma^{-2}(\sigma^+ + \sigma^-)} \right) \left(1 - \delta \frac{\sigma^{+2} - \sigma^{-2}}{\sigma^{+3} + \sigma^{-3}} \right), \quad (7.3.4)$$

where σ^+ and σ^- are the upward and downward errors respectively, and which is constrained to pass through a χ^2 of 1 at the 1σ fluctuations. This form is valid, and preferential to other simpler forms, provided that the asymmetry between the σ^+ and σ^- errors does not exceed $\sim 20\%$, which was the case for all data points [118].

Region	d (°)	d (pc)	X-ray Index	γ -ray Index	e^\pm Index	E (10^{47} erg)	B (μG)
5	0.12°	9	2.02 ± 0.05	2.09 ± 0.02	2.7 ± 0.1	(2.7 ± 0.4)	7.8 ± 0.8
1	0.5°	36	1.91 ± 0.04	2.12 ± 0.02	2.70 ± 0.07	(4.2 ± 0.5)	6.5 ± 0.5
3	0.62°	45	2.1 ± 0.3	2.21 ± 0.02	2.99 ± 0.06	(3.8 ± 0.2)	3.6 ± 0.3
4	1.0°	72	2.3 ± 0.4	2.29 ± 0.025	3.0 ± 0.1	(3.8 ± 0.7)	1.9 ± 0.3
2 (UL)	0.93°	67	2.2	2.30 ± 0.02	3.02 ± 0.04	(5.0 ± 0.3)	1.7 ± 0.1

Table 7.3: Results of a joint spectral fit to the X-ray and VHE γ -ray data over the HESS J1825-137 region. A broken power law with an exponential cut-off, given in equation (7.3.5), was used to describe the particle spectrum, with a fixed value of $\alpha_1 = 1.8$. The magnetic field strength, B was found to decrease with increasing distance from the pulsar. The X-ray spectral point in region 2 is an upper limit, derived under an assumed index of 2.2, and corresponds to an upper limit on B.

As can clearly be seen in figure 7.11, the X-ray emission is strongest in regions 5 and 1, (far left) covering the pulsar and core of the emission respectively. As these two regions also partially overlap (see figure 7.10), it is unsurprising that the results are similar in these two cases. With increasing distance from the pulsar, the strength of the X-ray component reduces. In region 2 (far right) there was no significant X-ray emission detected, and an upper limit was instead derived assuming a spectral index of 2.2 for the undetected emission. The fit to the joint SED of the X-ray and γ -ray data, was done treating the derived upper limit as a flux point. The magnetic field value obtained in this case, is then taken as an upper limit of the true nebula magnetic field. Results of the fits to these regions are given in table 7.3.

The spectrum of the underlying particle distribution $Q(E_e, t)$ was assumed to follow a broken power law with an exponential cut off:

$$Q(E_e, t) = Q_0(t) \exp\left(-\frac{E_e}{E_c}\right) \begin{cases} \left(\frac{E_e}{E_b}\right)^{-\alpha_1} & E_e \leq E_b \\ \left(\frac{E_e}{E_b}\right)^{-\alpha_2} & E_e > E_b \end{cases}, \quad (7.3.5)$$

with a low index of $\alpha_1 = 1.8$; the break energy E_b , spectral index α_2 , total particle energy, the maximum particle energy E_c (corresponding to the exponential cut-off) and the magnetic field strength were left as free parameters of the fit. The spectrum of the parent electron population is broadly similar in all cases, with a fitted index α_2 around 3. Clearly, from the fit results in table 7.3, the magnetic field strength decreases with increasing distance from the pulsar, whilst the spectral index of the particle population gets softer with increasing distance (reflecting the trend in the power law indices fitted to the γ -ray data).

In order to obtain a rough estimate on the systematic errors inherent in the procedure, the same fit was performed using a broken power law model without an exponential cut-off; the indices, energies and magnetic fields strengths obtained in this case are quoted in table 7.4. The obtained values are compatible within errors of those obtained from the broken power law with exponential cut-off fit model, listed in table 7.3.

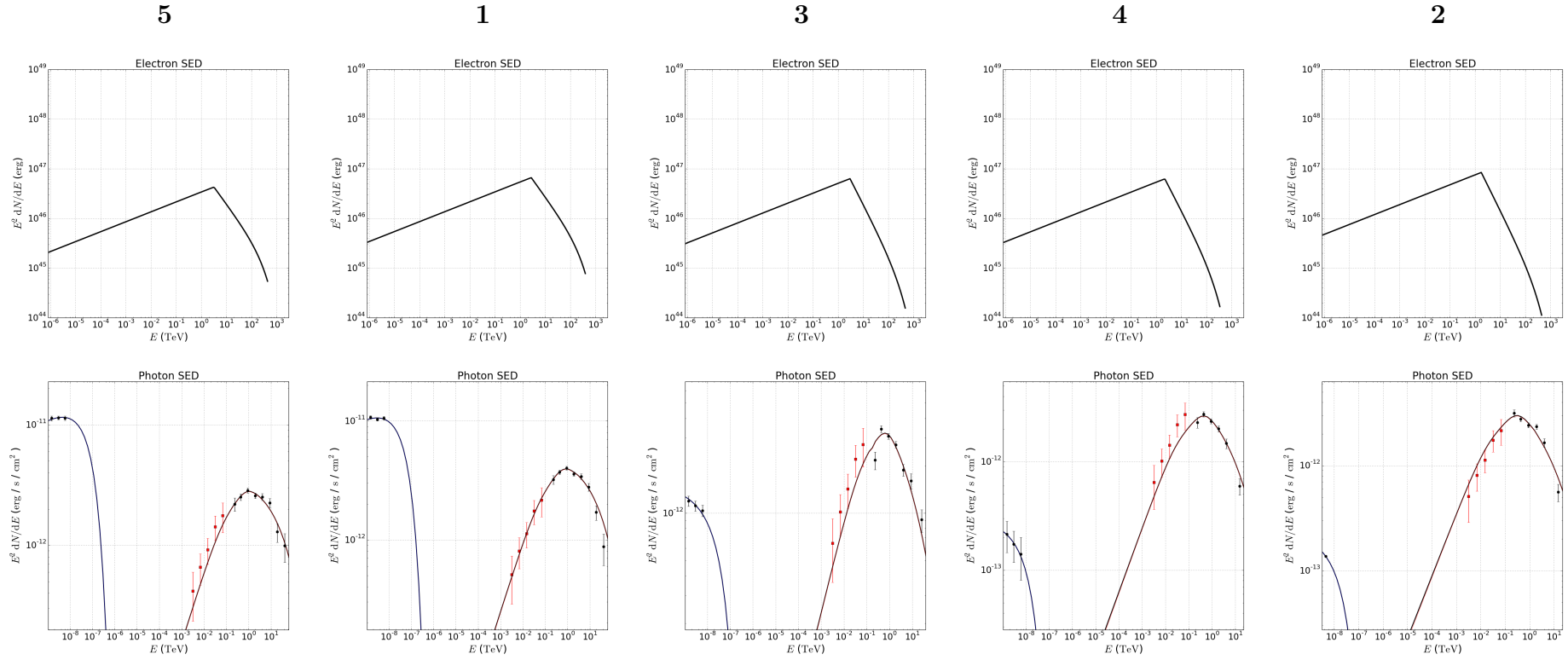


Figure 7.11: Spectral fit results corresponding to the boxes 5, 1, 3, 4 and 2 (from left to right) as labelled in figure 7.10. Above: the modelled spectrum of electrons in the PWN environment at this location, responsible for the γ -ray emission. A broken power law with an exponential cut-off was used, the low spectral index was fixed to $\alpha_1 = 1.8$. Below: Joint X-ray and γ -ray SEDs, with both Synchrotron and Inverse Compton emission components fitted to the Suzaku X-ray and H.E.S.S. γ -ray data. In all cases, the final fit result is shown in black and the scaled Fermi-LAT points (not used in the minimisation) are overlaid in red. The relative strengths of the X-ray and VHE Synchrotron and Inverse Compton components allow the magnetic field in the region to be constrained.

Region	e^\pm Index	E (10^{47} erg)	B (μG)
5	2.90 ± 0.09	(1.5 ± 0.1)	8.8 ± 0.8
1	2.76 ± 0.08	(2.4 ± 0.3)	6.5 ± 0.6
3	3.2 ± 0.1	(2.0 ± 0.2)	3.8 ± 0.6
4	3.0 ± 0.1	(2.1 ± 0.3)	1.6 ± 0.3
2	3.09 ± 0.06	(2.6 ± 0.4)	1.6 ± 0.1

Table 7.4: Results of a joint fit to the X-ray and VHE γ -ray data over the HESS J1825-137 nebula using a broken power law model without an exponential cut-off and with $\alpha_1 = 1.5$ for the electron spectrum.

In figure 7.11, alongside the Suzaku and H.E.S.S. points used in the fitting procedure, Fermi-LAT points are also overlaid in red. These points were obtained from the 2011 published Fermi-LAT analysis [111], and were rescaled to account for the different spectral extraction areas. The 2D Gaussian model used for the Fermi-LAT spectral analysis in [111] was also quoted in the third Fermi-LAT source catalogue (3FGL), for which the extended source templates are publically available [119]. To obtain an appropriate rescaling for each of the boxes used in the H.E.S.S. and Suzaku analyses, the corresponding region of the Fermi-LAT source template was integrated. The ratio of the integrated region to the integrated whole source template provided the appropriate rescaling for each box. These were found to be typically of the order of 3% – 4%. In all cases, the slope of the Fermi-LAT points was consistent with that obtained in the model fit.

7.3.3 Physical Properties of Nebula Regions

From the values obtained for the magnetic field in each region, it is possible to estimate some relevant physical parameters characterising the nebula, such as the magnetic and electron pair energy densities in each region.

Particles accelerated close to the pulsar and escaping the immediate vicinity of the pulsar at the light cylinder by travelling along open magnetic field lines form a pulsar wind, transporting some of the magnetic flux with them. Over time, the pulsar spins down and loses energy via these particles into the pulsar wind. The magnetisation parameter, σ relating the amount of energy stored in the magnetic field and in the particles, is provided by $\sigma = U_B/U_{e^\pm}$ (or equivalently, the energy flux ratio). In current models, high values of $\sigma \sim O(10^4)$ are required within the pulsar wind; however, models and observations obtain much lower values of $\sigma \ll 1$ beyond the shock within the nebula [86, 120, 121]. How the transition between these two values occurs at the termination shock is currently not well understood, a topic referred to as the “ σ -problem” in the literature [122]. As particles are continually injected via the pulsar wind into the nebula, they transport some of the magnetic flux with them, continually replenishing the magnetic flux in nebula regions near to the pulsar. As the particles drift away from the pulsar, the magnetic flux dissipates into the surroundings and the field strength gradually decreases. This conceptual picture is in accordance with the fitted values of the magnetic field in table 7.3, which show the magnetic field strength reducing with increasing distance to the pulsar. Of particular interest to model constraints is the relative amount of energy stored in the magnetic field and in the particles in each of the regions. This is summarised in table 7.5.

Region	Vol. (10^4pc^3)	U_B	$U_{e\pm}$ ($\alpha_1 = 1.5$)	σ ($\alpha_1 = 1.5$)	$U_{e\pm}$ ($\alpha_1 = 1.8$)	σ ($\alpha_1 = 1.8$)
5	0.40 ± 0.04	1.5 ± 0.3	0.8 ± 0.1	1.8 ± 0.5	1.4 ± 0.2	1.1 ± 0.3
1	1.7 ± 0.2	1.1 ± 0.2	0.30 ± 0.04	3.5 ± 0.7	0.52 ± 0.08	2.0 ± 0.4
3	2.1 ± 0.2	0.32 ± 0.05	0.21 ± 0.03	1.5 ± 0.5	0.39 ± 0.04	0.8 ± 0.2
4	3.3 ± 0.3	0.09 ± 0.03	0.13 ± 0.02	0.7 ± 0.2	0.24 ± 0.05	0.4 ± 0.1
2	3.1 ± 0.3	$< 0.07 \pm 0.01$	0.18 ± 0.04	$< 0.4 \pm 0.1$	0.35 ± 0.04	0.21 ± 0.04

Table 7.5: Physical quantities derived from the joint SED fits to the independent regions. For each region, the assumed volume, the magnetic (U_B) and electron positron particle ($U_{e\pm}$) energy densities in units of (eVcm^{-3}) and the derived energy density ratio σ are given. The particle energy density and ratio obtained for fits to figure 7.11 using a particle spectrum low index of 1.5 (instead of 1.8) are also quoted.

Energy Densities

For each region from which the magnetic field was measured, the magnetic field density could be obtained directly from $U_B = B^2/8\pi$. The total energy contained within the particles was a free parameter of the fit; to obtain the particle energy density, an estimate for the 3D volume corresponding to each box is necessary. This was calculated as the box area \times depth, where the depth of each box was assumed to be the same as the distance from the box centre to the pulsar position. (The error on this distance was estimated as $\sim 10\%$). The particle energy densities were hence obtained, $U_{e\pm}$, and found to be lower than the magnetic energy densities for the regions nearest to the pulsar. With increasing distance from the pulsar, both energy densities reduced. The σ parameter, was found to peak in region 1, corresponding to the brightest γ -ray emission. However, the values obtained for σ are considerably higher than expected for the nebula, $\sim O(0.01 - 0.1)$, indicating either an overestimate of the magnetic energy density or an underestimate of the particle energy density [123].

The greatest uncertainties introduced so far are likely to be in the assumed depth of each box, and in the comparatively unconstrained low index of the particle spectrum. The depth estimate could introduce an overestimated volume, leading to an underestimated energy density. Alternatively, if the assumed particle spectrum index is too hard, then a softer index would increase the total energy in the particles, thereby increasing the energy density, meaning that the values quoted in table 7.5 are again underestimated.

The fits were performed using a fixed low indices to the particle spectrum of 1.5 and 1.8; the magnetic field strengths obtained were found to be consistent within errors between the two fits (see table 7.3). As expected, with the softer low index ($\alpha_1 = 1.8$), the total energy in the particles increased, consequently reducing the σ values obtained; yet these are still above expectation in both cases. The true particle index is poorly constrained by the current data, and may still be softer (although the Fermi-LAT points give some indication of this). Moreover, the low index has been assumed to be the same between all boxes, which may not be the case.

If, however, the volume estimate is the primary uncertainty, this would indicate either that the physical extent of the nebula along the line of sight is significantly less than the apparent extent, or that the X-ray emission originates from a far more concentrated region than the γ -ray emission, such that the two energy densities do not probe the same physical volume. A combination of these effects is likely to contribute to the results in table 7.5.

This finding is similar to the case of the nebula around the pulsar PSR B1706-44, as discussed in [17], in which it was found that in order to match the X-ray and γ -ray fluxes observed, a magnetic field considerably lower than that of the interstellar medium (ISM), $B \sim 3\mu\text{G}$, was required. Alternatively, an additional radiation field providing photons for Inverse Compton

Region	$\tau(E_e)$ (kyr)	$\tau(E_\gamma)$ (kyr)	R_d (pc)	R_a (pc)
5	1.7 ± 0.3	2.5 ± 0.5	51 ± 5	26 ± 3
1	2.3 ± 0.2	3.6 ± 0.5	61 ± 4	32 ± 3
3	5.6 ± 0.7	$12. \pm 2.$	110 ± 10	68 ± 7
4	15 ± 4	40 ± 10	140 ± 20	90 ± 10
2	17 ± 2	52 ± 7	140 ± 20	90 ± 10

Table 7.6: Using the magnetic field strengths determined from each region, the lifetimes of electrons to produce 1 keV photons due to Synchrotron cooling $\tau(E_X)$ and for 10 TeV electrons to Inverse Compton scatter $\tau(E_e = 10 \text{ TeV})$ are calculated. The corresponding diffusion radius, R_d , and advection radius, R_a , were calculated from equation (7.2.4) and by integrating equation (7.2.8) for the shortest of $\tau(E_e = 10 \text{ TeV})$, $\tau(E_X)$ and T , the age of the system. A diffusion index of $\delta = 0.4$ was used for R_d , and a value of $\beta = 0.6$ for R_a , as obtained in section 7.2.

scattering could also account for the high γ -ray flux in comparison to the low X-ray flux; however this requires considerable changes in the ambient medium near the pulsar in comparison to the ISM, and was not considered here. In both cases, a conceivable explanation is that the X-ray nebula is far more compact than the γ -ray nebula, both in angular extent (as is known) and along the line of sight, such that the two measurements, whilst spatially coincident in the flat 2D projections, do not probe the same electron population. This would imply that the γ -ray flux originating from the same 3D spatial region as the X-ray flux is considerably less than the total γ -ray flux measured in each region, reducing the difference between the synchrotron and inverse Compton peaks in figure 7.11; a correspondingly higher average magnetic field would then be consistent with the data.

The best fit interpretation of particle transport found in section 7.2 was advection, under the assumptions of a steady-state system with density independent of radius, with $v(r) \propto r^{-0.6}$. In this case, high values of σ (in the range 0.1 – 1) are not unexpected, although values of $\sigma > 1$ as presented in table 7.5 are highly unlikely. According to [121], for values of $\sigma \approx 1$, the flow velocity has only a weak distance dependence, and high σ flows have an approximately constant velocity, with a magnetic field dependence of roughly $B \propto 1/r$. Low values of $\sigma \approx 0.01$, however, correspond to more spherical flow behaviour with $\beta = 2$. Additionally, [121] show that with lower values of σ , the peak magnetic field is expected to occur further out in the nebula. The rough $1/r$ dependence of the magnetic field values found and the corresponding high σ values (tables 7.3 and 7.5) are therefore consistent with the interpretation in section 7.2 of an advective flow with weak distance dependence of the velocity.

From table 7.5, the particle energy density also seems to decline with increasing distance from the pulsar, roughly as $1/r$. Through equation (7.2.7), it can be seen that to maintain a steady-state, a $1/r$ density profile would correspond to advection into a disc ($A(r) = 2\pi r$) if the velocity was constant, or 3D advection into a sphere ($A(r) = 4\pi r^2$) if both the velocity and density vary as $1/r$. Alternatively, such a profile could be interpreted under the diffusion scenario in the case of continuous injection [124].

Particle Lifetimes

The lifetime of 10 TeV particles against Inverse Compton cooling (Thomson limit) was calculated via:

$$\tau(E_e = 10 \text{ TeV}) \sim 4.8 \text{ kyr} B^{-2} (10 \mu\text{G}) E^{-1/2} (\text{TeV}) , \quad (7.3.6)$$

Region	$E_b(\text{TeV})$ (fit)	$E_b(n = 3)(\text{TeV})$	n
5	$3. \pm 1.$	21.0 ± 0.3	1.78 ± 0.03
1	2.8 ± 0.7	22.0 ± 0.1	1.71 ± 0.03
3	2.96 ± 0.01	23.92 ± 0.02	1.70 ± 0.01
4	2.2 ± 0.7	24.555 ± 0.002	1.60 ± 0.04
2	1.76 ± 0.01	24.594 ± 0.001	1.54 ± 0.01

Table 7.7: Fitted break energies E_b for the underlying broken power law particle spectrum in each region. For comparison, the break energy corresponding to a braking index of $n = 3$ is calculated from equation (7.3.8), and the braking index required to produce the fitted break energy is calculated.

and of particles producing keV photons against synchrotron cooling from the expression:

$$\tau(E_X) \sim 1.2\text{kyr}B^{-3/2}(10\mu\text{G})E_e^{-1/2}(\text{keV}) . \quad (7.3.7)$$

This enabled the corresponding diffusion and advection radii to be estimated. The diffusion radius R_d for 1 TeV particles from each box was calculated using equation (7.2.4), taking a representative value of $\delta = 0.4$ and a literature value for the diffusion coefficient of $D_0 = 1. \times 10^{28} \text{ cm}^{-2}\text{s}^{-1}$. The advection radius was calculated by integrating equation (7.2.8) up to a time τ , adopting values of $v_0 = c/\sqrt{3}$ and $r_0 = 0.1 \text{ pc}$, as was done in section 7.2.2. The value of τ , for the age of the particles in each region, was taken to be whichever was the shorter of the calculated lifetime for Inverse Compton scattering (equation (7.3.6)) and the age of the system (21 kyr). Interestingly, the diffusion and advection radii of $\sim 30 - 60 \text{ pc}$ obtained for the innermost regions of the nebula (boxes 5 and 1) are somewhat below the observed size ($\sim 100 \text{ pc}$). This could imply that the transport was faster in the past, that the lifetime of particles against cooling losses is longer than that calculated by equation (7.3.6) or that the adopted standard values are a poor description of this region.

Break Energy of the Particle Spectrum

An expression to determine the break energy of the electron spectrum, including a Klein-Nishina suppression factor, was obtained in [114] by setting the spindown age of the pulsar equal to the total radiation lifetime:

$$E_b = \frac{6.2\text{TeV}(n - 1)^2}{(1 + 0.144B^2(\mu\text{G})^2)} . \quad (7.3.8)$$

This expression can be used to calculate the expected break energy for a particular braking index n . As the break energy of the intrinsic underlying particle spectrum was also a free parameter of the fit, however, expression (7.3.8) could also be rewritten to yield the braking index required in order to obtain the measured break energy. Table 7.7 lists both the fitted break energy, the calculated break energy for a braking index of $n = 3$, corresponding to a magnetic dipole, and the required braking index for the fitted break energy.

In table 7.7, the fitted break energies for the particle spectra are listed together with the break energies corresponding to the typically assumed braking index of $n = 3$, calculated using equation (7.3.8). The required braking index to produce the fitted break energy is also calculated, and is found to be significantly lower. Interestingly, the values lie between the value measured for the Vela pulsar ($n = 1.4$) and the value obtained in the most advanced model of the multi-zone HESS J1825-137 modelling of [109] ($n = 1.9$). As the values gradually decrease away from the pulsar, this could imply that the pulsar braking index has varied over time and that the values

obtained in table 7.7 correspond to the braking index of the pulsar at the time that the particles in that region were first injected into the nebula.

7.4 Previous Models of HESS J1825-137

Generally, models attempt to follow the evolution of a PWN through one or more of the major distinct evolutionary phases, comprising the initial free expansion stage, prior to interaction with the supernova; through the interaction with the supernova reverse shock, sometimes also explicitly including the crushing of the PWN by the shock; and the subsequent expansion of the PWN in the Sedov-Taylor phase of its evolution. Additionally, different dynamics may be used to describe the PWN evolution on timescales less or greater than the spin-down timescale, τ_0 . This evolutionary change may occur either before or after the interaction with the reverse shock, and depends both on the initial conditions at the time of the pulsar's birth, and on the properties of the surrounding medium. In general, it is far more common that the pulsar surpasses its characteristic age prior to the interaction with the reverse shock [92].

Previous attempts at modelling HESS J1825-137 have ranged from one zone models reproducing the overall spectrum [111], to those attempting to reproduce the energy dependent morphology, focusing either on fitting the spectral results [109] or both the spectral variation and spatial distribution [110].

A one-zone time dependent model was applied to the joint Fermi-LAT and H.E.S.S. spectral energy distribution (SED) in the 2011 Fermi analysis [111], following the evolution of the PWN through the free expansion and subsequently the Sedov phases, using three primary photon fields (of CMB, dust and starlight) for inverse Compton scattering.

A similar one-zone time-dependent approach was implemented in previous spectral modelling of H.E.S.S. results by A. Lemière [125]. However, given the significant spectral variation across the nebula and its distorted morphology, one-zone models (which are by definition homogeneous) are likely to be inadequate for reproducing precisely the observed properties of HESS J1825-137. Nevertheless, they can provide a useful means of deriving and constraining overall properties of the nebula, such as its age, the spectrum of injected particles and the overall cooling, to within an order of magnitude.

Spatial modelling of the evolution of the PWN was explored by J. Brucker [110], in an attempt to reproduce the observed morphology. In a similar vein, a more complex multi-zone approach to reproducing the spectral variation was presented in [109]. Both of these models focused on the diffusion and cooling of electrons over time, travelling away from the pulsar. Twelve sequential zones of particles, to match the 12 radial spectral regions used in the 2006 H.E.S.S. analysis [95], were used in the modelling of [109], tracking each zone from their injection at the pulsar position through their transport away from the pulsar and subsequent energy loss. Leakage of particles from one zone into a neighbouring zone was also accounted for; this model is shown schematically in figure 7.12.

In total, four models were considered in the multi-zone modelling work [109], of gradually increasing complexity. The first, of uniform expansion and a constant magnetic field, overpredicted the VHE flux in the innermost region whilst underpredicting it at the edge of the nebula. The second model, using a velocity profile of decreasing velocity with increasing radial distance from the pulsar and a constant magnetic field of $5.6 \mu\text{G}$, reproduced the VHE flux in the middle regions well, yet underpredicted the X-ray flux close to the pulsar and overpredicted the outermost VHE flux. This implied that near to the pulsar, the magnetic field must be $> 5 \mu\text{G}$, yet

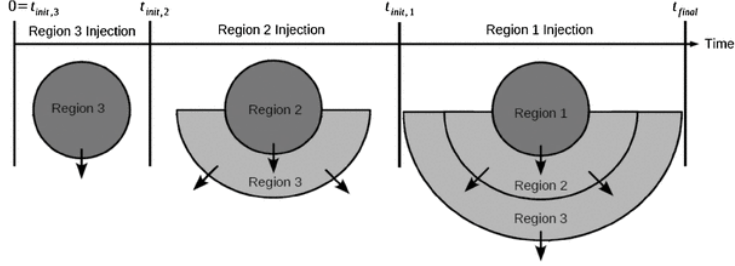


Figure 7.12: Figure taken from [109], illustrating their multi-zone approach. Each zone is injected at the same central location, yet separated in time, with the same size, zone shape and injection spectrum. The particles then diffuse away and into neighbouring zones (arrows) cooling in the process (light grey).

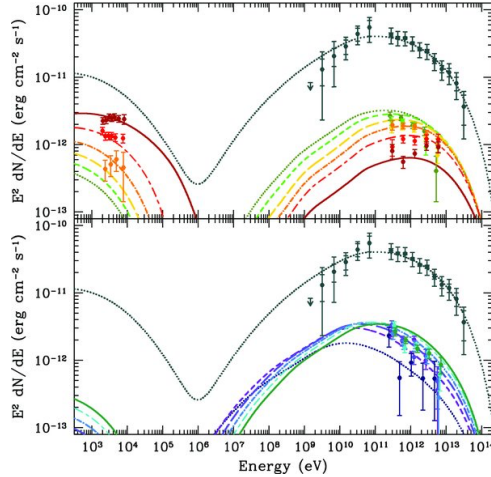


Figure 7.13: Fit to data from Fermi-LAT (2011 analysis [111]), H.E.S.S. (2006 analysis [95]) and Suzaku (from a re-analysis by van Etten et al. [109]), provided by fourth model of [109], incorporating magnetic field and velocity profiles, and diffusion. The colours run from red for the youngest (innermost) region to violet for the oldest, (outermost) region. The six inner regions (above) and six outer regions (below) are shown separately for clarity, with the total SED corresponding to the full nebula plotted in black above the zones in both panels.

significantly lower further out, in agreement with the findings of the magnetic field mapping in section 7.3 and requiring a non-uniform magnetic field. Including a magnetic field profile (as a function of radius and time) in their third model improved the matching to the X-ray flux, but the discrepancy with the VHE flux in the outermost regions remained. Finally, the best fit to all data was provided by a fourth model, which included fast energy-dependent diffusion as well as the velocity and magnetic field profiles. In the absence of re-acceleration within the nebula, by (for example) reverse shock interactions, strong diffusion is required to account for high-energy particles still producing TeV emission at large radial distances from the pulsar, especially given the strong energy losses due to synchrotron cooling in the inner regions of the nebula. This fit is illustrated in figure 7.13.

7.5 One-Zone Pulsar Wind Nebula Model

To learn about some properties of the HESS J1825-137 PWN, the H.E.S.S. spectral data presented in chapter 6 was modelled. For simplicity, a one-zone approach was initially adopted, aiming to fit the spectrum obtained from the full region, as shown in figure 6.15. For this purpose, the GAMERA modelling package (along with its python based distribution, GAPPA) was used, which is designed for spectral modelling of non-thermal astrophysical sources [126]. To

Parameter	Model 1 [127]	Model 2 [125]
Injection Spectrum	(7.5.1)	(7.5.1)
Luminosity Evolution	(7.5.2)	(7.5.2)
Maximum Particle Energy	(7.5.3)	(7.5.11)
Radius Evolution	(7.5.13)	(7.5.13)
Velocity Evolution	(7.5.7)	(7.5.7)
Magnetic Field Evolution	(7.5.8)	(7.5.12)
Radiation Fields	table 7.9	table 7.9

Table 7.8: The two models used in sections 7.5.3 and 7.5.4 are broadly similar; both are one-zone free expansion models and many of the equations governing the evolution are common to both. The major difference is in the description of the magnetic field evolution; in the case of model 1, this includes adiabatic losses as the PWN shock expands in the ambient medium. These losses are not accounted for in model 2.

help constrain the models, points taken from the 2011 Fermi-LAT analysis are also included in the modelling [111]. A comparison of two alternative one-zone free expansion models is made, followed by their enhancement with inclusion of a kinematic description of the reverse shock.

7.5.1 Free Expansion Model: description

An established time-dependent model for freely expanding PWN by Martín et al. [127], has been successfully applied to a number of young PWN systems in [128]. An alternative yet similar free expansion approach was applied to HESS J1825-137 by A. Lemière [125]. Here, a fit to the spectral analysis of the whole region is performed using two models; the aforementioned models by Martín et al. [127] and by Lemière [125]. These models shall henceforth be referred to as models 1 and 2 respectively. A brief overview of the equations governing the models is given in table 7.8, referencing the relevant parts of sections 7.5.3 and 7.5.4 where they are described in more detail. Models 1 and 2 have many common components as summarised in table 7.8; for clarity, model 1 will be described here in full, with those changes specific to model 2 outlined in section 7.5.4.

Both of these are simple one-zone free expansion models, assuming continuous injection and expansion over time into a low density environment. In reality, given the age and observed highly asymmetric shape of the nebula, this PWN is the archetypal example of a PWN which has already undergone the passage of the reverse shock from the progenitor SNR, possibly crushing the nebula in one direction and contributing to its asymmetric shape. The molecular clouds found to the North of HESS J1825-137 add credence to this interpretation [113]. Another possibility is a significant contribution of diffusion and/or advection to the particle transport. In these scenarios, a one-zone free expansion model is not expected to be an accurate description of the properties of the nebula.

With these caveats in mind, however, one can nevertheless proceed to investigate a set of model parameters consistent with the measured data points. Insofar as this can reflect the true situation of the nebula, model curves consistent with the data are presented in sections 7.5.3 and 7.5.4 for both models.

A broken power law spectrum was adopted for the injection of particles into the pulsar wind

Radiation Field	Temperature (K)	Energy density (eV cm ⁻³)
CMB	2.7	0.25
Dust	50	1.
Starlight	5000	1.

Table 7.9: Radiation fields contributing to the inverse Compton emission in the spectral modelling. For each contribution, their thermal temperature and energy density is given.

nebula;

$$Q(E_e, t) = Q_0(t) \begin{cases} \left(\frac{E_e}{E_b}\right)^{-\alpha_1} & E_e \leq E_b \\ \left(\frac{E_e}{E_b}\right)^{-\alpha_2} & E_e > E_b \end{cases} \quad (7.5.1)$$

with power law indices α_1 and α_2 corresponding to energies below and above the break energy E_b respectively. The particle population was assumed to be purely leptonic (or equivalently that the contribution from ions is negligible).

The one-zone model was adjusted to data from the Fermi-LAT [111] and from the full spectrum of dataset A. The emission was treated as predominantly due to Inverse Compton scattering on three radiation fields; dust, starlight and the Cosmic Microwave Background (CMB), listed in table 7.9, whilst Bremsstrahlung and synchrotron losses were also taken into consideration.

The model was evolved over a timespan running from the birth time of the pulsar, $t = 0$, to the present age of the system, with the age as an input parameter (taken to be the characteristic age of the pulsar). In practice, the evolution of a pulsar wind typically does not begin until a few decades after the time of the pulsar's birth; however, this was not treated explicitly, as the time for which there was no evolution is short compared to the age of the pulsar.

The pulsar spin-down luminosity (L) evolution was governed by the expression:

$$L(t) = (1 - \eta_b)L_0 \left(1 + \frac{t}{\tau_0}\right)^{-\frac{n+1}{n-1}}, \quad (7.5.2)$$

where n is the braking index, η_b a measure of the amount of energy transferred into the magnetic field, L_0 the initial luminosity and τ_0 , the initial spin-down time. All of these are generally unknown parameters, however a value of $b = 3$ is often taken for the braking index, which corresponds to losses by a dipolar magnetic field. The maximum energy of the particles was obtained as a function of the luminosity, constraining the highest energy emission of the system:

$$E_{\max} = 3\varepsilon e \sqrt{\frac{\eta_b L(t)}{(1 - \eta_b)c}}, \quad (7.5.3)$$

where ε is the fractional size of the PWN shock radius; e the electron charge and c the speed of light. This expression is obtained by imposing confinement of the particles within the PWN system, constraining the Larmor radius of the particles gyrating around magnetic field lines to be less than the termination shock radius. Particles with energies beyond this maximum would be sufficiently energetic to leave the system, subsequently no longer contributing to the emission.

The evolution of the PWN radius $R(t)$ over time is governed by the expression [129]:

$$R(t) = C \left(\frac{L_0 t}{E_0}\right)^{1/5} V_{ej} t, \quad (7.5.4)$$

where E_0 is the initial energy released by the supernova explosion and V_{ej} is the velocity of the supernova ejecta, which forms the surrounding medium into which the PWN is expanding. V_{ej} is obtained as a function of E_0 and the ejected mass M_{ej} :

$$V_{ej} = \sqrt{\frac{10E_0}{3M_{ej}}} . \quad (7.5.5)$$

The constant C in expression (7.5.4) is dependent on the properties of the PWN gas via the ratio of specific heats γ_p ;

$$C = \left(\frac{6}{15(\gamma_p - 1)} + \frac{289}{240} \right)^{-1/5} , \quad (7.5.6)$$

with a value of $\gamma_p = 4/3$ assumed for the inner PWN environment. The velocity of the particles in the system is simply taken as the derivative of expression (7.5.4), that is:

$$V(t) = \frac{dR(t)}{dt} = 1.2 \frac{R(t)}{t} , \quad (7.5.7)$$

since $R(t) \propto t^{6/5}$, from equation (7.5.4). The only remaining time dependent quantity is the magnetic field, which was expected to evolve in time due to its radius dependence; $B \propto R^{-3}$, reducing in strength as the nebula expands. The expression governing the evolution of the magnetic field B was:

$$W_B = \frac{4\pi}{3} R^3(t) \frac{B^2}{8\pi} , \quad (7.5.8)$$

where the magnetic energy, W_B , is defined as the magnetic energy density U_B multiplied by the volume V , and is obtained from the luminosity by numerically solving:

$$RW_B = \int_0^t \eta_b L(t) R(t) dt . \quad (7.5.9)$$

This treatment of the magnetic field, taken from [128], takes into account the energy losses from the system as the nebula expands, due to the work done on the surroundings. Subsequently, in the case of using equation (7.5.8) to describe the magnetic field, a larger fraction of energy in the magnetic field is generally required than for models which do not take these losses into account.

7.5.2 Parameter Constraints

Several input parameters of the model are assigned canonical values, representative of similar systems in the literature. These are listed in table 7.10.

A number of parameters entering into the model could be constrained from observations and measurements of the system. The period, P and period derivative \dot{P} of the pulsar can be measured to great accuracy, and have the values $P = 0.1014867942076(3)s$ and $\dot{P} = 7.525170(1) \times 10^{-14} s s^{-1}$ [96].

Although the true age of the system is unknown, the characteristic age, $\tau_c = P/2\dot{P}$ could be used as a proxy for the age, T , and has a measured value 21 kyr. A caveat of using the current values for the period and period derivative of the pulsar is that they change between events known as ‘glitches’. A pulsar glitch is thought to occur when angular momentum from the superfluid core of a pulsar is transferred to its crust (which are usually decoupled), leading to dynamical adjustment and relaxation, causing a change in spin frequency [130]. Consequently, the observed spin-down frequency of the pulsar (and hence its period) abruptly increases, followed by a period

Parameter	Value
Age, T	21 kyr
Ejected mass, M_{ej}	$8 M_{\odot}$
SN energy, E_0	10^{51} erg
Distance, d	4.12 kpc
Ambient density, ρ_n	0.3 cm^{-3}
Braking Index, n	3.
Fractional size, ε	0.5
Fractional energy, η_b	0.03
Initial magnetic field, B_0	$5 \mu\text{G}$
Energy ratio, σ	0.1
α	0.7

Table 7.10: Input parameters of the models. Parameters below the dashed line apply to model 2 only (section 7.5.4). ε is the fractional size of the shock radius and η_b the fraction of the energy transferred to the magnetic field; σ and α are defined in section 7.5.4. The value for the distance, d is measured from the dispersion measure, and the age T from the characteristic pulsar age (see text); all other values are representative and taken from the literature.

of recovery typically lasting a few days, during which the spin frequency and period recover to their pre-glitch values. The characteristic age is also only a good estimator of the true age under the assumptions that the age is much larger than the spin-down timescale, $T \gg \tau_0$, and that the braking index is $n = 3$. Hence, τ_c is often an overestimate of the age of the pulsar; a case in point is the Crab pulsar, which has a characteristic age of roughly 1.3 kyr, although its true age is known to be 962 years [96]. For PSR B1823-13, there have been six glitches since measurements began, three of which have occurred since the start of H.E.S.S. data taking on this region in 2004 [130]. This pulsar is also considered Vela-like (through the similarity of its rotational parameters and characteristic age), and was found to also fulfil the criterion for a pulsar undergoing particularly large glitches, with quasi-periodicity [130].

From the measurements made in section 7.3, it has been shown that the magnetic field reduces to at least $1.6 \mu\text{G}$ at an angular distance of 1° from the pulsar. Therefore, the magnetic field was constrained to drop from its initial value to $\sim O(\mu\text{G})$ at the current time ($t = T$). Additionally, from the measurements of the extent made in chapter 6 and in section 7.2, the radius was required to reach a size of 100 pc at the current time. As spectra have been extracted from regions out to 100 pc, the emission appears to still be at the $\sim 10\%$ level (of the peak flux) and that the characteristic age is likely to be overestimated; a radius of 100 pc can be considered as a conservative lower limit to the true extent of the nebula.¹

The spin-down luminosity of the pulsar can also be measured to good precision by current instruments; hence the luminosity was constrained to today's value, such that $L(t = T) = 2.8 \times 10^{36} \text{erg s}^{-1}$.

By rewriting equation (7.5.4) in terms of $R(t = T) = 100 \text{ pc}$, it is possible to obtain the required initial luminosity:

$$L_0 = \left(\frac{R(t = T)}{CV_{ej}T} \right)^5 \frac{E_0}{T}, \quad (7.5.10)$$

¹Note that this radius in the model corresponds to the distance from the pulsar to the outermost edge of the nebula, i.e. the 100 pc diameter in this case, since the pulsar is severely offset from the nebula centre.

Parameter	Model 1	Model 2
α_1	0.5 ± 0.1	0.5 ± 0.3
α_2	2.876 ± 0.007	2.82 ± 0.02
E_b (TeV)	1.809 ± 0.003	1.62 ± 0.05

Table 7.11: Spectral parameters for the broken power law particle spectrum, used for the SEDs shown in figures 7.15 and 7.16.

yielding a value for the initial luminosity of $3.95 \times 10^{39} \text{erg s}^{-1}$, for an E_0 as given in table 7.10. From the determined value of L_0 , it was also possible to constrain the value of τ_0 , typically unknown, through equation (7.5.2), provided that values of the braking index n and of η_b were assumed. From the values listed in table 7.10, an initial spin-down time $\tau_0 = 572$ yrs was found.

7.5.3 Model 1

In order to match the spectral points, a braking index of 3 was found to be incompatible, with lower values for the braking index improving the compatibility. A good match was obtained for a braking index of between 2 and 2.5; following the modelling studies of [109], a value of 2.2 was adopted. This value was obtained for their “model 3”; which comprises velocity evolution and magnetic field evolution, similar to this simple model although the precise expressions differ. The best fit obtained in [109] was their “model 4”, which also includes diffusion losses in the system, and led to a braking index of 1.9 ± 0.2 . Measured braking indices are typically less than 3, and a value of 1.4 ± 0.2 has been measured for the Vela pulsar (also compare to the values obtained in section 7.3.3, table 7.7). Since the spin properties of PSR B1823-13 are similar to those of Vela, lowering the braking index can be considered a reasonable parameter adjustment for describing this system. The remaining free parameters described the spectrum of the system, and were adjusted to match the data. These are listed in table 7.11.

The evolution of the luminosity, radius and magnetic field (constrained parameters) is shown in figure 7.14. The particle spectrum and γ -ray spectral energy distribution (SED) is shown in figure 7.15; the resulting curve is compatible with the measured data.

7.5.4 Model 2

This model is broadly similar to that presented in the previous section; more details are given in [125], much of which is already included in the GAMERA package used for this modelling [126]. The implementation of this model within the GAMERA package only differed from the previous model in two main aspects: the equations governing the time evolution of the maximum energy and of the magnetic field. The maximum energy evolution is governed in much the same way as equation (7.5.3), yet differs in some efficiency coefficients:

$$E_{\max} = \epsilon e \sqrt{\frac{\sigma}{1 + \sigma}} \times \sqrt{\frac{\kappa L(t)}{c}}, \quad (7.5.11)$$

where $k = 3(1 - 4\sigma)$ and $\sigma = L_{E,B}/L_e$ is the ratio of the amount of energy stored in the electromagnetic field to the energy stored in the particles. The similarity to equation (7.5.3) is immediately obvious, with the terms involving σ quantifying the relative amount of energy in the magnetic field playing the same role as the parameter η_b in (7.5.3). The time dependence of

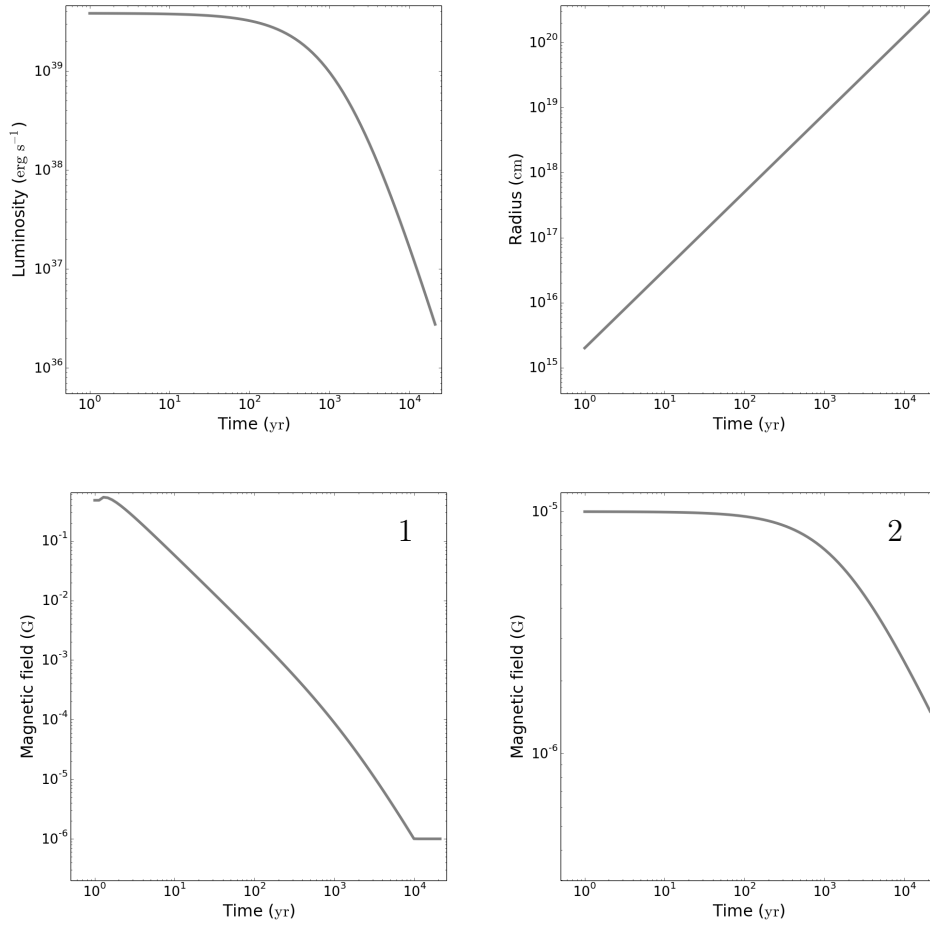


Figure 7.14: Evolution of the luminosity, radius and magnetic field of a PWN under the assumption of free expansion. The luminosity and radius evolution was the same for both models 1 and 2, whilst the magnetic field evolution (below) had a different time dependence in models 1 and 2. All three parameters are constrained to reach currently measured values at $t = T$; $L(T) = 2.8 \times 10^{36} \text{ erg s}^{-1}$, $R(T) = 100 \text{ pc}$ and $B(T) \sim O(\mu\text{G})$.

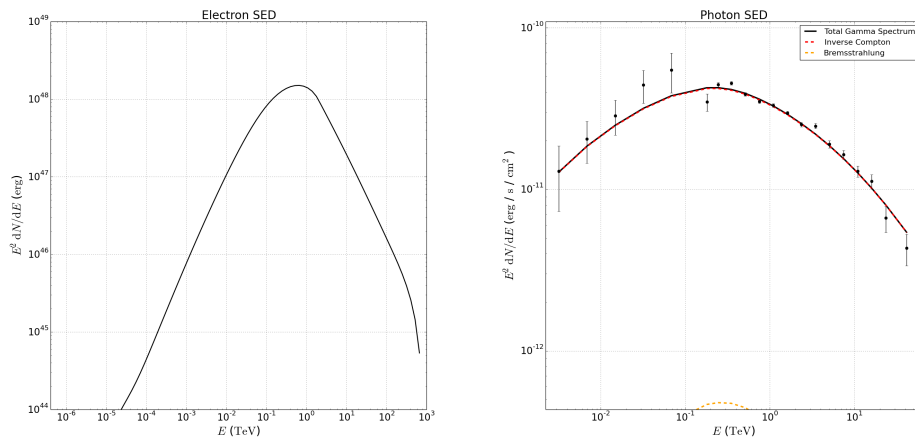


Figure 7.15: The evolved particle spectrum and resulting γ -ray spectrum from the free expansion model 1. The γ -ray spectrum is dominated by Inverse Compton emission, with a small Bremsstrahlung contribution. The parameters of the initial particle spectrum are listed in table 7.11. Systematic errors have been used for the Fermi-LAT points from Grondin et al [111], whereas the H.E.S.S. points from the dataset A analysis of chapter 6 are shown with statistical errors only.

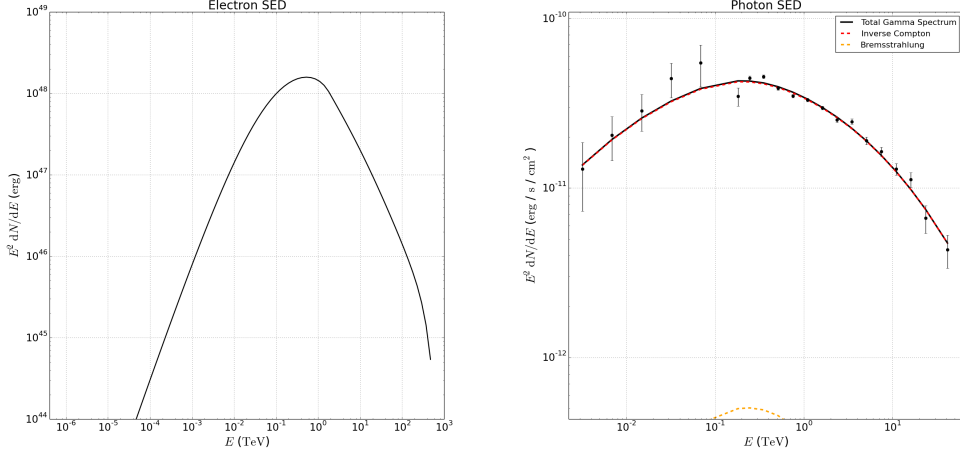


Figure 7.16: The evolved particle spectrum and resulting γ -ray spectrum from the free expansion model 2. The γ -ray spectrum is dominated by Inverse Compton emission, with a small Bremsstrahlung contribution. Systematic errors have been used for the Fermi-LAT points from Grondin et al [111], whereas the H.E.S.S. points from the dataset A analysis of chapter 6 are shown with statistical errors only.

the magnetic field in model 2 is somewhat simpler than equation (7.5.8):

$$B(t) = \frac{B_0}{\left(1 + \frac{t}{\tau_0}\right)^\alpha}, \quad (7.5.12)$$

where B_0 is the initial magnetic field at $t = 0$, and α determines the strength of the reduction in magnetic field over time, typically within the range $0.3 < \alpha < 0.75$. Adopting a value of 2.2 for the braking index, as was used in model 1, high values of α were favoured, and a value of 0.7 was adopted. The set of spectral parameters found to be compatible with the data are listed in table 7.11, along with the spectral parameters of model 1.

The evolution of the luminosity and radius were essentially the same as that of Model 1, the major difference being in the evolution of the magnetic field, which in this model does not take adiabatic losses into account (see figure 7.14). As can be seen from the parameters given in table 7.11, the spectral parameters were compatible, such that the resulting curves for model 2 (shown in figure 7.16) did not differ greatly from those shown in figure 7.15.

7.5.5 Reverse Shock Evolution

Given the measured age of the pulsar, it is highly likely that the system has already surpassed the free expansion phase and entered the Sedov phase of evolution. One-zone models, such as those presented in section 7.5, even if they cover later evolutionary stages such as the interaction of the supernova reverse shock, make the intrinsic assumption of radial symmetry, which is clearly not adequate to explain the morphology of HESS J1825-137.

A simple extension of these models is to add the expected kinematical evolution of the radius and velocity following the passage of the reverse shock, without considering the reverse shock interaction dynamics in detail. In the context of the overall lifetime of the nebula, the length of time over which the reverse shock interaction dynamics play a significant role is treated as short with respect to the overall timescale. As such, the reverse shock interaction is not treated explicitly, with the radius pre- and post-shock normalised to be in agreement (except

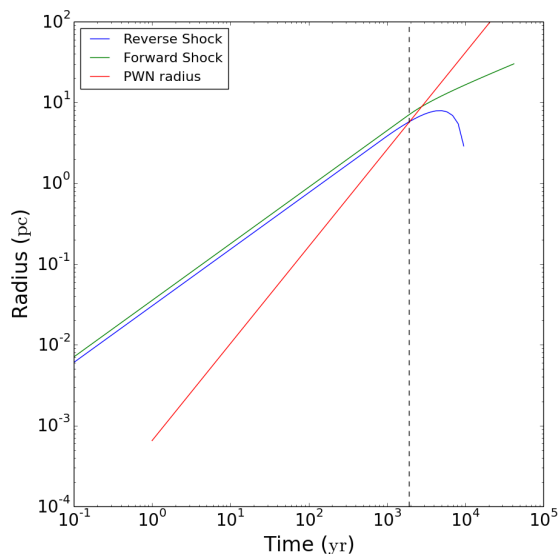


Figure 7.17: Evolution of the SNR forward shock, SNR reverse shock and PWN forward shock with time. The SNR reverse shock meets the PWN forward shock at ~ 2000 yrs. The PWN has been assumed to start evolving after the SNR.

for an arbitrary compression factor), and continuous expansion, at a reduced rate, is considered afterwards. Explicit treatment of the reverse shock interaction is well accounted for in the more advanced model of [123], which considers compressional evolutionary phases, in addition to the expansion phases considered here. Due to its thorough treatment of the magnetic field, taking into account adiabatic losses, the extension into multiple evolutionary stages was made using model 1.

To investigate the time at which the reverse shock from the progenitor SNR is expected to interact with the forward shock of the PWN, the analytical treatment of Truelove and McKee is adopted for the parameters of this system, assuming a density index of $n = 10$ [131]. This description of the shock radii, readily available within the GAMERA package, is shown in figure 7.17, together with the evolution of the PWN forward shock in the free expansion treatment.

From the simple evolution of the shock radii shown in figure 7.17, a time of $t = 2000$ yrs was adopted for the reverse shock interaction.

The dynamical evolution of the PWN within three evolutionary stages, defined by the initial spin-down timescale τ_0 and the time of the reverse shock passage t_{rs} was described by the equations given below, adjusting the radial profiles [92]:

$$R \propto \begin{cases} t^{6/5} & \text{for } t \leq \tau_0 \\ t & \text{for } \tau_0 < t \leq t_{rs} \\ t^{3/10} & \text{for } t > t_{rs} \end{cases}$$

where the expressions have been taken for the usual case of the reverse shock passage, $t_{rs} > \tau_0$. In [92], a fourth evolutionary phase is also discussed, occurring between the first and second phases listed in equation (7.5.13), in the case that the SNR forward shock sweeps up all of the ejecta mass within a time shorter than τ_0 . In this simple treatment, it has been assumed that the spin-down timescale τ_0 elapses prior to the SNR mass being swept up. In the less frequent case of the reverse shock interaction occurring at $t_{rs} < \tau_0$, expressions (7.5.13) become:

$$R \propto \begin{cases} t^{6/5} & \text{for } t \leq \tau_0 \\ t^{11/15} & \text{for } \tau_0 < t \leq t_{rs} \\ t^{3/10} & \text{for } t > t_{rs} \end{cases} \quad (7.5.13)$$

modifying the evolution of the middle phase only. The corresponding velocity profiles are obtained from the derivative of the radial profiles, $v = dR/dt$.

When using the same parameters as were obtained for the free expansion treatment in this description, in order to impose the same parameter constraints, whilst the constraint on the final luminosity remained similar, the radius constraint was rather more complex. The full expression for the radius at the current time, $R(t = T)$ for the age of the system $T = 21$ kyr, was obtained by propagating through the different evolutionary stages:

$$R(t = \tau_0) = K\tau_0^{6/5} \quad (7.5.14)$$

$$R(t = t_{rs}) = R(t = \tau_0) \frac{t_{rs}}{\tau_0} \quad (7.5.15)$$

$$R(t = T) = \frac{1}{\eta} R_{rs} \left(\frac{T}{t_{rs}} \right)^{3/10} \quad (7.5.16)$$

where $K = cL_0v_{ej}$ with L_0 determined by expression (7.5.2) at $t = T$ and η is the compression ratio at the reverse shock (the factor by which the system was crushed as the reverse shock interaction occurred, when treating the event as instantaneous). Typical values for η lie in the range 1.1 to 5, and a low value of $\eta = 1.2$ was adopted.

By setting the final radius to a fixed value, $R(t = T) = R_{\text{PWN}}$, the expression (7.5.16) ($R(t = T) - R_{\text{PWN}} = 0$) could be solved for τ_0 using a numerical solver algorithm. (Brentq, [132]). A reduced size of the nebula R_{PWN} was adopted, as no solutions were found for $R(t = T) = 100$ pc, and the reverse shock evolution was consequently presumed to affect the core of the system (the brightest part) most, with emission at larger radii being attributed to diffusion processes (as demonstrated in section 7.2). Two plausible radii of 20 pc and 40 pc were considered, corresponding to total nebula sizes of 40 pc and 80 pc respectively. Implicitly, this assumes radial symmetry of the nebula around a pulsar located at the centre of the nebula, which is known not to be the case in this system, a major caveat of this model. After τ_0 had been determined, the required value for L_0 could also be obtained.

In figure 7.18, the radius is compressed by a factor 1.2 at the reverse shock interaction, whilst the change in velocity is more dramatic. The evolution of the magnetic field strength with radius follows the same curve, such that as the system is compressed, the magnetic field increases.

The resulting spectrum was consistent with the data points in both cases (figures 7.19 and 7.20), yet provided a better match in the case of the larger PWN radius. The spin-down timescale obtained from these constraints was shorter than in the free expansion case ($\sim O(10^2)$ yrs). This occurs such that the radius evolution is considerably faster than in the free expansion case, in order to compensate for the subsequent crushing of the nebula and slower radius evolution, and still reach the required radius at $t = T$. Additionally, the initial luminosity was found to be much greater than in the free expansion case. With this parameter combination, the energy losses by electrons in the early phases of the nebula evolution is much more rapid, leading to an underestimate in the expected amount of emission at the highest energies, although the emission is grossly overestimated across most of the energy range.

Given the extreme size of the PWN and its highly asymmetric morphology, one-zone models are inadequate to account for both the distance over which the particles have been transported

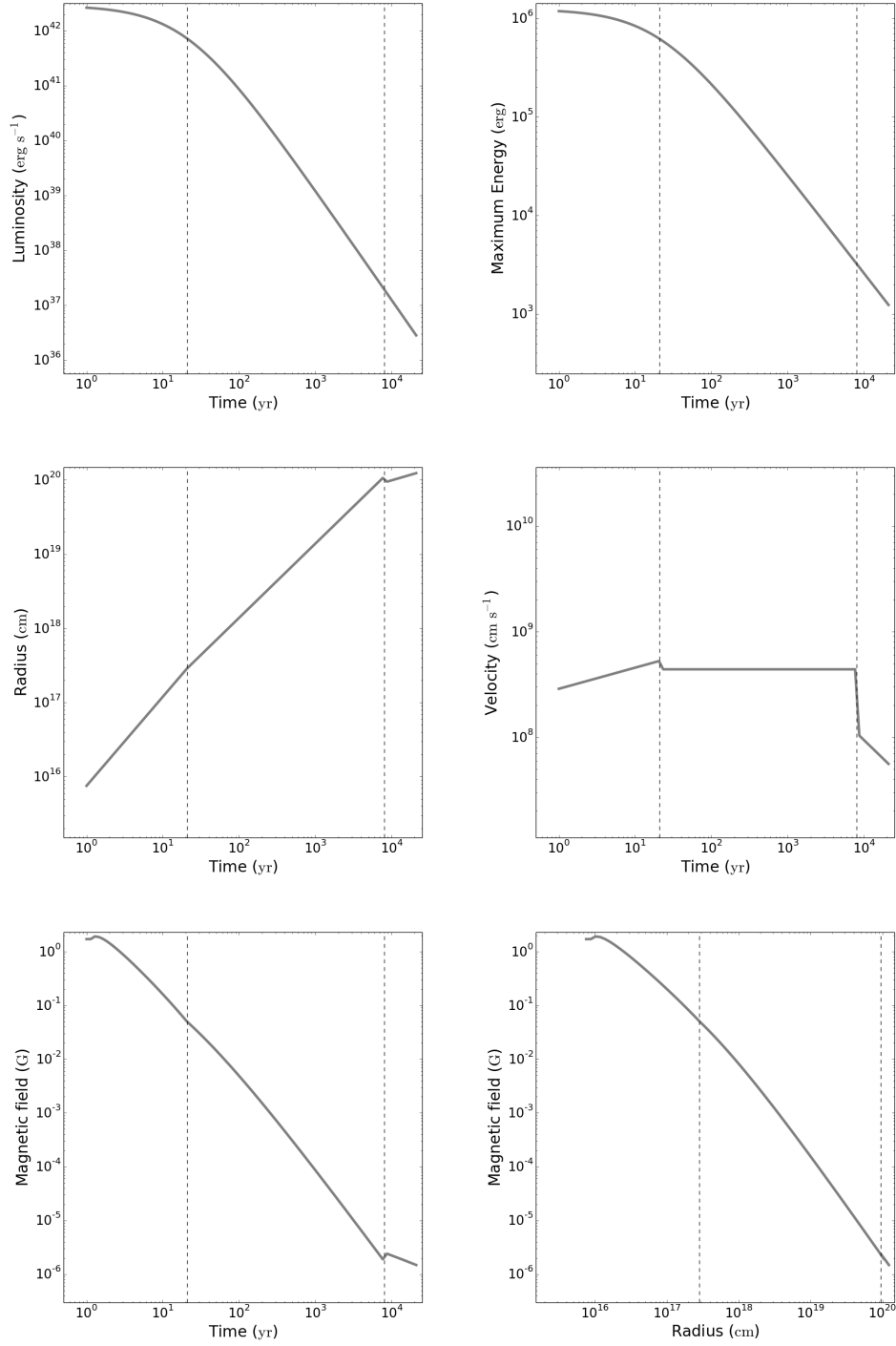


Figure 7.18: Evolution of the luminosity, radius and magnetic field of a PWN under a three phase description of the reverse shock evolution. The luminosity, magnetic field and radius are again constrained to reach measured values today, with, $R(T) = 40$ pc. The maximum energy evolves similarly to the luminosity. Times τ_0 and t_{rs} are indicated by dashed lines, with $\tau_0 < t_{rs}$. For the magnetic field against radius plot, the equivalent radius reached at the times τ_0 and t_{rs} was used.

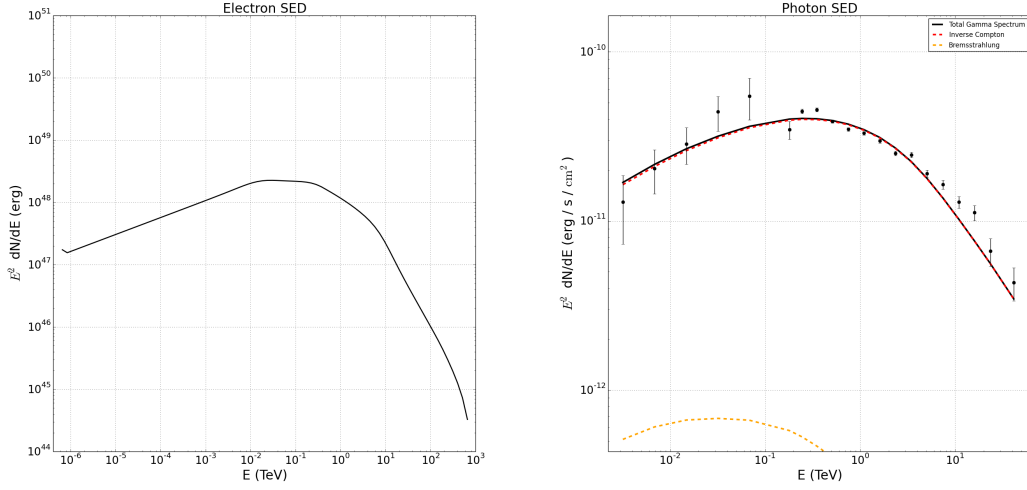


Figure 7.19: The evolved particle spectrum and resulting γ -ray spectrum from model 1 with enhanced kinematic evolutionary phases. In this case, the radius is constrained to reach 20 pc at $t = T$. The γ -ray spectrum is dominated by Inverse Compton emission, with a small Bremsstrahlung contribution.

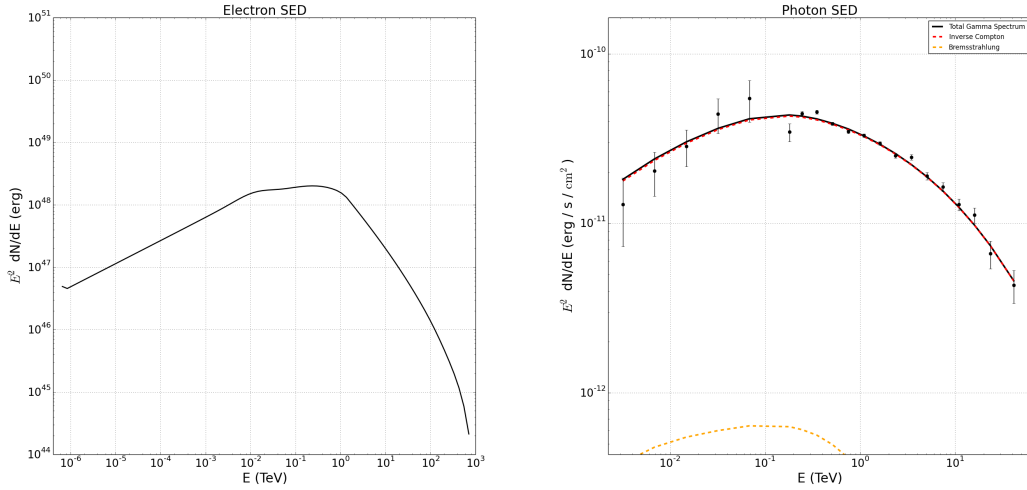


Figure 7.20: The evolved particle spectrum and resulting γ -ray spectrum from model 1 with enhanced kinematic evolutionary phases. In this case, the radius is constrained to reach 40 pc at $t = T$. The γ -ray spectrum is dominated by Inverse Compton emission, with a small Bremsstrahlung contribution. The data points seem to be better matched with a 40 pc radius than the 20 pc of figure 7.19.

Parameter	$R(T) = 20$ pc	$R(T) = 40$ pc
$\alpha 1$	1.73 ± 0.02	1.63 ± 0.01
$\alpha 2$	2.29 ± 0.02	2.78 ± 0.01
E_b (TeV)	0.59 ± 0.01	1.35 ± 0.01

Table 7.12: Spectral fit parameters for kinematical reverse shock model, with radius at the current age of the system T constrained to 20 pc and 40 pc.

and the asymmetric nature of the nebula. The simple kinematical description of the nebula evolution with reverse shock dynamics is inconsistent with the observations; one can conclude that the observed nebula extent is not solely from an isolated, radially symmetric PWN bubble, (although this may account for the core emission) but that a large proportion of the extent is due to diffusion of the particles away from the central PWN region.

7.6 Conclusions on Modelling of HESS J1825-137

From the simple evolutionary studies in section 7.4, it can be seen that although a one-zone free expansion model can be made to fit the system within the observational constraints, this scenario does not tie in well with the observed morphology of the system, particularly the strong gradient in surface brightness and the overall asymmetry. Both the free expansion and reverse shock descriptions (sections 7.5.1 and 7.5.5) treat the emission as due to particles continually injected into a PWN bubble, which is then subsequently evolved as a single system over time. To reproduce both the observed morphology and spectral parameters, the following scenario may be considered more likely:

The initial injection of particles forming the PWN took place rapidly, yet particles have been continually injected by the wind ever since. A PWN bubble was formed, freely expanding into the ambient medium which had been evacuated by the progenitor supernova. In some directions, the supernova forward shock proceeded unimpeded, and can be seen at large distances of ~ 120 pc from the pulsar today (figure 7.2). In other directions, the supernova was drastically slowed at early times by the presence of several molecular clouds in the region, the shock interaction causing them to become turbulent [113]. Due to these molecular clouds (such as R1 in figure 7.2), the supernova reverse shock formed and passed through the nebula from these directions comparatively early in its evolution, offsetting the particle distribution and consequently the observed emission from the pulsar position, maybe even contributing to the transport of particles in the Southerly direction.

Over the history of the nebula, particles accelerated in the pulsar wind were continually injected into the nebula, forming the bright core to the emission observed today, and undergoing advective flow. In the case of a steady-state with $\dot{\rho} = 0$, a velocity profile of $v \propto r^{-0.6}$, corresponding to more disc-like flow than spherical expansion. As the particles travel further out into the nebula, they continually undergo synchrotron cooling losses, and the magnetic field gradually dissipates to the ISM level (or lower, possible in the case of a rarefied medium, evacuated due to the SNR), corresponding to the measurements shown in section 7.11. Under the interpretation of the system evolution as a balance between transport and cooling losses, the required velocity profile for advection (in a steady-state scenario) could be measured from the observed variation in extent with energy, whilst a pure diffusion scenario was found to be incompatible with the data (section 7.2).

The low magnetic field estimates found (lower than ISM values) may indicate that the physical extent of the nebula along the line of sight is greater for the γ -ray nebula (less energetic electrons undergoing Inverse Compton scattering) than for the X-ray nebula (more energetic electrons producing synchrotron radiation). Nevertheless, the overall trend of magnetic field strength reducing as roughly $\sim 1/r$ and fairly high σ values (although those in table 7.5 are likely to be overestimated) is consistent with the predominantly advective flow scenario with constant density, ($\beta = 0.6$) with velocity nearer constant ($\beta = 0$) than a spherically expanding flow ($\beta = 2$), as discussed in sections 7.2 and 7.3.

As demonstrated in section 7.5.5, simple kinematic descriptions are inappropriate to describe the reverse shock passage fully. However, all of the models explored in this chapter were able to reproduce the Fermi-LAT and H.E.S.S. SED to a reasonable level of agreement. Future modelling efforts could follow the multi-zone modelling approach of [109] to reproduce the spectral variation across the nebula, or attempt to reproduce the observed morphology of the system under various transportation models, including a combination of diffusion and advection, such as that shown in [110]. An interesting possibility would also be to consider the 3D morphology, taking projection effects of the system into account. This may be necessary to explain the steep drop in emission and brightness observed towards the Northern side of the nebula (see also appendix C). Additional data and observations from lower wavelengths, including X-ray, IR and radio data encompassing the whole nebula, would help to constrain the nebula properties even further.

Further TeV observations of HESS J1825-137, especially increasing statistics with CT5 of the H.E.S.S. array or with CTA, would permit the sensitivity to low surface brightness regions to be enhanced, as well as expanding the available energy range. The existence of more emission at larger distances from the pulsar still yet at lower surface brightness/flux levels cannot be ruled out from current observations. It may be the case that the particles in the nebula cannot be considered part of an isolated system, but rather that they have since diffused into the ISM, and may contribute to the overall cosmic ray flux of the Galaxy. With more measurements of the physical nebula extent at both low and high ends of the current energy range, the apparent decreasing size at low energies and transition into the Klein-Nishina regime at high energies could be verified.

Techniques for observing complex regions containing multiple sources with potential source contamination and overlap, similar to the HESS J1825-137 field of view, is an important issue for future VHE observations, especially IACT experiments such as CTA. With enhancement in sensitivity, it becomes increasingly important to be able to distinguish weaker sources from brighter sources, requiring sophisticated analysis techniques, such as that performed with H.E.S.S. in the Galactic centre region in order to detect emission from the Galactic centre ridge, for example [133].

Lessons learned from detailed studies of HESS J1825-137 can be transferred to models of other PWN systems with similar morphological trends and pulsar properties, such as Vela X and HESS J1303-631. Studies following those presented in this and the previous chapter, will help to constrain and provide input to physical models, ever improving our understanding of PWN systems and their VHE emission.

8 Conclusion

Imaging Atmospheric Cherenkov Telescope (IACT) arrays have proven themselves as powerful tools for uncovering the Very High Energy (VHE) γ -ray universe, and have great potential for future studies aimed towards answering some of the still outstanding open questions in the field. This includes identifying the major accelerators of cosmic rays, and the contributions from each source type (see chapter 1).

IACTs collect information about astrophysical sources through extensive air showers, caused by γ -rays and cosmic rays entering the Earth's atmosphere. Particles within these air showers travelling faster than the local speed of light generate Cherenkov radiation; subsequently detected by IACTs (see chapter 2). An important aspect of this IACT approach is precise knowledge of the telescope optical efficiency, relating the amount of light collected by the telescope to the amount originally produced. This can be calibrated absolutely through the use of muon rings, a natural calibration Cherenkov light source, where the light yield can be analytically related to the geometry of the image. Given that muons produce ring-shaped images, one can be certain that light from all parts of the Cherenkov cone hit the telescope mirror and reach the camera, hence any discrepancy between theory and observation indicates a miscalibration in the telescope efficiency. This calibration method was already applied to the H.E.S.S. experiment during its first phase. A new algorithm for calibration with muons was adapted to incorporate multiple telescope types and telescope geometries, as well as improving the overall calibration performance (see chapter 3).

Currently, the field is transitioning into an era of telescope arrays comprising multiple telescopes of varying sizes and types, in the context of which, inter-telescope calibration becomes increasingly important. An inter-telescope calibration approach for recovering the optical efficiencies of many telescopes was developed, utilising comparisons of cosmic ray shower events seen by multiple telescopes. This was shown to function under two complementary approaches; through image size comparisons (mainly for telescopes of the same size, inter-calibration) and through comparison of the reconstructed energy (all telescope types, including cross calibration). This algorithm was proven to work on both H.E.S.S. simulations and data, and shown to work effectively across the extensive CTA system, not least due to an increased number of telescope pairs available for independent measurements. In the context of CTA, with many more telescopes both in number and variety, this genre of calibration across telescope types takes on a more important role (see chapter 4). As this cross calibration is a relative measurement across all telescopes, it is complementary to the muon calibration, an absolute measurement done for each telescope separately. This aspect was explored in more detail in chapter 5.

With the current H.E.S.S. II facility, a detailed study of the pulsar wind nebula (PWN) HESS J1825-137 was performed, using a much increased dataset over the previously published analysis [95] and using data from the second phase of H.E.S.S., for which the aforementioned new methods of optical efficiency calibration were required. The data was calibrated using the muon calibration algorithm, and again checked with the cross calibration algorithm. In an analysis of HESS J1825-

137, strong evidence for energy dependent morphology emerged, in agreement with [95]. It was found that the spectrum of the nebula softened with increasing distance from the pulsar, and that the flux and surface brightness also reduced with increasing distance. Equivalently, by constructing maps of the region in different energy bands, it was found that the size of the nebula reduced with increasing energy, as measured from the radial profile (see chapter 6). This is interpreted under the scenario of leptonic emission from electrons accelerated initially in the pulsar wind, subsequently being transported (predominantly by advection) into the nebula, also conveying some magnetic flux into the surrounding medium. At its largest extent, the nebula of HESS J1825-137 was found to reach at least 1.4° , corresponding to an intrinsic physical size of 100 pc across at the currently accepted distance of 4.12 kpc. From the age of the pulsar of ~ 21 kyr, this would imply an average transport speed of at least 1.5% of the speed of light, under the assumption that all of the electrons originated close to the pulsar. A simple fit to the drop in Southerly nebula extent with increasing energy was found to be incompatible with diffusion as the dominant transport mechanism, yet in agreement with advective transport, as shown in figure 7.7. The advective velocity profile subsequently obtained was $v \propto r^{-0.6}$. A break in the extent with energy is expected, occurring at the energy at which the cooling time equals the age of the system. This was also seen in figure 7.7 around an energy of 500 GeV. Further measurements enhancing the energy range would help to verify this maximum extent, as well as the apparent drop at the highest energies corresponding to a possible transition from the Thomson into the Klein-Nishina regime.

Coverage of the nebula region closest to the pulsar by the Suzaku satellite coincident with the H.E.S.S. data, could be used to obtain estimates of the magnetic field strength and properties of the underlying particle population. By fitting a simple SED, the magnetic field could be constrained and was found to decrease with increasing distance from the pulsar, within the range of $1 - 10 \mu\text{G}$. The rather low absolute values, especially in the outer regions of the nebula, may indicate a difference in physical extent along the line of sight between the X-ray and γ -ray nebulae. High values of σ , the ratio of magnetic and particle energy densities (although less than those obtained in chapter 7), are consistent with advective transport and fairly weak dependence of the velocity with distance, such as the $v \propto r^{-0.6}$ variation obtained.

One-zone free expansion models of PWNe could fit the spectral data and observed parameters reasonably well, yet poorly agree with the observed morphology of HESS J1825-137. Simple kinematical descriptions of PWN evolution following the reverse shock interaction also poorly reproduce all measured properties of the nebula. There are plenty of opportunities for more detailed models to improve on the results shown in chapter 7.

More observations of other PWNe at VHE would provide a cross-section of the population at all ages. Vela X and HESS J1303-631 have both been shown to exhibit energy dependent morphology, albeit to a lesser extent. Observations with CTA will improve the angular resolution of IACT based experiments, enabling more detailed studies of other extended and old pulsar wind nebulae, helping to establish whether this energy dependent morphology is ubiquitous to PWNe. CTA will also lower the sensitivity, with the potential to uncover a large number of previously undetected pulsar wind nebulae.

Future studies are bound to challenge and refine current models of PWNe and cosmic ray acceleration, from which further insights into some of the longest standing unanswered questions may be gleaned. To learn from new observations, instruments and data must be well understood, to which calibration of CTA plays a vital role. Many further avenues for development lie open; the next generation facilities are bound to help in the endeavour of an ever fuller understanding of our universe.

Appendix A Further Applications of Pair-wise Telescope Comparisons

The principle of inter-telescope calibration is broadly applicable to a range of variables. Several such methods have been previously explored with the H.E.S.S. array, with contemporary experiments such as VERITAS and MAGIC, and with their forerunners such as HEGRA, CANGAROO and Whipple. On the whole, these techniques are often a secondary calibration approach, used as a cross-check of the primary methods and/or as an alternative backup solution in case of problems or delays with implementation of the primary method, yet they rarely constitute the primary method themselves. In general, such techniques were developed for systems comprising telescopes of identical specifications; with the advent of CTA and large, multi-type or multi-site facilities, the ability to calibrate between telescopes of varying designs and indeed between experiments is of increasing importance. An overview of a few of these methods is presented below, with examples of their extension to the H.E.S.S. II array. Further extension of these methods to CTA may be considered, for use during development and characterisation of the primary calibration methods and/or as a backup during regular operation.

A.1 Cosmic Ray Rate Comparison

In a method first applied to the Whipple telescope, the temporal variation of telescope efficiency due to varying atmospheric conditions may be accounted for by monitoring the cosmic ray rate. This method was extended for relative efficiency calibration across telescope arrays on the CELESTE experiment (comprising 40 heliostats, such that the relative throughput is a measure of the relative PMT gains) [80]. Temporal monitoring of atmospheric conditions via the cosmic ray throughput was utilised for development of the ‘Cherenkov Transparency Coefficient’ (CTC) parameter, currently used within H.E.S.S. for atmospheric calibration, particularly in recognising a ‘hazy’ atmosphere [38]. For H.E.S.S., hazy atmospheres are an annual occurrence, coinciding with biomass burning by Namibian farmers. The variation of cosmic ray rate with zenith angle θ_z has a known behaviour, as the area of the Cherenkov light pool illuminating the ground varies as $1/\cos^2 \theta_z$, and can hence be accounted for in the rate calibration. Above a certain energy, the rate of cosmic ray events occurring should be the same across all telescopes. The variation in cosmic ray rate with image size is shown in figure A.1 on MC.

The most noticeable difference between the curves in figure A.1 is the shifted distribution for CT5; for the same rate of events (at the same energy) the intrinsic image size will be larger in CT5 than in CT1-4, hence the distribution appears shifted. Whilst the absolute event rate decreases with increasing zenith angle, in figure A.1, the rate is normalised in each case to arbitrary units (with a maximum rate of 1), such that the change in rate with increasing image size is approximately the same for all zenith angles.

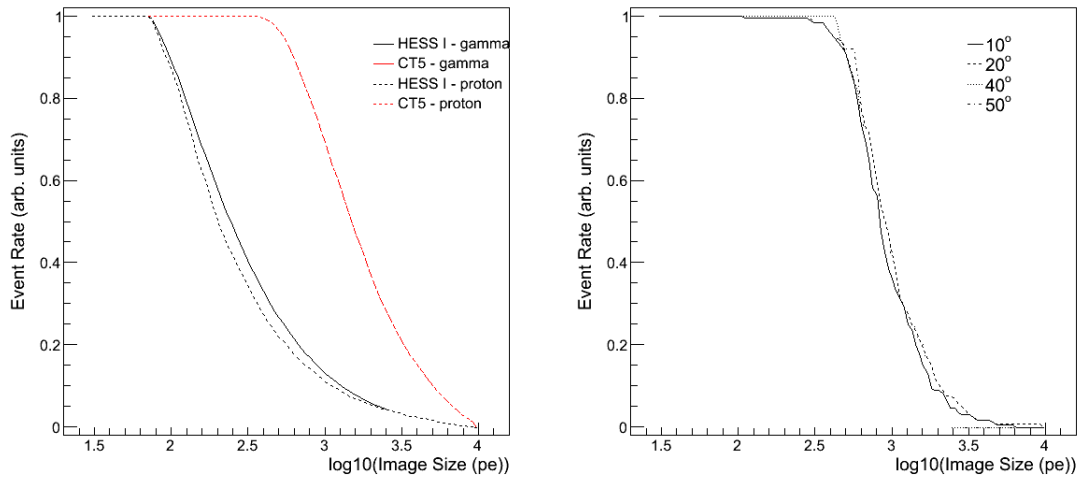


Figure A.1: Cosmic ray rate (in arbitrary units) variation with image size as determined from Monte Carlo. Left: The shape of the curve remains similar between γ -ray and proton Monte Carlo, with almost no discernible change for CT5 with respect to CT1-4. Right: There is no considerable change in the shape of the curve with zenith angle (the curves having been normalised to a maximum of 1).

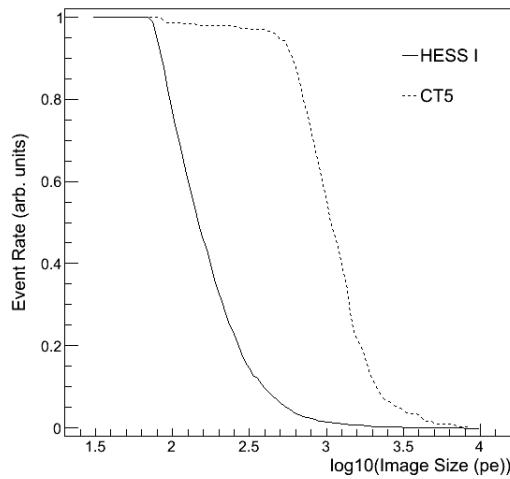


Figure A.2: Event rate with image size as obtained from H.E.S.S. II data taken on the Galactic centre. The overall shape of the distribution is as expected from figure A.1, although the event rate at a given image size is lower (probably due to some optical efficiency degradation).

Figure A.2 shows this rate calibration on data. In practice, a camera miscalibration could be identified by a change in the shape of the rate curve, whilst a change in atmospheric conditions would be identifiable via a measurable change in the normalisation factor between curves. The relative normalisation of the telescopes to each other also indicates their independent optical efficiencies. In both figures A.1 and A.2 however, the average of CT1-4 is taken for the H.E.S.S. I curve.

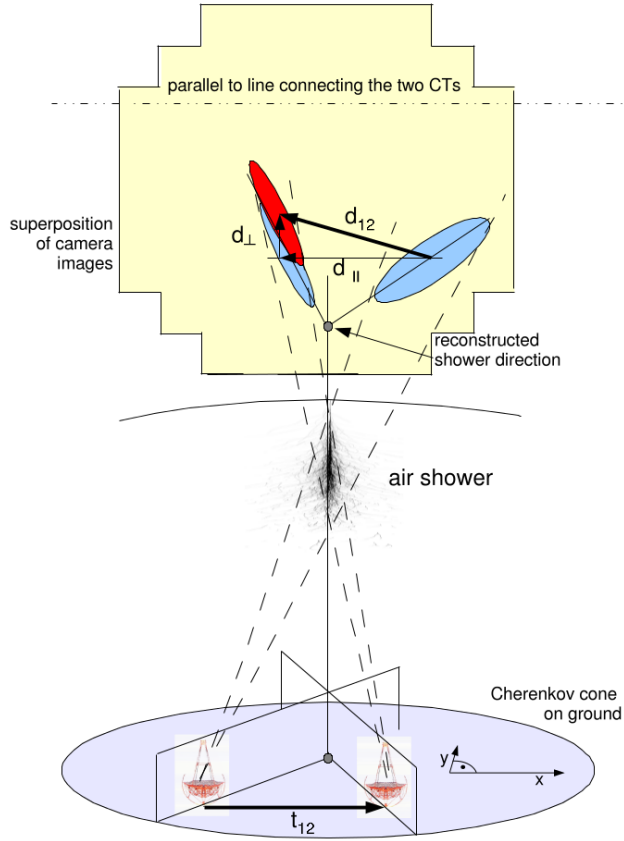


Figure A.3: Geometry of shower image comparison for pointing calibration, taken from [39]. The parallel ($d_{||}$) and orthogonal (d_{\perp}) offsets in the centres of gravity may indicate a pointing miscalibration.

A.2 Pointing Calibration

Whilst the pointing calibration is achieved successfully to a high precision with standard methods, it is possible to perform a cross-check using comparison of event image orientations between telescopes. Relative calibration of the telescope pointing accuracy was demonstrated in a method described in chapter 5 of [39] and in [134]. Figure A.3, taken from [39], clearly illustrates the geometry of the situation. The pointing system of the telescopes may also be calibrated pairwise based on the geometry of the camera images. Superimposing the images into the same coordinate system and rotating, the core centre of gravity of the shower should be in the same position in those two telescopes which view and reconstruct the event, again with the air shower falling half-way in-between them. Any residual asymmetry between the two is indicative of an error in the pointing. In a histogram of orthogonal against parallel offsets for a given telescope pair, the orientation of the histogram distribution depends on the geometry of the telescopes relative to each other within the array, as shown in figure A.4.

In order to measure the offsets due to each telescope pair in a consistent way, the distributions are rotated and/or translated appropriately, such that they lie along the positive parallel offset, centred on the orthogonal offsets (as for CT4 in figure A.4), following the approach in [39]. (This rotation has, however, not been applied in figure A.4.) For each telescope pair, the distribution has a roughly triangular shape and is symmetric around the true value of the orthogonal offset (middle of the base of the triangle), with the distribution broadest to low parallel offsets and

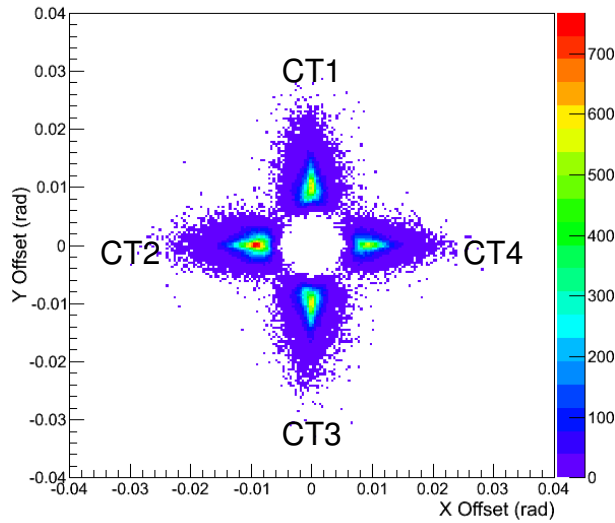


Figure A.4: Offset distributions between CT5 and each of CT1-4, obtained from gamma simulations at $\theta_z = 20^\circ$. The orientation of the distribution depends on the geometry of the array layout, with distributions from each pairwise comparison clearly isolated. Anticlockwise from the top, these correspond to offsets between CT5 and CT1, CT2, CT3, CT4 respectively.

tapering off towards larger parallel offset values. The centroid of the distribution along the length of the triangle corresponds to the mean parallel offset. Performing this comparison on H.E.S.S. II data, there is a systematic trend towards larger parallel offsets with increasing altitude (nearing zenith) within CT1-4 pairs, whilst comparisons with CT5 tend to flatten, as shown in figure A.5 for data without pointing corrections applied.

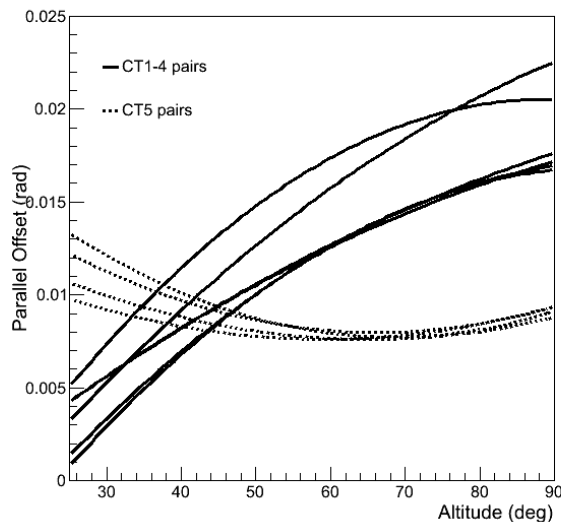


Figure A.5: Parallel pointing offset between telescopes without standard pointing corrections applied. Offsets in H.E.S.S. I pairwise comparisons tend to increase with increasing altitude, whilst pairs involving CT5 tend to decrease and flatten.

This behaviour may be understood from figure A.3 as follows. As the altitude of observation increases to near zenith, the mean parallel offset of the centres of gravity converges to a constant value, corresponding to the distance between the telescopes on the ground. Hence pairs involving CT5 converge to the lowest values, with the CT1-4 pairs located along the edges of the array at

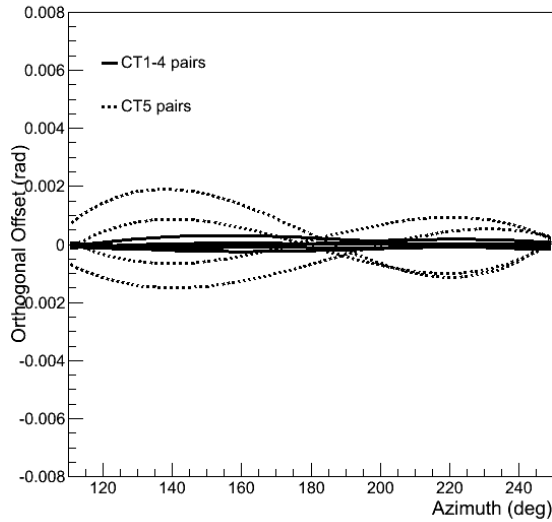


Figure A.6: Orthogonal pointing offset distributions between telescopes without pointing corrections applied. The offsets show some mild variation with azimuth angle, although the magnitude of the effect may be somewhat exaggerated by the sinusoidal fit used.

a larger constant, similar to each other. The largest two offsets correspond to the pairs CT3 - CT1 and CT4 - CT2; situated furthest apart from each other, diagonally opposite in the H.E.S.S. array, approximately double the constant value for CT5 pair offsets. According to [39], the size of the parallel offset components depends simply on the height of the observed shower, and is not a cause for concern in the pointing calibration. For decreasing altitudes, this offset also decreases for CT1-4 pairs, as the amount of atmosphere through which the shower has developed increases, such that the offset between images decreases. For CT5, the offset gradually increases with decreasing altitude, due in part to the better angular resolution of CT5 with respect to CT1-4.

By contrast, an orthogonal offset may indicate an error in the pointing calibration. Figure A.6 shows the orthogonal offsets found between telescope pairs prior to application of pointing corrections. Whilst there is no significant offset for pair comparisons between CT1-4, comparisons involving CT5 seem to show an azimuthal dependence of the orthogonal offset. This could be due to the difference in height above the ground of the cameras from CT5 and CT1-4, although such a dependence may also occur if there is an error in the merging of multiple camera images. A sinusoidal fit was found to provide a reasonable description of the variation, however, this may have slightly exaggerated the magnitude of the effect as seen by eye in figure A.6. Moreover, this effect is much less pronounced than the parallel offset and reduces when pointing corrections are applied, indicating that it is accounted for via the standard calibration procedures.

A.3 Light Yield

A method outlined in [73] and demonstrated on the HEGRA array enables the radial distribution of Cherenkov light generated by TeV showers to be measured. In this section, the method is applied to H.E.S.S. II, as a check of the standard expected distribution from Monte Carlo. The basic principle is to define standard criteria for reference showers in one telescope, fixing the core distance and image size, and measuring how the image size varies with core distance for the same shower as seen by a second telescope. This enables the characteristic properties of the radial distribution of Cherenkov light to be probed. In [73], this was done for the 8.5 m² mirror area HEGRA telescopes, in three image size bands (100-200 pe, 200-400 pe and 400-800 pe), corresponding to three different energy bands. Variation of the radial Cherenkov light distribution with zenith angle was also explored, in four different zenith angle bands.

The main motivation for repeating this analysis with H.E.S.S. II is that the increased mirror area of all the H.E.S.S. telescopes with respect to HEGRA, and subsequent lower energy threshold enables a wider energy range to be tested, potentially with finer energy bins. Furthermore, measurements across a wider range of zenith angles are enabled with the extensive Monte Carlo and data available, including the light distribution corresponding to sources at large off-axis angles. Likewise, the Cherenkov light distribution from hadronic showers and as a function of cosmic ray primary mass could also be investigated. The physics of Extensive Air Shower development is well established and understood, such that only small (if any) deviations are anticipated between measurement and simulations.

In the following plots, four image size bands in the reference telescope are used; 100-200 pe, 200-400 pe, 400-800 pe and over 800 pe which may be interpreted as corresponding to different energy ranges. These are plotted together; expected (from Monte Carlo) and measured (data from the bright blazar PKS 2155-304) variation with zenith angle and with off-axis angle. In all cases, the distributions are normalised to 1 at 100 m.

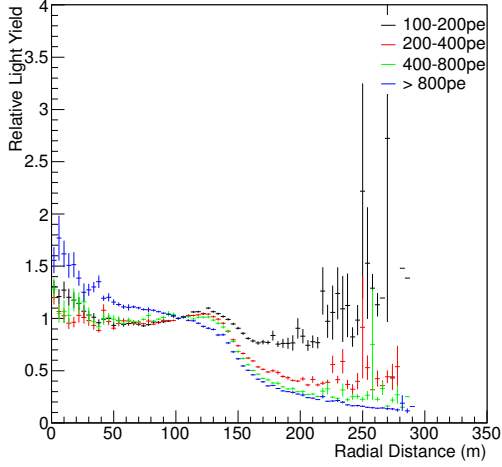
The relative light yield is taken as the ratio of the image size in one telescope to the reference telescope. The two cases of pairs between H.E.S.S. I type telescopes and pairs with CT5 as a reference are made separately. In the case of on-axis gammas at a typical zenith angle (θ_z) of 20°, reasonable agreement is seen between the simulations and data (taken after γ /hadron separation cuts) for pairs of H.E.S.S. I telescopes, although the largest image size band may suffer from poor statistics. For pairs with CT5 as a reference, there seems to be a discrepancy between the expected light yield ratio and that actually measured, for radial distances less than 100 m. This would imply either that there is less light recorded in CT1-4 than expected, or that there is more light recorded in CT5 than expected. The discrepancy seems to be most prominent in figures A.7, A.9 and A.11 in γ -ray dominated situations, whereas the agreement is quite good for the proton simulations in figure A.8.

One possible interpretation is that the emission of light close to the detector is well reproduced by the simulations, as verified by figure A.8; whereas, for light originating higher up in the atmosphere, the simulations under predict the amount of light reaching CT5. For low developing showers, the expected distribution is similar to that seen for hadronic showers, without a prominent shoulder at the edge of the Cherenkov light pool (~ 120 m). For showers developing high in the atmosphere, however, a stronger dip at low radial distances is expected, with a prominent shoulder featuring at the Cherenkov light pool edge [18]. As CT5 has a far larger reflector area than any previous air Cherenkov telescope, it is possible that even though the optical efficiency for the telescope is well matched (after calibration as outlined in chapters 3 and 4), the

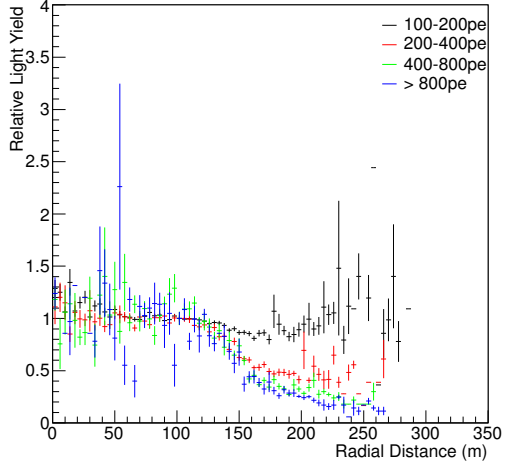
height from which the shower and Cherenkov photons have been simulated underestimates the height from which CT5 is capable of receiving light. Such a difference in altitude from which the emission originated could contribute to the discrepancy in the light yield seen at ground level. Beyond the Cherenkov shoulder, however, the data seems to match the simulations well. This is in agreement with the interpretation of an altitude discrepancy, as at higher altitudes, the opening angle of Cherenkov emission is smaller, such that a difference would manifest itself more clearly towards the centre of the Cherenkov light pool.

Figure A.8 compares proton simulations to data prior to γ /hadron selection cuts, which is dominated by the hadronic background contribution. In this case, the data has increased statistics, and reasonable agreement is seen between MC and data, in both types of pair comparisons. With hadronic events, the location of the Cherenkov shoulder is smeared out in comparison to γ -ray events and is less easily identifiable. This is a consequence of both the increased scattering of light from hadronic showers, including their increased lateral spread, and also of the lower altitude from which the Cherenkov light originates.

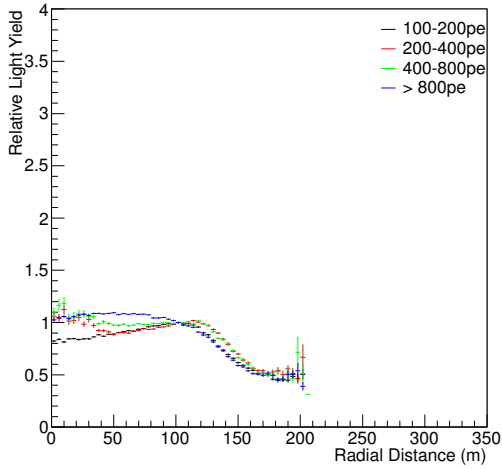
Figure A.9 shows the relative light yield variation with zenith angle, whilst figures A.10 and A.11 show variation with increasing off-axis angle.



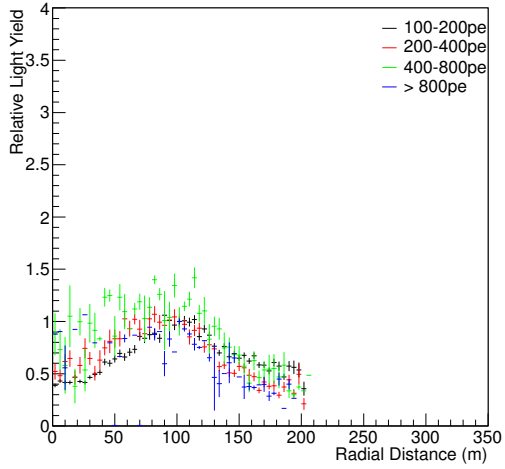
MC $\theta_z = 20^\circ$, on axis



Data $15^\circ < \theta_z < 25^\circ$, offset $< 0.5^\circ$

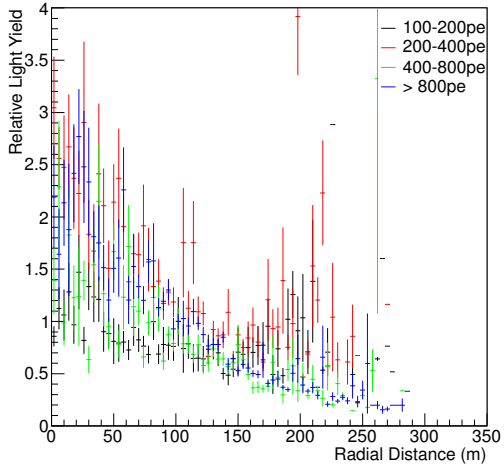


MC $\theta_z = 20^\circ$, on axis, CT5 as reference

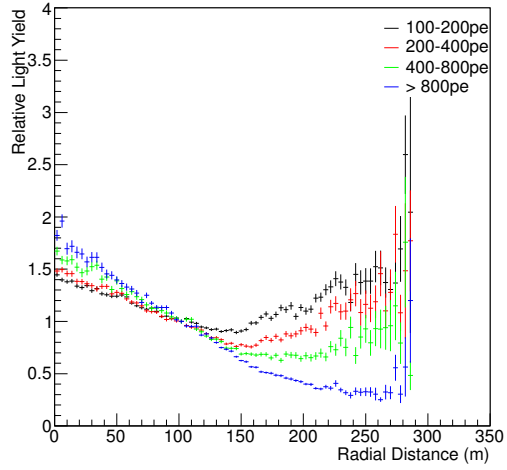


Data $15^\circ < \theta_z < 25^\circ$, offset $< 0.5^\circ$, CT5 as reference

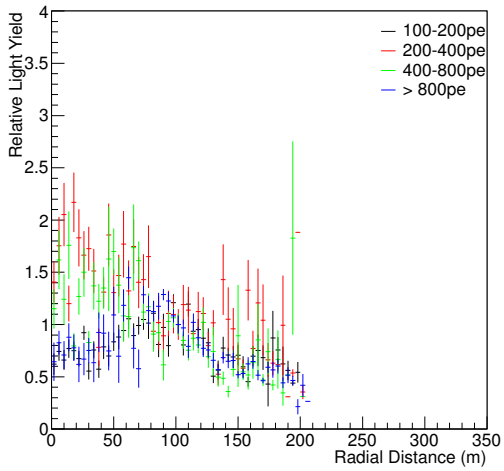
Figure A.7: MC (left) and PKS 2155-304 data (right) with H.E.S.S. I pairs (top) and using CT5 as a reference (bottom). Taken from γ -ray simulations and data post γ /hadron separation cuts. Good agreement is seen for H.E.S.S. phase I, some discrepancy is seen between simulations and data at low radial distances for CT5.



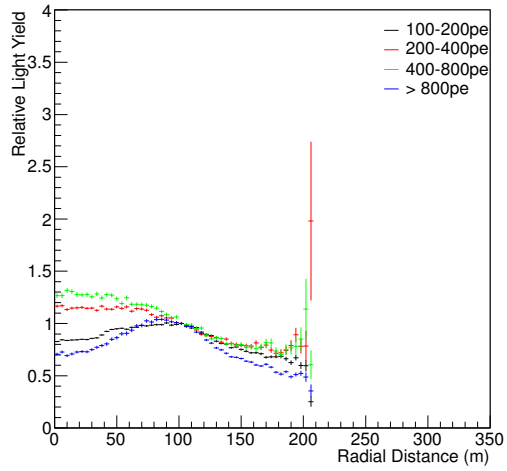
MC $\theta_z = 20^\circ$, on axis



Data $15^\circ < \theta_z < 25^\circ$, offset $< 0.5^\circ$

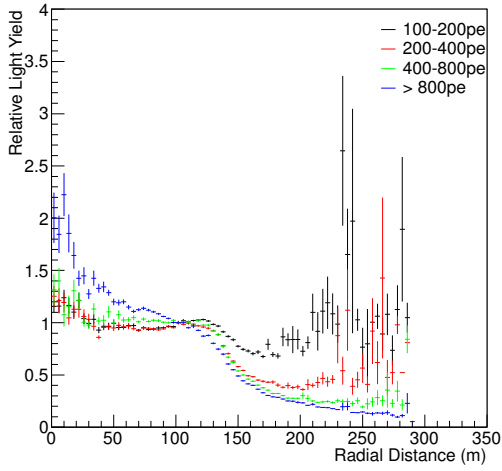


MC $\theta_z = 20^\circ$, on axis, CT5 as reference

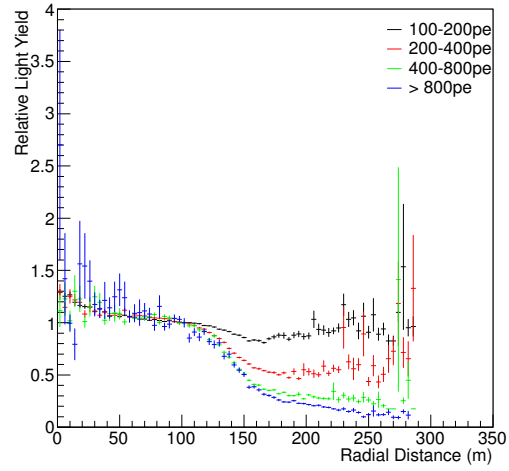


Data $15^\circ < \theta_z < 25^\circ$, offset $< 0.5^\circ$, CT5 as reference

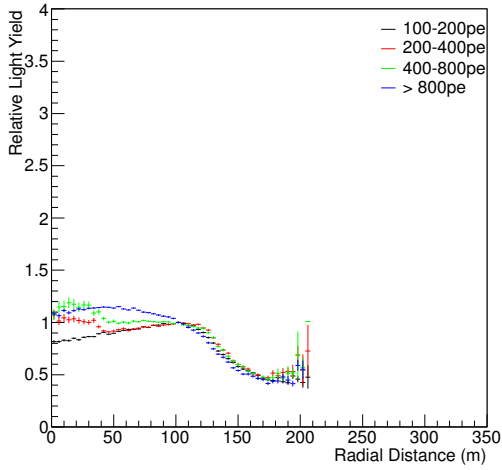
Figure A.8: MC (left) and PKS 2155-304 data (right) with H.E.S.S. I pairs (top) and using CT5 as a reference (bottom). Taken from proton simulations and data prior to γ /hadron selection cuts (hadron dominated). The location of the Cherenkov shoulder is smeared out in comparison to figure A.7.



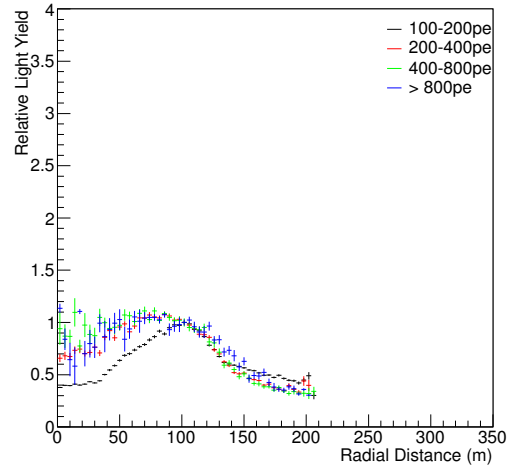
MC $\theta_z = 10^\circ$



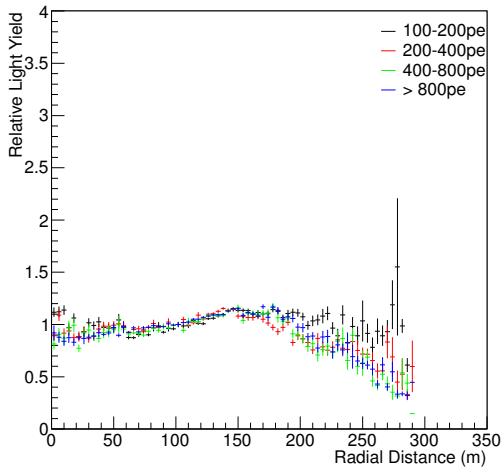
Data $\theta_z < 15^\circ$



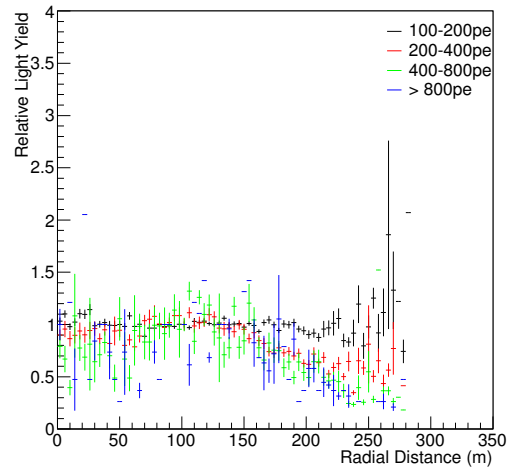
MC $\theta_z = 10^\circ$, CT5 as reference



Data $\theta_z < 15^\circ$, CT5 as reference

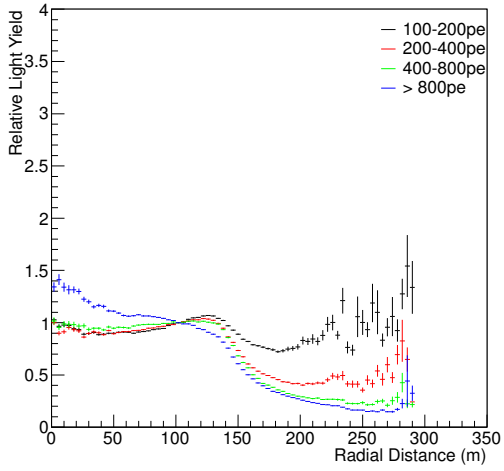


MC $\theta_z = 50^\circ$

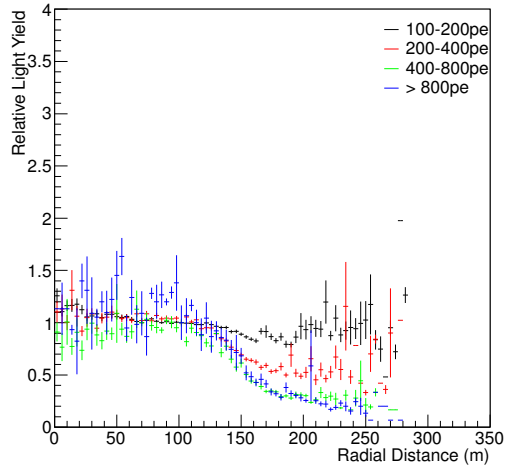


Data $45^\circ < \theta_z < 55^\circ$

Figure A.9: Relative light yield with radial distance for two HESS telescopes; shown for MC (left) and PKS 2155 data (right). There is good agreement seen between the two for comparisons between CT1-4 (top and bottom), whilst there seems to be a slight deficit with respect to the simulations when using CT5 as a reference. The position of the Cherenkov shoulder clearly shifts outwards to larger radial distances with increasing zenith angle.

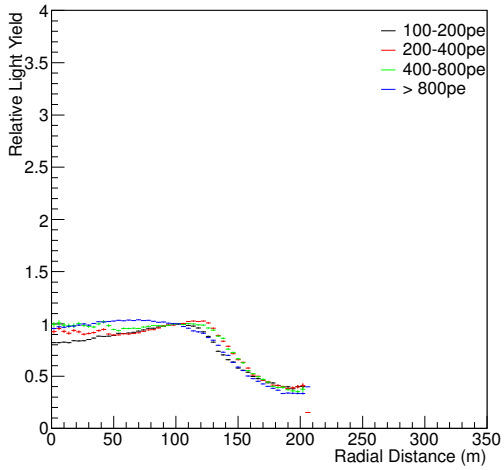


MC $\theta_z = 20^\circ$, offset = 1.0°

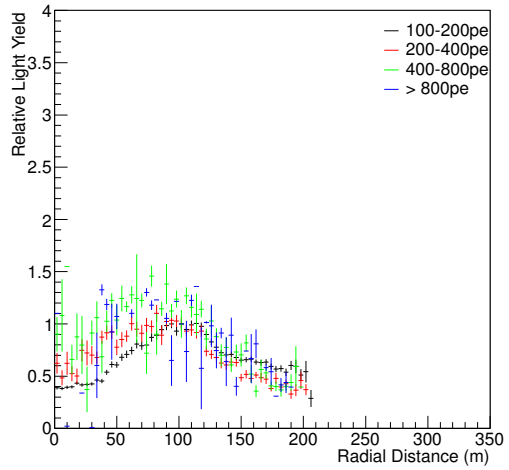


Data $25 < \theta_z < 35^\circ$, $0.75 < \text{offset} < 1.25^\circ$

Figure A.10: Relative light yield with radial distance for two HESS I telescopes; shown for MC (left) and PKS 2155 data (right). Good agreement is seen between the two.



MC $\theta_z = 20^\circ$, offset = 1.0°



Data $25 < \theta_z < 35^\circ$, $0.75 < \text{offset} < 1.25^\circ$

Figure A.11: Relative light yield with radial distance for a HESS I telescope with reference in CT5; shown for MC (left) and PKS 2155 data (right). Some low-level discrepancy is seen at small radial distances, similar to figures A.7 and A.9.

A.4 Timing Calibration

In chapter 4, a method of telescope cross calibration using pair-wise comparisons between telescopes was outlined, in order to calibrate the optical throughput efficiency of all telescopes within an array. The underlying principle, of comparisons of an invariant parameter between telescope pairs, may be extended to other applications; in this section, an extension to calibration of telescope timing is presented.

Using Monte Carlo simulations, comparisons of the time delay at the central trigger were made between telescope pairs, with pairs selected in the same manner as outlined in section 4.6 (all pairs with a separation distance $\lesssim 450$ m), with the exception that in this case pair comparisons were also made between telescopes of different types. The time delay is defined as the time (in ns) at which the signal from a given telescope arrives at the central trigger after $t = 0$ ns, where 0 ns is the time at which the first signal from a triggered telescope arrives. Rather than the asymmetry (as utilised in chapters 4 and 4.6) the time delays are compared via the time delay difference. One would naively expect that the difference in time delays between any two telescopes will average over time to zero. MC studies were made on γ -rays only, using the 2B array layout as shown in figure 4.16, which includes LSTs, MSTs and 4 m Schwarzschild-Couder SSTs.

A.4.1 Comparisons Between Telescopes of the Same Type

When making comparisons of the mean time delay between telescopes of the same type (LST, MST and SST combined in figure A.12) there was no systematic offset seen. Various cuts were applied to the events used in determining the time delay, including cuts on image size, image shape, core distance and on equidistance. The equidistance cut is defined as requiring that the core distances to each of the two telescopes in the pair are within 20 % of each other. However, there was no significant improvement in either the mean time delay or the delay RMS by using either the image size or the image shape cuts. Hence results are shown for the core distance (< 200 m) and equidistance (within 20 %) cuts only.

The mean time delay between telescope pairs was found to be improved most by the equidistance cut, which was also the most severe cut in terms of surviving events yet demonstrated the largest improvement in overall RMS (figure A.12). Whilst the core distance cut also showed some improvement in mean time delay for low telescope separations (figure A.12, separation < 300 m), the RMS was actually shown to degrade after application of this cut.

A.4.2 Comparisons Between Telescopes of Different Types

Whereas for the CTA cross calibration studies as outlined in chapter 4.6 scaling factors between subsystems were found separately between the LST-MST and MST-SST subsystems as a whole, for the purposes of this timing delay calibration, pair-wise comparisons were also made across telescope types. At the central trigger, the time stamp assigned to a given event should be independent of telescope type. Between LSTs and MSTs, a small systematic offset $\sim O(3$ ns) was seen (figure A.13), whilst for MST-SST comparisons, a larger systematic offset $\sim O(30$ ns) was seen (figure A.14).¹

¹In the case of studies with layout 2A, which utilises single 7 m reflector Davies-Cotton SSTs, a smaller systematic offset $\sim O(7$ ns) was seen.

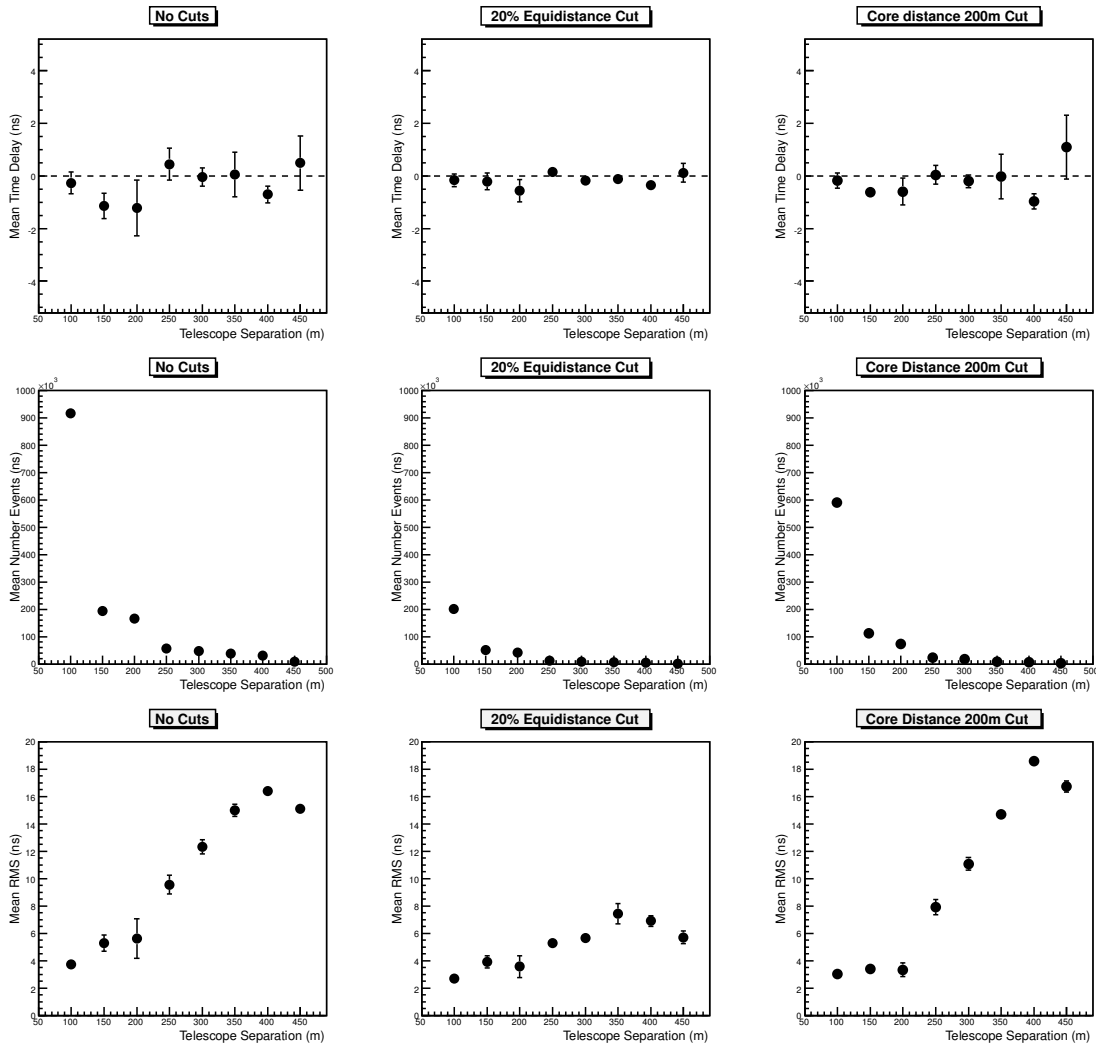


Figure A.12: Mean time delay (top), number of events (middle) and rms (bottom) between telescope pairs of the same type, averaged per telescope separation band. Shown for the cases of no cuts (left), equidistance cut (middle) and core distance cut (right).

Telescope types	Δf (m)	Δt (ns)	Measured Δt (ns)
LST - MST	28 – 16	~ 23	~ 3
MST - dc-SST	16 – 11.2	~ 9	~ 7
MST - sc-SST	16 – 2.15	~ 27	~ 28

Table A.1: Time delays between telescope types. The delays obtained between MSTs and SSTs agree to first order, whilst the LST-MST delay obtained is considerably less than that expected.

For comparisons between LSTs and MSTs, the best improvement in the average time delay was achieved through the cut on core distance to both telescopes. The same cut when applied to MST-SST pairs, however, did not remove many events, and almost no change was seen in the delay. As was found for the same type comparisons, the time delay was reduced by the equidistance cut; although with the large reduction in events, the errors on the mean delay were significantly increased. In this case, the delay was reduced yet remained systematically offset, at $\sim O(20 \text{ ns})$. Across subsystems, a systematic time lag of smaller telescopes with respect to larger telescopes is seen. Comparisons between LSTs and SSTs were not used, as the number of eligible pairs is low (and biased towards the centre of the array) and the number of events triggering both LSTs and SSTs generates only low statistics.

Understanding the origin of this systematic offset is a non-trivial exercise, requiring a thorough understanding of the characterisation of many experimental and physical aspects of the simulations. These include: optics of the telescope camera system, including focal lengths; electronics of the cameras; distance to the central trigger unit; camera read-out rates (which may result in different definitions of $t = 0$); and taking the correct shape of the Cherenkov light wavefront into account in the simulations. In the case that the telescopes are not situated at a flat location, then the altitude difference can also contribute (similarly, the height difference can influence the offset between telescopes of different sizes). One potential cause of a systematic offset in timing delays between telescopes is likely to originate in the different heights and focal lengths f of the telescope types. The height of a telescope is dominated by the size of the mirror dish, such that the mean telescope height H_t can be approximated as slightly over half of the mirror dish size, D . The ratio of a telescope’s focal length f to the mirror dish size, D is approximately 1.2 in the majority of cases. For light originating at the same height H_0 , yet arriving at two different telescopes, the difference in light arrival time will be dominated by the difference in the path lengths travelled to reach the telescopes. This is comprised of the difference in the telescope height, with light reaching higher telescopes sooner, and the difference in focal lengths, with light taking longer to travel along longer path lengths. As $H_t \approx D/2 \approx f/2.4$, and the total path length travelled by light to reach a telescope is $H_0 - f/2.4 + f$, such that the difference in path lengths to two telescopes from the same event is $\Delta d = 1.4\Delta f/2.4 \approx 7\Delta f/12$. Hence the expected difference in arrival times due to this effect alone is $\Delta t \approx \Delta f/2c$; the values obtained for the prod-2 simulations are summarised in table A.1.

Whilst the delays obtained between MSTs and SSTs are of the same order of magnitude as that expected from this effect, the delay between LSTs and MSTs is considerably less than that expected, if the path length difference is the main contributor to the observed delay. This effect is therefore likely to already be compensated for in the simulations.

The dominant effect is likely to be due to the differences in the ways in which the camera triggers are defined and in their respective pulse shapes for a signal. For the LSTs and MSTs, the trigger uses an analogue sum, for the dc-SSTs this is a digital sum, whilst the sc-SSTs use a

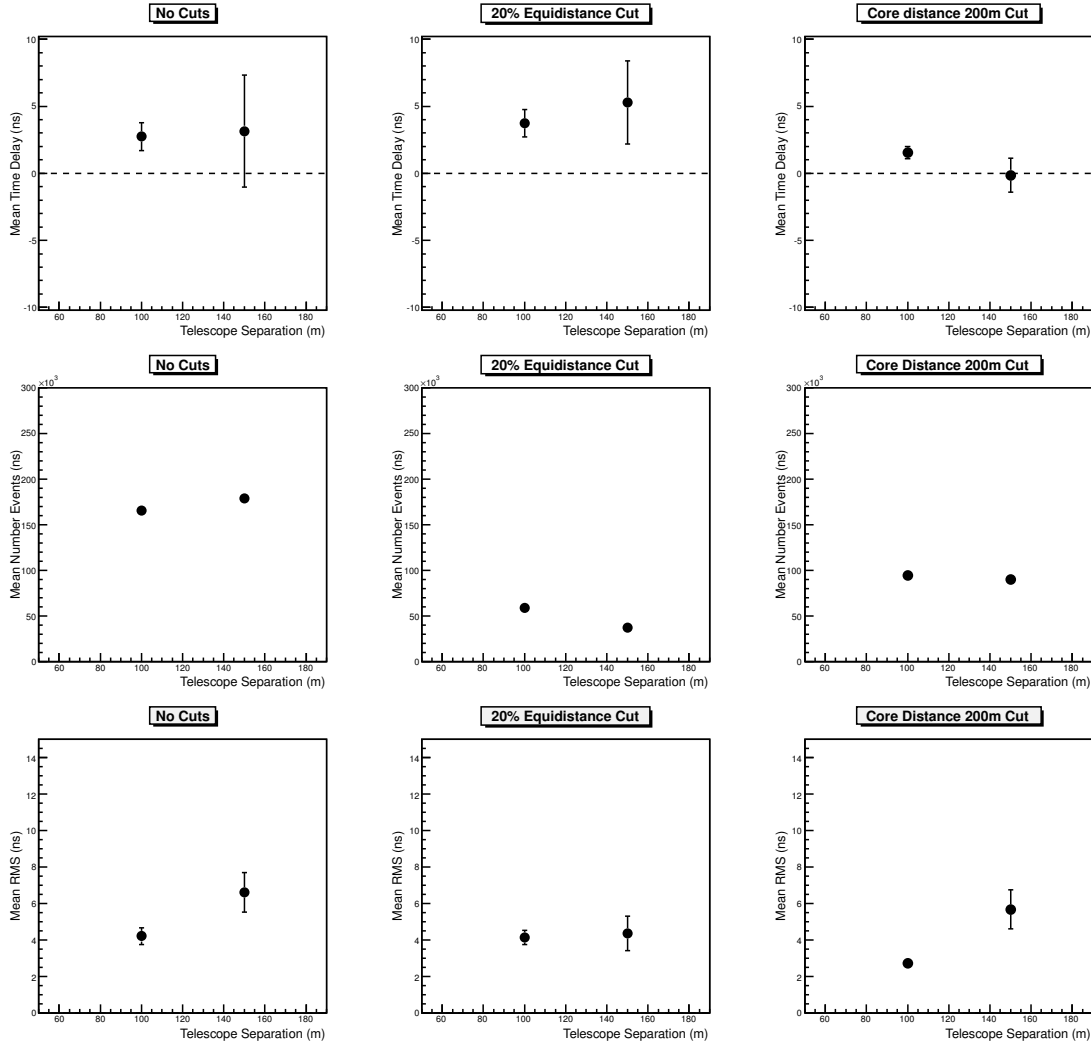


Figure A.13: Mean time delay (top), number of events (middle) and RMS (bottom) between telescope pairs with one LST and one MST, averaged per telescope separation band. Shown for the cases of no cuts, equidistance cut and core distance cut.

majority trigger. Although the LSTs and MSTs use the same trigger definition, there remains a small delay of ~ 3 ns for the MSTs with respect to the LSTs. This is likely to be simply due to the lesser reflector dish area of the MSTs meaning that they receive less light on average for the same event, thereby requiring a slightly longer time on average to collect the required charge for a trigger (depending on the trigger threshold conditions).

Clearly, future studies would help to clarify the origin of the systematic offsets between telescope and camera types, and to ensure that these are well understood.

A.4.3 Application

The primary application of this timing calibration is as an independent cross-check of standard timing calibration methods. Potential drawbacks of this calibration are mainly the following assumptions: that there is no event mixing (cameras are performing as expected); that the time stamps correspond to the same event (no delays larger than the trigger coincidence window), and that any timing error is smaller than the readout window (the time between events). The current time window for a coincident trigger used in the simulations is 1000 ns, such that the delay

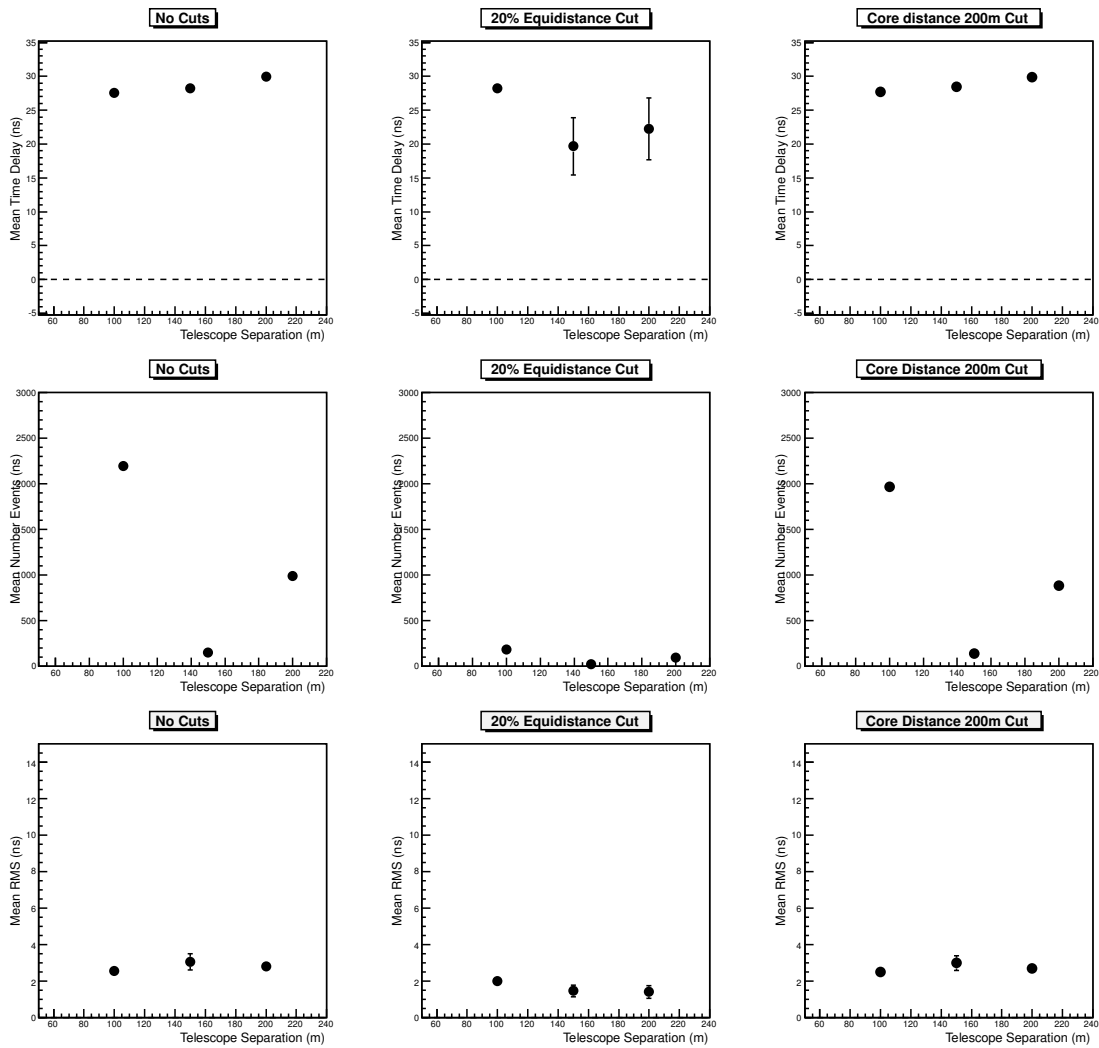


Figure A.14: Mean time delay (top), number of events (middle) and RMS (bottom) between telescope pairs with one MST and one sc-SST, averaged per telescope separation band. Shown for the cases of no cuts (left), equidistance cut (middle) and core distance cut (right).

between telescope types shown here is unlikely to significantly affect the stereo trigger or analysis, unless timing is used for event cleaning (already shown to be useful on the MAGIC experiment [42]). For the CTA, the use of a highly accurate White Rabbit based electronic timings system is foreseen. This basic approach to timing calibration on a nanosecond scale cannot compete with the picosecond accuracy promised by White Rabbit timing schemes. Nevertheless, systematic offsets between camera and telescope types should be well understood prior to such a system coming online, and the method could provide a useful sanity check, particularly during the commissioning phase of CTA [74].

Appendix B Derivation of the Mirror Distance for Muons

Whereas single dish IACTs with Davis-Cotton optics may use equation (3.1.7) to describe the chord across the reflector dish without complications, IACTs using Schwarzschild-Couder optics (with two mirror dishes) are additionally foreseen for CTA. In this case, the analytical expression for the chord across the mirror still holds true, with two conditions for whether or not the impact parameter ρ is less than the mirror radius R . However, one also needs to consider the effect of shadowing of the primary mirror by the secondary as follows. For simplicity, we initially assume that the incoming muon is not inclined (on-axis, $i = 0$), the geometry is the same as that shown in figures 3.1 and 3.37.

The distance is integrated over all ϕ angles, and whether or not the intensity in a given pixel is affected by shadowing depends on the azimuthal angle ϕ . An important term to determine which case is relevant is $d = \rho \sin \phi$, which is the distance from the center of the mirror to the line D , along the perpendicular intersection with D . The part of D traversing the secondary mirror and therefore affected by shadowing is D' . Here, we assume also that the shadowing is complete; if not, then the total distance along which the light must be integrated, C is $C = D - \alpha D'$, where α is the strength of shadowing (here $\alpha = 1$).

1. $\rho > R$ and $\rho \sin \phi > R'$

The muon falls outside of both mirrors. In this case, there is no shadowing by the secondary mirror, the chord D traverses the primary mirror at a radial distance from the centre larger than the radius R' of the secondary mirror. The expression to use is the first one in equation (3.1.7) and $C = D$.

$$D(\rho, \phi) = 2R \sqrt{1 - \left(\frac{\rho}{R}\right)^2 \sin^2 \phi} \quad (\text{B.0.1})$$

2. $\rho > R$ and $\rho \sin \phi < R'$

The muon falls outside of both mirrors. In this case, the cord traverses both the primary mirror and the secondary mirror. A term similar to that in the previous case expresses the length D' traversing the secondary mirror and hence affected by shadowing (replacing R by R').

$$D'(\rho, \phi) = 2R' \sqrt{1 - \left(\frac{\rho}{R'}\right)^2 \sin^2 \phi} \quad (\text{B.0.2})$$

Length D' should always be less than D , the total distance $C = D - D'$

3. $\rho < R$ and $\rho \sin \phi > R'$

The muon hits the primary mirror. The chord does not traverse the secondary mirror, hence the expression to use is the second part of equation (3.1.7):

$$D(\rho, \phi) = R \left[\sqrt{1 - \left(\frac{\rho}{R}\right)^2 \sin^2 \phi} + \frac{\rho}{R} \cos \phi \right] \quad (\text{B.0.3})$$

and total distance $C = D$.

4. $\rho < R$ and $\rho \sin \phi < R'$

In this case, the chord is affected by shadowing again. The basic chord across the primary mirror is given by (B.0.3). Note that with $\rho \sin \phi < R'$, it is still possible to have $\rho > R'$ and $\rho < R$, so there are two sub-cases for the shadowing term D' :

(a) $\rho > R'$

In this case, the path traverses across the secondary mirror fully, as in case 2, so the expression for D' is (B.0.2). The full term is then (B.0.3) with shadowing term (B.0.2) ($C = D - D'$).

(b) $\rho < R'$

The last case, in which the term for $D' \rightarrow D'/2 + \rho \cos \phi$ (with D' retaining it's previous definition). Shadowing term in this case is then:

$$D'(\rho, \phi) = R' \left[\sqrt{1 - \left(\frac{\rho}{R'}\right)^2 \sin^2 \phi} + \frac{\rho}{R'} \cos \phi \right] \quad (\text{B.0.4})$$

The full term is then (B.0.3) with shadowing term (B.0.4) ($C = D - D'$).

In section 3.8, it was found that adding the two contributions to the chord from both mirrors (instead of subtracting) gave a better description of the light distribution around the muon ring. For the light which reaches the mirror, this is a more accurate description of the path taken by photons reaching a particular pixel on the camera. This is equivalent to setting $\alpha = -1$, such that $C = D + D'$. The improvement to the description of the path taken by the Cherenkov light notwithstanding, the shadowing of the secondary mirror must still be taken into account. To this end, a factor β was introduced,

$$\beta = \frac{A_p - (A_s - A_{sh})}{A_p - A_{ph}}, \quad (\text{B.0.5})$$

where A_p , A_s , A_{ph} and A_{sh} are the areas of the primary and secondary mirrors and the areas of the inner dish holes respectively (see figure 3.34). This is effectively the ratio of the primary dish area A_p less the area blocked by the secondary ($A_s - A_{sh}$), to the area of the primary without the secondary mirror present ($A_p - A_{ph}$).

All of the above is derived in the case of on-axis muons. The effect of a muon arriving off-axis, with an inclination angle $i \neq 0$ is to shift the muon ring away from the centre of the camera, and this will also shift the position of the shadow from the secondary mirror on the primary mirror dish.

As long as the shadow is wholly contained within the primary mirror dish, then the term D' can be accounted for as usual; total integration distance $C = D - D'$, and it does not matter where the shadow is located.

The inclination angle i is given by the offset of the centre of the muon ring in the camera from the camera centre. For the inclination angle to be large enough to shift the shadow from the

secondary mirror such that it no longer falls entirely on the primary mirror dish, the following must be true:

$$\Delta m \sin i > R - R' \quad (\text{B.0.6})$$

where Δm is the distance between the two mirror dishes, and R and R' are the radii of the primary and secondary mirror dishes respectively.

If by replacing i by the (radius of the) field of view of the telescope, the condition

$$\Delta m \sin i < R - R' \quad (\text{B.0.7})$$

is always true, then the inclination will never shift the shadow outside of the primary mirror whilst the image is still captured by the camera, and the inclination does not need to be considered.

Appendix C HESS J1825-137 Emission Profiles

For completeness, it is interesting not just to study the overall excess profile of HESS J1825-137 in slices of excess counts, as shown in section 6.7.2. In addition to the radial emission profiles in different energy bands, the excess profiles along strips made in different energy bands are shown here. This includes not just the emission profile going outwards from the pulsar, but also crossing the pulsar in two directions. On the Southern side of the nebula, there is a change in slope at $\sim -0.7^\circ - -1^\circ$, which could indicate the presence of two components to the nebula emission.

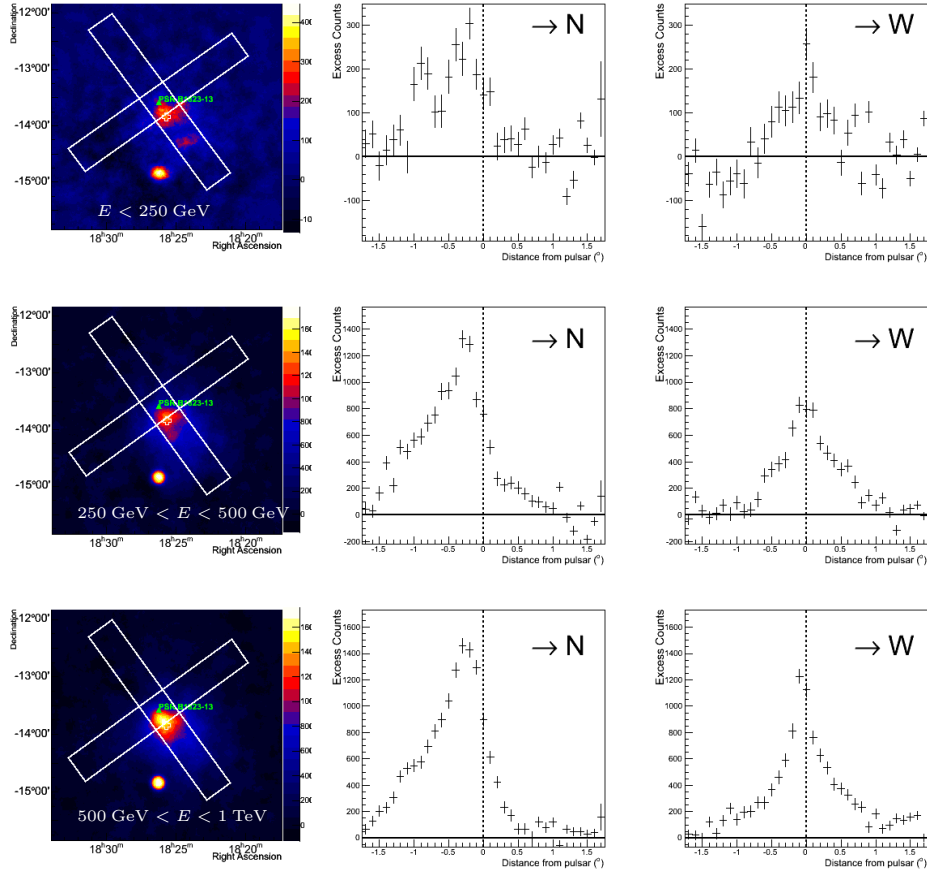


Figure C.1: Excess sky maps and slice profiles of the emission made with dataset A in three energy bands below 1 TeV.

As can be seen from figures C.1 and C.2, the emission drops off steeply on the Northern side of the pulsar in all energy bands; emission is still present beyond the pulsar position, yet at a much reduced level. Otherwise, the distribution of emission becomes less broad in both the N-S and E-W directions with increasing energy, the position of the peak shifting slightly closer to the pulsar.

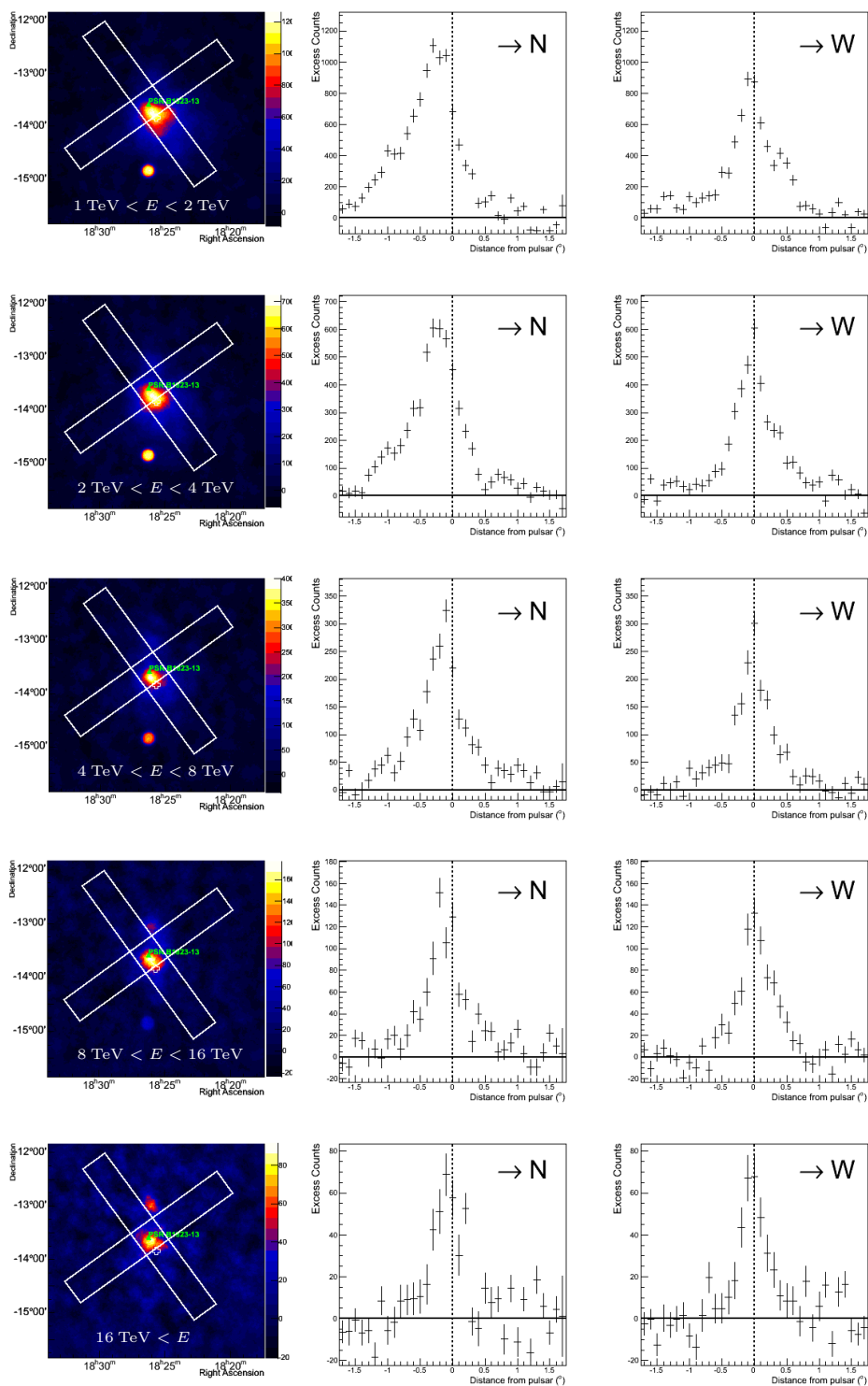


Figure C.2: Excess sky maps and slice profiles of the emission made with dataset A in five energy bands above 1 TeV.

Bibliography

- [1] Nobelprize.org. The Nobel Prize in Physics 1936. http://www.nobelprize.org/nobel_prizes/physics/laureates/1936/, 2014. Accessed: 09-01-2016.
- [2] B. W. Carroll and D. A. Ostlie. *An Introduction To Modern Astrophysics*. Pearson, Addison Wesley, Weber State University, 2007.
- [3] K. A. Olive et al. Particle Data Group. *Chin. Phys. C*, 38:090001, 2014.
- [4] K. Greisen. End to the Cosmic-Ray Spectrum? *Physical Review Letters*, 16:748–750, April 1966.
- [5] G. T. Zatsepin and V. A. Kuz'min. Upper Limit of the Spectrum of Cosmic Rays. *Soviet Journal of Experimental and Theoretical Physics Letters*, 4:78, August 1966.
- [6] J. W. Cronin, T. K. Gaisser, and S. P. Swordy. Cosmic rays at the energy frontier. *Scientific American*, 276:32–37, January 1997.
- [7] S. Funk. *A new population of very high-energy γ -ray sources detected with H.E.S.S. in the inner part of the Milky Way*. PhD thesis, Ruprecht-Karls-Universität Heidelberg, 2005.
- [8] M. S. Longair. *High Energy Astrophysics*. Cambridge University Press, University of Cambridge, 1982.
- [9] A. M. Hillas. The Origin of Ultra-High-Energy Cosmic Rays. *Annual Review of Astronomy and Astrophysics*, 22(1):425–444, 1984.
- [10] F. Fraschetti. On the acceleration of ultra-high-energy cosmic rays. *Philosophical Transactions of the Royal Society of London Series A*, 366:4417–4428, December 2008.
- [11] J. A. Hinton and W. Hofmann. Teraelectronvolt Astronomy. *Annual Review of Astronomy & Astrophysics*, 47:523–565, September 2009.
- [12] J. Holder. TeV gamma-ray astronomy: A summary. *Astroparticle Physics*, 39:61–75, December 2012.
- [13] F. M. Rieger, E. de Oña-Wilhelmi, and F. A. Aharonian. TeV astronomy. *Frontiers of Physics*, 8:714–747, December 2013.
- [14] E. Lorenz and R. Wagner. Very-high energy gamma-ray astronomy. A 23-year success story in high-energy astroparticle physics. *European Physical Journal H*, 37:459–513, August 2012.

- [15] B. R. Martin and G. Shaw. *Particle Physics*. Wiley, School of Physics and Astronomy, Faculty of Sciences, University of Manchester, 2008.
- [16] F. Aharonian, L. Bergström, and C. Dermer. *Astrophysics at Very High Energies*. Springer, Société Suisse d’Astrophysique et d’Astronomie Observatoire de Genève, ch. des Maillettes 51, CH-1290 Sauverny, Switzerland, 2013.
- [17] F. A. Aharonian, A. M. Atoyan, and T. Kifune. Inverse Compton gamma radiation of faint synchrotron X-ray nebulae around pulsars. *Monthly Notices of the Royal Astronomical Society*, 291:162–176, October 1997.
- [18] Peter K. F. Grieder. *Extensive Air Showers: High Energy Phenomena and Astrophysical Aspects*. Springer, University of Bern, Physikalisches Institut, Sidlerstr. 5, 3012 Bern, Switzerland, 2010.
- [19] J. Matthews. A Heitler model of extensive air showers. *Astroparticle Physics*, 22:387–397, January 2005.
- [20] D. Berge. *A detailed study of the gamma-ray Supernova remnant RX J1713.7-3946 with H.E.S.S.* PhD thesis, Ruprecht-Karls-Universität Heidelberg, 2006.
- [21] Nobelprize.org. The Nobel Prize in Physics 1958. http://www.nobelprize.org/nobel_prizes/physics/laureates/1958/, 2014. Accessed: 11-01-2016.
- [22] H. J. Völk and K. Bernlöhr. Imaging very high energy gamma-ray telescopes. *Experimental Astronomy*, 25:173–191, August 2009.
- [23] A.M. Hillas. Evolution of ground-based gamma-ray astronomy from the early days to the cherenkov telescope arrays. *Astroparticle Physics*, 43:19 – 43, 2013. Seeing the High-Energy Universe with the Cherenkov Telescope Array - The Science Explored with the {CTA}.
- [24] M. Ageron et al. ANTARES: The first undersea neutrino telescope. *Nuclear Instruments and Methods in Physics Research A*, 656:11–38, November 2011.
- [25] J. Abraham et al. Properties and performance of the prototype instrument for the Pierre Auger Observatory. *Nuclear Instruments and Methods in Physics Research A*, 523:50–95, May 2004.
- [26] A. U. Abeysekara et al. Sensitivity of the high altitude water Cherenkov detector to sources of multi-TeV gamma rays. *Astroparticle Physics*, 50:26–32, December 2013.
- [27] IceCube Collaboration, A. Achterberg, et al. First year performance of the IceCube neutrino telescope. *Astroparticle Physics*, 26:155–173, October 2006.
- [28] A. Hillert. *GRASP: Development of an event reconstruction method using a Gamma Ray Air Shower Parameterisation and application to gamma-ray sources with H.E.S.S.* PhD thesis, Ruprecht-Karls-Universität Heidelberg, 2014.
- [29] The H.E.S.S. Collaboration. H.E.S.S. : High Energy Stereoscopic System. <https://www.mpi-hd.mpg.de/hfm/HESS/>, 2016. Accessed: 14-01-2016.

- [30] J. A. Hinton and for the HESS Collaboration. The status of the HESS project. *New Astronomy Reviews*, 48:331–337, April 2004.
- [31] E. Lorenz and The MAGIC Collaboration. Status of the 17 m MAGIC telescope. *New Astronomy Reviews*, 48:339–344, April 2004.
- [32] T. C. Weekes et al. VERITAS: the Very Energetic Radiation Imaging Telescope Array System. *Astroparticle Physics*, 17:221–243, May 2002.
- [33] B. S. Acharya et al. Introducing the CTA concept. *Astroparticle Physics*, 43:3–18, March 2013.
- [34] D. Horan and S. Wakely. TeVCat. tevcat.uchicago.edu, 2016. Accessed: 14-01-2016.
- [35] K. Bernlöhner et al. The optical system of the H.E.S.S. imaging atmospheric Cherenkov telescopes. Part I: layout and components of the system. *Astroparticle Physics*, 20:111–128, November 2003.
- [36] F. Aharonian et al. Calibration of cameras of the H.E.S.S. detector. *Astroparticle Physics*, 22:109–125, November 2004.
- [37] K. Bernlöhner. Impact of atmospheric parameters on the atmospheric Cherenkov technique. *Astroparticle Physics*, 12:255–268, January 2000.
- [38] J. Hahn, R. de los Reyes, K. Bernlöhner, P. Krüger, Y. T. E. Lo, P. M. Chadwick, M. K. Daniel, C. Deil, H. Gast, K. Kosack, and V. Marandon. Impact of aerosols and adverse atmospheric conditions on the data quality for spectral analysis of the H.E.S.S. telescopes. *Astroparticle Physics*, 54:25–32, February 2014.
- [39] I. Braun. *Improving the Pointing Precision of the H.E.S.S. Experiment*. PhD thesis, Ruprecht-Karls-Universität Heidelberg, 2007.
- [40] F. Aharonian et al. Observations of the Crab nebula with HESS. *Astronomy and Astrophysics*, 457:899–915, October 2006.
- [41] T. Murach, M. Gajdus, and R. D. Parsons. A Neural Network-Based Monoscopic Reconstruction Algorithm for H.E.S.S. II. In *Proceedings of the 34th International Cosmic Ray Conference*, September 2015.
- [42] MAGIC Collaboration, E. Aliu, et al. Improving the performance of the single-dish Cherenkov telescope MAGIC through the use of signal timing. *Astroparticle Physics*, 30:293–305, January 2009.
- [43] A. M. Hillas. Cherenkov light images of EAS produced by primary gamma. *International Cosmic Ray Conference*, 3:445–448, August 1985.
- [44] Y. Becherini, A. Djannati-Ataï, V. Marandon, M. Punch, and S. Pita. A new analysis strategy for detection of faint γ -ray sources with Imaging Atmospheric Cherenkov Telescopes. *Astroparticle Physics*, 34:858–870, July 2011.
- [45] S. Ohm, C. van Eldik, and K. Egberts. γ /hadron separation in very-high-energy γ -ray astronomy using a multivariate analysis method. *Astroparticle Physics*, 31:383–391, June 2009.

- [46] M. de Naurois and L. Rolland. A high performance likelihood reconstruction of γ -rays for imaging atmospheric Cherenkov telescopes. *Astroparticle Physics*, 32:231–252, December 2009.
- [47] R. D. Parsons and J. A. Hinton. A Monte Carlo template based analysis for air-Cherenkov arrays. *Astroparticle Physics*, 56:26–34, April 2014.
- [48] W. Hofmann, I. Jung, A. Konopelko, H. Krawczynski, H. Lampeitl, and G. Pühlhofer. Comparison of techniques to reconstruct VHE gamma-ray showers from multiple stereoscopic Cherenkov images. *Astroparticle Physics*, 12:135–143, November 1999.
- [49] D. Berge, S. Funk, and J. Hinton. Background modelling in very-high-energy γ -ray astronomy. *Astronomy and Astrophysics*, 466:1219–1229, May 2007.
- [50] L. Oakes, E. Birsin, G. Maier, U. Schwanke, and for the CTA Consortium. Impact of the Cherenkov Telescope Array (CTA) altitude on Dark Matter searches in the Milky Way Halo. *ArXiv e-prints*, July 2013.
- [51] T.-P. Li and Y.-Q. Ma. Analysis methods for results in gamma-ray astronomy. *The Astrophysical Journal*, 272:317–324, September 1983.
- [52] D. Heck, J. Knapp, J. N. Capdeville, G. Schatz, and T. Thouw. CORSIKA: A Monte Carlo Code to Simulate Extensive Air Showers. *Forschungszentrum Karlsruhe Report*, 6019, 1998.
- [53] K. Bernlöhr. Simulation of imaging atmospheric Cherenkov telescopes with CORSIKA and sim_telarray. *Astroparticle Physics*, 30:149–158, October 2008.
- [54] R. D. Parsons, M. Gajdus, T. Murach, and for the HESS Collaboration. HESS II Data Analysis with ImPACT. In *Proceedings of the 34th International Cosmic Ray Conference*, July 2015.
- [55] W. Hofmann. Performance Limits for Cherenkov Instruments. In *Cherenkov 2005 Workshop, Palaiseau*, March 2006.
- [56] M. Holler, D. Berge, C. van Eldik, J.-P. Lenain, V. Marandon, T. Murach, M. de Naurois, R. D. Parsons, H. Prokoph, D. Zaborov, and for the H. E. S. S. collaboration. Observations of the Crab Nebula with H.E.S.S. Phase II. In *Proceedings of the 34th International Cosmic Ray Conference*, July 2015.
- [57] F. Piron et al. Temporal and spectral gamma-ray properties of Mkn 421 above 250 GeV from CAT observations between 1996 and 2000. *Astronomy and Astrophysics*, 374:895–906, August 2001.
- [58] G. Vacanti, , P. Fleury, Y. Jiang, E. Paré, A. C. Rovero, X. Sarazin, M. Urban, and T. C. Weekes. Muon ring images with an atmospheric Čerenkov telescope. *Astroparticle Physics*, 2:1–11, February 1994.
- [59] O. Bolz. *Absolute Energiekalibration der abbildenden Cherenkov-Teleskope des H.E.S.S. Experiments und Ergebnisse erster Beobachtungen des Supernova Überrests RX J1713.7-3946*. PhD thesis, Ruprecht-Karls-Universität Heidelberg, 2004.

- [60] A M Hillas and J R Patterson. Characteristics and brightness of Cerenkov shower images for gamma-ray astronomy near 1 TeV. *Journal of Physics G: Nuclear and Particle Physics*, 16(8):1271, 1990.
- [61] R. Mirzoyan, D. Sobczynska, E. Lorenz, and M. Teshima. Tagging single muons and other long-flying relativistic charged particles by ultra-fast timing in air Cherenkov telescopes. *Astroparticle Physics*, 25:342–348, June 2006.
- [62] N. Leroy. *Observations avec les télescopes H.E.S.S. du rayonnement gamma émis par le Noyau Actif de Galaxie PKS 2155-304 au-delà de 100 GeV*. PhD thesis, l'Ecole Polytechnique, Paris, 2004.
- [63] A. C. Rovero, J. H. Buckley, P. Fleury, Y. Jiang, E. Pare, X. Sarazin, M. Urban, and T. C. Weekes. Calibration of the Whipple atmospheric Čerenkov telescope. *Astroparticle Physics*, 5:27–34, June 1996.
- [64] M. Shayduk, O. Kalekin, K. Mase, and N. Pavel. Calibration of the MAGIC telescope using muon ring images. In *Proceedings, 28th International Cosmic Ray Conference (ICRC 2003)*, pages 2951–2954, 2003.
- [65] T. B. Humensky. Calibration of VERITAS Telescope 1 via muons. In *29th International Cosmic Ray Conference (ICRC 2005) Pune, India, August 3-11, 2005*, 2005.
- [66] R. Chalme-Calvet, M. de Naurois, J.-P. Tavernet, and for the H.E.S.S. Collaboration. Muon efficiency of the H.E.S.S. telescope. In *Proceedings of the Atmospheric Monitoring for High-Energy Astroparticle Detectors (AtmoHEAD) Conference, Saclay (France)*, March 2014.
- [67] Bidyut Baran Chaudhuri and P Kundu. Optimum circular fit to weighted data in multi-dimensional space. *Pattern Recognition Letters*, 14(1):1–6, 1993.
- [68] F. James and M. Roos. Minuit - a system for function minimization and analysis of the parameter errors and correlations. *Computer Physics Communications*, 10:343–367, December 1975.
- [69] A. M. W. Mitchell, V. Marandon, R. D. Parsons, and for the H.E.S.S. Collaboration. A Generic Algorithm for IACT Optical Efficiency Calibration using Muons. In *Proceedings of the 34th International Cosmic Ray Conference*, July 2015.
- [70] M. Gaug, T. Armstrong, K. Bernlöhr, M. Daniel, M. Errando, M. C. Maccarone, P. Majumdar, T. Mineo, A. Mitchell, R. Moderski, R. D. Parsons, E. Prandini, and S. Toscana. *Using Muon Rings for the Optical Throughput Calibration of the Cherenkov Telescope Array*, September 2015.
- [71] W. Hofmann. Intercalibration of Cherenkov telescopes in telescope arrays. *Astroparticle Physics*, 20:1–3, October 2003.
- [72] R. Gast. Investigating Systematics in the Energy Reconstruction of the H.E.S.S. telescopes. Master's thesis, Ruprecht-Karls-Universität Heidelberg, 2009.

- [73] HEGRA Collaboration, F. A. Aharonian, et al. Measurement of the radial distribution of Cherenkov light generated by TeV gamma-ray air showers. *Astroparticle Physics*, 10:21–29, January 1999.
- [74] M. Gaug, D. Berge, M. Daniel, M. Doro, A. Förster, W. Hofmann, M. C. Maccarone, R. D. Parsons, R. de los Reyes Lopez, and C. van Eldik. Calibration strategies for the Cherenkov Telescope Array. In *Society of Photo-Optical Instrumentation Engineers (SPIE) Conference Series*, volume 9149 of *Society of Photo-Optical Instrumentation Engineers (SPIE) Conference Series*, page 19, August 2014.
- [75] K. Bernlöhr, *et al.*, and for the CTA Consortium. Progress in Monte Carlo design and optimization of the Cherenkov Telescope Array. In *Proceedings of the 33rd International Cosmic Ray Conference*, July 2013.
- [76] J. M. Davies and E. S. Cotton. Design of the quartermaster solar furnace. *Solar Energy*, 1:16–22, April 1957.
- [77] V. V. Vassiliev and S. J. Fegan. Schwarzschild-Couder two-mirror telescope for ground-based γ -ray astronomy. *International Cosmic Ray Conference*, 3:1445–1448, 2008.
- [78] K. Bernlöhr, *et al.*, and for the CTA Consortium. Monte Carlo design studies for the Cherenkov Telescope Array. *Astroparticle Physics*, 43:171–188, March 2013.
- [79] A. M. W. Mitchell, R. D. Parsons, W. Hofmann, and K. Bernlöhr. Cross calibration of telescope optical throughput efficiencies using reconstructed shower energies for the Cherenkov Telescope Array. *Astroparticle Physics*, 75:1–7, February 2016.
- [80] S. Lebohec and J. Holder. The cosmic ray background as a tool for relative calibration of atmospheric Cherenkov telescopes. *Astroparticle Physics*, 19:221–233, May 2003.
- [81] W. Baade and F. Zwicky. On Super-novae. *Proceedings of the National Academy of Science*, 20:254–259, May 1934.
- [82] W. Baade and F. Zwicky. Cosmic Rays from Super-novae. *Proceedings of the National Academy of Science*, 20:259–263, May 1934.
- [83] A. Hewish, S. J. Bell, J. D. H. Pilkington, P. F. Scott, and R. A. Collins. Observation of a Rapidly Pulsating Radio Source. *Nature*, 217:709–713, February 1968.
- [84] Nobelprize.org. The Nobel Prize in Physics 1974. http://www.nobelprize.org/nobel_prizes/physics/laureates/1974/, 2014. Accessed: 21-01-2016.
- [85] MAGIC Collaboration, E. Aliu, et al. Observation of Pulsed γ -Rays Above 25 GeV from the Crab Pulsar with MAGIC. *Science*, 322:1221, November 2008.
- [86] B. M. Gaensler and P. O. Slane. The Evolution and Structure of Pulsar Wind Nebulae. *Annual Reviews of Astronomy and Astrophysics*, 44:17–47, September 2006.
- [87] P. Goldreich and W. H. Julian. Pulsar Electrodynamics. *The Astrophysical Journal*, 157:869, August 1969.
- [88] P. A. Sturrock. A Model of Pulsars. *The Astrophysical Journal*, 164:529, March 1971.

- [89] J. Arons. Pair creation above pulsar polar caps - Geometrical structure and energetics of slot gaps. *The Astrophysical Journal*, 266:215–241, March 1983.
- [90] K. S. Cheng, C. Ho, and M. Ruderman. Energetic radiation from rapidly spinning pulsars. I - Outer magnetosphere gaps. II - VELA and Crab. *The Astrophysical Journal*, 300:500–539, January 1986.
- [91] P. A. Caraveo. Gamma-Ray Pulsar Revolution. *Annual Reviews of Astronomy and Astrophysics*, 52:211–250, August 2014.
- [92] S. P. Reynolds and R. A. Chevalier. Evolution of pulsar-driven supernova remnants. *The Astrophysical Journal*, 278:630–648, March 1984.
- [93] A. Abramowski et al. Probing the extent of the non-thermal emission from the Vela X region at TeV energies with H.E.S.S. *Astronomy and Astrophysics*, 548:A38, December 2012.
- [94] H.E.S.S. Collaboration, A. Abramowski, et al. Identification of HESS J1303-631 as a pulsar wind nebula through γ -ray, X-ray, and radio observations. *Astronomy and Astrophysics*, 548:A46, December 2012.
- [95] F. Aharonian et al. Energy dependent γ -ray morphology in the pulsar wind nebula HESS J1825-137. *Astronomy and Astrophysics*, 460:365–374, December 2006.
- [96] R. N. Manchester, G. B. Hobbs, A. Teoh, and M. Hobbs. The Australia Telescope National Facility Pulsar Catalogue. *The Astronomical Journal*, 129:1993–2006, April 2005.
- [97] E. de Oña-Wilhelmi, *et al.*, and for the CTA Consortium. Prospects for observations of pulsars and pulsar wind nebulae with CTA. *Astroparticle Physics*, 43:287–300, March 2013.
- [98] G. G. Pavlov, O. Kargaltsev, and W. F. Brisken. Chandra Observation of PSR B1823-13 and Its Pulsar Wind Nebula. *The Astrophysical Journal*, 675:683–694, March 2008.
- [99] J. P. Finley, R. Srinivasan, and S. Park. The Morphology of Young Neutron Stars: PSR B1823-13, Its Compact Nebula, and Its Interstellar Neighborhood. *The Astrophysical Journal*, 466:938, August 1996.
- [100] B. M. Gaensler, N. S. Schulz, V. M. Kaspi, M. J. Pivovarov, and W. E. Becker. XMM-Newton Observations of PSR B1823-13: An Asymmetric Synchrotron Nebula around a Vela-like Pulsar. *The Astrophysical Journal*, 588:441–451, May 2003.
- [101] F. A. Aharonian. A search for TeV gamma-ray emission from SNRs, pulsars and unidentified GeV sources in the Galactic plane in the longitude range between -2 deg and 85 deg. *Astronomy and Astrophysics*, 395, December 2002.
- [102] S. J. Fegan et al. A Survey of Unidentified EGRET Sources at Very High Energies. *The Astrophysical Journal*, 624:638–655, May 2005.
- [103] R. C. Hartman et al. The Third EGRET Catalog of High-Energy Gamma-Ray Sources. *The Astrophysical Journal Supplement*, 123:79–202, July 1999.

- [104] F. A. Aharonian et al. A possible association of the new VHE γ -ray source HESS J1825-137 with the pulsar wind nebula G18.0-0.7. *Astronomy and Astrophysics*, 442:L25–L29, November 2005.
- [105] F. Aharonian et al. 3.9 day orbital modulation in the TeV γ -ray flux and spectrum from the X-ray binary LS 5039. *Astronomy and Astrophysics*, 460:743–749, December 2006.
- [106] F. Aharonian et al. Discovery of Very High Energy Gamma Rays Associated with an X-ray Binary. *Science*, 309:746–749, July 2005.
- [107] C. Deil, *et al.*, and for the HESS Collaboration. H.E.S.S. Galactic plane survey. In *Proceedings of the 34rd International Cosmic Ray Conference*, July 2015.
- [108] A. Abramowski et al. Diffuse Galactic gamma-ray emission with H.E.S.S. *Physical Review D*, 90(12):122007, December 2014.
- [109] A. Van Etten and R. W. Romani. Multi-zone Modeling of the Pulsar Wind Nebula HESS J1825-137. *The Astrophysical Journal*, 742:62, December 2011.
- [110] J. Brucker. *Simultaneous Modelling of the Morphological and Spectral Features of the Pulsar Wind Nebula HESS J1825-137 in TeV γ -rays*. PhD thesis, Friedrich-Alexander-Universität Erlangen-Nürnberg, 2013.
- [111] M.-H. Grondin, S. Funk, M. Lemoine-Goumard, A. Van Etten, J. A. Hinton, et al. Detection of the Pulsar Wind Nebula HESS J1825-137 with the Fermi Large Area Telescope. *The Astrophysical Journal*, 738:42, September 2011.
- [112] M. Ackermann et al. 2FHL: The Second Catalog of Hard Fermi-LAT Sources. *The Astrophysical Journal Supplement*, 222:5, January 2016.
- [113] F. Voisin, G. Rowell, M. G. Burton, A. Walsh, Y. Fukui, and F. Aharonian. ISM gas studies towards the TeV PWN HESS J1825-137 and northern region. *Monthly Notices of the Royal Astronomical Society*, March 2016.
- [114] O. C. de Jager and A. Djannati-Ataï. Implications of HESS Observations of Pulsar Wind Nebulae. In W. Becker, editor, *Astrophysics and Space Science Library*, volume 357 of *Astrophysics and Space Science Library*, page 451, 2009.
- [115] H. Uchiyama, H. Matsumoto, T. G. Tsuru, K. Koyama, and A. Bamba. Suzaku Observation of HESS J1825-137: Discovery of Largely-Extended X-Rays from PSR J1826-1334. *Publications of the Astronomical Society of Japan*, 61:S189–S196, January 2009.
- [116] HAWC Collaboration, A. U. Abeysekara, et al. Search for TeV Gamma-Ray Emission from Point-like Sources in the Inner Galactic Plane with a Partial Configuration of the HAWC Observatory. *The Astrophysical Journal*, 817:3, January 2016.
- [117] G. R. Blumenthal and R. J. Gould. Bremsstrahlung, Synchrotron Radiation, and Compton Scattering of High-Energy Electrons Traversing Dilute Gases. *Reviews of Modern Physics*, 42:237–271, 1970.
- [118] R. Barlow. Asymmetric Systematic Errors. *ArXiv Physics e-prints*, June 2003.

- [119] Fermi-LAT Collaboration, F. Acero, et al. Fermi Large Area Telescope Third Source Catalog. *The Astrophysical Journal Supplement*, 218:23, June 2015.
- [120] M. J. Rees and J. E. Gunn. The origin of the magnetic field and relativistic particles in the Crab Nebula. *Monthly Notices of the Royal Astronomical Society*, 167:1–12, April 1974.
- [121] C. F. Kennel and F. V. Coroniti. Confinement of the Crab pulsar’s wind by its supernova remnant. *The Astrophysical Journal*, 283:694–709, August 1984.
- [122] O. Porth, S. S. Komissarov, and R. Keppens. Solution to the sigma problem of pulsar wind nebulae. *Monthly Notices of the Royal Astronomical Society*, 431:L48–L52, April 2013.
- [123] J. D. Gelfand, P. O. Slane, and W. Zhang. A Dynamical Model for the Evolution of a Pulsar Wind Nebula Inside a Nonradiative Supernova Remnant. *The Astrophysical Journal*, 703:2051–2067, October 2009.
- [124] A. M. Atoyan, F. A. Aharonian, and H. J. Völk. Electrons and positrons in the galactic cosmic rays. *Physical Review D*, 52:3265–3275, September 1995.
- [125] A. Lemièrè. *Electrons reliques de très haute énergie dans les nébuleuses de pulsar*. PhD thesis, Université Paris 7 - Denis Diderot, 2006.
- [126] J. Hahn. GAMERA - A Modular Framework for Spectral Modelling in VHE Astronomy. In *Proceedings of the 34th International Cosmic Ray Conference*, July 2015.
- [127] J. Martín, D. F. Torres, and N. Rea. Time-dependent modelling of pulsar wind nebulae: study on the impact of the diffusion-loss approximations. *Monthly Notices of the Royal Astronomical Society*, 427:415–427, November 2012.
- [128] D. F. Torres, A. Cillis, J. Martín, and E. de Oña Wilhelmi. Time-dependent modeling of TeV-detected, young pulsar wind nebulae. *Journal of High Energy Astrophysics*, 1:31–62, May 2014.
- [129] E. van der Swaluw, A. Achterberg, Y. A. Gallant, and G. Tóth. Pulsar wind nebulae in supernova remnants. Spherically symmetric hydrodynamical simulations. *Astronomy and Astrophysics*, 380:309–317, December 2001.
- [130] C. M. Espinoza, A. G. Lyne, B. W. Stappers, and M. Kramer. A study of 315 glitches in the rotation of 102 pulsars. *Monthly Notices of the Royal Astronomical Society*, 414:1679–1704, June 2011.
- [131] J. K. Truelove and C. F. McKee. Evolution of Nonradiative Supernova Remnants. *The Astrophysical Journal Supplement*, 120:299–326, February 1999.
- [132] R. P. Brent. An algorithm with guaranteed convergence for finding a zero of a function. *Computer Journal*, 14:422–425, 1971.
- [133] F. Aharonian et al. Discovery of very-high-energy γ -rays from the Galactic Centre ridge. *Nature*, 439:695–698, February 2006.
- [134] S. Gillessen. *Sub-Bogenminuten-genaue Positionen von TeV-Quellen mit H.E.S.S.* PhD thesis, Ruprecht-Karls-Universität Heidelberg, 2004.

List of Figures

1.1	Cosmic ray spectrum	2
1.2	Schematic of Diffusive Shock Acceleration	3
1.3	Astrophysical particle acceleration sites	4
2.1	Schematic of the Heitler model of air shower development	12
2.2	Simulated electromagnetic and hadronic showers	13
2.3	Schematic of Cherenkov radiation	14
2.4	Simulations of the Cherenkov cone and Cherenkov light pool	15
2.5	IACT imaging geometry and CT5 at zenith	17
2.6	Integral Sensitivity of CTA in comparison to other experiments	18
2.7	The H.E.S.S. II array	19
2.8	Definition of Hillas parameters	26
2.9	Illustration of the ring and reflected background methods	28
2.10	Angular resolution of H.E.S.S. II	31
2.11	Effective area of H.E.S.S. II	32
2.12	Energy bias of H.E.S.S. II	33
2.13	Changing H.E.S.S. energy threshold with zenith angle	33
2.14	Differential sensitivity of H.E.S.S. II	34
3.1	Geometrical situation of a muon incident on a Cherenkov telescope	38
3.2	Formation of a muon ring in the camera	39
3.3	Example muon events in H.E.S.S.	40
3.4	Muon ring radius as a function of energy	41
3.5	Ring broadening effects	43
3.6	Spectrum of Cherenkov light from muons and γ -rays	44
3.7	Reflector dishes of the H.E.S.S. telescopes	47
3.8	Distance to the mirror edge as a function of azimuth angle for CT1-4	48
3.9	Distance to the mirror edge as a function of azimuth angle for CT5	48
3.10	Azimuth muon intensity profile variation with impact distance	49
3.11	Example selected muon events and model expectations	50
3.12	Angular light distribution profile	51
3.13	Monte Carlo muon efficiency distributions for CT5	54
3.14	Ratio of Monte Carlo muon efficiencies between different algorithms	55
3.15	Linearity of the muon correction factor from Monte Carlo	56
3.16	Muon efficiency from one run of data using two different algorithms	56
3.17	Evolution of fractional muon efficiency over time	58
3.18	Comparison of muon correction factor between algorithms on data	59
3.19	Number of muon events per run	60

3.20	Impact parameter and ring width with muon efficiency	61
3.21	Muon efficiency with impact position	62
3.22	Muon efficiency variation with zenith angle and azimuth angle	63
3.23	Monte Carlo muon images with broken pixels	64
3.24	Muon efficiency with increasing amounts of broken pixels	64
3.25	Number of muon events passing cuts with increasing numbers of broken pixels . .	65
3.26	Number of muons passing different cuts with increasing numbers of broken pixels	66
3.27	Muon efficiency with aerosol content	67
3.28	Muon efficiency with temperature, pressure and humidity	67
3.29	Monte Carlo muon efficiency with mass of the primary cosmic ray	68
3.30	Muon Efficiency correction factor for Monte Carlo phase optimisation	70
3.31	Effective area ratio with increasing correction factor	71
3.32	Muon efficiency evolution with run-wise, night-wise and period-wise averaging . .	72
3.33	Variation of run-wise muon values around nightly average	72
3.34	Schematic of potential CTA reflector dishes	74
3.35	Simulated Muon events in CTA cameras	75
3.36	Variation of distance to mirror edge with azimuth angle for an LST	76
3.37	Schematic of a muon incident on a dual mirror telescope	76
3.38	Variation in distance traversed across the reflector dishes of an SST with azimuthal angle	77
3.39	Muon efficiency distributions for a Schwarzschild-Couder SST	78
3.40	Linearity of the muon correction factor with optical degradation, shown on CTA telescope simulations	79
3.41	Number of muons passing cuts for CTA telescopes	80
4.1	Monte Carlo histogram of size asymmetry against distance asymmetry, with pro- jection	85
4.2	Two components of a size asymmetry against distance asymmetry histogram . . .	86
4.3	Monte Carlo histogram of energy asymmetry against shower energy, and zenith angle variation	87
4.4	Correlation of image size and shower energy response efficiencies, as found on data	88
4.5	Monte Carlo test of cross calibration	89
4.6	Monte Carlo histogram of image size asymmetry between CT1 and CT5	90
4.7	Monte Carlo histogram of energy asymmetry between one of CT1-4 and CT5, and zenith angle variation	91
4.8	Energy asymmetry histogram showing the fit to find a safe cut on the energy bias from data	92
4.9	Image size ratio with zenith angle	93
4.10	Image amplitude against reconstructed energy	94
4.11	Cross calibration results as a function of zenith angle	94
4.12	Energy bias cut as a function of zenith angle	95
4.13	CTA Monte Carlo histograms of image size asymmetry against distance asymme- try for an LST pair and an SST pair	97
4.14	Linear fit to the distance asymmetry profile for two SSTs	98
4.15	Schematic of part of a potential CTA layout, showing which telescope pairs are used in this calibration	100
4.16	Monte Carlo array layouts used for the CTA cross calibration studies	101

4.17	Correlation of the measured asymmetries from the Monte Carlo reconstruction to the expected values	102
4.18	Correlation of the recovered telescope response efficiencies to the expected values	104
4.19	Distribution of residuals in the recovered optical efficiencies	105
4.20	Correlation of measured asymmetries with expected values from hadron simulations	107
4.21	Correlation of measured asymmetries to the expected values in the case of a biased energy reconstruction	108
4.22	Distribution of measured telescope pair asymmetries with an iterative approach .	109
5.1	Cross calibration with image size against muon efficiency	113
5.2	Energy cross calibration results over time	114
5.3	Improved energy cross calibration results with the new muon phases	115
5.4	Cross calibration with image size against run number	116
5.5	Cross calibration results with no muon correction applied	116
5.6	Cross calibration with reconstructed energy against muon efficiency	117
6.1	Schematic of a pulsar environment	122
6.2	Schematic of an SNR/PWN system	125
6.3	Vela X and HESS J1303-631: offset PWN at TeV energies	126
6.4	Radio Pulsar Population: spin-down power and age distribution	127
6.5	Excess sky map of HESS J1825-137 from [95]	128
6.6	Observation positions for datasets A and B on the HESS J1825-137 region	130
6.7	Cross calibration results for dataset A1	132
6.8	Cross calibration results for dataset B	132
6.9	Cross calibration checks	133
6.10	Significance maps and exclusion regions used for dataset A	134
6.11	Diagnostic plots from the dataset A analysis	135
6.12	Dataset B significance maps	136
6.13	Excluded significance in the stereo analysis of dataset B	136
6.14	Map showing the boxes used for spectral extraction	137
6.15	Spectrum from the full HESS J1825-137 extent	139
6.16	Power law index and flux with distance from the pulsar	139
6.17	Flux and photon index compared to [95]	140
6.18	Spectra extracted from wedges, from [95]	141
6.19	Power law index with distance using regions defined in [95]	142
6.20	Ring-shaped regions centred on the pulsar	142
6.21	Power law index and surface brightness from a spectral analysis of ring-shaped regions	143
6.22	Overlaid spectra from increasing radial distances	144
6.23	Azimuthal profile of the emission	144
6.24	Significance map showing regions for spectral extraction from wedges	145
6.25	Power law index and surface brightness from a spectral analysis of wedge-shaped regions with fixed opening angle	146
6.26	Azimuthal profiles of emission from rings around the pulsar at different radii . . .	148
6.27	Gaussian mean and width from fits to azimuthal profiles around rings, going radially outwards from pulsar.	149
6.28	Excess map and slices from [95]	149

6.29	Slices along the major and minor axes from the excess map	150
6.30	Regions used for characterising the extent of the nebula	152
6.31	Radial profile fitting for extent measurements	153
6.32	Radial extent with energy, variation with order of the polynomial fit	153
6.33	Energy band maps and radial profiles < 2 TeV	154
6.34	Energy band maps and radial profiles > 2 TeV	155
6.35	Low energy maps	156
6.36	Radial extent as a function of energy along the Northern and Southern sides of the pulsar	157
6.37	Southern extent dataset comparison using a reduced livetime	158
6.38	Extent of the nebula in quadrants A and B	159
7.1	HESS J1825-137 region in infrared and radio bands	161
7.2	H α map of the HESS J1825-137 region	162
7.3	Suzaku X-ray maps of the HESS J1825-137 region	162
7.4	Radial profile of X-ray brightness of HESS J1825-137	163
7.5	Fermi and H.E.S.S. joint SED from [111]	164
7.6	HAWC significance map of the inner Galactic plane	165
7.7	Linear fit to the physical extent with energy	166
7.8	Radius against energy gradients for different transport scenarios	168
7.9	Radius against energy curves for different transport scenarios	171
7.10	Suzaku X-ray observation positions and spectral extraction regions	172
7.11	Fitted joint X-ray and γ -ray SEDs to the box extraction regions	175
7.12	Schematic of a multi zone modelling approach	181
7.13	Model fit to an SED from [109]	181
7.14	Model 1: luminosity, radius and magnetic field evolution	187
7.15	Particle and γ -ray spectrum from free expansion model 1	187
7.16	Particle and γ -ray spectrum from free expansion model 2	188
7.17	SNR and PWN shock radius evolution	189
7.18	Kinematical Reverse Shock: luminosity, radius, velocity and magnetic field evolution	191
7.19	Particle and γ -ray spectrum from free expansion model 1	192
7.20	Particle and γ -ray spectrum from free expansion model 1	192
A.1	Cosmic ray event rate with image size (Monte Carlo)	198
A.2	Cosmic ray event rate with image size (data)	198
A.3	Geometry for pointing calibration via image comparison	199
A.4	Pointing offset distributions from Monte Carlo	200
A.5	Parallel pointing offset with altitude	200
A.6	Orthogonal pointing offset with azimuth	201
A.7	Light yield with radial distance, from gamma simulations and data	204
A.8	Light yield with radial distance, from hadron simulations and background domi- nated data	205
A.9	Relative light yield with radial distance for two HESS I telescopes as a function of zenith angle	206
A.10	Relative light yield with radial distance for two HESS I telescopes at 1 $^\circ$ off-axis .	207
A.11	Relative light yield with radial distance between CT5 and a HESS I telescope at 1 $^\circ$ off-axis	207

A.12	Time delay between same type telescope pairs	209
A.13	Time delay between LST and MST telescope pairs	211
A.14	Time delay between MST and SST telescope pairs	212
C.1	Energy band excess maps and slice profiles < 1 TeV	217
C.2	Energy band excess maps and slice profiles > 1 TeV	218

List of Tables

3.1	Muon image selection cuts	53
3.2	Monte Carlo muon phases	69
3.3	Muon selection cuts for simulations of CTA telescopes	78
4.1	Intercalibration event selection cuts	83
4.2	Number of telescopes and telescope pairs used for cross calibration	101
4.3	Cut values used for the different CTA telescope types in this cross calibration study	101
4.4	RMS percentage residuals of the recovered optical efficiencies	105
4.5	RMS percentage residuals of the recovered optical efficiencies from hadronic simulations	107
4.6	RMS percentage residuals of the recovered optical efficiencies in the case of a biased energy reconstruction	109
6.1	Data contributing to the HESS J1825-137 analysis	130
6.2	Spectral fit parameters	138
7.1	X-ray spectral fit parameters	164
7.2	Parameters of a linear fit to the radial extent with energy	167
7.3	Fit results for magnetic field of HESS J1825-137	174
7.4	Fit results for the magnetic field of HESS J1825-137 using a broken power law model	176
7.5	Derived energy densities based on the X-ray fit results	177
7.6	Derived lifetimes and diffusion radii based on the X-ray fit results	178
7.7	Particle spectrum break energy	179
7.8	Summary of equations governing the PWN models used	182
7.9	Radiation fields contributing to the Inverse Compton emission	183
7.10	Input parameters used in the models	185
7.11	Spectral parameters for the one-zone model used for SED fitting	186
7.12	Fitted spectral parameters for reverse shock model	192
A.1	Time delays between telescope types	210

Acknowledgements

First and foremost, I would like to thank Prof. Dr. W. Hofmann, for the chance to complete my PhD in Heidelberg, to join the MPIK group and to work on a variety of topics. Also for his uncanny ability to identify and correct mistakes at a glance. Prof. Dr. S. Wagner for the thesis committee supervision and his willingness to travel out of his way for the purpose. Prof. Dr. Jim Hinton, for the scientific guidance and advice, especially for asking some interesting, leading questions. Prof. Dr. S. Funk, I'd also like to thank for agreeing to referee this work.

Dan Parsons and Vincent Marandon, for their patience and help with answering endless questions, HAP queries and bug fixes, and without whom a large proportion of this thesis would not have been possible. Also for reading through and checking the majority of this work, not just the final thesis, but also the results at every step along the way.

Joachim Hahn for his guidance with the modelling aspect and help with using the GAMERA/GAPPA package. Peter Eger for doing the Suzaku analysis and helping convert the X-ray data. Christoph Deil for help with python-related questions and finding a few bugs I accidentally introduced. Raquel de los Reyes and Andreas Förster for their feedback and interaction on CTA calibration topics. Thanks also to Joachim, Peter and Raquel for reading parts of this thesis.

Axel Donath and Johannes King, for the office discussions that helped us to understand new concepts, for the impromptu music playing, for yet more python questions, and for having a laugh now and then. For the innumerable times you heard “err, Axel ...” Luigi, for some rather last minute improvements relating to Fermi data. A big thank you to Ruth Crespo who is absolutely indispensable in navigating bureaucracy, translating “Amtsdeutsch ” for the rest of us.

To the rest of the MPIK group past and present, thank you for an excellent working environment, for the friendly atmosphere, for there being someone for nearly every problem and for making the experience a good one.

Thank you to all the H.E.S.S. colleagues from other institutes, for the collaborative atmosphere and constructive meetings, both online and in person. A special thanks to those with whom I went on shift at the H.E.S.S. site, Iurii, Jarryd, Jill and Matthias, for making it a great experience. Thanks also to those who helped to resolve problems remotely, especially Arnim Balzer, Faiçal Ait Benkhali and Thomas Murach.

Thank you to all the H.E.S.S. site crew; Albert, Frikkie, Toni and Volker; for making the time in Namibia a welcoming and unforgettable one, and for your tireless work in keeping H.E.S.S. running. (A special thanks to Frikkie for extending that welcome beyond the shift and into Windhoek, not once but twice.)

To the CTA calibration colleagues, thank you for the recommendations and comments which helped to improve the versatility of the calibration methods, and thank you to everyone involved in making [79] possible.

A big thank you to Dr. Christian Fendt and the International Max Planck Research School for Astronomy and Cosmic Physics at the University of Heidelberg (mercifully shortened to IMPRS-HD) for the multifaceted support and the opportunity to study in Heidelberg.

To my fellow IMPRS students, thanks for the socialising, for many laughs and the enjoyable times together; I wish you all the best of luck in finishing your PhDs and in the future.

Meinen Freunden aus dem Uni-Orchester und den schottischen Tänzern, ich bedanke mich ganz herzlich für die tolle Zeit, die Gelegenheit bei verschiedenen Aufführungen mitzuwirken, und auch für die Verbesserung meines Deutschen! Ihr habt mir sehr geholfen, dass ich mich in Heidelberg wohl fühle.

To my friends in the UK, thanks for your steadfastness despite the miles, for the emails and Skype calls, and the infrequent catch-ups. Thank you for your support and encouragement before I arrived in Heidelberg.

To Peter, what can I say? Thank you for being there and for brightening up my life, for all our happy times together, past, present and future. Eine ganz Herzlichen Dank auch an deine Familie. Ihr habt mich in eurer Familie herzlich aufgenommen. Ich genieße die Zeit mit euch sehr.

Mum, for your support, generosity and love over more than a quarter of a century, “thank you” feels inadequate. Nevertheless, thanks for sticking by me and putting me back on track, for keeping me motivated, for your encouragement and for reminding me to hyphenate!

To anyone who feels themselves forgotten, please accept my apologies and consider yourself remembered here.